Nuclear reaction codes development for the particles and nuclei production in meteoroids and planetary atmospheres

Inaugural dissertation
of the Faculty of Science,
University of Bern

presented by

Jason Hirtz

from France

Supervisor of the doctoral thesis:
Prof. Dr. Ingo Leya
Physics Institute

Accepted by the Faculty of Science.

Bern, September 30th 2019

The Dean
Prof. Dr. Zoltan Balogh

I do have faith.
I don't have faith that a God exists, nor do I have faith that one does not;
I have absolute faith that I do not know, cannot know, am only human, am an infinitesimal creature packed onto a cramped planet crowded with seven billion bodies, and as many yearning hearts, and as many questioning minds.

Marya Hornbacher

Acknowledgment

Une thèse de doctorat est une étape majeure dans la vie d'un scientifique. C'est notamment un travail Gargantuesque dont on se demande sans arrêt s'il aura jamais une fin (spoiler alert: la réponse est non!). Pour autant, une thèse, c'est bien plus que ça. C'est aussi un cheminement philosophique, des voyages, des émotions... mais c'est aussi et surtout des rencontres et des discussions (pour ne pas dire des débats acharnés). Tout cela aurait été bien différent, voir complètement impossible sans la présence de bien d'autres personnes qui m'ont entouré. Il convient donc de remercier toutes ces personnes qui m'ont permis de réaliser cette thèse dans de si bonnes conditions en m'apportant leur collaboration et/ou leur soutient. Je vais donc faire ça dans l'ordre chronologique.

Les premières personnes que je voudrais remercier sont mes parents. Ce sont d'abord eux qui ont fait de moi celui que je suis devenu. Ma mère m'a donné le goût des mathématiques quand mon père m'a transmis une curiosité insatiable pour la nature et ses règles fondamentales. Il m'a aussi appris à me poser les bonnes questions. Vient ensuite Bruno, à la fois mon oncle et mon parrain, qui m'a offert mon premier télescope et qui a sûrement été un des premiers à se rendre compte que "quand je serai grand, je serai astrophysicien" n'était pas qu'un rêve d'enfant mais que j'allais en faire une réalité. C'est que, quand j'ai une idée arrêtée dans la tête, il est difficile de me faire changer d'avis! Robin, certes nous avons eu beaucoup de dispute, de bagarre et de désaccord étant plus jeune, mais moi aussi je t'aime (enfin pas trop non plus; il faut pas déconner!). Je souhaite aussi la bienvenu dans la famille à ma nouvelle sœur, Justine. Plus généralement, je voudrais remercier l'ensemble de ma famille qui a toujours cru en moi et ont toujours été un support sur lequel je pouvais compter. Vous êtes tous si différents les uns des autres que je voudrais écrire un paragraphe pour chacun d'entre vous. Malheureusement, il va falloir que je me restreigne. En tout cas, merci pour tout ces bons moments passés ensemble dans les réunions de famille qui me rappel que, même si mon esprit tend vers les étoiles, j'ai de bonne raison de revenir sur Terre de temps en temps.

Viennent ensuite les amis que j'ai connu avant ma thèse. J'ai toujours dit que les amis, se sont les membres de ma famille que j'ai choisi. Pour moi, peu de choses sont plus importantes que ces amitiés que j'ai su nouer dans mon enfance contre toute attente considérant mon naturel solitaire. En tête de ces amitiés, je mettrai Julien, mon alter ego: un solitaire curieux de toutes choses (dignes d'intérêt) et avec des solutions géniales pour changer le monde en mieux mais qui ne les partages pas, pas parce qu'il considère que personne ne mérite de les entendre, mais parce qu'il fait beau dans le Champsaur et que les glaçons dans le pastis fondent. On ne peut pas être partout à la fois! Vient avec lui, Sébastien. Nos différences sont bien plus marquées. Quand je me défini comme un solitaire avec la tête dans les étoiles, Sébastien a une intelligence sociale rare et est bien plus terre à terre, sauf quand il s'agit de faire des plans sur la comète. Cependant, ce qui nous a rapproché et a fait de Julien, Sébastien et moi même un trio inséparable, ce sont nos passions communes. On citera les passions respectable pour la nature, la montagne et l'histoire des grandes guerres, mais aussi des passions d'un autre genre pour les barbecues

et méchouis avec des proportions de viande que je qualifierai de “déraisonnable” et pour les alcools faits maison. La dernière dans la liste de mes amis de longue date est en fait la première de mes amis. 22 ans déjà que nous sommes amis avec Marie. À se niveau là, elle relève plus de la petite sœur que de l'amie pour moi. Une fois encore, je me demande comment une aussi longue amitié a pu s'installer considérant nos différences de caractère. Il faut croire que l'amour pour les montagnes du Champsaur et des mères prof de maths furent extrêmement efficace pour nourrir cette longue amitié. Il y a encore beaucoup d'autre amis que je voudrais citer parmi lesquels Dorian et Julie (c'est toujours un plaisir de partager un repas avec vous), Nicolas (la graine de folie dans ma vie) et Enzo, l'allemand qui parlait mieux français que bien des natifs.

Viennent ensuite les personnes que j'ai rencontrées pendant ma thèse. Pour faire bonne mesure, Je vais diviser les personnes en 2 catégories. Les francophones et les English speakers (j'ai toujours su que j'étais xénophobe au fond de moi). Si vous parlez les deux langues, il va falloir chercher où vous êtes cité!

Pour les francophones, je commencerai par remercier Jean-Christophe, mon superviseur au CEA, pour m'avoir donné la chance de faire mes preuves, pour l'écoute dont il a su faire preuve et pour avoir passé de longues heures à corriger mes fautes d'anglais et à essayer de comprendre le bazar dans ma tête. Non des moindres vient ensuite Georg, un pro de l'informatique très doué quand il s'agit de faire des ponts en chaine et pour lancer 15 000 jobs sur iclust “sans faire exprès”. Quand je fus ton professeur de français, tu fus mon maître à penser en statistique bayésienne. Aujourd'hui, je ne jure plus que par ça! Vient ensuite Loïc, le co-fondateur des “précaires” de DPhN, ex-SPhN. Nous avons partagé beaucoup de bon moment depuis les repas aux algo jusqu'à la Grèce dont je me souviendrai longtemps. En parlant de la Grèce, je voudrais dire un grand merci à $\Mu\alpha\rho\acute{\iota}\alpha$, qui nous y a invité à l'occasion de son mariage, et à sont mari, $\Beta\alpha\sigma\acute{\iota}\lambda\eta\varsigma$ pour nos trop rares parties de basket. J'ai adoré découvrir votre magnifique pays. Vient ensuite l'ensemble des précaires du CEA. Notamment, je citerai Nancy, qui m'a bien aidé pour l'organisation des cafés et des sorties précaires et qui, après mon départ, a accepté de reprendre le flambeau de la présidence. Ensuite, je citerai en vrac les théoriciens, Arthur, Medhi, Benjamin et Nabil, le groupe du milieu du couloir avec Antoine et Aurélie, et le marseillais Christophe aux grands pieds.

For the English speakers, the first person I want to thank is Ingo, my supervisor in Bern, who chose me among all the other candidates to carry out this PhD and gave me the liberty I need to make the most of myself along this PhD. I hope you do not regret your past choice even after all the mess I brought. Then, I want to thank Hammad, who was a real friend and helped me to improve my English with our regular conversations. The Polish are numerous in the list of persons I met along this PhD. I would like to thank Michał, Michalina, and Małgorzata in the order of meeting, for in the disorder, the good moments around coffees, sharing dinner and drinks or on the shore of a wonderful lake in Italy (I know, it was a secret but I could not keep it :P). Just a thought: other letter than -M also exists to start your first name you know? Then comes the Italians with Alessendro (I still have compromising pictures of you in my swimming pool!) and Andreina for their Italian temperament, which always brings the Sun of the South that missed me so much when I was in Paris. The Indians are even more numerous than the Polish in the world of science! It seams that being a billions of them on Earth would increase the probability to meet one of them. If only I knew someone who could calculate the probability... Between all of them, I would like to thank Surya, who shared my office for an entire year, and Saba, who is not scared to participate in French conversations. I also thank all the people I worked and published with. I know it is hard to work with someone who goes in every direction at the same time but does not look back to be sure people are still following.

Between all the people I met only a few times or not at all but provided me an assistance when I needed it, I would like to thanks Laurent Desorgher, who gave me access to the source code of PlanetoCosmic. I used the reading of this code as an accelerated class about planetology, and I gained a lot of time thanks to this. I also want to thank Dennis Wright for our discussions and the validation of the calculations we did with the Bertini model and Jozef Masarik who accept to be in the jury of my defence. Finally, I thank

the people who allowed me to reuse their work and their figures in my publications.

J'espère n'avoir oublié personne. Pour autant, il y a tellement de gens à remercier qu'il serait surprenant que ce ne soit pas le cas, qui plus est avec ma réputation de tête dans la Lune. Je tiens donc à présenter mes excuses à ceux que j'aurais pu oublier. Je vous autorise à m'enlever de votre propre liste de personne à remercer dans votre thèse. Si vous n'avez pas prévu de passer votre doctorat ou si vous avez déjà soutenu votre thèse, je vous enjoins respectivement à changer d'avis ou à en préparer une nouvelle. Sinon, tant pis pour vous!

Contents

Celui qui ne sait pas d'où il vient ne peut savoir où il va car il ne sait pas où il est.
En ce sens, le passé est la rampe de lancement vers l'avenir

Otto von Habsburg (Le nouveau défi européen)

Chapter I

Introduction

Through history, humans always tried answering the two existential questions: "Where do we come from?" and "Where shall we go?". While it belongs to philosophers, to governments, to social sciences, and to each of us to answer the question "Where shall we go?", we should be able to have at least a partial answer to the question "Where do we come from?". Only knowing the past enables one to make useful predictions for the future.

The question "Where do we come from?" is not only a philosophical one. It is foremost a question with an answer based on facts and observations, which can be studied scientifically. Thereby a major task of historians, archaeologists, palaeontologists, geologists, and (astro)physicists is to study facts and observations and to understand how the world evolved. While the scientists study the history at different time scales; the sum of their researches allows us to have a better understanding of what happened since the beginning of the universe. With a good knowledge of our past, we can understand the present and predict the future more precisely. The different studies are very often based on the traces left by the various events that happened in the past. These traces are often analysed using methods coming either from physics (^{14}C dating) or from chemistry (chemical composition analysis). Based on the experimental data, scientists propose scenarios to explain the observations. Finally, a good theory also studies the likelihood of the hypothesis considering all available information.

The group in Berne at the time of writing this thesis comprised of four members: a geologist, a chemist, a physicist, and an astrophysicist. The objective of our group is mainly focused on the study of meteorite histories. "Where do they come from?", "How long was their journey?", and "How long have they been on Earth?" are common questions we try to answer. This quest is aided and guided by the measurements of isotopes in meteorites. They are produced by cosmic rays and known as cosmogenic nuclides. The group studies also cosmogenic nuclide production high in the atmosphere as well as at the surface of moons and planets. The analysis of cosmogenic nuclide abundances in the studied objects gives crucial information about their irradiation histories. However, we can go one step further and try to understand the history of the cosmic rays and, by extension, to better understand the history of the solar system, galaxy, and the universe. The actual works of the different group members are very different but complementary in the objective to answer the question "Where do meteorites, cosmic rays, etc. come from?". And, as we know: "We" are all stardust, "We" are the result of the interaction between different types of stars, dust, and cosmic rays since the beginning of the universe. In this sense, we can also say that the objective of our group is to help answering the fundamental question "Where do we come from?".

Nowadays, we understand the origin and the physics of the cosmic rays relatively well, even if fundamental questions are still not answered. Cosmic rays are free elementary particles and atomic nuclei travelling though the universe. They are mainly produced by dying stars, mostly supernova explosions. Then, they propagate in the vacuum of space with a velocity often close to the speed of light. Finally, the particles end their lives in hard collisions with massive objects like planets and meteoroids (the name of

meteorites before they fall on Earth or another planet). In addition, there are also interactions within the galactic cosmic rays (GCR) itself, *i.e.*, GCR particles interacting with other GCR particles. Taking into account their quantities and their effects, the cosmic ray spectrum relevant for our studies is dominated by hadrons (mainly protons and alpha particles) with energies in the range of few GeV. When such particles collide with a nucleus in a meteoroid, a planet, or an atmosphere, it results in a phenomenon known as nuclear spallation.

Nuclear spallation (hereafter simply called spallation) is a complex phenomenon, which happens when a light particle collides with a heavier nucleus with energies in the energy range of a few GeV. This collision leads to a fragmentation of the involved nucleus, often leading to a smaller nuclide and to the emission of hadrons and small clusters. A good example of such a type of reaction is the case of a proton colliding with a lead nucleus at a relatively high energy. This can result in the formation of a gold nucleus with the ejection of some protons and neutrons. It does make us wonder what would the alchemists of the past centuries say if they knew that lead can naturally turn into gold while being irradiated in space? Could we perhaps find the famous philosopher's stone in the cosmic rays? Behind this nice but very specific example, it is important to emphasis that the chemical composition of an object in space can be and actually is modified. The nuclei in the objects exposed to cosmic rays can be transformed into other elements through spallation reactions and this is a naturally occurring phenomenon. The study of the isotope composition of the irradiated objects allows us to get information about their exposure history. Moreover, some of the often studied cosmogenic nuclides are radioactive. Therefore, an equilibrium between production and decay will be reached after some irradiation time, which depends on the half-life of the studied nuclide. This equilibrium not only depends on the irradiation history but is also disturbed if changes happen in the irradiation set-up (*e.g.*, if the meteorite fall on Earth where it is shielded from cosmic rays). Therefore, studying isotope ratios makes it also possible to obtain information about the history of the objects after being exposed to cosmic rays. As an example, for a meteorite, the measurement of some of the isotope ratios involving radioactive cosmogenic nuclides allows us to determine when the meteorite fell on Earth and it also provides information about the journey of the meteorite and finally about the cosmic rays themself.

A reliable interpretation of the measured nuclide abundances and isotope ratios requires a deep understanding of the irradiation process. Notably, the fluxes of primary and secondary cosmic ray particles must be known with high precision as a function of particle types, energy, and depth within the irradiated object as well as a function of the size and chemical composition of the irradiated object. In addition, there is a need to know the interaction cross sections between the different elements present in the target and the cosmic ray particles. The complexity of all involved processes makes it impossible to understand cosmogenic nuclides synthesis only based on experimental data. The best solution available for this problem is to carry out sophisticated physical simulations, which allows to study all involved processes at minimal cost in terms of time and money. However, such simulations must be validated by experiments for various representative cases to ensure the reliability of the prediction for unknown and/or not well-studied regions.

This is in this context that my thesis took place. My work was to develop a program simulating the cosmic ray irradiation of meteoroids and (exo)planetary atmospheres. This program is named Cosmic-Transmutation. The objective of this program is to predict the fluxes of light particles (protons, neutrons, and alpha particles) together with the radioisotope production in meteorites and atmospheres. Another point of interest of this program is to study the links between the irradiation spectrum and the effects on the exposed object. This would help to better understand and interpret the experimental data. For example, detection thresholds could be established, which can guide future experiments.

The first two years of my PhD were spent at the CEA Saclay (France), in the DPhN (Département de Physique Nucléaire). My work there was to improve and validate the IntraNuclear Cascade model of Liège (INCL), which describes and quantifies the output of spallation reactions. The code INCL is included in the transport model Geant4. The objectives were threefold. The first objective was an improvement of the INCL model *i.e.*, an extension to high energies, which resulted in a better prediction of spallation

reactions. The second objective was to develop a deep understanding of the Geant4 and INCL models and of the associated physics, which are crucial parts of the final CosmicTransmutation model. The last objective was to further develop my programming skills, especially in C++, which were highly useful during the development of the CosmicTransmutation model.

After the improvement of the INCL code and its implementation into the public version of Geant4, the last two years of my thesis took place at the University of Bern, in Switzerland and were devoted to the development of the CosmicTransmutation model and to the analysis of first results.

The first phase of this thesis allowed me to answer two important questions coming with the development of any program: "How much can we trust this program?" and "What are the important input parameters that should be taken into account to make correct predictions?". In the second phase, I learned what type of predictions are needed to understand the history of meteorites. This thesis develops and explains the work done during the PhD with the development and the validation of the different models I worked on. Additionally, I will discuss how the different types of data can be interpreted.

The thesis is organised as follows. First, chapter II describes the basic concepts of this thesis, which are cosmogenic nuclides, cosmic rays, and spallation. In chapter III, I presents the IntraNuclear Cascade model INCL that has been developed and used all along this PhD. Chapter IV is devoted to the implementation of strange particles into INCL realised at the CEA Saclay. It is followed by chapter V, which describes the variance reduction scheme introduced to boost the study of strange particle production in INCL by avoiding statistical problems. Next, chapter VI corresponds to the final part of the work carried out at CEA Saclay; it presents the results obtained with the newly developed version of INCL. Similarly, chapter VII summarises the development of the CosmicTransmutation model realised at the University of Bern. Thereafter, chapter VIII presents first results obtained with the CosmicTransmutation model. Finally, chapter IX draws a conclusion of the work carried out during this PhD and I will discuss some possibilities for future work.

Chapter II

Basic concepts and applications

The work carried out during this thesis can been divided into two relatively independent parts. The development of INCL, which was the first part of this work, was motivated by the second part, *i.e.*, by the application for cosmogenic nuclides. However, besides the study of cosmogenic nuclides, there was a variety of further motivating points for improving and further developing INCL. Consequently, such a heterogeneous project is based on a large number of basic concepts, which are introduced in this chapter.

Here I give a general overview of the arguments why is was necessary to improve INCL with a special emphasis on combining the two different parts of this PhD. To do so, I develop the scientific context of this thesis, its basic concepts, and its motivations and applications.

II.1 Concepts and Context

This thesis is centred around three concepts: cosmogenic nuclides, cosmic rays, and nuclear spallation. All three concepts already exist for a long time (1934 [1], 1912 [2], and 1937 [3] respectively). However, the possibilities to simulate and predict these phenomena are relatively recent. Major progress was made thanks to the improvement of computing power that has been realised in the last few decades. This created a renewed interest in the three concepts relevant for this thesis. The number of publications about these subjects increased by orders of magnitude in the past decades. Here, I summarise only the very basic concepts, which are important for a proper understanding of the thesis at hand.

II.1.1 The cosmic rays

The cosmic rays were first identified when the scientists realised that the level of natural radiation increases with increasing altitude in contrast to the expected decrease if the radiation would have been originated in the ground [2]. This observation led to the conclusion that a significant part of the radiation observed at the ground level comes actually from above. With time, physicists measured the flux and the nature of cosmic rays not only on or close to the ground level but also in the atmosphere and even in space.

Two main types of cosmic rays can be distinguished. First, the solar cosmic rays that are produced by solar flares and/or solar energetic particle events on the sun. The composition of these cosmic rays correspond to solar composition and the flux varies with the solar activity and generally decreases with the square of the distance to the sun. The spectrum consists mostly of relatively low energy (< 10 MeV) protons but some particles can reach energies in the range of hundreds of MeV. The second type of cosmic rays are the galactic cosmic rays, which are supposed to be created in explosive stellar events like supernovae. The galactic cosmic rays consist mostly of protons and alpha particles (see Figure II.1). In contrast to solar cosmic rays, the flux decreases when the solar activity, and with it the solar magnetic

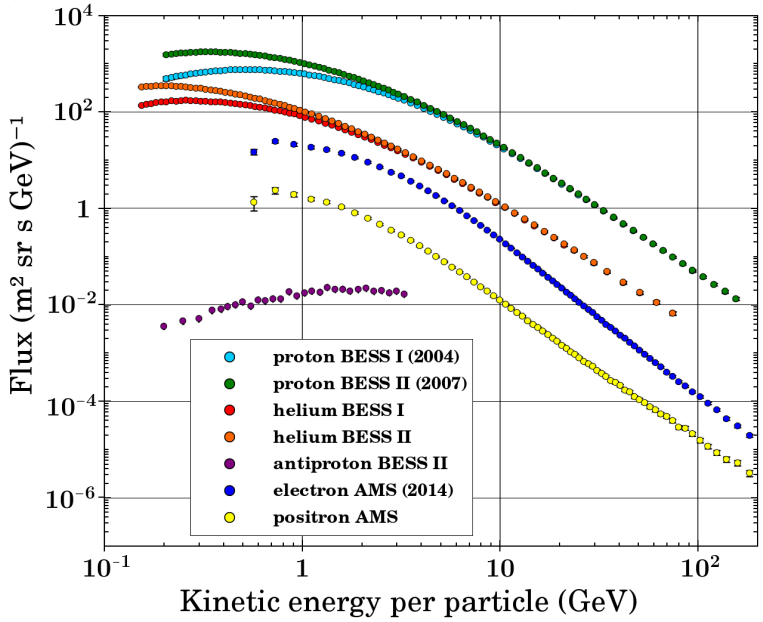

Figure II.1: Galactic cosmic ray spectra in the 100 MeV-200 GeV energy range. Data for protons, alphas, antiprotons were measured by the the BESS-Polar collaboration [4, 5] and data for electrons and positrons were measured by the the AMS collaboration [6].

field, increases. The shielding effect of the solar magnetic field rejects the lowest energy part of the galactic cosmic ray spectrum. The typical energy for particles reaching the Earth magnetosphere is in the GeV range. It is this second type of cosmic rays that is predominantly responsible for cosmogenic nuclides production.

The cosmic rays are already studied for some time. However, there are sill some open questions. For example, there is the problem of the matter/antimatter asymmetry (see electron and positron flux in Figure II.1). Another question that has not yet been satisfyingly answered is how is the galactic cosmic ray spectrum far away from the Earth magnetic field and also far away from the solar magnetic field? The effects induced by magnetic fields from, *e.g.*, the planets or the Sun, disturb the cosmic ray flux. These magnetic fields are often variable, making the cosmic ray flux time dependent. Consequently, there are significant differences in the irradiation spectra depending on when and where the target is irradiated. The possibility to sent detectors in space to measure these fluxes at various location is limited by the financial cost for such missions. Therefore, the best way to experimentally study the cosmic ray flux at least outside the Earth's magnetosphere is by measuring their impact on mediators like the meteoroids and/or cosmic dust.

Recently, cosmic rays are mainly studied for two reasons: first, for their impact on either onboard electric devices and on humans in aircrafts and especially in space missions. Second, cosmic rays are studied to obtain information about the history of cosmic rays with respect to our galaxy. In this thesis, I will focus on the second topic; more specifically, I will focus on the types of information that are experimentally studied in our group. The theoretical approach of this thesis is motivated by the needs of the experimentalists to interpret their data in terms of, *e.g.*, how measured cosmogenic nuclide concentrations can be used to study the temporal constancy of galactic cosmic rays, how measured cosmogenic nuclide activities can be used to study the irradiation history of the meteoroid or the cosmic dust particles, and finally, how the measured cosmogenic nuclide activities can be used to study terrestrial ages of meteorites and with it the influx rate of extraterrestrial material on Earth

II.1.2 The nuclear spallation

Basically, spallation is a phenomenon happening when a light particle (typically a proton) collides with a heavy nucleus at an energy between a few tens of MeV and some GeV. During this spallation process there is the production of numerous particles, predominantly neutrons. The process can be divided into two stages [7]. In the first stage of the collision, the light particle enters the heavy nucleus. Considering the energies involved, the hadrons can be considered as free particles evolving in a mean nuclear potential. The incoming projectile with its high kinetic energy induces a cascade of binary collision between the hadrons. These hard binary collisions often lead to the creation of new unstable hadrons like, *e.g.*, pions or kaons. Additionally, some of the scattered particles can have high enough energies to pass over the potential barrier and leave the nucleus as so-called ejectiles. This first stage is called the intranuclear cascade and its typical duration time scale is given by the time needed for a particle with a velocity close to the speed of light to travel through the nucleus having a radius of few femtometer. This corresponds to a travel time about $10^{-23} - 10^{-22} s$. The nucleus left after this first stage is called the remnant. The energy remaining after the intranuclear cascade often makes the remnant highly unstable. The second stage of the spallation will therefore be the de-excitation of the remnant. During this phase, different processes are in competition to release the excess energy (*e.g.*, fission, evaporation, ...). This stage is responsible for the majority of emitted neutrons, which are relatively easily ejected due to the missing coulomb barrier. The typical duration time scale of this stage is about $10^{-20} s$. Potentially, the de-excitation can even be much longer. However, processes like internal conversion or beta decay are usually not considered when discussing the spallation and nuclei with half-lives longer than $10^{-17} s$ are considered stable.

A distinction should be done between the microscopic spallation, which corresponds to one individual collision as described above, and the macroscopic spallation, which corresponds to a cascade of microscopic spallation reactions induced by particles emitted during the intranuclear cascade of the microscopic spallation. The emitted particles from one spallation reaction can induce multiple further spallation reactions. Therefore, a single proton with a relatively high energy can induce tens of microscopic spallation reactions.

During the first chapters of this thesis describing the development and improvement of INCL, the term spallation refers to microscopic spallation. However, the spallation induced by cosmic rays discussed in the second part of the thesis refers to the macroscopic spallation.

II.1.3 The cosmogenic nuclides

The study of cosmogenic nuclides started accidentally in 1934 [1] with the discovery of an unknown radioactivity emitted by minerals originating from Greenland. This discovery was associated to cosmic rays even if the phenomenon was not understood by then. Cosmogenic nuclides are the results of spallation reactions induced by cosmic rays. They are produced directly through spallation reactions or indirectly through the decay of short-lived nuclei resulting from spallation reactions.

In 1946, cosmogenic nuclides found their first real application with the use of the famous ^{14}C dating method [8]. Since then, many other cosmogenic nuclides (^{10}Be, ^{26}Al, ^{40}K, etc.) resulted in various dating methods and they found various applications ranging from archaeology, hydrology, and oceanography to geology and geochemistry not to mention astrophysics (see subsection II.2.2). The astrophysical applications, which are the main topic of this thesis, started with the study of cosmogenic nuclides in meteorites because they are directly exposed to cosmic rays leading to relatively high cosmogenic production rates. Later, it was extended to lunar samples. The terrestrial applications started much later because of the significantly lower cosmogenic nuclides production due to the shielding effects of the atmosphere and the Earth magnetic field.

As mention before, the production of cosmogenic nuclides is dominated by hadrons, notably by protons and alpha particles. This is well illustrated in Figure II.1 where it can be seen that the electron and antiproton fluxes in the galactic cosmic rays are at least 2 and 4 orders of magnitude lower than the proton

flux, respectively. Additionally, electrons interact with matter only via the electroweak interaction whereas the hadrons interact via the strong interaction. In Figure II.1, one can also see that the flux of particles decreases quickly with increasing energy. Actually, the proton flux decreases according to $\Phi \propto E^{-2.7}$. This explains why only protons and alphas around the GeV scale are usually considered in studies of cosmogenic nuclides production.

II.2 Motivations and applications

Two different simulation programs were improved and/or developed during this PhD. The first program, INCL, does not depend on the second one, CosmicTransmutation, and the improvements realised in INCL are important but not crucial for the CosmicTransmutation model.

The objectives of this section are threefold. First, I give the motivation for the renewed interest for cosmic rays, cosmogenic nuclides, and spallation reactions. These motivations go beyond the framework of the thesis. Next, the arguments why these phenomena are studied using Monte Carlo simulations are explained. Finally, the connections between both phases of this thesis are discussed.

II.2.1 The cosmic rays

Cosmic rays are abundant and everywhere in space. They are able to penetrate parts of planetary atmospheres and for Earth, as an example, the secondary particles produced by the interactions of primary cosmic ray particles with atoms from the atmosphere even reach the surface and produce so-called terrestrial cosmogenic nuclides. The effects caused by cosmic rays can be used as a source of information. The dominant measurable effects of cosmic rays are actually induced by nuclear spallation reactions. Via cosmogenic nuclides, which will be discussed in the next subsection, the induced radioactivity can be used to remotly study the chemical composition of objects in space if they cannot be directly studied in a laboratory. It is interesting to note that cosmic rays also have an impact on the composition of cosmic rays itself. The spallation induced by cosmic ray particles with other cosmic ray particles is responsible for a significant part of the light elements (Li, Be, etc...) available in the universe.

In addition to nuclide production processes, the cosmic ray spectrum can be used to obtain some direct information. For example, the detection of electron and positron spectra in the cosmic ray flux obtained by looking in different directions can be used to determine the asymmetry of matter/antimatter in the primitive universe, in galaxies, or in clusters. The detection of neutrino pulses can be used to anticipate the observation of supernovae.

However, cosmic rays also have negative aspects, which must be studied and taken into account, notably for space missions and in aircrafts. The irradiation of on-board electronic devices and humans can cause irreversible damages. This is crucial for the planning of space missions but it is also important for commercial airliner where a significant increase in the cosmic ray flux induced by, *e.g.*, a solar eruption can be mortal for passengers. Additionally, with the miniaturisation of electronic devices, cosmic ray effects become more likely and some effects can already be measured at sea level.

II.2.2 The cosmogenic nuclides

Cosmogenic nuclides cover a large range of atomic mass and charge numbers. However, for most of them there is no scientific application. To be scientifically useful, a cosmogenic nuclide must fulfil four conditions. First, the natural abundance of the nuclide must be low to be able to resolve the production against the natural background. To give an impression, the order of magnitude for the production of cosmogenic nuclides is in the range of a few thousand atoms per gram per year. Therefore, very often the amount of newly produced nuclides is small compared to the amount of already naturally occurring nuclides. The second condition is that the nuclide is either stable or has a half-life greater than or

comparable to the events of interest. If the half-life is too short, the nuclide reaches equilibrium (potentially below the level of detection) too fast to give any useful information about the past of the object. The third condition is the feasibility of the experimental measurement. Some nuclides are extremely challenging to measure and, sometimes, the uncertainties and/or the systematic errors for them are too large to obtain meaningful results. The final condition is a good theoretical understanding of the production and loss mechanisms of the studied nuclide. If these processes are not well understood, the analysis of the experimental results cannot lead to firm conclusions. The two first requirements are natural constraints and cannot be bypassed. However, the two other requirements are technical constraints and one of the major tasks of our research group is to push the limits. Notably, this thesis is devoted to the fourth requirement with the aim to provide a state-of-the-art understanding of the cosmogenic nuclide production.

The first application of cosmogenic nuclides was their use in a dating system. It started in 1946 with the development of the ^{14}C dating method [8]. Still, dating is the goal for most cosmogenic nuclide studies and depending on the time scale to be dated, specific nuclide pairs are used like, *e.g.*, ^{26}Al/^{21}Ne or ^{40}K/K. To obtain reliable ages the applicability of each individual dating system must be known. For some applications, however, there is still no dating system available. This motivates many experimentalists to further push the state-of-the-art measurement methods for cosmogenic nuclides, which becomes more and more challenging. This allows not only to improve the precision of existing methods, it also creates new fields of application.

The physical basics of all dating methods are relatively easy. For a given cosmic ray flux, the production and loss rate of the relevant cosmogenic nuclides are calculated. Then, the time dependent nuclide ratio can relatively easily be determined. The very same methods can be applied to various fields of application. Here I mention the study of cosmic ray exposure ages, *i.e.*, the time the meteoroid has been exposed to cosmic rays, or terrestrial ages, *i.e.*, the time the meteorite is shielded from cosmic rays while being on Earth. In geology, the age of geological surfaces can be calculated. Taking into account shielding effects of the studied surfaces, it is possible to measure erosion rates. Going even deeper in the analysis, it is possible to obtain information about variations of the cosmic rays flux. It is then also possible to study the dynamics of small bodies in the solar system. Additionally, the exposure age (together with the terrestrial age) of meteorites can help to constrain if two of them share the same origin, *i.e.*, were ejected from the same parent body. Actually, studies demonstrated that the majority of the meteorites found on Earth come from just a few major collisions between massive objects. Finally, with the increasing precision of measurements, it is possible to study mountain uplift since the cosmic rays flux depends on the altitude. For a more exhaustive description of the various application of cosmic rays, see ref. [9].

II.2.3 The spallation

Spallation is a complex phenomenon, which plays a crucial role in a large variety of fields. The major applications can be divided into two subgroups: the fields related to natural spallation induced by cosmic rays and the fields related to human controlled spallation. The interest in natural spallation is part of our interest in cosmic rays and cosmogenic nuclides. However, natural spallation induced by cosmic rays is only a minor part of all the applications related to spallation.

The human controlled spallation can directly or indirectly be used as a tool in a large variety of fields. The most famous field of application is its use in neutronics. As already mentioned, the neutron production cross section in spallation reactions is very high (several barns). This makes spallation reactions a suitable source for neutrons as it is already done in various existing or planned facilities (*e.g.*, nToF, ESS) using neutrons as projectiles or studying them. Using the spallation process for the production of neutrons provides significant advantages compare to other neutron sources like nuclear reactors. The flux of neutrons of such so-called spallation sources is relatively easy to control in terms of intensity, energy, time dependence, and direction. The secondary fast neutrons can be slowed down and used to explore the structure and the dynamic of, for example, condensed matter. Considering nuclear power

plants, the long-lived radioisotopes in the nuclear waste are known as a major hazard because of their long lifetime and their high radiotoxicity. A solution might be found using the MYRRHA project. This nuclear reactor project plans to demonstrate the feasibility of an Accelerator Driven System (ADS). In this set-up, the nuclear waste, notably the long-lived radioisotopes, are used as combustible and are irradiated with a spallation source. The reactions induced not only lead to the transmutation of the various long-lived radioisotopes into stable or short-lived isotopes, the entire process is able to produce energy, *i.e.*, electricity. In more fundamental research, spallation reactions are used for the creation of exotic nuclei like neutron- or proton-rich nuclei or hypernuclei. Finally, spallation is used in medicine. It plays a crucial role in hadron therapy where light nuclei are accelerated at very specific energies ($\sim 100\ MeV$) in order to irradiate tumours.

In summary, spallation is a very interesting tool for physicist. It is not only relevant for fundamental research, the applications range for astrophysics, to energy production, and medicine. Therefore, there are good reasons to study and better understand the spallation process.

II.2.4 INCL and CosmicTransmutation

As mentioned above, the study of cosmogenic nuclides requires a good theoretical understanding of the underlying production and loss mechanisms. On a more general level, current research in physics is often very sophisticated and complex. The data obtained in sophisticated and specialised experiments, need a theoretical framework to be interpreted and to give rise to predictions and conclusions. However, a deterministic approach of complex phenomena is often unrealistic and/or needs some approximations and hypotheses, which in turn reduces the predictive power. The recent increase in computing power enables that in many fields simulations can be a realistic alternative to the deterministic approach. The approach used in this thesis is based on Monte Carlos simulation codes and is therefore not deterministic. In such codes, some a priori hypotheses are made. For example, the question of what are the relevant nuclear parameters to be considered needs to be answered. Then, theoretical predictions obtained with the codes are compared to experimental data. These comparisons give information about the predictive power of the used models. Finally, the models are used to make theoretical predictions for unmeasured and often so-far unstudied processes.

In particle physics, simulation of macroscopic events are based on a relevant and useful underlying environment. The Geant4 toolkit [10] is such an environment and it is likely the most famous environment for high energy physics simulations. In this environment, various independent models are implemented in order to treat the different aspects of the entire physical problem. Sometimes, there are different models proposed for simulating the same process. This allows to make comparisons and to choose the physics list that gives the best results. The reliability of Geant4 based programs is directly linked to the reliability of the implemented models. In the context of cosmic ray interaction, the dominant process is spallation in the GeV energy range. What we consider as the most promising model implemented in Geant4, which treats spallation, is the IntraNuclear Model of Liège (INCL). This is why the first stage of this PhD was devoted to the improvement of INCL to a state-of-the-art model.

The new version of the INCL model, which was developed during this thesis, will be described in detail in chapter III. Basically, the code simulates the IntraNuclear Cascade (INC) phase of the spallation reaction. In combination with a suitable de-excitation code, it simulates the microscopic spallation. When implemented and used in a transport code like Geant4, macroscopic spallation can be simulated. The stand-alone version of INCL can be used directly to simulate experiments on thin targets in order to calculate, *e.g.*, cross sections for the particle production or for the production of residual nuclides. On the other hand, such experiments provide data, which are essential to test the reliability of the INCL model.

Either as stand-alone models or implemented into a transport code, models like INCL are only applicable to specific particles and energy ranges. The different models included in a transport code that are all needed to fully cover all physical aspects, need to overlap in energy to guarantee a complete coverage of the energy range of interest. Usually, the larger the overlap, the smoother the transition between the

models, which is necessary to avoid discrepancies and/of jumps in the predictions

Improvements in INCL have thus two types of motivation. On the one hand, they improve and extend the range of application for INCL. On the other hand, the extended range guarantees a better overlap with the other models in Geant4, consequently improving its predictive power.

The CosmicTransmutation model was developed from scratch during the second phase of this PhD. This model simulates the irradiation of meteoroids and planets with protons and α particles from cosmic rays. The CosmicTransmutation model was developed for a specific purpose: to support the prediction of cosmogenic nuclides production. The program was developed to be as versatile as possible, *i.e.*, it considers meteoroids, atmospheres, and the surface of planets, moons, and asteroids without atmospheres. Similar codes already exist but they are often limited to very specific targets, which were in the focus of the researches that developed the models. In contrast, the development of the CosmicTransmutation model was not linked to a specific target with a specific composition or with any specific characteristic. It has been planned and developed in the most general way possible. In addition to its flexibility, the development of a new code allowed to implement new possibilities, which were not found in other codes like, *e.g.*, the simulation of non spherical objects.

II.2.5 The dual development

Both INCL and CosmicTransmutation, which were both developed during this thesis, are Monte Carlo simulation codes. Therefore, their predictive power is directly linked to their basic hypotheses.

The CosmicTransmutation model is based on Geant4, which can be seen as a toolkit code. Geant4 is not a simulation model by itself. It notably provides C++ classes, which can treat numerous physical aspects. In this context, Geant4 is often used as a black box. The problem is therefore to estimate the errors and uncertainties of the predictions and the limitations of the code itself. Additionally, the models implemented in Geant4 are black boxes for Geant4 itself. Consequently, the errors and limitations of the individual programs propagate, often without being quantified or even estimated, to the final result. To overcome this limitation it is necessary to go inside the sub-models and to understand their relevant limits, strengths, and weaknesses.

In the case of CosmicTransmutation, which is based on Geant4 and, by extension, on INCL, the hypotheses of Geant4 and INCL affect the reliability of the results obtained using the CosmicTransmutation model. Even if the limits of Geant4 and INCL can be relatively well understood using the documentation of both codes, the estimation of errors and how they propagate is very complex for the users. The participation in the INCL and Geant4 collaborations gave me a profound understanding of both codes. The knowledge of the strengths and weaknesses of both codes allows me to better estimate the reliability of the results obtained using CosmicTransmutation and to go deeper into the analysis of the results.

Chapter III

The IntraNuclear Cascade model of Liège

A thesis is a good place to go back to the history of a model and to reunify and summarise its various references. Two models have been developed during this PhD. However, the CosmicTransmutation model has no history since the model has been created from scratch for this PhD. Therefore, this chapter will be fully devoted to INCL. The objective here is twofold: understanding the INCL operation, which is at the core of this thesis, and discussing the various subjects of improvement treated over time. This will be useful for users who want to know the strengths and weaknesses of the model. To this effect, this chapter is divided into three sections. In a first section, the history of the model is summarised. It is followed by a discussion about the initialisation of INCL before the intranuclear cascade simulation. Lastly, the global operation of the actual INCL model is described in some detail.

III.1 History

INCL is almost 40 years old and during this time the code went through many phases of development. They can be divided into three main phases; a first phase during which the code was developed in order to study specific physical aspects with various corresponding extensions. There was no generalised purpose. It was followed by a second phase in which the code was recast to become a code for general applications and to fit in transport codes for a wide distribution. In the final phase, which is the current phase, constant efforts are made to improve and extend the capabilities of INCL and to maintain the structure of the code in state-of-the-art spallation simulation models.

III.1.1 From origins to a well founded model

INCL is a code simulating the intranuclear cascade in nuclear collisions. The code was created in 1980 by J.Cugnon, T.Mizutani, and J.Vandermeulen [11]. It was initially devoted to heavy nucleus-nucleus collisions in the GeV energy range, with studies focussing on the dynamics and the production of particles during a collision [12, 13].

With the second major version of INCL in 1987 [14], the code evolved and focused on the spallation with a light projectile and a heavier target. A constant effort has been made in the following decade to extend the capabilities of INCL with new versions or parallel extensions [15–21]. It has notably been seen the first apparition of strange particles in $\overline{p}$-nucleus collisions [16]. I will discuss this specific extension in chapter IV.

III.1.2 Transport codes and benchmarks: the era of recognition

After various developments, INCL was recast at the beginning of the millennium and came back to the fundamentals of the spallation simulation with a special focus on proton-induced spallation reactions with energies between 200 MeV and 2 GeV. This new version, INCL4.2 [22], is the base on which the current INCL model is built.

In 2001, INCL was implemented for the first time in a transport model. The model in question is the Los Alamos High Energy Transport (LAHET) model [23]. This was of high importance for both parties. For LAHET, it represented a new model available with excellent results obtained with the stand alone version of INCL. Moreover, INCL was able to treat light nuclei (up to $A = 4$) as projectiles, this was an issue in LAHET. Up till this point, only the Isabel model [24] was able to consider light clusters as projectiles in this transport model and the comparison between physics list was not possible.

In 2010, a benchmark of the spallation models was carried out by the IAEA [25]. This benchmark compared various combinations of intranuclear cascade and de-excitation models for energies up to 3 GeV. A the end of this study, the INCL model was recognised as one of the best spallation models when associated to the ABLA07 [26] de-excitation model. An example of notations obtained by the various models tested is given in Figure III.1.

III.1.3 High energy and new particles

The conclusions of the IAEA benchmark confirmed the quality of the combination of INCL and ABLA models. However, the quality of this combination in the 200 MeV-2 GeV energy range was already well accepted for many years. The two models showed excellent results with a good reproduction of the total and differential cross sections as well as the particle multiplicities. This led to a new policy: the extension of INCL capabilities. During the 2000's, we can notably cite the increase of the energy range treated [27, 28], with a focus in direction of high energies, and a better description of the target nucleus with the implementation of a correlation momentum/position for nucleons in the initial nucleus.

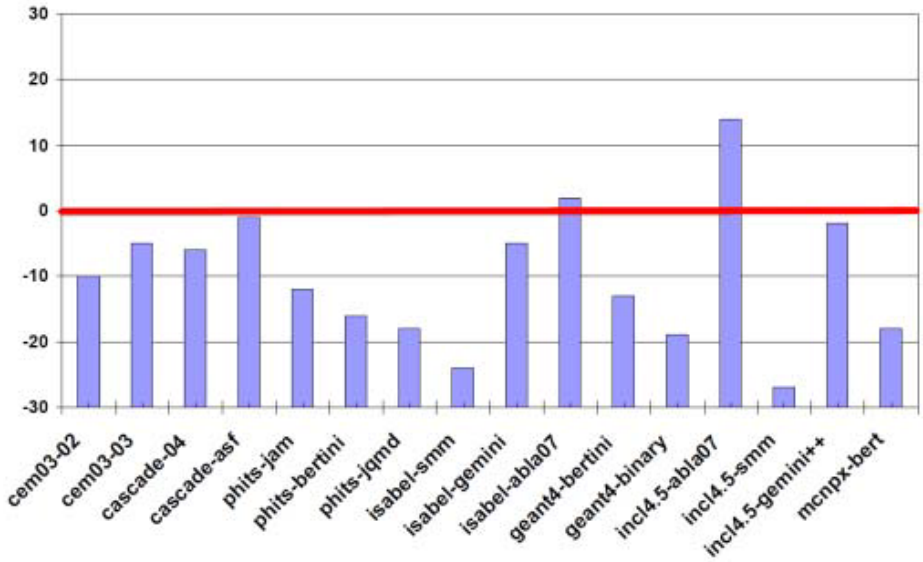

Figure III.1: Notation obtained by the different models tested during the IAEA benchmark for isotopic distributions. The reaction tested were $p + Fe$ at 300 and 1000 MeV/nucleon, $p + Pb$ at 500 and 1000 MeV/nucleon, and $p + U$ at 1000 MeV/nucleon and the experimental data used for the comparisons came from refs. [29–36]. A notation of 0 or more indicates a model is able to reproduce experimental data with, at least, the minimal precision fixed by the authors of the benchmark.

The improvements in the direction of the high energies ($\sim$ 15 GeV) were possible thanks to the implementation of reactions producing many pions in the final state during the cascade (see sect. III.2 for details). This version is called the multipions version.

One of the main changes in the INCL model after the IAEA benchmark was the translation of the Fortran version of INCL into C++. This work was done by P. Kaitaniemi for the version INCL4.2 in 2011 [37] and by D. Mancusi in 2012 for the version INCL4.5. It was realised in order to implement INCL in Geant4. This resulted in a large number of new possibilities for the model. Soon after, the decision was taken to stop the parallel development of both the Fortran and C++ version in the benefit of the C++ version alone.

For Geant4, the main objectives with the implementation of INCL were to get better junctions between the different hadronic models thanks to a large overlap between models treating high energies and those treating low energies; and to have an up-to-date and still actively developed model, which is well documented and validated. These objectives were motivated by various reasons but I will only mentioned an increased interest in nuclear interactions coming from space applications and the cosmic ray interactions. Since the first implementation of INCL4.5, every new public version of INCL has been implemented in Geant4.

Between the implementation of INCL4.5 in Geant4 and the beginning of this PhD, a new public version of INCL has been distributed: INCL4.6 [38]. In this version, several features were added or improved. For the novelties, one can notably cite the emission of clusters and a Coulomb deflection for entering and outgoing charged particles. Since this version, three main subjects where improved: the description of light ions induced reactions [39], the inclusion of quantum effects based on Hartree-Fock-Bogoliubov calculations for a better nucleus surface description [40, 41], and the high energy improvement. This high energy improvement was the base of a new major version of INCL: INCL5.0 [42] with the implementation of new particles, which are the η and the ω mesons. In addition, because of their physics, photons can be created in INCL5.0 but they cannot interact.

My work carried out at the CEA in France started slighlty before the finalisation of INCL5.0 and was included in this idea of high energy development. This work resulted in a new major version of INCL: INCL6.0 [43, 44]. In this new major version, a new aspect of the physics has been opened for simulation: the strangeness.

III.2 Operation of INCL

INCL is a complex model. However, as the development of INCL is a major part of this thesis, the reader should have at least a basic understanding of its global operation. In this section, the most important aspects of the operation of INCL are discussed.

III.2.1 Initialisation

The initialisation of the projectile and the target plays a crucial role in INCL. It directly influences the reliability of the results. It also defines a validity range and it must be, at least partially, understood for the proper analysis of the final results.

Projectile and target handled by INCL

INCL is able to accommodate various particles as projectiles. At the beginning of this PhD, the allowed projectiles were the nucleons (p and n), the pions (π^-, π^0, and π^+), and light nuclei with $A < 18$. With the implementation of strange particles realised during this PhD, a new zoology of particles are now available as projectiles. Namely, the kaons (K^+ and K^0), the antikaons ($\overline{K}^0$ and K^-), the Lambda (Λ),

and the Sigmas (Σ^-, Σ^0, and Σ^+). Additionally, light hypernuclei can be used as projectiles following the same rules as for "normal" nuclei.

Note that it is technically possible to use projectiles with $A \geq 18$. However, the hypotheses of INCL are less and less valid with increasing projectile mass (see sect. III.2.1 for details). Therefore, it is recommended to not go higher than this upper limit.

The targets, which can be handled by INCL, cover the set of nuclei with $A > 4$. Once again, this PhD opened new possibilities with hypernuclei, which are now available as targets. It should be noticed that the larger the target mass is, the more valid will be the basic hypotheses of INCL. These hypotheses are the same as the Serber hypotheses [7], which can be summarised using the following inequality [9]:

$$\lambda\!\!\!^{-} \ll d < \Lambda < R \tag{III.1}$$

with $\lambda\!\!\!^{-}$ the reduced de Broglie wavelength, d the distance between two nucleons inside the target nucleus, Λ the mean free path of the particle in the nucleus, and R the radius of the nucleus. The physical meanings of the sub-inequalities are:

- $\lambda\!\!\!^{-} \ll d$ - The size of the wave packet describing the particle is much lower than the internucleonic distance. Consequently, all nucleons appear distinct and well defined in momenta and positions for the incoming projectile. This allows a classical treatment of the particles propagation.
- $\lambda\!\!\!^{-} \ll \Lambda$ - The scattered wave reaches its asymptotic state before the next interaction and interactions can be treated in a classical approach.
- $d < \Lambda$ - Interactions are independent from each other (assuming that the time between two collisions is larger than the interaction time scale). Interactions and transport can be treated independently.
- $\Lambda < R$ - The possible interferences between the scattered waves cancel out due to the large number of interactions.

These hypotheses define a range of validity for intranuclear cascade models. Notably, it defines an energy range for the projectiles. At low energy, *i.e.*, below 100 MeV/Nucleon, the wavelength of particles increases. However, the mean free path increases due to the Pauli blocking. Therefore, the second condition remains valid. Moreover, for peripheral collisions, the projectile will have more difficulties to penetrate deep in the nucleus and the first inequality stays true since the nucleonic density is lower in periphery of the nucleus. Special attention to the low energy domain showed that results down to a few tens of MeV could be as good as those obtained via models dedicated to the description of low energy nuclear reactions [45]. At very low energy and when the collision is central, no cascade is instantiated, the projectile is absorbed, and a compound nucleus is directly formed. At high energy, the wavelength of particles is small enough to be sensitive to the sub-structure of baryons, which are the quarks and gluons. Therefore, the collisions cannot be treated as nucleon-nucleon collision any more, the hadronisation time must be taken into account, and the interactions and the propagation cannot be treated using a classical approach. The high energy limit of validity of Serber hypotheses is between 10 and 40 GeV/Nucleon [46] and likely around 20 GeV/Nucleon.

We can state the Serber hypotheses define an energy range covering the major part of the relevant energies for cosmogenic nuclides production, which is the topic of this PhD (see Figure II.1).

Nucleons distribution

The description of the target is crucial for a proper simulation of the spallation reactions. Therefore, it is described with high precision. A special attention is paid to the generation of nucleons inside the target nucleus. Moreover, some ingredients are implemented in the code to mimic the quantum mechanical features.

In the target nucleus, nucleons travel freely in a potential well and they have various momenta and positions. The couples position and momentum are not distributed completely randomly. The momentum defines a radius of action inside the nucleus. Therefore, a correlation exists between momentum and position (r-p correlation).

In previous versions of INCL [22], the radius of action was treated with a classical approach where all the momentum below the Fermi momentum p_F (= 270 MeV/c) in a Fermi's sphere had an equal probability of realisation and the radius of action $R(p)$ is well defined. The nucleons with a momentum p cannot cross the limit $R(p)$ as illustrated in Figure III.2.

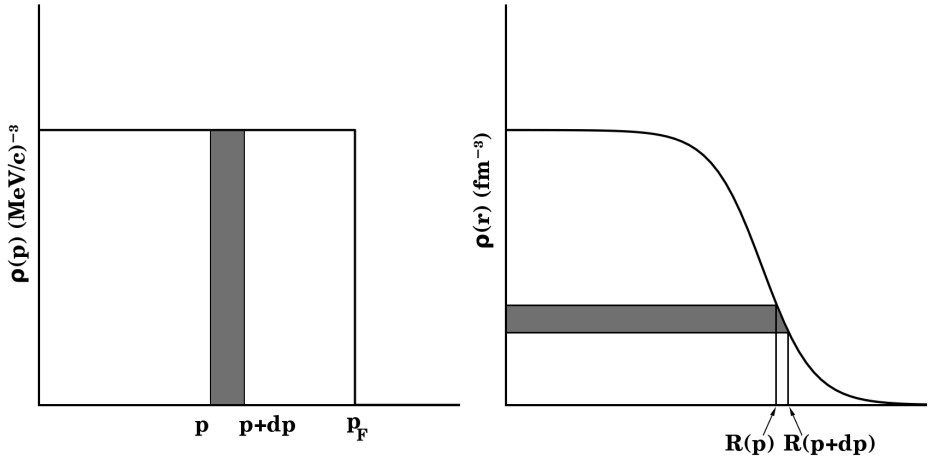

Figure III.2: Repartition of nucleons in space phase. Left graph: space-momentum density. Right graph: space-radius density. The shaded zone on the two graphs are occupied by the same nucleons.

The previous statement illustrated in Figure III.2 can be written as:

$$A_T \frac{4\pi\ p^2 dp}{\frac{4\pi}{3}\ p_F^3} = -\frac{4\pi}{3}\ R^3(p)\ d\rho(R(p)). \tag{III.2}$$

with A_T the mass number of the target nucleus and ρ the nuclear density.

In the latest version of INCL, $\rho(r)$ for $r < R_{max}$ is defined as:

$$\rho(r) = \begin{cases} \dfrac{\rho_0}{1+\exp(\frac{r-R_0}{a})} & \text{for } A > 19 \\ \rho_0\ \dfrac{1+\alpha(r/a)^2}{\exp((r/a)^2)} & \text{for } 6 < A \leq 19 \\ \dfrac{\rho_0}{\exp((r/a)^2)} & \text{for } A \leq 6 \end{cases} \tag{III.3}$$

with a and α, two parameters defined as functions of the target mass number and ρ_0 the normalisation term to get the right target mass. R_{max} is the maximal radius of the nucleus and is also defined as a function of the target mass. For $r \geq R_{max}$, $\rho(r)$ is zero regardeless of the nucleus mass number. These distributions are called the Woods-Saxon, the modified-harmonic-oscillator, and the Gaussian density distributions, respectively. The values for the parameters a and α can be found in ref. [22] for the Woods-Saxon distribution and in ref. [47] for the two other distibutions. More details can be found in ref. [41].

The radius of action of a particle with momentum p can be deduced from the integration of eq. III.2, which leads to the formula:

$$A_T \left(\frac{p}{p_F}\right)^3 = -\frac{4\pi}{3} \int_0^{R(p)} \frac{d\rho(r)}{dr} r^3 dr \tag{III.4}$$

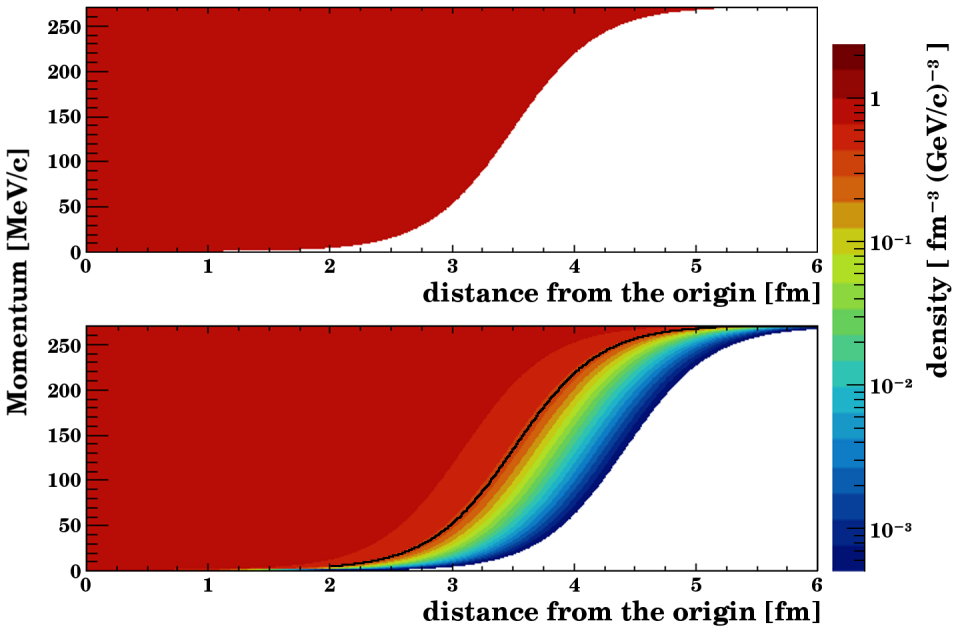

Figure III.3: Phase space distribution of protons in a nucleus of ^{27}Al. Upper panel: proton distribution in the classic approach. Lower panel: proton distribution in the quantum approach of ref. [40]. The black line in the lower panel represents the classical phase space limit of the proton distribution seen in the top panel.

Once $R(p)$ has been determined, the nucleons can be generated in the joined probability density:

$$f(\vec{r}, \vec{p}) = \frac{d^6 n}{d\vec{r}^{\,3} d\vec{p}^{\,3}} = A_T \frac{\Theta(R(p) - r)\ \Theta(p_F - p)}{\frac{4\pi}{3} R^3(p) \times \frac{4\pi}{3} p_F^3} \tag{III.5}$$

with Θ the Heavyside function. In practice, the momentum p was generated in the uniform Fermi sphere distribution and the position was generated in a uniform sphere of radius $R(p)$.

In order to improve the description of the surface, two main improvements have been made in the latest version of INCL [40, 41]. First, the radius of action of protons and nucleons are defined independently since the number of nucleons of each type can be different. Additionally, the Fermi's momentum can be different for protons and neutrons because of the N-Z asymmetry. For most of bound nuclei in the nuclear chart, the number of neutrons are higher than the number of protons. In these cases, a "neutron skin" naturally appears around the nucleus. Second, the quantum mechanics is taken into account with the possibility for a nucleon with a momentum p to cross the corresponding radius of action $R(p)$. In the new approach, the term $\Theta(R(p) - r)$ in eq. III.5 becomes a Wood-Saxon distribution and, in practice, the positions of nucleons are no longer distributed uniformly in the Fermi's sphere of radius $R(p)$. The positions are now corrected following the aforementioned Wood-Saxon distribution as shown in Figure III.3, as detailed in refs. [40, 41].

In the case where Λ particles are present in the initial target, they follow the same rules as nucleons. However, no test has been performed on target hypernuclei since no experimental data exists for such systems.

The description of the projectile is less crucial for the simulation. Therefore, the target and the projectile are treated asymmetrically in INCL for sake of simplicity. Whereas the nucleons in the target travel freely in a potential well, the nucleons in the projectile are frozen.

III.2.2 Spectators and Pauli blocking

With a classical approach of the nucleons and their interactions unphysical processes would happen in INCL. Some special rules have been implemented to the model to avoid such unphysical processes and to mimic the quantum mechanical effects.

The first problem with a classical approach is that the nucleons inside the target would naturally collide and exchange energy. This would happen without the contribution of any projectile. In such a case, the momentum of some nucleons could cross the Fermi momentum and escape the target nucleus even if this nucleus is stable. This phenomenon is known as the spontaneous Fermi sea boiling. In order to avoid this phenomenon, the concept of spectator and participant nucleons has been introduced in INCL. The spectator nucleons are prohibited to interact with each other. Only the participant-participant and spectator-participant interactions are allowed. At the beginning of the cascade, every nucleon in the target is spectator and particles in the projectile are participants. Then, when a participant interacts with a spectator, the spectator becomes participant as well as the eventual particles produced. The other way around, when the energy of a nucleon participant is below a threshold energy, its status change back to spectator in INCL4.2. The low limit had been defined as the Fermi energy plus a small quantity fixed to 18 MeV. This procedure was motivated by various considerations (*e.g.*, the localisation of nucleon are not precisely defined at very low energy). This procedure was inspired by the Isabel code [24]. In addition to avoid unphysical processes, this solution reduced significantly the computational time. However, this limit had been fixed arbitrary and is not representing any physical process. Moreover, some unphysical processes were avoided but others appeared in the neutron spectra at very low energy. In INCL4.6, the limit to turn a participant nucleon into a spectator was fixed to 7 MeV for neutrons and to the emission threshold plus two thirds of the Coulomb barrier for protons.

The second main problem that could happen with a classical approach is the production of states that cannot be realised in reality. As an example, the creation of states that are blocked by the Pauli principle must be avoided. In INCL, two tests are applied to the collisions to reproduce the Pauli blocking. The first one is applied to every interaction except the first one. This test controls the presence of nucleons of the same type in the final state of the interaction in a phase space defined by $\Delta r = 3.185$ fm and $\Delta p = 200$ MeV/c. Then the state is randomly blocked or not based on the number of particles detected. The probability to be not blocked is given by:

$$P = \prod_i \left(1 - \frac{1}{2} \frac{h^3}{\frac{4\pi}{3}(\Delta r)^3 \times \frac{4\pi}{3}(\Delta p)^3} \sum_{k \neq i} \Theta(\Delta r - |\overrightarrow{r_k} - \overrightarrow{r_i}|)\ \Theta(\Delta p - |\overrightarrow{p_k} - \overrightarrow{p_i}|) \right), \tag{III.6}$$

with h the Plank constant and i and k stand for the nucleons of the same type created by the binary collision and those in the nucleus, respectively. The 1/2 accounts for the spin because it is not directly considered in INCL. Explicitly, the probability for the collision to be accepted is reduced by 21% for each nucleon of the same type present in the phase space previously defined. In the case of the first collision, the test applied is strict and prohibits the production of nucleons below the Fermi momentum. The second test is applied to every collision. This test controls the presence of holes in the Fermi sea, which would result in a negative excitation energy for the nucleus. If any of these tests is positive, the interaction is blocked.

III.2.3 Projectile-target collision

The first step after the initialisation of the projectile and the target in INCL is the collision between projectile and target. First of all, an impact parameter is generated randomly. The impact parameter is then modified because of the Coulomb force between the projectile and the target. Thereafter, when the projectile enters the target nucleus, its energy is corrected according to the nuclear potential. When the projectile is a cluster, it is possible that only some of its components enter the target nucleus. In such a

case, the nucleons of the projectile that do not enter the target nucleus travel freely and no modification or correction is applied to the remaining cluster.

Inside the nucleus, a nuclear potential is felt by the particles. This potential is a square well potential. Consequently, the kinetic energy of the particles entering or leaving the nucleus is modified when the particles cross the surface and inside the nucleus all particles travel freely along straight lines.

III.2.4 Cascade

After the particles enter the target nucleus, the most important part of the simulation starts. This stage gave its name to the entire process: the intranuclear cascade (INC). The INC is a cycle of three steps. First, the particles inside the nucleus are propagated until two particles collide. In INCL, interactions with three or more particles are not treated except with the Pauli blocking. This is justified by the inequality $d < \Lambda$ in eq. III.1 representing the basic hypotheses of every INC model. In practice, INCL calculates the location of every possible collision, interaction with the surface, or decay (grouped under the name of avatar) and when they will take place. This first step updates the list of the avatars for every particle that has been created, modified, or destroyed in the previous collision, which is described by the two others steps of the cycle. In the approach of INCL, a collision occurs when the distance between two particles is below the minimal distance of approach based on their total interaction cross sections and given by: $d_{max} = \sqrt{\sigma_{tot}/\pi}$. At the end of this step, the next avatar to be treated by the following steps is determined. The second step is applied only in case if the next avatar is a binary collision, which is the majority of cases. In this step, the type of the next binary collision is randomly chosen based on the respective reaction cross sections. For example, the reaction chosen can be $NN \to N\Delta$. In the last step, the phase space and the charge repartition of particles in the final state of the avatar is generated. In case of binary collisions, they are randomly generated either based on differential cross sections (if available) or on phase space generators. At the end of this step, tests like the Pauli blocking are performed. If any of these tests forbids the final state, the last steps 2 and 3 are cancelled and the corresponding avatar is removed from the list of avatars to be proceed further. Then, the cycle is repeated until the end of the intranuclear cascade.

A special constraint has been implemented in INCL to avoid the treatment of reactions that would be invariably blocked by the Pauli principle. These reactions are the very low energy nucleon-nucleon collisions. When there are two nucleons with an energy in their center of mass below 1920 MeV, the two particles cannot interact except for the first collision. This energy correspond to a kinetic energy available of ~ 40 MeV.

For a better representation of a cascade in INCL, a representation of a simple INC is given in Fig-

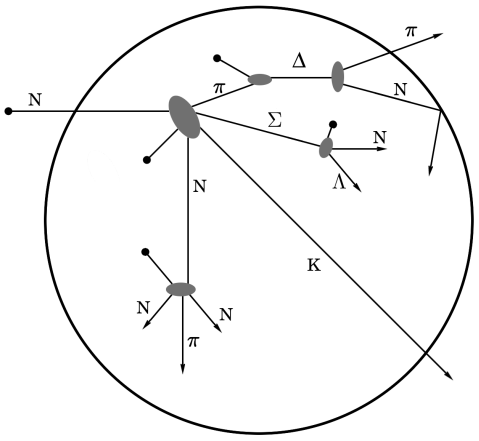

Figure III.4: Representation of an IntraNuclear Cascade.

ure III.4.

III.2.5 Short life and resonant particles

A special particle, which can be created during the INC, is the Δ particle. The standard half-life of this particle ($\sim 6\times10^{-24}$ s) is smaller than the typical duration of an INC ($\sim 10^{-22}-10^{-21}$ s). Therefore, its decay ($\Delta \rightarrow N\pi$) must be taken into account. Moreover, this very short half-life also means the particle is resonant. The particle width is $\sim$ 117 MeV and its nominal mass is $\sim$ 1232 MeV [48].

In INCL, when a Δ particle is created, its mass is randomly chosen based on its nominal mass and its width. The maximal possible mass is defined based on the available energy in the collision and the minimal mass corresponds to the sum of the masses of a pion and a nucleon to be sure that the Δ particle can properly decay. Additionally, the Δ particle can decay in-flight (understand: inside the nucleus). Its half-life is determined based on the deviation from its nominal mass and on the phase space of the final state.

Other particles have life time comparable to the typical duration of an INC since the new improvements [42, 43]. These particles are the meson ω ($\tau \sim 8\times10^{-23}$ s), the meson η ($\tau \sim 5\times10^{-19}$ s), and the Σ^0 particle ($\tau \sim 7\times10^{-20}$ s) [48]. These particles are rare compared to Δ particles. However, they play a role in specific processes, specifically in the strangeness production for the Σ^0. The widths of these particle are small compared to their respective masses. Therefore, they always have their nominal masses in INCL. However, the question of in-flight decay for these particles is open. A maximal half-life of 10^{-19} s has been defined as the limit to take into account the in-flight decay of particle. Consequently, the in-flight decay of the meson ω and the Σ^0 particle are considered in INCL but not the in-flight decay of the meson η.

III.2.6 Reflection, transmission, and cluster formation

In addition to binary collisions and the in-flight decay of particles, there is another type of avatar playing a crucial role in the INC. This avatar type corresponds to the interaction with the surface of the nucleus. Namely, when a particle reaches the surface of the nucleus, the particle can be reflected or transmitted.

When a particle reaches the surface, the transmission probability is computed. If the average nuclear potential felt by a particle is repulsive, this transmission probability is 1 and the particle is automatically transmitted. Otherwise, the transmission probability P_t is given by:

$$P_t = \frac{4\times p_{in}\times p_{out}}{\left(p_{in}+p_{out}\right)^2} e^{-2G}, \tag{III.7}$$

with p_{in} the momentum of the particle inside the nucleus, p_{out} the future momentum of the particle outside of the nucleus, and G the Gamow factor [49]. p_{out} takes into account the mean nuclear potential as well as a correction for the modification of the binding energy of the nucleus. G is zero for neutral and negatively charged particles.

By default, the refraction of particles is not taken into account and particles are transmitted without any change of propagation direction. However, an input option of INCL allows to compute this refraction.

When a proton, a neutron, or a Λ particle is transmitted, INCL scans the other particles, which are close in terms of phase space. The potential cluster including the first particle are considered to be formed and ejected. The maximal dimensions of clusters are $A_{max} = 12$ (default 8), $Z_{max} = 8$, and $|S|_{max} = 3$, with A the baryonic number, Z the electric charge, and $|S|$ the absolute strange charge (the number of Λ particle in our case. See subsection IV.3.2 for details). Then, the better candidate is selected based on its binding energy. Finally, tests are performed to know if the cluster will be effectively formed. These tests control that i) the cluster energy is above the emission threshold energy, ii) the cluster succeeds in

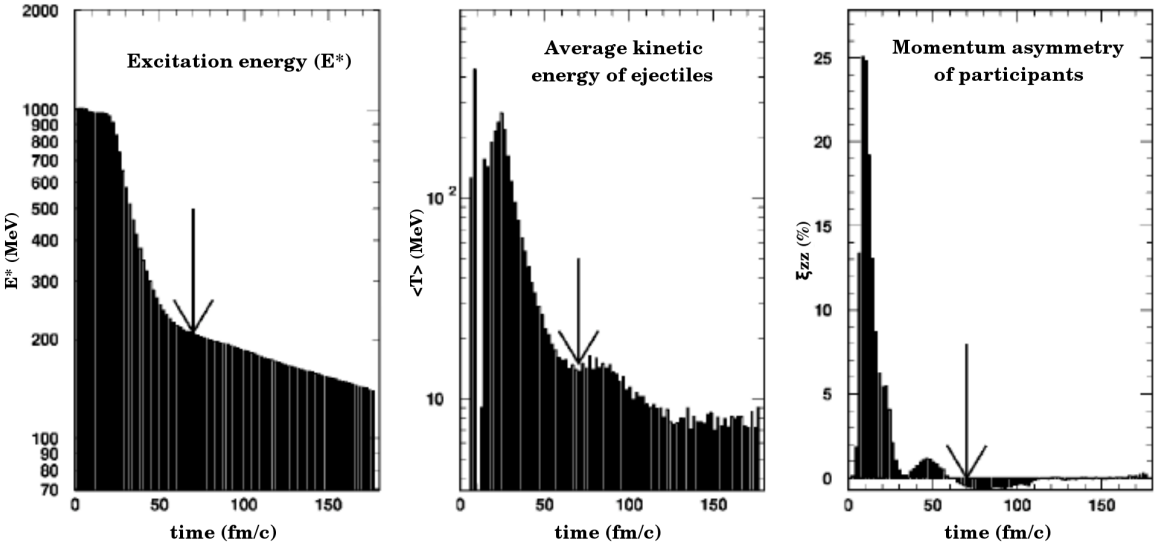

Figure III.5: Evolution of, from left to right, the exitation energy of the nucleus, average kinetic energy of particle emitted, and momentum assymetry of participants as a function of time in a typical case of an INCL cascade. This figure is from ref. [22]

passing the Coulomb barrier, and iii) the cluster trajectory is not "too tangential" ($cos(\theta) \leq 0.7$) to not be splintered because of the nuclear deformation. If all these tests are positive, the cluster is emitted. Otherwise, only the first particle is transmitted. Details can be found in [38].

III.2.7 End of the cascade

The INC is the part of the spallation in which energetic particles are emitted. At the end of the cascade, the nucleus is left in an exited state and it has lost its initial state memory. The nucleus at the end of the cascade is called the remnant or the hyperremnant if strange particles are inside. In Figure III.5 three indicators of the cascade state in a typical INCL case are plotted as a function of the time. In this figure, one can see relatively well distinguished phases, which allowed us to determine the end of the cascade (indicated with the arrows in Figure III.5). A previous study [22] led to the stopping time limit formula:

$$t_{stop} = 29.8 \times A_T^{0.16} \qquad [fm/c], \tag{III.8}$$

with A_T the baryonic number of the target at the beginning of the cascade.

In INCL, when the cascade duration reaches this limit, the cascade is stopped. Additionally, if no particle in the nucleus has an energy of at least 10 MeV above the Fermi energy, the cascade is also stopped in order to gain computational time without changing the final result.

Once the INC ends, post-cascade features are applied to the particles inside the remnant. For example, the pions are absorbed and their energy is transformed into nuclear excitation energy. Then, every particle that escaped along the cascade and with a half-life below a limit are forced to decay (the default limit value is 10^{-19} s). Afterwards, INCL controls conservation rules. Namely, INCL checks the conservation of the relevant quantum numbers; which are the baryonic number, the electric charge, and the strange charge. These quantum numbers are a priori always conserved. Then, the conservation of the energy-momentum four-vector is controlled. Actually, this test allows us to calculate what is the momentum of the remnant. Finally, the angular momentum conservation rule is applied to fix the intrinsic angular momentum of the remnant.

This last step marks the end of an INCL simulation and the information is registered in a root file. However, an additional step is needed to complete the simulation of the spallation: the deexcitation.

III.2.8 Deexcitation

INCL takes care of the intranuclear cascade as explained before. However, most of the observables of the spallation like the neutron multiplicity cannot be reproduced without a proper deexcitation model. This is why INCL needs to be coupled to a deexcitation model to produce results, which can be compared to experimental data.

No direct work has been carried out in this thesis considering deexcitation. However, I have been indirectly involved in the development of the "strange" ABLA model [50], a new version of ABLA developed specially to fit the needs of INCL with the deexcitation of hyperremnants. Moreover, the crucial role played by this phase will be discussed at some points of this work. In this thesis, the limit between INCL and the deexcitation model will not always be explicit.

At the end of the cascade, the remnant is often highly exited. The nucleus have various possible deexcitation channels. Namely, the nucleus can emit light particles like γ's, nucleons, hyperons, or α particles. Heavier clusters, called intermediate mass fragments, can also be emitted. Another possibility of deexcitation is nuclear fission. All of these processes are in competition and the remnant uses several channels of deexcitation in series or in parallel. Finally, a process of multi-fragmentation can occur if the energy of the remnant is high enough.

Once the remnant has released all its excess energy and has reached a bound state; the deexcitation and therefore the simulation of the spallation ends. It is also important to mention that the final nucleus is in its ground state and is bounded. However, it can be highly radioactive. For many experiments, like the production of cosmogenic nuclides, the results of the INCL-ABLA model must be analysed taking into account radioactive decay chains.

Chapter IV

Extension of INCL

In this chapter, the first phase of my work carried out at the DPhN, CEA Saclay in France will be presented. This first phase was the implementation of strange particles and their physics into INCL. This chapter corresponds partially to the work published in ref. [44] where the main ingredients needed for the strange particle implementation (the interaction and double differential cross sections) were displayed. There is also some correspondences with the first part of a work to be published [43].

The needed ingredients to account for strange particles (limited here to kaons, antikaons, Lambda, and Sigmas) are their characteristics, the average nuclear potentials they feel, the reaction cross sections involving strange particles in the initial and/or final state, angular distributions, and momentum and charge repartition of the particles in the final state. Since these ingredients are independent of the code considered, the characteristics summarised and the parametrisation proposed in this chapter can be used in any other code. It is worth mentioning that hyperon and kaon production from a nucleus are already modelled in several codes, *e.g.*, GiBUU [51, 52], JAM [53], LAQGSM [54], INCL2.0 [16, 55] (no more available), and Bertini [56].

Numerous scenarios exist to treat the production of strange particles. Some models split the energy range in two parts: a low-energy part with a center-of-mass energy roughly below 3-4 GeV and a high-energy part. The low-energy part is described either by resonance or directly by their decay products. However, the cross sections are then often treated differently compared to INCL; there are often given in resonant and non-resonant terms. For the high energy part the LUND string model [57] is usually used. Some other models, like Bertini and INCL, which both focus on the energy domain considered here, *i.e.*, below 15 GeV, consider directly the decay products of the resonances and they rely on experimental data, calculation results (*e.g.*, from string models), and approximations. Therefore, some information already exists. However, I investigated new parametrisations by using all available materials (experimental data, hypotheses, and models). The ref. [44] has been the opportunity to report our best knowledge of the thus determined cross sections and to improve some parametrisations. The goal was also to provide a rather comprehensive set of cross sections and angular distributions in an as simple and accurate as possible form, that can be used by other model builders and/or end-users. In addition, the work published in ref. [44] attempts to a systematic and coherent elaboration of fitted cross sections, largely based on symmetry and simple hadronic models, as reported in detail in this chapter.

This chapter is divided into seven sections. First, I come back on the reasons of the implementation of strange particles in INCL. Second, the particles implemented in INCL and the associated reactions are introduced as well as the criteria of their selection. Then, the main ingredients which are needed for the strange particle implementation excluding cross sections are displayed. It is followed by two sections which describe the most important part of the work carried out at the DPhN: the parametrisation of the interaction and double differential cross sections. Then, comparisons of the earlier parametrisations with experimental data and parametrisations from other models are discussed. Finally, the last section is devoted to a conclusion about the parametrisation work, which come back on the difficulties faced.

IV.1 Motivation for the strange particles in INCL

The INCL version I started with has been described in chapter III. At the beginning of this PhD, the hadrons, which were treated in the nucleus were the nucleons (n and p), the Deltas (Δ^-, Δ^0, Δ^+, and Δ^{++}), and the pions (π^-, π^0, and π^+). However, when the energy rises above a few GeV, various other particles can be produced in the nucleus. For a better description of the high energy domain (up to $15-20$ GeV), these additional particles should be implemented.

The strange particles can be produced in spallation reactions. The relevance of these particles increases with increasing energy. The implementation of strange particles was motivated by various reasons. First, there is a need to make better transition between string models as the FTF model [58], for which the few GeV scale represents the low-energy part, and IntraNuclear Cascade (INC) models as INCL where the few GeV scale represents the high-energy part. The strange particle production represents few percent of the total cross section in nucleon-nucleon reactions and even more in Delta-nucleon collisions with around $15-20\%$ of the total interaction cross section at 5 GeV. Therefore, the implementation of strange particles in INCL can significantly improved the modelling of spallation reactions in the energy range of transition between string models and INCL. A second motivation is the fact that comparisons of model calculation with experimental data may also probe the nuclear medium effects. A last motivation for the implementation of strange particles in INCL is the interest in exotic physics appearing in the high energy region. One can cite the production of strange particles themself as well as hypernuclei and neutron or proton rich nuclei production, which can be stabilised by strange particles. In addition, the new version of INCL obtained has been implemented into the transport code Geant4 [10, 59]. Thus, it can be used in the simulation of macroscopic systems. This allows other collaborations to freely access the last version of INCL. It can notably be used it for the design of new experiments dedicated to the study of strange particles and hypernuclei in the foreseeable future, such as for the HypHI [60], Panda [61], and CBM [62] experiments at the FAIR facility.

IV.2 Particles and reactions implemented

The very first step in the implementation of strange particles in INCL was the choice of the list of particles to implement. Inserting all the strange particles was neither realistic nor consistent. This was not realistic because there is a set of 20 particles with a charge of strangeness when there was only 9 non-strange particles in INCL at the beginning of my thesis. It was not consistent either because the production of a Ω^- for example is less likely than the creation of an antiproton in a spallation process but antiparticles are not currently considered in INCL.

The choice of the list of particles to be implemented had to correspond to the INCL needs. INCL is developed to be able to simulate spallation reactions for a projectile kinetic energy ranging from few tens of MeV to 20 GeV. Therefore, an obvious criterion used to select particles to be implemented was base on the production rate in NN and πN collisions, which are the most common reaction types involved in intranuclear cascades in the energy range considered. However, we also considered the quantity of available information in addition to a priori knowledge.

Based on the criteria displayed above, we decided to include only particles with a nuclear spin $J = 0$ and $J = 1/2$ and with a strangeness charge of ± 1. The corresponding implemented particles are the kaons (K^0 and K^+), the antikaons ($\overline{K}^0$ and K^-), the Sigmas (Σ^-,Σ^0, and Σ^+), and the Lambda (Λ). It should be mention that the distinction between kaons and antikaons is relevant in this thesis whereas in other publications both types are often grouped under the name of kaons. The distinction is made because the opposite hypercharge leads to significant differences, notably in the production, scattering, and absorption reactions. In this chapter, "a kaon" always represents a K^+ or a K^0. The heavier strange particles were not considered, due to lower production rates (they might be added in future extensions). The Φ meson ($s\overline{s}$) was not explicitly taken into account due to the lack of experimental data, even if it

may be relevant in the kaon-antikaon pair production. Part of its contributions are, however, hidden in the cross sections as it is the case for other resonant particles.

The types of particles considered and the energy range of INCL application define the types of reactions that must be considered. The need to implement a specific type of reaction is based on its relative importance, given by the experimental cross sections. Knowing that the main particles that evolve during the intranuclear cascade are nucleons and pions, we decided to consider reactions contributing at least 1% to the NN and πN total cross section and at least 10% of the total cross section for $YN(Y = \Lambda$ or $\Sigma)$, $\overline{K}N$, and KN reactions. The reactions taken into account in INCL are listed in Table IV.1. This choice is based on available experimental data.

Table IV.1: List of considered reactions involving strangeness based on experimental data.

NN	$\rightarrow$	$N\Lambda K$	πN	$\rightarrow$	ΛK	$N\overline{K}$	$\rightarrow$	$N\overline{K}$	NK	$\rightarrow$	NK
	$\rightarrow$	$N\Sigma K$		$\rightarrow$	ΣK		$\rightarrow$	$\Lambda\pi$		$\rightarrow$	$NK\pi$
	$\rightarrow$	$N\Lambda K\pi$		$\rightarrow$	$\Lambda K\pi$		$\rightarrow$	$\Sigma\pi$		$\rightarrow$	$NK\pi\pi$
	$\rightarrow$	$N\Sigma K\pi$		$\rightarrow$	$\Sigma K\pi$		$\rightarrow$	$N\overline{K}\pi$	$N\Lambda$	$\rightarrow$	$N\Lambda$
	$\rightarrow$	$N\Lambda K\pi\pi$		$\rightarrow$	$\Lambda K\pi\pi$		$\rightarrow$	$\Lambda\pi\pi$		$\rightarrow$	$N\Sigma$
	$\rightarrow$	$N\Sigma K\pi\pi$		$\rightarrow$	$\Sigma K\pi\pi$		$\rightarrow$	$\Sigma\pi\pi$	$N\Sigma$	$\rightarrow$	$N\Lambda$
	$\rightarrow$	$NNK\overline{K}$		$\rightarrow$	$NK\overline{K}$		$\rightarrow$	$N\overline{K}\pi\pi$		$\rightarrow$	$N\Sigma$

In addition, we included two other types of reactions. The first one considers strangeness production via ΔN reactions. Δ's are less numerous than nucleons and π's, but are nevertheless expected to contribute significantly to the strangeness production according to the study of Tsushima et *al.* [63]. The second type is the strange production in reactions where many particles are produced in the final state but no exclusive measurements are available. Since their contributions increase significantly with increasing energy, a specific study was necessary to get the correct inclusive strangeness production cross section [64]. Table IV.2 lists the channels for both types of reactions also taken into account.

Table IV.2: List of the reactions involving strangeness and requiring information to be taken exclusively from models. Meaning of X is explained in sect. IV.4 and excludes the reactions cited in Table IV.1

ΔN	$\rightarrow$	$N\Lambda K$	NN	$\rightarrow$	$K + X$
	$\rightarrow$	$N\Sigma K$			
	$\rightarrow$	$\Delta\Lambda K$	πN	$\rightarrow$	$K + X$
	$\rightarrow$	$\Delta\Sigma K$			
	$\rightarrow$	$NNK\overline{K}$			

In the reactions listed in Table IV.2, kaon production is equivalent to strangeness production, since it is the only particle with strangeness $+1$ in the energy range under consideration in INCL, which can counterbalance the production of strangeness -1 of Λ, Σ, and $\overline{K}$ particles (strangeness is conserved in strong interaction processes).

Considering isospin, there are 488 channels, excluding the reactions $NN \rightarrow K + X$ and $\pi N \rightarrow K + X$ of Table IV.2, which must be characterised by their reaction cross sections (sect. IV.4) and their final state, *i.e.*, charge repartitions, emission angle, and energy of the particles (sect. IV.5).

IV.3 Strange particle characteristics and physics

The main ingredients needed for the implementation of strangeness can be divided into three main type of information: the particle characteristics (mass, charge, isospin, decay modes, and average nuclear

potential), the particle interaction cross sections, and the post-cascade treatment of the new particles. The determination of interaction cross sections and double differential cross sections are developed in sect. IV.4 and sect. IV.5, respectively. Here, the information from the literature or concerning the post-cascade treatment of strange particles are summarised.

IV.3.1 Average nuclear potentials and characteristics

The mass, charge, isospin, decay modes, and half-life of each considered particle are taken from the Particle Data Group review [48]. The average nuclear potential is much more difficult to determine. Only some of the implemented particles are relatively well known (Λ, K^+, and K^-). Studies on the Σ's potential are rather sparse and it is not yet clear whether the Σ's potential is attractive or repulsive. The K^0 and $\overline{K}^0$ are also problematic regarding their nature with the propagation eigenstates being different to the interaction eigenstates.

Because few experimental measurements exist, the average potentials for strange particles in INCL are considered constant for sake of simplicity. In the case of the Λ particle, a dependence on the nuclear asymmetry [65] is introduced to improve hypernuclei physics. Typically, the potential used for the Λ is a 28 MeV attractive potential for the symmetric nuclei that grows up to a 41 MeV attractive potential for the highest asymmetries ($(A-2\ Z)/A = 0.25$). The K^+ and K^- have been relatively well studied and it is commonly accepted that the K^+ potential is slightly repulsive and that the K^- is strongly attractive [66]. The values retained in this paper are a 25 MeV repulsive potential for the K^+ and a 60 MeV attractive potential for the K^-. It was decided to consider the same potential for K^0 ($\overline{K}^0$) as for $K^+(K^-)$ with a slight correction (10 MeV) due to Coulomb repulsion. This choice is consistent with experimental measurements summarised in [66]. The potential for Σ particles is extremely difficult to measure because of in-medium effects. A repulsive potential of 16 MeV for all Σ's is used in INCL based on a recent study [67].

In summary, the potentials used in this new version of INCL are:

$$\begin{cases} 25\ MeV, & K^+, \\ 15\ MeV, & K^0, \\ -60\ MeV, & K^-, \\ -50\ MeV, & \overline{K}^0, \\ 16\ MeV, & \Sigma's, \\ [-28,-41]\ MeV, & \Lambda\ \text{(Ref.[65])}. \end{cases} \tag{IV.1}$$

Note that the difference between the potentials for kaons and antikaons potentials is not considered in other codes that we use for our comparisons (in chapter V). This produces significant differences in cross section predictions near threshold energies.

IV.3.2 Post-cascade treatment

The implementation of strangeness can lead to a new situation at the end of the intranuclear cascade; a hyperremnant can be produced in which at least one strange particle is still inside the target nucleus at the end of the intranuclear cascade. Therefore, we had to decide how to treat the remaining strange particle after the end of the cascade.

Owing to the repulsive average nuclear potential for kaons, we decided to eject the trapped kaons at the end of the cascade and to correct their kinematics according to their potential.

All Σ's and antikaons have high absorption cross sections ($N\Sigma \to N\Lambda$ and $N\overline{K} \to \Lambda\pi$) at low energy. Therefore, we decided to absorb all of them when they are trapped inside the nucleus and to convert the excess energy and the mass energy of the possible pions into nuclear excitation energy.

After kaon emission and Σ and antikaon absorption, the hyperremnant contains only protons, neutrons, and Λ's. The hyperremnant is then de-excited using a new version of the ABLA07 code [50], which will be presented in a future paper.

IV.4 Reaction cross sections

Among the ingredients needed to include new particles in an INC model, reaction cross sections are the most important. As far as possible they are taken from experimental data. However, measurements are not always performed over the entire energy range, rarely for all isospin channels, and are often inexistent when numerous particles exist in the final state. To overcome these limitations a step-by-step procedure has been developed to obtain parametrisations of the required cross sections (see Table IV.1 and Table IV.2). First, a search of the available experimental data has been performed. Second, two methods based on isospin symmetry allowed to extend our database by increasing the available information. Third, the still missing cross sections were determined using models and/or similar reactions with the help of plausible hypotheses. Finally, generic formulae, which can be applied to parametrise cross sections, are given in the last subsection.

All cross section parametrisations determined by this procedure are given in Appendix A.

IV.4.1 Available experimental data

The number of measured data for each reaction from Table IV.1 are given in Table IV.3. The energy range goes up to 32 GeV and the data are taken from Landolt-Börnstein [64] and two other papers [68, 69].

Since some of the published experimental data are rather old, our study offers the possibility to check and summarise our knowledge of the cross sections. We therefore give for each reaction the number of isospin channels, number of experimental data points, and the Gini coefficient.

The Gini coefficient[70] is a statistical tool used typically in economy to measure the dispersion of a system (usually the income distribution of the residents of a nation). The coefficient takes values between 0 (perfect repartition) and 1 (maximal inequality). The Gini coefficient for the discrete case is calculated as follows:

$$G = \frac{2\sum_{i=1}^{n} i\ y_i}{n\sum_{i=1}^{n} y_i} - \frac{n+1}{n}, \tag{IV.2}$$

with y_i the number of data in the i$^{\text{th}}$ channel arranged as $y_{i+1} \geq y_i$ (non-cumulative). This coefficient measures the repartition of data in the different isospin channels and, in our case (with a very high inequality and a high number of channels), correspond to the missing part of data for each reaction. For example, if $G = 0.8$ approximatively 80% of additional data are needed to complete the 20% of existing data and to make the entire database for each channel as precise as for the most precise channel.

Table IV.3 shows that the number of data depends strongly on the given reaction. For example, in average there are only 2-3 points per channel for the NN collisions while for the $N\overline{K}$ reactions more than 35 data per channel are available. However, the Gini coefficients exhibit an important inhomogeneity ($G > 0.5$) with respect to the isospin channels. There is also a significant inhomogeneity, not given by the Gini coefficient, with respect to the energy range studied, with more data at the threshold and in the resonances region (see Figure IV.1). When available, these data nevertheless enable a reliable parametrisation over the entire considered energy range (up to 15 GeV).

Using only experimental data the reaction cross sections were determined (sometimes partially) only for about 17% of the channels listed in Table IV.1. For the remaining 83% various hypotheses were necessary, which are explained in detail in the next subsections.

Table IV.3: Available experimental data points for reactions studied in my work

Reaction	# of channels	# of data	Gini coefficient
NN to			
$N\Lambda K$	4	31	0.62
$N\Sigma K$	10	44	0.69
$N\Lambda K\pi$	10	29	0.63
$N\Sigma K\pi$	26	43	0.74
$N\Lambda K\pi\pi$	16	14	0.77
$N\Sigma K\pi\pi$	44	15	0.87
$NNK\overline{K}$	10	16	0.71
πN to			
ΛK	4	108	0.75
ΣK	10	158	0.74
$\Lambda K\pi$	10	68	0.72
$\Sigma K\pi$	26	148	0.77
$\Lambda K\pi\pi$	16	60	0.81
$\Sigma K\pi\pi$	44	63	0.86
$NK\overline{K}$	14	57	0.81
ΛN to			
$N\Lambda$	2	44	0.5
$N\Sigma$	4	11	0.75
ΣN to			
$N\Lambda$	4	11	0.75
$N\Sigma$	10	21	0.80
$\overline{K}N$ to			
$N\overline{K}$	6	687	0.61
$N\overline{K}\pi$	14	500	0.72
$N\overline{K}\pi\pi$	22	124	0.87
$\Lambda\pi$	4	349	0.52
$\Sigma\pi$	10	685	0.59
$\Lambda\pi\pi$	6	256	0.66
$\Sigma\pi\pi$	16	496	0.73
KN to			
NK	4	134	0.69
$NK\pi$	14	223	0.62
$NK\pi\pi$	22	123	0.89

IV.4.2 The Bystricky procedure

The first method used to get information about missing isospin channels is based on the assumption of isospin symmetry, which is described in detail in ref. [71]. Their goal was to provide a phenomenological

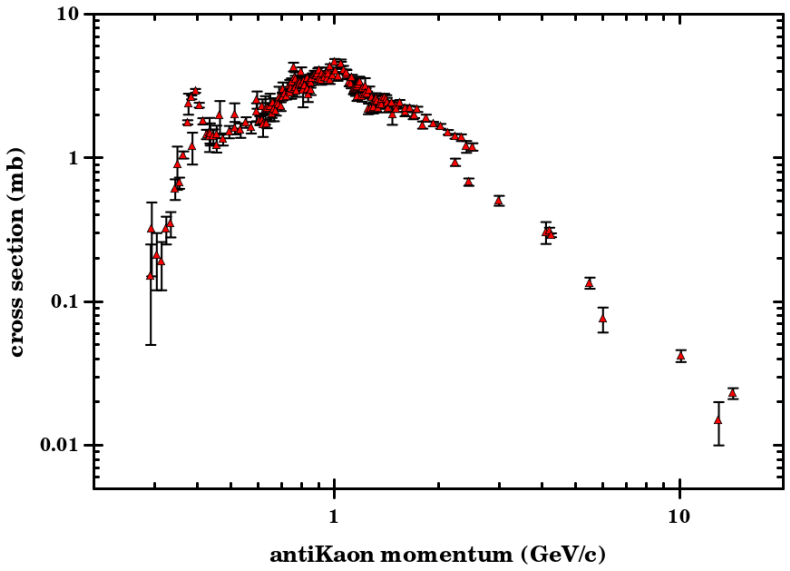

Figure IV.1: $K^- p \to \Lambda \pi^+ \pi^-$ reaction cross section as a function of the K^- momentum. Data taken from [64].

calculation tool for elastic and inelastic cross sections in the framework of isospin symmetry for the reactions $NN \to NN\pi$ and $NN \to NN\pi\pi$.

The procedure, which is based on the isospin decomposition of systems, was used in a previous work [72] to find missing cross sections in channels involving multiple pion production in INCL. The procedure was applied up to the production of four pions and the determined cross sections were then implemented in a previous version of INCL. Briefly, the initial state of two nucleons $|NN\rangle$ is projected on the final state, which is decomposed into the nucleon final state $\langle NN|$ and the pion final state $\langle x\pi|$. The amplitude of the reaction is given by the following equation:

$$\mathcal{M}(NN \to NNx\pi) = (\langle NN| \otimes \langle x\pi|)\, M\, |NN\rangle\,, \tag{IV.3}$$

with M the reduced matrix element. Eq. IV.3 is subsequently decomposed using isospin projection:

$$\langle I^{(1)} I_3^{(1)}\ I^{(2)} I_3^{(2)}|\, M\, |I^i I_3^i\rangle = CG\ M_{I^{(1)} I^{(2)} I^i}, \tag{IV.4}$$

with CG the associated Clebsch-Gordan coefficient, $I^{(1)}$ and $I_3^{(1)}$ isospin of the NN system and its projection, $I^{(2)}$ and $I_3^{(2)}$ the isospin of the $x\pi$ system and its projection, $I^{(i)}$ and $I_3^{(i)}$ the isospin of initial state and its projection and $M_{I^{(1)} I^{(2)} I^i}$ the reduced matrix element for the isospin decomposition $I^i I^{(1)} I^{(2)}$. This equation can be written as the isospin decomposition into each multiplet system involved in the initial and final state contracted on the reduced matrix element.

Next, by integrating over all kinematic variables of the final state and summing over all permutations we obtain a decomposition of the cross section into isospin states, which is then compared with others to establish relations between the different cross sections.

This same procedure was then applied to reactions involving strange particles. In our case, eq. IV.3 can be written as the tensor product of the nucleon, pion, kaon, antikaon, Lambda, and Sigma systems of the initial and final state contracted on the reduced matrix element. With this eq. IV.3 becomes:

$$\begin{aligned}\mathcal{M}\left(Initial\ state \to x_N N\ x_\pi\pi\ x_Y Y\ x_K K\ x_{\overline{K}}\overline{K}\right) &= \left(\langle x_N N| \otimes \langle x_\pi\pi| \otimes \langle x_Y Y| \otimes \langle x_K K| \otimes \langle x_{\overline{K}}\overline{K}|\right) M\, |Initial\ state\rangle \\ &= \left(\langle system1| \otimes \langle system2|\right) M\, |Initial\ state\rangle\,,\end{aligned} \tag{IV.5}$$

with $\langle system1|$ and $\langle system2|$ a contraction of the final multiplet systems in two arbitrary systems. Note that the final result does not depend on the choice of contraction since it is consistent across the channels of a same reaction.

The so obtained results are either simple equalities between individual cross sections, resulting from the Clebsch-Gordan coefficients associated with isospin symmetry, or equations between several cross sections resulting from the cross sections associated with a given total value of the isospin, which can be expressed as sums of partial cross sections on various final charge states. Non trivial expressions of this kind are reported in Appendix B in bold. As example, for the reaction $N\pi \to NK\overline{K}$ we get:

$$\sigma(\pi^+ p \to pK^+\overline{K}^0) = \sigma(\pi^- n \to nK^0K^-), \tag{IV.6}$$

$$\begin{aligned}\sigma(\pi^- p \to nK^0\overline{K}^0) + \sigma(\pi^- p \to nK^+K^-) + \sigma(\pi^- p \to pK^0K^-) + \sigma(\pi^+ p \to pK^+\overline{K}^0) \\ = 2\sigma(\pi^0 p \to nK^+\overline{K}^0) + 2\sigma(\pi^0 p \to pK^0\overline{K}^0) + 2\sigma(\pi^0 p \to pK^+K^-).\end{aligned} \tag{IV.7}$$

Errors arising from this procedure are introduced by the isospin invariance hypothesis and are estimated to be in the range of a few percent, which is approximately the mass differences between particles belonging to a same multiplet.

The Bystricky procedure allowed us to increase the knowledge of the reaction cross sections by about a factor of 2. Thus, at this stage 35% of the channels were parametrised but still 65% were missing. For establishing a complete database another method, also based on isospin symmetry, was used (see next section).

IV.4.3 Hadron exchange model

In order to complete the dataset, a procedure based on the hadron exchange model (HEM) was developed. The basic of this model is to apply the isospin symmetry at the Feynman diagram level, considering only diagrams at leading order, to obtain cross section ratios. This way, once again, unknown cross sections can be determined from known cross sections.

This procedure is an adaptation of the method used by Li [73] and Sibirtsev [74]. In this method, complete Feynman diagrams are considered and not only the initial and final states as in the Bystricky procedure [71]. The method used by Li and Sibirtsev treats the case of pion and kaon exchange. Here, baryon exchange is also considered because of the type of the studied cross sections. Initially, the hadron exchange model was developed with the idea to calculate explicitly a cross section and then using the isospin symmetry to determine easily other channel cross sections for a specific type of reaction. Here, the explicit calculation is replaced by a fit of experimental data. In the following, the method is explained and illustrated in an example.

Similar to the Bystricky method, the procedure determines in a first step relations between matrix elements and, in a second step, the cross section ratios by integrating over all kinematic variables of the squared matrix elements:

$$\sigma = \int |\mathcal{M}_{fi}|^2 d\Omega. \tag{IV.8}$$

To make things easier, the method used by Li and Sibirtsev neglects interferences between diagrams. They estimated that this hypothesis could change their results by about 30%. In our case, first we consider only the ratios between cross sections and second we check, as far as possible, the results by comparing them to experimental data or results arising from the Bystricky procedure. Doing so, the cross section of a specific isospin channel can be rewritten as the sum of all individual diagram contributions:

$$\sigma(channel) = \sum_i \int |\mathcal{M}_{X_i}(channel)|^2 d\Omega, \tag{IV.9}$$

with $\mathcal{M}_{X_i}(channel)$ the diagram amplitude of the isospin channel with the exchange particle X_i. In the reduced matrix element amplitude, there are three types of contribution: the initial and final fields,

the propagators, and the vertices. Due to isospin symmetry, in the case of the same type of exchange particles, propagators and fields are identical. Therefore, the only difference between matrix elements comes from the vertices. However, the vertices have the same structure when the same particle types are involved. Consequently, these vertices are linked together by the isospin symmetry and this link can be obtained using Clebsch-Gordan coefficients. Note that kaons and antikaons have the same field and the same propagator because of the matter/antimatter symmetry. Considering a specific vertex with two incoming particles and one outgoing particle, the contribution can be written as:

$$\langle I^{out} I_3^{out} | \, \mathcal{V} \, | I^{in(1)} I_3^{in(1)}, I^{in(2)} I_3^{in(2)} \rangle = CG \; \mathcal{V}_{X,Y,Z}, \tag{IV.10}$$

with I^{out} and I_3^{out} the outgoing particle isospin and its projection, $I^{in(i)}$ and $I_3^{in(i)}$ the isospin and the projection of the i^{th} incoming particle, $\mathcal{V}$ the matrix element associated to the vertex, CG the associated Clebsch-Gordan coefficient, and $\mathcal{V}_{X,Y,Z}$ the projected matrix element for the incoming and outgoing particles of type X, Y, Z. Since Clebsch-Gordan coefficients are scalar, diagrams with the same type of exchange particle are linked by a coefficient that is independent of energy. The matrix element of one diagram can be rewritten as:

$$\mathcal{M}_{X_i}(channel) = a_{X_i}(channel) \times \mathfrak{M}_{X_i}, \tag{IV.11}$$

with $\mathfrak{M}_{X_i}$ the isospin-independent part of the matrix element and $a_{X_i}(channel)$ the product of all Clebsch-Gordan coefficients coming from each vertex (isospin-dependent part). A factor $n!$ appears in the case of n identical particles in the final state. The matrix element $\mathfrak{M}_{X_i}$ contains all the propagators, field contributions, and the structure of the vertices. The $a_{X_i}(channel)$ coefficient is a real scalar, which contains only the factor linking the different matrix elements. Using eq. IV.11, eq. IV.9 can be rewritten as:

$$\sigma(channel) = \sum_i |a_{X_i}(channel)|^2 \int |\mathfrak{M}_{X_i}|^2 d\Omega. \tag{IV.12}$$

Two cases must be distinguished. In the first case, all $|a_X(channel_j)/a_X(channel_k)|$ ratios are equal, independent of the diagram. In such a case, the cross section ratio of the two channels can easily be determined. In the second case with unequal ratios, extra information and hypotheses are required. In a first step, global relations obtained from the Bystricky procedure were systematically used as extra information. In a second step, hypotheses linking diagrams together or neglecting some diagrams are needed. Small coupling constants involved and/or small disintegration rates of the intermediate particles allow to leave out some diagrams. Note that all resonances (the Δ particle is not considered as a nucleon resonance from an isospin point of view: $J_\Delta \neq J_N$) are automatically considered because a given particle and its resonances have the same isospin and the same isospin projection. Therefore the a_X coefficients are identical. Consequently, the sum over all diagram amplitudes with the same type of exchange particle can be treated as:

$$\begin{aligned} \sum_{X_i^{(*)}} |a_{X_i}(channel)|^2 \int |\mathfrak{M}_{X_i}|^2 d\Omega &= |a_{\mathcal{X}}(channel)|^2 \sum_{X_i^{(*)}} \int |\mathfrak{M}_{X_i}|^2 d\Omega \\ &= |a_{\mathcal{X}}(channel)|^2 \int |\mathfrak{M}_{\mathcal{X}}|^2 d\Omega, \end{aligned} \tag{IV.13}$$

with $X_i^{(*)}$ the particle and its resonances $(*)$ and $\mathfrak{M}_{\mathcal{X}}$ the isospin independent general matrix element of the particle type $\mathcal{X}$ defined as:

$$|\mathfrak{M}_{\mathcal{X}}|^2 = \sum_{X_i^{(*)}} |\mathfrak{M}_{X_i}|^2. \tag{IV.14}$$

In order to illustrate the basic procedure, the way to solve the difficulties but also to demonstrate the limits, we discuss an illustrative case based on the $\pi N \rightarrow \Sigma K$ reaction. Sadly, the hadron exchange

model gives no solution in this case but instead presents the rare advantage to be relatively simple but to exhibit numerous problems, which often appear in more complex cases.

Five diagrams (three types), listed in Figure IV.2, are considered.

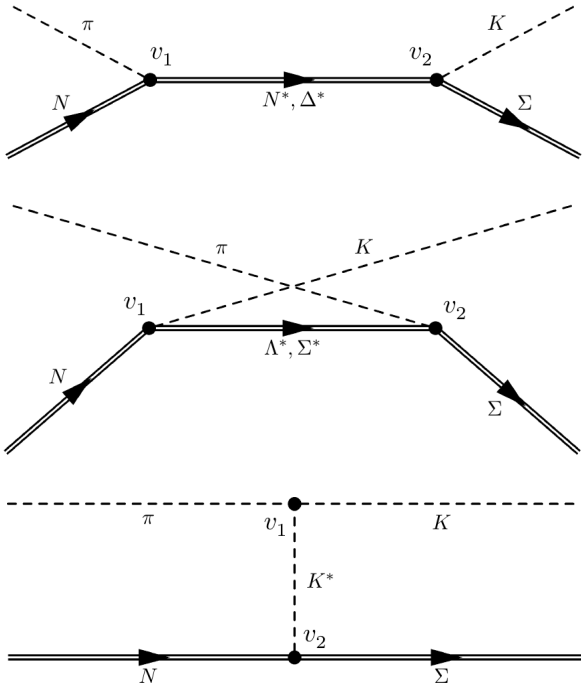

Figure IV.2: List of Feynman diagrams at leading order for the $\pi N \to \Sigma K$ reaction.

Using eq. IV.12 the cross section is given by:

$$\sigma(\pi N \to \Sigma K) = a_K^2 \int |\mathfrak{M}_K|^2 d\Omega + a_\Lambda^2 \int |\mathfrak{M}_\Lambda|^2 d\Omega + a_\Sigma^2 \int |\mathfrak{M}_\Sigma|^2 d\Omega + a_N^2 \int |\mathfrak{M}_N|^2 d\Omega + a_\Delta^2 \int |\mathfrak{M}_\Delta|^2 d\Omega. \quad \text{(IV.15)}$$

In this example, there are two vertices in each diagram called v_1^X and v_2^X as shown in Figure IV.2. The Σ exchange in the case $\pi^+ p \to \ \Sigma^+ K^+$ is a Σ^0. Then, the projection on isospin eigenstates at v_1^Σ is:

$$\begin{aligned} P_r(v_1^\Sigma)(\pi^+ p \to \Sigma^+ K^+) &= (\langle K^+| \otimes \langle \Sigma^0|)\mathcal{V}\,|p\rangle \\ &= \left(\left\langle \frac{1}{2}\frac{1}{2}\right| \otimes \langle 10|\right)\left|\frac{1}{2}\frac{1}{2}\right\rangle \mathcal{V}_{K\Sigma N} = \sqrt{\frac{1}{3}}\mathcal{V}_{K\Sigma N}. \end{aligned} \quad \text{(IV.16)}$$

Table IV.4: List of normalised $a_{X_i}(channel)$ squared coefficients for the reaction $\pi N \to \Sigma K$.

	a_K^2	a_Λ^2	a_Σ^2	a_N^2	a_Δ^2
$\pi^+ p \to \Sigma^+ K^+$	1	1	1/2	0	1
$\pi^0 p \to \Sigma^+ K^0$	1/2	0	1	1/2	2/9
$\pi^0 p \to \Sigma^0 K^+$	1/4	1	0	1/4	4/9
$\pi^- p \to \Sigma^0 K^0$	1/2	0	1	1/2	2/9
$\pi^- p \to \Sigma^- K^+$	0	1	1/2	1	1/9

Doing the same calculation for each diagram, each channel, and each vertex gives the coefficients a_{X_i} once a global normalisation has been chosen. The counterweight of this normalisation is hidden in the

isospin-independent part of the matrix element. Here the choice is that the largest a_{X_i} is equal to 1. All $a^2_{X_i}$ are given in Table IV.4. Only channels with an incoming proton are given here since channels with an incoming neutron can easily be deduced from this. It can be seen that the $a^2_{X_i}$ coefficients of the $\pi^0 p \to \Sigma^+ K^0$ channel are equal to the ones of the $\pi^- p \to \Sigma^0 K^0$ channel. Therefore, we can infer:

$$\sigma(\pi^0 p \to \Sigma^+ K^0) = \sigma(\pi^- p \to \Sigma^0 K^0). \tag{IV.17}$$

Second, another interesting point is given by the following relations:

$$2a_N^2 = a_\Lambda^2 + 2a_\Sigma^2 - 2a_K^2, \tag{IV.18}$$
$$9a_\Delta^2 = 2a_\Lambda^2 - 2a_\Sigma^2 + 8a_K^2. \tag{IV.19}$$

Thus, if we define three new matrix elements:

$$|\mathfrak{M}_1|^2 = |\mathfrak{M}_K|^2 - |\mathfrak{M}_N|^2 + \frac{8}{9}|\mathfrak{M}_\Delta|^2, \tag{IV.20}$$
$$|\mathfrak{M}_2|^2 = |\mathfrak{M}_\Lambda|^2 + \frac{1}{2}|\mathfrak{M}_N|^2 + \frac{2}{9}|\mathfrak{M}_\Delta|^2, \tag{IV.21}$$
$$|\mathfrak{M}_3|^2 = |\mathfrak{M}_\Sigma)|^2 + |\mathfrak{M}_N|^2 - \frac{2}{9}|\mathfrak{M}_\Delta|^2, \tag{IV.22}$$

eq. IV.15 becomes:

$$\sigma(\pi N \to \Sigma K) = a_K^2 \int |\mathfrak{M}_1|^2 d\Omega + a_\Lambda^2 \int |\mathfrak{M}_2|^2 d\Omega + a_\Sigma^2 \int |\mathfrak{M}_3|^2 d\Omega. \tag{IV.23}$$

The $|\mathfrak{M}_i|^2$ being unknown, extra hypotheses are needed to obtain other relations between the cross sections of the different channels. Their reliability will, however, directly affect the reliability of the final result. The hypotheses for this show-case are: the experimental data exhibit some similarities between the known channel cross sections (3 channels in the 10 that which should be parametrised are reasonably well measured). It can be reasonably argued that:

$$\sigma(\pi^- p \to \Sigma^0 K^0) \approx \sigma(\pi^- p \to \Sigma^- K^+). \tag{IV.24}$$

That implies:

$$|\mathfrak{M}_1|^2 = 2|\mathfrak{M}_2|^2 - |\mathfrak{M}_3|^2. \tag{IV.25}$$

Finally, two more hypotheses are necessary to link the isospin channel cross sections of the reaction $\pi N \to \Sigma K$. First N and/or Δ exchanges were neglected, because the strange decay ratio is very weak for most of the resonances. Second, the graphs with a Λ exchange and a Σ exchange are supposed to be equivalent because of their similar nature. Doing so, it follows:

$$|\mathfrak{M}_K|^2 = |\mathfrak{M}_\Lambda|^2 = |\mathfrak{M}_\Sigma|^2. \tag{IV.26}$$

We finally get:

$$\begin{aligned}
&\sigma(\pi^+ p \to \Sigma^+ K^+) = \sigma(n\pi^- \to \Sigma^- K^0) \\
&= \frac{5}{3}\sigma(\pi^0 p \to \Sigma^+ K^0) = \frac{5}{3}\sigma(\pi^- p \to \Sigma^0 K^0) \\
&= \frac{5}{3}\sigma(n\pi^+ \to \Sigma^0 K^+) = \frac{5}{3}\sigma(n\pi^0 \to \Sigma^- K^+) \\
&= 2\sigma(\pi^0 p \to \Sigma^0 K^+) = 2\sigma(n\pi^0 \to \Sigma^0 K^0) \\
&= \frac{5}{3}\sigma(\pi^- p \to \Sigma^- K^+) = \frac{5}{3}\sigma(n\pi^+ \to \Sigma^+ K^0).
\end{aligned} \tag{IV.27}$$

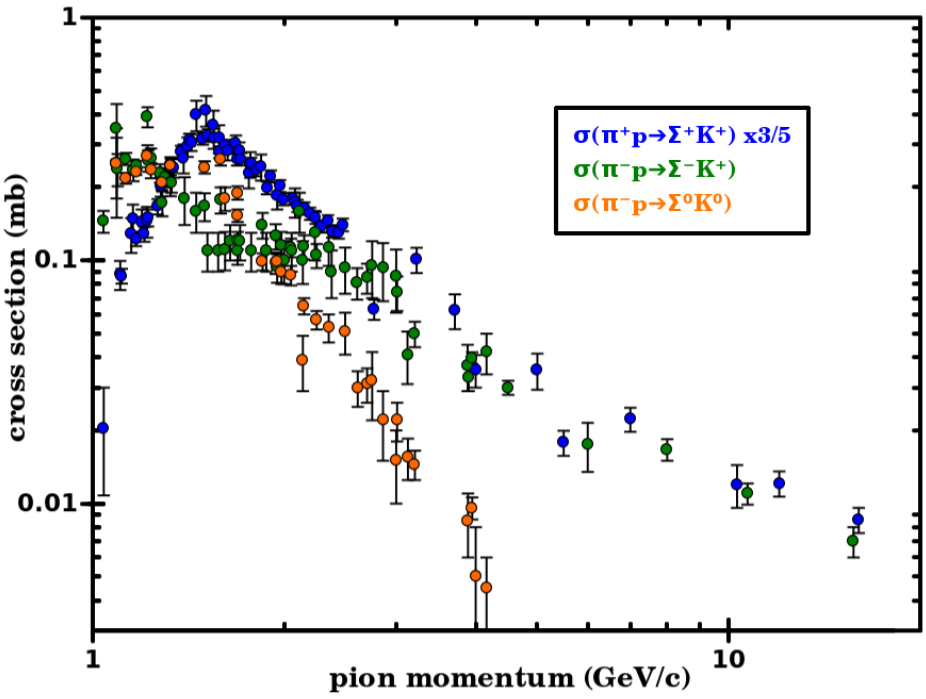

Figure IV.3: Experimental $\pi N \to \Sigma K$ cross sections

After all necessary relations have been found, the result is always compared to the experimental data and/or the predictions of the Bystricky procedure, if available, in order to check if the hypotheses used are reasonable. Unfortunately, in this special case the result obtained by the HEM procedure is not very reasonable (see Figure IV.3), likely due to unreliable hypotheses.

We anticipate that the Bystricky procedure predictions associated to available experimental data are sufficient for parametrising all $\pi N \to \Sigma K$ channels. Then, exclusive cross sections were fitted channel per channel for the ones with experimental data and the other cross sections are determined using the symmetries from the Bystricky procedure. However, in cases without enough experimental data, the relations obtained with sometimes questionable hypotheses must be kept. In general, the reliability of the relations found using this method decreases with increasing number of outgoing particles. This is due to the increasing number of Feynman diagrams, which should be taken into account and which then increases the number of hypothesis needed. An example of a case that works well even if the prediction does not match perfectly over the entire energy range the experimental data for many channels is shown in Figure IV.4.

The errors introduced by this method on the isospin average cross sections are estimated to be around $10\% - 20\%$, supposing that hypotheses are wisely chosen because, even if a specific isospin channel is under- or overestimated by a large factor, the Bystricky procedure provides relatively strong constraints on the isospin average cross sections. The list of all graphs considered and relations found are available in Appendix B.

Thanks to the use of isospin symmetry in the hadron exchange model, combined with experimental data and the Bystricky procedure, around 72% of the required information (Table IV.1) can be obtained.

IV.4.4 Enlarging the data set

Unfortunately, both methods, which are based on isospin symmetries in combination with experimental data, are not sufficient to provide a parametrisation for all reactions listed in Table IV.1 . The missing

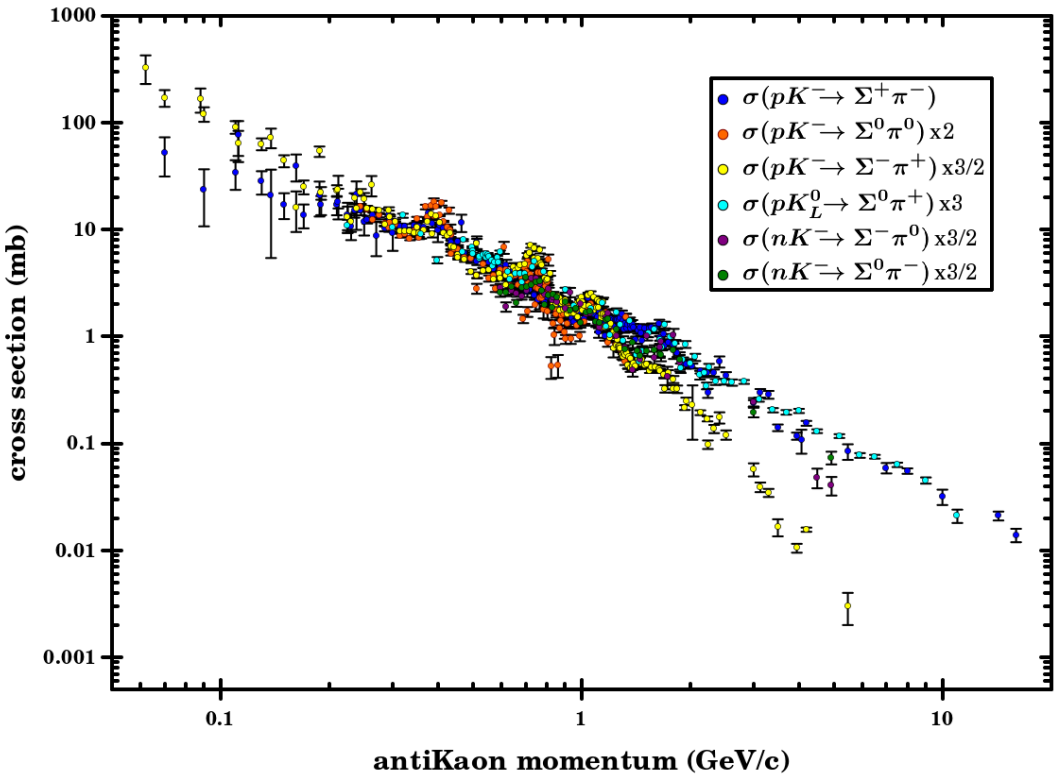

Figure IV.4: Experimental $\overline{K}N \rightarrow \Sigma\pi$ cross section showing the cross section of known channels normalised using the coefficients given by the HEM are equivalent.

cross sections were either obtained from models or from our best knowledge of *similar* reactions (notably based on reactions already studied in a previous version of INCL [39]). The reactions in question are:

- $NN \rightarrow NNK\overline{K}$,
- $NN \rightarrow N\Lambda K\pi$, $NN \rightarrow N\Sigma K\pi$,
- $NN \rightarrow N\Lambda K\pi\pi$, $NN \rightarrow N\Sigma K\pi\pi$.

The parametrisation of the $NN \rightarrow NNK\overline{K}$ reaction cross section is taken from ref. [74] (Eq. 21).

For the other four reactions we assume similarities with the already included reactions $\sigma(NN \rightarrow NN\pi)$ and $\sigma(NN \rightarrow NN\pi\pi)$, taking into account the center of mass energy ($\sqrt{s}$ in MeV in the following equations). Actually, in these cases, the changes in the shape of the cross sections, when adding a pion in the final state, is supposed to be the same as if a hyperon and a kaon replace a nucleon and a pion.

$$\sigma_{NN\rightarrow N\Lambda K\pi}(\sqrt{s}) = 3\ \sigma_{NN\rightarrow N\Lambda K}(\sqrt{s}) \times \frac{\sigma_{NN\rightarrow NN\pi\pi}(\sqrt{s}-540)}{\sigma_{NN\rightarrow NN\pi}(\sqrt{s}-540)}, \tag{IV.28}$$

$$\sigma_{NN\rightarrow N\Sigma K\pi}(\sqrt{s}) = 3\ \sigma_{NN\rightarrow N\Sigma K}(\sqrt{s}) \times \frac{\sigma_{NN\rightarrow NN\pi\pi}(\sqrt{s}-620)}{\sigma_{NN\rightarrow NN\pi}(\sqrt{s}-620)}, \tag{IV.29}$$

$$\sigma_{NN\rightarrow N\Lambda K\pi\pi}(\sqrt{s}) = \sigma_{NN\rightarrow N\Lambda K\pi}(\sqrt{s}) \times \frac{\sigma_{NN\rightarrow NN\pi\pi}(\sqrt{s}-675)}{\sigma_{NN\rightarrow NN\pi}(\sqrt{s}-675)}, \tag{IV.30}$$

$$\sigma_{NN\rightarrow N\Sigma K\pi\pi}(\sqrt{s}) = \sigma_{NN\rightarrow N\Sigma K\pi}(\sqrt{s}) \times \frac{\sigma_{NN\rightarrow NN\pi\pi}(\sqrt{s}-755)}{\sigma_{NN\rightarrow NN\pi}(\sqrt{s}-755)}. \tag{IV.31}$$

The factor 3 used in eq. IV.28 and eq. IV.29 is a normalisation factor needed to fit the few available experimental data. The method was tested using the same type of reaction cross sections (strangeness produced or not) with the πN initial state that are already relatively well described. It appears also a factor of approximatively 3 between the cross section ratio $\sigma_{\pi N \rightarrow N\pi\pi\pi}/\sigma_{\pi N \rightarrow N\pi\pi}$ and the cross section ratio $\sigma_{\pi N \rightarrow YK\pi}/\sigma_{\pi N \rightarrow YK}$ with the appropriately shifted center of mass energy. Note that this verification starts with the $\pi N \rightarrow N\pi\pi$ reaction, because the reaction $\pi N \rightarrow N\pi$ is an elastic reaction and therefore, is clearly not similar to $\pi N \rightarrow YK$.

The charge repartition is determined using the work done in subsection IV.4.3 for the $NN \rightarrow NNK\overline{K}$, $NN \rightarrow N\Lambda K\pi$, and $NN \rightarrow N\Sigma K\pi$ reactions. As discussed previously, the method based on the hadron exchange model is not used to calculate the total cross sections for those reactions (too many hypotheses needed), but it can be used to determine charge repartition. The charge repartition for $NN \rightarrow N\Lambda K\pi\pi$ and $NN \rightarrow N\Sigma K\pi\pi$ were determined using an approach by Iljinov et *al.* [75], simplified to take into account only the combinatorics of the final state as it was done in the Bertini model [56]. The method determines the ratio of channel cross sections from a same reaction based only on the particle multiplicities in the final state as:

$$\frac{\sigma\left(A+B \rightarrow \sum\limits_{i=n,p,\pi^+,\ldots} x_i i\right)}{\sigma\left(A'+B' \rightarrow \sum\limits_{j=n,p,\pi^+,\ldots} x_j j\right)} = \frac{\prod\limits_{i=n,p,\pi^+,\ldots} x_i!}{\prod\limits_{j=n,p,\pi^+,\ldots} x_j!} \tag{IV.32}$$

with x_i the number of particles i in the final state.

In addition and as mentioned in sect. IV.2 and Table IV.2, two additional reaction types must be considered: strangeness production reactions with numerous particles in final states and Δ-induced strange production reactions.

With increasing energy, kaon production is associated with an increasing number of particles in the final state and, consequently, the reactions listed in Table IV.1 are not sufficient to account for kaon production. Actually, the additional particles are mostly pions as demonstrated by the Fritiof model [58] (see Figure IV.5). Therefore, regarding the high-energy reactions $NN \rightarrow K + X$ and $\pi N \rightarrow K + X$, inclusive parametrisations of the cross sections are determined from experimental measurement and individual cross sections can be generated by trying to reproduce as good as possible the particle multiplicities given by the Fritiof model [58] using a random generator.

The parametrisation for Δ-induced strangeness production cross sections listed in Table IV.2 are taken from ref. [63], except for the reaction $\Delta N \rightarrow NNK\overline{K}$, which is discussed below and is given in Appendix A. Since the estimates given by ref. [63] for the cross sections related to ΔN collisions are very large compared to the cross sections related to NN collisions with the same final states (factor $\sim$10), it was decided to take the isospin average cross section $\sigma(\Delta N \rightarrow NNK\overline{K})$ as 10 times the isospin average cross section $\sigma(NN \rightarrow NNK\overline{K})$.

Even if the number of Δ particles present in the nuclear volume during the collision is significantly lower than the number of pions and nucleons, Δ-induced reaction are expected to contribute significantly to the strangeness production. Indeed, the cross sections calculated by Tsushima et *al.* [63] for Δ-induced reactions are much larger than those measured for pion-induced or nucleon-induced reactions. However, for these parametrisations, they used hypotheses, which are not obviously fair for the entire energy range studied in this work and the experimental data in $NN \rightarrow NYK$ calculated with the same hypotheses are not always well reproduced (see [63], Fig.7). Considering the rather large uncertainties associated to these theoretical cross sections, this kind of reaction is supposed to be the largest source of error on strangeness production in our code.

The charge repartition was determined based on information obtained from the Bystricky procedure and the Hadron Exchange Model.

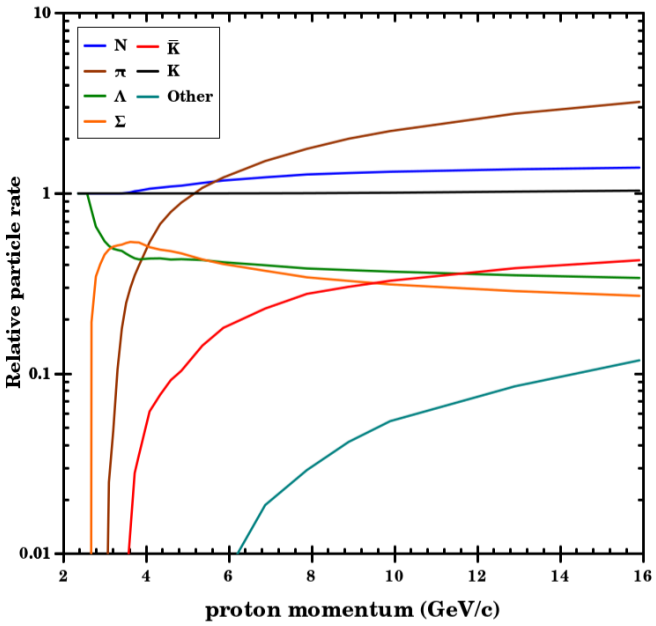

Figure IV.5: Particle rate per reaction in $pp \to K + X$ reactions in the Fritiof model [58] as a function of the incident proton momentum.

IV.4.5 Parametrisations

Different generic formulae were used to parametrise the reaction cross sections. The reactions considered are of two types: elastic and inelastic. This section presents our choice of fit functions. We give below the generic formulae and in Appendix A the parametrisations for all reactions in the whole energy domain considered (momentum in laboratory frame of reference below 15 GeV).

The elastic scattering cross sections become extremely large when the incoming particle momentum goes down to zero. Upper limits are placed at low energies to avoid cross section divergences. The limits have no consequences on the final result if placed high enough, because the cross sections are only used to determine which reaction will contribute. The elastic cross sections appear relatively complex in the energy range studied here to be defined by a singular function. Consequently, the energy ranges studied were split into several parts in order to get better parametrisations of the cross sections. The following functions were used:

$$\sigma(p_{Lab}) = a + b\ e^{-c\ p_{Lab}}, \tag{IV.33}$$

$$\sigma(p_{Lab}) = a + b\ p_{Lab}^{-c}. \tag{IV.34}$$

Note that this kind of reaction is often resonant; the resonances are fitted by adding bumps of Gaussian shape on the underlying background.

The quasi-elastic reactions, which are $NK \to N'K'$, $N\overline{K} \to N'\overline{K}'$, and $N\Sigma \to N'\Sigma'$, are especially problematic at low energies with respect to the assumption of isospin symmetry because of the existence or absence of reaction thresholds. This asymmetry is taken into account by a cross section shift, which "breaks" the isospin symmetry hypothesis for both reactions.

The inelastic cross sections are the most important for the physics studied here. A lot of different formulae were tested. The following function, which is similar to formulae found in literature, gives good results for most reactions. We used the basic formula over the entire energy range even for those reactions

where only few data concentrated in a narrow energy range exist.

$$\sigma(p_{Lab}) = a\frac{(p_{Lab} - p_0)^b}{(p_{Lab} + p_0)^c\ p_{Lab}^d}, \tag{IV.35}$$

with p_0 the threshold momentum and a, b, c, and d positive fitting parameters. In a few cases, Gaussian functions are added in order to fit resonances.

IV.5 Double differential cross sections

After fixing the type of reaction, the final state must be determined. Doing so, charge and momentum must be assigned to each particle in the final state.

In most cases, charge repartition is determined using isospin symmetry and the hadron exchange model, which both predict relations between the isospin channel cross sections. The ratios are given in Appendix B. We then randomly chose charge repartition using the ratios determined before. For the reaction $NN \to NYK\pi\pi$, the Bystricky procedure and the hadron exchange model discussed in sect. IV.4 are not able to provide any ratio. Therefore, the simplified Iljinov et *al.* approach [75] is used.

The other information needed to define the final state is the three-momentum of outgoing particles. In INCL, there are two different options to determine the kinematics of outgoing particles: the first one is to provide an angular distribution based on experimental measurements. The second one is to use a phase space generator, which is isotropic for the simplest cases or more sophisticated for more complex cases (Kopylov [76] or Raubold-Lynch [77]). Typically, no experimental data are available and therefore, phase space generators are used. Nevertheless, studies providing Legendre coefficients have been carried out for $\overline{K}N$[78–91] and πN[92–98] elastic and quasi-elastic reactions. The results are used to provide angular distributions for $\overline{K}N$ and πN reactions. Details are given and summarised in Table IV.5 .

Table IV.5: List of reactions for which the angular distributions were studied experimentally. Momentum range and references are given.

$\Delta p(MeV/c)$	Reaction	Refs
225 - 2374	$K^-p \to K^-p$	[78–86]
235 - 1355	$K^-p \to \overline{K}^0n$	[83–88]
436 - 1843	$K^-p \to \Lambda\pi^0$	[85–87, 89–91]
436 - 865	$K^-p \to \Sigma^0\pi^0$	[85, 89, 91]
436 - 1843	$K^-p \to \Sigma^\pm\pi^\mp$	[85–87, 91]
930 - 2375	$\pi^-p \to K^0\Lambda^0$	[92–94]
1040 - 2375	$\pi^-p \to K^0\Sigma^0$	[95, 96]
1105 - 2473	$\pi^+p \to K^+\Sigma^-$	[97, 98]

The angular distributions for a given energy are usually parametrised using Legendre polynomials as follows:

$$\frac{d\sigma(\sqrt{s}, \Theta_{c.m.})}{d\Omega} = \lambda\!\!\!^{-2}(\sqrt{s}) \sum_{l=0}^{n} A_l(\sqrt{s}) P_l(\cos\Theta_{c.m.}), \tag{IV.36}$$

with $\lambda\!\!\!^{-}$ the c.m. reduced wavelength, A_l the l^{th} Legendre coefficient, $\sqrt{s}$ the center of mass energy, $\Theta_{c.m.}$ the angle of the outgoing particle with its initial momentum in the center of mass reference frame, and P_l the l^{th} order Legendre polynomial.

The experimental papers studying angular distributions often provide A_l at different energies [78–97]. If it is not the case, like in ref. [98], I determined the Legendre coefficients from the experimental data (c.f. eq. IV.36). However, the Legendre coefficients determined in experiments strongly depend on the experimental set-up, like the backward detection and the angular binning, and can therefore provide an

angular distribution that is only valid in a partial angular range. Sometimes, aberrations like negative density probability also appear. In an intranuclear cascade model, a description of Legendre coefficients as a function of the energy is needed. Doing so, a direct (non-parametric) fit of the A_l using all Legendre coefficients coming from the experiments were done. Using these fitted A_l, we observed that most of the negative density probability problems disappeared. When negative probability density problems persisted, the density was set to zero. Thanks to the cross section parametrisation (see sect. IV.4), only the $A_i(\sqrt{s})/A_0(\sqrt{s})$ fittings are needed. Below, we elaborate on the two methods used to define the $A_i(\sqrt{s})/A_0(\sqrt{s})$ ratios in the given energy range.

The first method used is the Nadaraya–Watson kernel regression [99]. The parametrisation of the ratios is obtained by determining the function $\hat{m_h}(x)$ given by:

$$\hat{m_h}(x) = \frac{\sum_{i=1}^{n} K_h(x - x_i).y_i}{\sum_{i=1}^{n} K_h(x - x_i)}, \tag{IV.37}$$

with (x_i, y_i) the set of n data, K_h is a kernel, here a Gaussian with a standard deviation defined so that their quartiles (viewed as probability densities) are at $\pm 0.25h$. The denominator in eq. IV.37 is the normalisation term. In our analyse, the bandwidth was chosen as h = 25, 50, 100, 150 or 200 MeV/c either on the whole energy range or according to available energy bins. The latter case is used when complex structures or narrow resonances appear, thereby avoiding fitting non physical fluctuations.

The second method used is the smoothing spline regression [100]. This method consists in the minimisation of the following function:

$$\sum_{i=1}^{n} (y_i - \hat{\mu}(x_i))^2 + \lambda \int_{x_1}^{x_n} \left(\hat{\mu}''(x)\right)^2 dx, \tag{IV.38}$$

with (x_i, y_i) the set of n data, $\hat{\mu}$ the non-parametric fit function (a spline), and λ the smoothing parameter. This method corresponds to the common χ^2 minimisation with a second term used to limit quick variations in the fit function. The smoothing parameter was for each case optimised by hand to obtain a good compromise between the smoothness and the proximity to the data in order to fit resonances but to avoid fitting the noise.

As already mentioned, there is no fit function for the two non-parametric methods. The result is a tabulation of Legendre coefficients as a function of momentum with bins as small as needed. An example is shown in Figure IV.6.

The two methods use completely different ways of fitting but give very similar results, as shown in Figure IV.6. The choice to use one or the other was made case-by-case. Out of the experimental data energy range, it was decided to use an isotropic distribution in the energy range below the experimental data and a more and more forward peaked distribution for higher energies

Tables used in INCL are available as electronic supplementary material of ref [44]. Note that the extrapolation of the $A_i(\sqrt{s})/A_0(\sqrt{s})$ outside the energy range considered here is not reliable and is likely to produce unphysical results.

IV.6 Comparison with other models

Here the cross sections, charge repartition, and phase space generation determined thanks to the procedures explained above are compared to the same input parameters available in the literature and already used in other models that consider strangeness production in the same energy range. These models are: (i) INCL2.0 [16, 55], a version of INCL no more available developed about 25 years ago to study anti-proton physics and including kaon physics, (ii) the Bertini Cascade model [56], and (iii) the GiBUU model [51, 52]. To do this comparison, different examples will be discussed in order to show the strength and the weakness of each model.

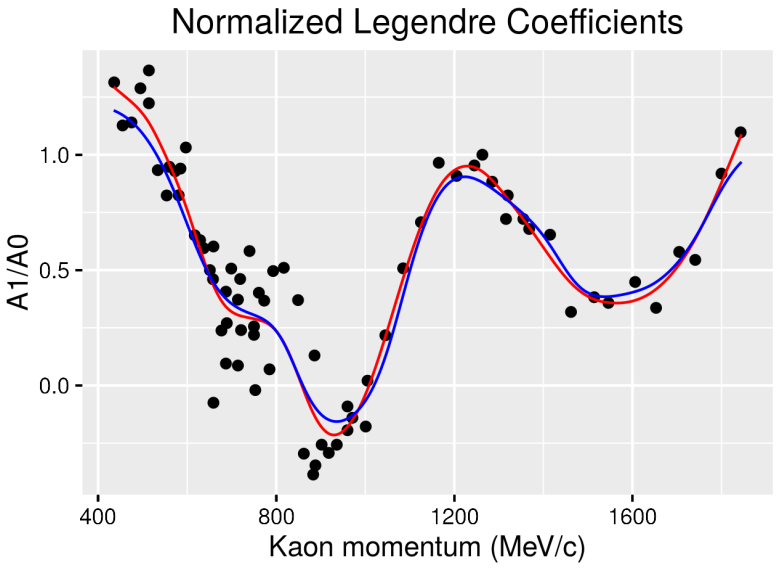

Figure IV.6: Example of $A_1(\sqrt{s})/A_0(\sqrt{s})$ fit in the case $K^- p \to \Lambda\pi^0$ using Nadaraya-Watson kernel regression (blue), and smoothing spline regression (red).

The different models parametrise the reactions using different methods. The Bertini cascade model tabulates the cross sections based on parametrisations and calculations at 30 kinetic energies corresponding to intervals whose width is increasing logarithmically with incident energy and spanning the 0 to 32 GeV domain. In INCL2.0, cross sections were parametrised only for reactions with two particles in the final state. The parametrisation is often a fit in one or two parts using a formula like $\sigma = a\ p^b$, with p the momentum in the laboratory frame of reference. In the GiBUU model, the energy range is divided in two parts: the *low-energy* part is fitted with parametrisations and the *high-energy* part is treated using PYTHIA [101], which is based on the Lund string model [102]. The transition between the *low-energy* parametrisation and the PYTHIA predictions is a smooth linear transition. The energy transition considered in GiBUU is $\sqrt{s} = 2.2 \pm 0.2$ GeV in meson-baryon collisions, which corresponds, in term of momentum, to 2.1 ± 0.5 GeV/c for pion nucleon collisions and to 1.9 ± 0.2 GeV/c for kaon nucleon collisions, and $\sqrt{s} = 3.4 \pm 0.1$ GeV in baryon-baryon collisions, which corresponds to 5.1 ± 0.4 GeV/c for nucleon-nucleon collisions.

Nucleon-nucleon collisions have a high contribution in strangeness production. The first open reaction channel with a proton as a projectile is the $pp \to p\Lambda K^+$ channel, which is important at low energies but which contributes less and less at high energies. As shown in Figure IV.7, all models reproduce well the experimental cross sections. However, in the range $3.7 - 5$ GeV/c, where there are no experimental data, there are significant differences between the different fits. Such differences are very common when experimental data are not available in some energy range and/or are rather inconsistent.

A typical problematic channel is $pp \to p\Sigma^+ K^0$ with the cross section parametrisation shown in Figure IV.8. The parametrisation from our work matches relatively well the experimental data at energies up to 4 GeV/c but underestimates the high energy part. This is due to the compromise between inclusive calculations from the Fritiof model [58] and exclusive cross section measurements. We have chosen to artificially reduce our fit in order to be consistent with the inclusive cross section data. However, this type of reaction could deserve extra work according to its contribution in INC models. Another crucial point for this type of reaction, which can also be observed in Figure IV.8, is the inconsistency of the experimental data. For example, the two measurements around 3.7 GeV/c in this last figure differ by a factor 3 and the data point at 10 *GeV* is suspiciously high compared not only to other data from this reaction but also compared to other isospin channels, which seem to show decreasing cross sections

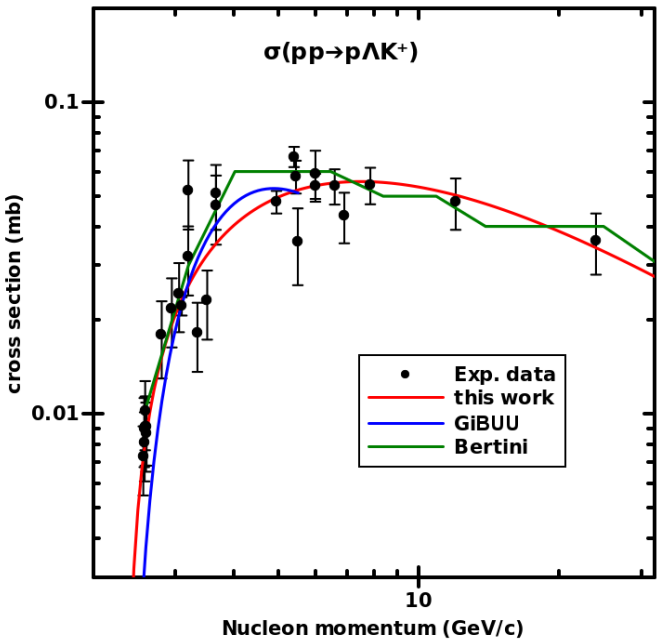

Figure IV.7: The $pp \rightarrow p\Lambda K^+$ cross section fits from the Bertini cascade model (green line), GiBUU (blue line), and my work (red line) compared to experimental data (black dots) as a function of incident proton momentum. Note that above 5.5 GeV/c GiBUU used Pythia and therefore has no proper parametrisation.

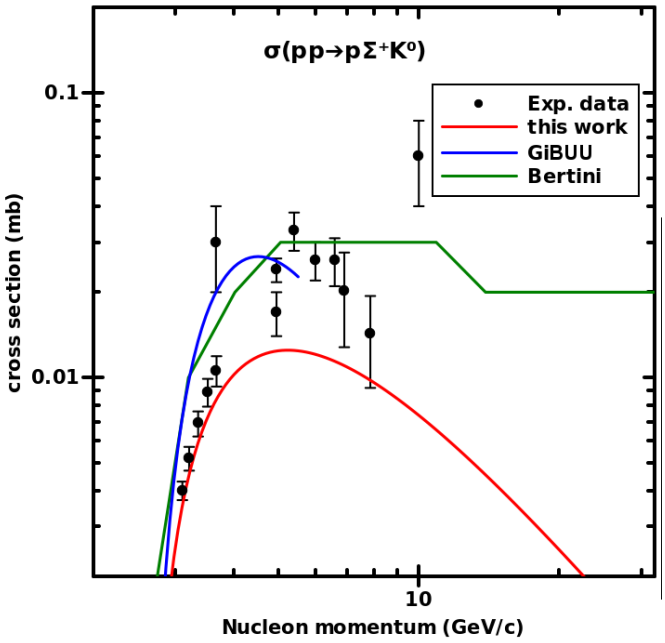

Figure IV.8: The $pp \rightarrow p\Sigma^+K^0$ cross section fits from the Bertini cascade model (green line), GiBUU (blue line), and my work (red line) compared to experimental data (black dots) as a function of incident proton momentum. Note that above 5.5 GeV/c GiBUU used Pythia and therefore has no proper parametrisation.

with increasing energy. The parametrisations in the other models differ significantly from our work. The Bertini cascade model and the GiBUU model, which uses the formula from [63] scaled by a factor 0.7, are two different compromises between the experimental data.

Figure IV.9 highlights a problem with the INCL2.0 parametrisations. The result of the parametrisation describes correctly the magnitude of cross sections but does not give good fits of the energy dependence of the cross sections. As seen in Figure IV.9, the cross section is slightly overestimated in the energy range $1.5-2$ GeV/c for the $\pi^- p \to \Lambda K^0$ reaction and in the energy range $1.5-10$ GeV/c for the $\pi^+ p \to \Sigma^+ K^+$ reaction. In the Bertini cascade model tabulations, because of the few energy intervals, quick variations in cross sections as a function of energy can be missed. For example, for the reaction $\pi^- p \to \Lambda K^0$ shown in Figure IV.9, the Bertini cascade model reproduces well the experimental data near the threshold and at high energies but, the first interval being too wide, some part of the cross section is underestimated. The $\pi^- p \to \Lambda K^0$ cross section from the GiBUU model is close to the experimental data up to 1.4 GeV/c but, surprisingly, there are relatively large deviations from the experimental data at higher momenta. However, this deviation is in the energy range of the transition between the parametrisation and the PYTHIA model (see above). Note also that the parametrisation for the reaction $\pi^+ p \to \Sigma^+ K^+$ from my work is slightly shifted to higher energies (about 10 MeV - seen only at low energies) because the isospin invariance considers an equal mass for all particles belonging to a same multiplet. Here, the mass for a multiplet was considered as the heaviest mass of this multiplet and therefore, can produce this artefact.

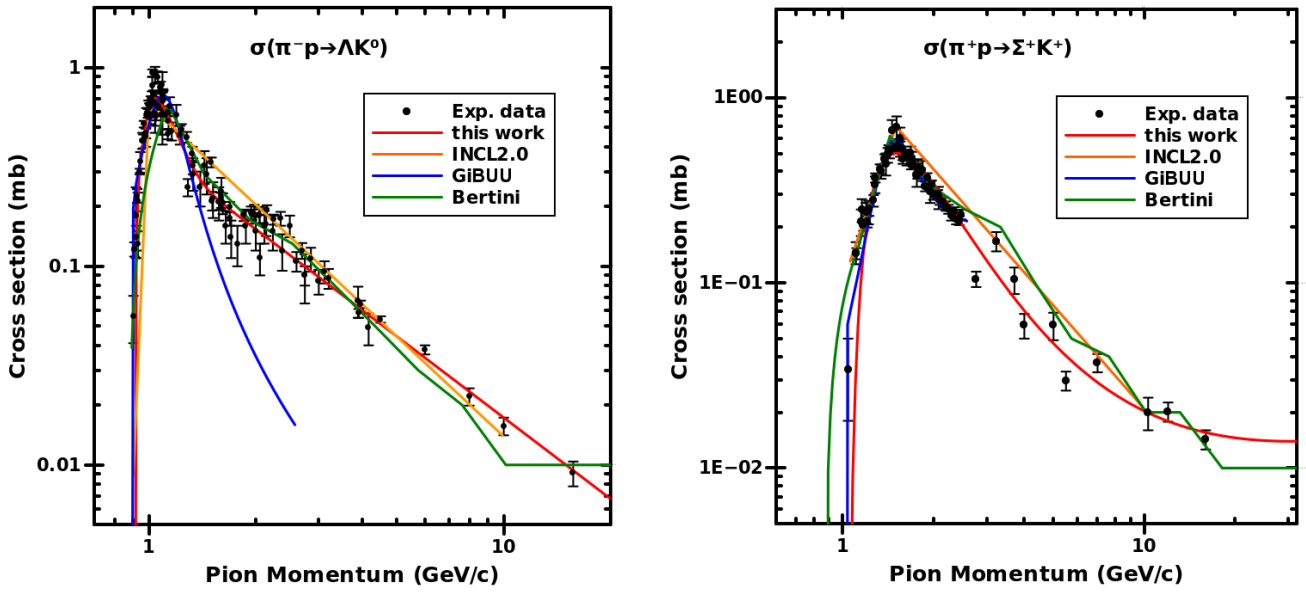

Figure IV.9: The $\pi^- p \to \Lambda K^0$ and $\pi^+ p \to \Sigma^+ K^+$ cross sections fits from the Bertini cascade model (green line), GiBUU (blue line), INCL2.0 (orange line), and my work (red line) compared to experimental data (black dots) as a function of incident pion momentum.

Figure IV.10 illustrates another important result: the predictions at high energies from the Bertini cascade model are significantly different from our results. However, since there are only very few experimental data in this energy range, we cannot state which model is more reliable. This phenomenon is also visible in Figure IV.11, though with more physical relevance. Deviations between experimental data and predictions are not very problematic when cross sections are relatively low because other reactions dominate. However, deviations of two orders of magnitude as seen for the reaction $K^- n \to \Sigma^0 \pi^-$ (Figure IV.11) are much more significant. Again, looking only at the experimental data, it is not obvious which of the parametrisations are correct. Fortunately, for this special case the deviations have a low impact on the entire cascade because antikaons, except if they are projectiles, play a minor role (very low production yield).

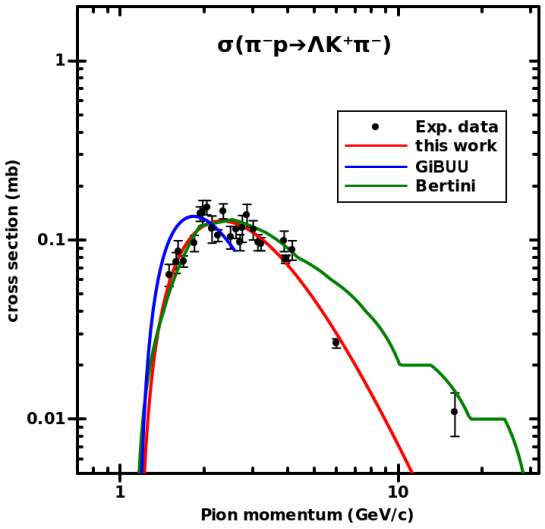

Figure IV.10: The $\pi^- p \to \Lambda K^+ \pi^-$ cross section fits from the Bertini cascade model (green line), GiBUU (blue line), and my work (red line) compared to experimental data (black dots) as a function of incident pion momentum.

Resonances are not treated directly in our work. However, they appear as Gaussians in the cross section parametrisation. If the hadron exchange model is used to determine a missing channel, those resonances also appear in the missing channel cross section even if they cannot be the intermediate state because of quantum number considerations. As an example, the resonances fitted for the reaction $K^- p \to \Sigma^0 \pi^0$ (Figure IV.11) appear also in the $K^- n \to \Sigma^0 \pi^-$ cross section fit, even if the third component of the isospin differs (0 for the former and -1 for the latter). Note that the GiBUU parametrisation is not shown in Figure IV.11 because the reaction is treated in a different way using resonant and non-resonant cross sections. Therefore, no simple formula can be given. Figures IV.11 and IV.12 also show another problem with the earlier INCL2.0 parametrisations: resonances are not reproduced. In contrast and as an improvement, the parametrisations proposed in this work and in the Bertini cascade model have no difficulties reproducing resonant cross sections.

Unlike antikaon-nucleon collision cross sections discussed above, the $K^+ p$ elastic cross section is important for spallation processes with either nucleons or pions as projectiles. This is due to the low production rate of antikaons compared to kaons. Figure IV.13 shows that the cross section is well reproduced using the results from this work and in the Bertini cascade model. Also the GiBUU model gives a good description of the experimental data. Differences between the three different approaches are observable at low energies where the differences are not very relevant because of the lack of competing processes in this energy range. In contrast, the INCL2.0 model underestimates the cross sections over the entire energy range.

In general, the parametrisations of the three different models fit the experimental data (if available) rather well. However, if experimental data are missing in an energy range, fits can be very different.

The two last subjects developed in this chapter are the charge repartition and phase space generation. Since information about phase space generation in other models is too scarce, a comparison between the different models is not possible. Considering charge repartition, different methods are used by the different models. The Bertini cascade model uses a simplified version [56] of the Iljinov et *al.* approach [75]. For the GiBUU model, the charge repartition is determined using isospin rules and, in the case $\pi N \to N K \overline{K}$, using the hadron exchange model with K^* and π exchange diagrams. In INCL2.0, the charge repartition was determined using isospin invariance rules by neglecting interferences.

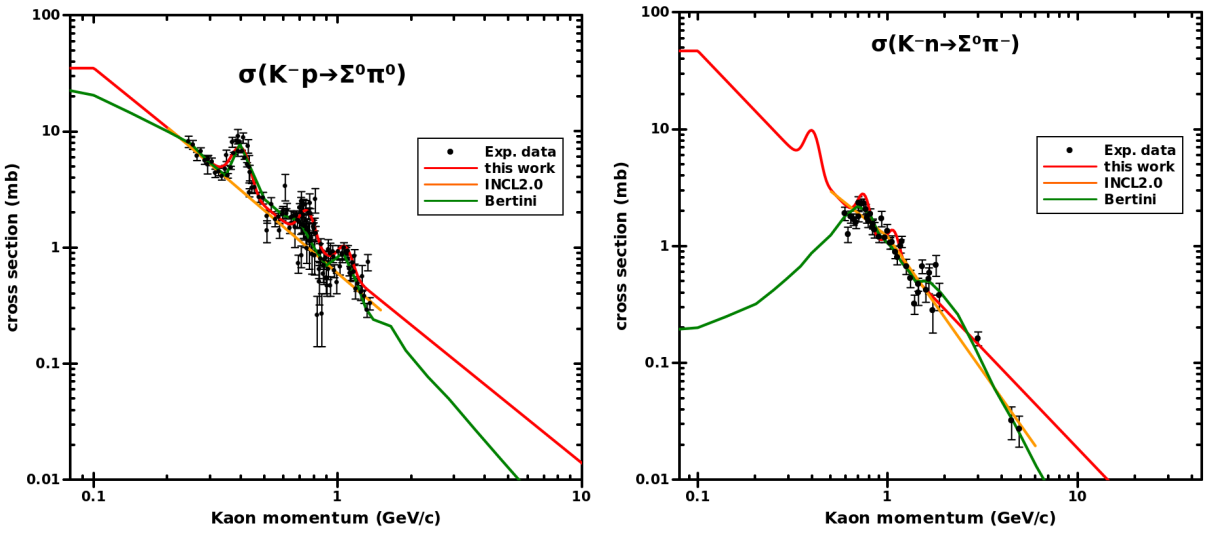

Figure IV.11: The $K^-p(n) \rightarrow \Sigma^0\pi^{0(-)}$ cross section fits from the Bertini cascade model (green line), INCL2.0 (orange line), and my work (red line) compared to experimental data (black dots) as a function of incident kaon momentum.

IV.7 Conclusion on the parametrisation work

The work discussed in this chapter was particularly challenging. It was absolutely necessary for the implementation of strange particles in INCL but the major part of the absolutely needed ingredients, which are the interaction and the double differential cross sections, were very scarce in the literature. Only 17% of the needed information to implement the reactions summarised in Table IV.1 were available. The Bystricky procedure, which allowed to double the information, were already a well established procedure. However, the development of the procedure based on the hadron exchange model detailed in subsection IV.4.3 and its application to every reaction in Table IV.1 and Table IV.2 has been very complex and extremely time consuming. Moreover, this procedure required a lot of creativity to draw reliable hypotheses needed to handle some of the reactions.

A second problem made the realisation of my work even more challenging. The problem appeared when the reactions summarised in Table IV.1 alone showed that they had difficulties to reproduce the experimental data (see chapter VI for details). These reactions represented the major part of the interaction cross sections measured experimentally. Various hypotheses were explored to explain the discrepancies with, for example, the possibility that the kaons were not produced on shell in the nucleus. It took some time before considering the Δ-induced strangeness production reactions of Table IV.2 because the Δ particles are much less numerous than nucleons and pions in the cascade and these reactions are not taken into account in other models.

The uncertainties linked to the ingredients discussed in this chapter were a major concern considering the various hypotheses required for the hadron exchange model procedure and the ones used by Tsushima *et al.* in ref. [63]. Hopefully, the comparisons with experimental data for elementary interaction cross sections, when available, showed good results. Moreover, these parametrisation has been validated a posteriori with the comparisons between INCL results and experimental data of spallation reactions shown in chapter VI.

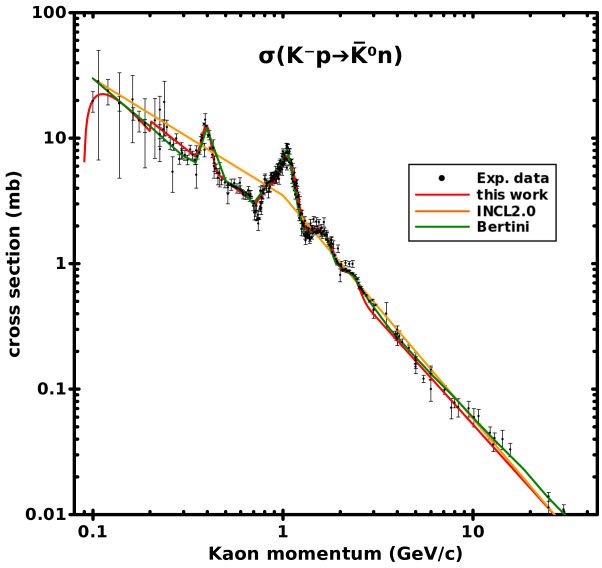

Figure IV.12: The K^-p quasi-elastic cross section fits from the Bertini cascade model (green line), INCL2.0 (orange line), and my work (red line) compared to experimental data (black dots) as a function of incident kaon momentum.

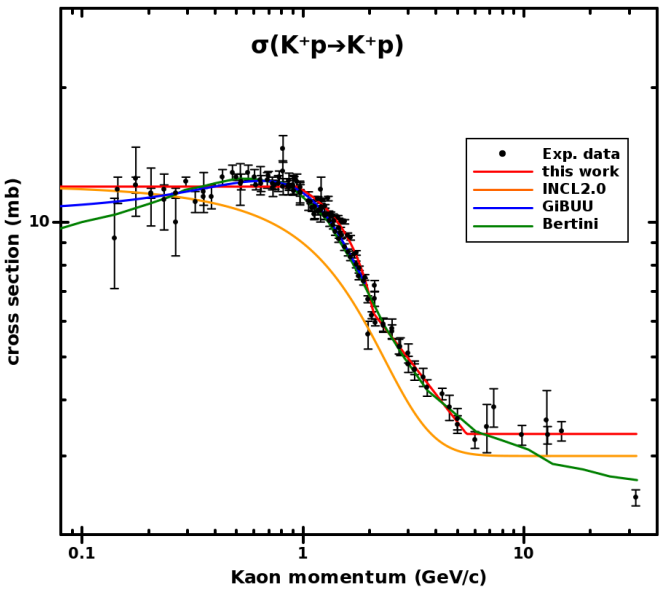

Figure IV.13: The K^+p elastic cross section fits from the Bertini cascade model (green line), INCL2.0 (orange line), GiBUU (blue line), and my work (red line) compared to experimental data (black dots) as a function of incident kaon momentum.

Chapter V

The variance reduction scheme

This chapter is devoted to the variance reduction scheme (VRS) implemented in INCL. This chapter corresponds partially to the work described in ref. [43]. The subject being atypical in nuclear physics, the chapter will also be the place to discuss some particular points of the method in more detail.

Note that, as in ref. [43], this chapter is not required for the discussing INCL results. The VRS developed here, and used in INCL, aims at getting results with lower uncertainties and in some cases is the only way to get results within a reasonable computation time but it does not change the conclusions.

The VRS born with a simple ascertainment: strangeness production is a rare process in spallation reactions, especially for energies below $5-6$ GeV. However, the user of INC models, and notably of INCL, might be interested in strangeness physics. Therefore, to get enough statistics, a calculation requires a large number of events. This needs a lot of computational time and results in useless information; taking a lot of space on a hard drive and slowing down the analysis.

The solution I proposed is to use variance reduction methods. The methods proposed are based on the importance sampling method. The VRS implemented in INCL artificially increases the statistics for the observables linked to the strangeness production, keeping the calculation time and the output file size unchanged.

Note that INCL already has an option allowing to write in the final ROOT file only if a certain condition is fulfilled. This makes the output size problem marginal for us. However, the information that does not fulfil the condition is lost with this option. With the new variance reduction scheme all information is kept.

The chapter is divided into two mains parts. In a first part, I develop the method. The reader will find some generalities (sect. V.1) presenting the topic, the constraints and the difficulties within INCL, the scheme developed together with the technical aspects (sect. V.2), and the case of correlations (sect. V.3). In the second part, the reliability of the method is tested (sect. V.4) and some examples of the VRS are shown (sect. V.5).

V.1 Generalities

Basically, a fully operational important sampling method consists of two successive steps. In a first step, the rules of the simulation, *i.e.*, the physics ingredients, are modified (biased) in order to improve the sampling. In our approach, we increase the strangeness production. In a second step, the simulation result is accordingly corrected. The goal of the variance reduction methods is to obtain the true observable of interest (*e.g.*, a cross section) with a reduced variance and therefore with reduced uncertainties within the same computational time.

For this study, all processes associated with strangeness production are of interest. Therefore, the

VRS in INCL was developed to increase the realisation probability for all of them, independent of the observable. However, even though the current VRS globally modifies the probabilities for processes involving strangeness, other schemes are in principle possible. The scheme could also be adapted to be more restrictive (*e.g.*, forward kaon production) or to work for another particle type (*e.g.*, η meson production) or physics (*e.g.*, peripheral collisions).

The reason for the low global strangeness production rates in INCL comes from the low elementary strangeness production cross sections. For example, the strangeness production represents 0.014%(0.15%) of the total cross section in proton-proton collisions at kinetic energies of 2(3) GeV. Therefore, in a first step, the VRS modifies the hadron-hadron cross sections in order to increase strangeness production. In a second step, it corrects a posteriori the bias introduced in order to obtain the unbiased observable estimators with reduced uncertainties.

In the general case, the second step (*i.e.*, the bias reversal) consists in determining the ratio of the probability to make an observation in the non-biased version to the probability to make the same observation in the biased version. This ratio is called the importance or the weight and can be calculated for a complete event (a cascade), a specific particle or for any observation during the event. Next, the importance is used to weight the contribution of observations. This number gives the information about how much this observable is biased. The importance for an observable X can be written as:

$$W_X = \frac{P(X|\text{no-bias})}{P(X|\text{bias})}. \tag{V.1}$$

This expression of the importance leads to a first requirement that events contributing to a variable of interest should have a non-zero probability of realisation in the biased version (the version using the variance reduction scheme) otherwise it will result in an arithmetic exception. In other words, every strange event in INCL that can be produced in the standard version must be attainable in the version using the variance reduction scheme. Only the probability of realisation can be changed. Because of this constraint and because it is not trivial to know whether strangeness production could occur later during an event, no channel cross section can be reduced to zero at the binary collision level in INCL.

The treatment of a particle during an INCL event can be subdivided into a three step cycle. First, the particles are propagated inside the nucleus. This step ends when two particles collide. A collision occurs when the distance between two particles is below a maximal interaction distance based on their total interaction cross sections. Second, the type of the reaction of the binary collision is randomly chosen based on the respective reaction cross sections. In the last step, the phase space and the charge repartition is randomly generated either based on differential cross sections (if available) or on phase space generators. Then, the cycle is repeated until the end of the intra-nuclear cascade.

The propagation along straight trajectories between collision events is deterministic. According to this, an artificial decrease of a total interaction cross section can lead to a situation of particles flying past each other where they would have collided using the original cross section. From such an event onwards, the subsequent cascade is outside the universe of possibilities based on the unbiased total interaction cross section. Therefore, the importance of this event would be null according to eq. V.1. The same argument can be made for an increased total interaction cross section. Hence, the total interaction cross sections must be conserved.

Thanks to the random treatment of the reaction choice and the phase space generation, both steps can be biased: changing the probability of realisation. In our case, only the step selecting the type of reaction needs to be biased to increase the global strangeness production. However, if the user is interested in the production of a particle in a specific phase space (*e.g.*, backward production), phase space generation can be biased with only minor modification in the code.

The two constraints, the prohibition to cancel a channel and the total cross section conservation, will be crucial for the INCL variance reduction scheme.

With the variance reduction scheme, the new weighted estimators and the associated variances of an

observable X [103] are given by:

$$E(X) = \frac{\sum_{i=1}^{M} w_i x_i}{N}, \tag{V.2}$$

$$V(X) = \frac{\sum_{i=1}^{M} (w_i x_i - E(X))^2}{M}, \tag{V.3}$$

with w_i the importance of the i^{th} observation x_i of the observable X and N the number of events. The natural summation in such a case is a sum over the events ($M = N$), with w_i the importance of the i^{th} event and x_i the number of observations corresponding to the observable X (*e.g.*, kaons) in the corresponding event.

An alternative summation is actually possible and preferred in our case. We can sum over the final particles ($M \neq N$) with w_i the importance of the i^{th} particle and $x_i = 1$ or 0 if the particle corresponds to the observable or not, respectively. With the natural summation, we estimate the mean value of the number of strange particles produced per reaction. In the alternative summation, we estimate the number of strange particles produced then we normalise by the number of reactions. It clearly appears that the observables estimated correspond to each other.

For INCL, it is simpler to sum over the particles considering the output generated. Moreover, for sake of simplicity, the relative uncertainties displayed in the figures below do not come from eq. V.3 but are calculated using the formula:

$$relat.\ uncer. = \frac{\sqrt{\sum (w_i x_i)^2}}{\sum w_i x_i}, \tag{V.4}$$

which is equivalent to the standard relative uncertainty equals to the inverse square root of the number of observations in the Monte Carlos simulations and which is an approximation of eq. V.3.

It is worth emphasising that the observable X can be anything. For example, it can be the presence or absence of a particle of a certain type, the number of particles of a certain type produced during the cascade, the presence of many particle correlated, an entire event, or a part of an event.

The minimum variance for a given number of events is achieved when all strange particle importances are equal according to eq. V.2 and eq. V.3. However, these importances are not always equal in INCL for reasons explained further below. Therefore, the objective is to keep them as close as possible to each other to minimise the variance and therefore uncertainties.

V.2 Variance reduction scheme in INCL

For a better understanding of the VRS used in INCL, a cascade can be seen as a time ordered graph where the edges (arrows) and vertices correspond to the particles propagating and to the binary collisions, respectively. Thus, a cascade is fully defined by the set of its vertices. The information about what happened before (*e.g.*, the projectile type, the impact parameter, ...) is hidden in the definition of the vertices initial state. A schematic example is displayed in Figure V.1.

As explained in the previous subsection, the VRS must increase strangeness production in a way that minimises the spread of the strange particle importances to achieve minimum variance and therefore to obtain the smallest possible uncertainties for a given number of events.

In our variance reduction scheme, if the particle Y shown in Figure V.1 is a strange particle, the event containing the set of vertices A, C, D, and F should have an increased probability of realisation. If the particle X is a strange particle, the events containing the set of vertices A, B, C, D, E, and G should be promoted. If both particles are strange particles, both paths should be promoted in the same way. Two solutions can be considered. The first one is to promote the vertices A, C, and D, which are common to both paths, and to continue as a standard cascade. In such an approach, it actually means only the first vertex can be biased. The problem is that we do not know whether a strange particle will be produced in

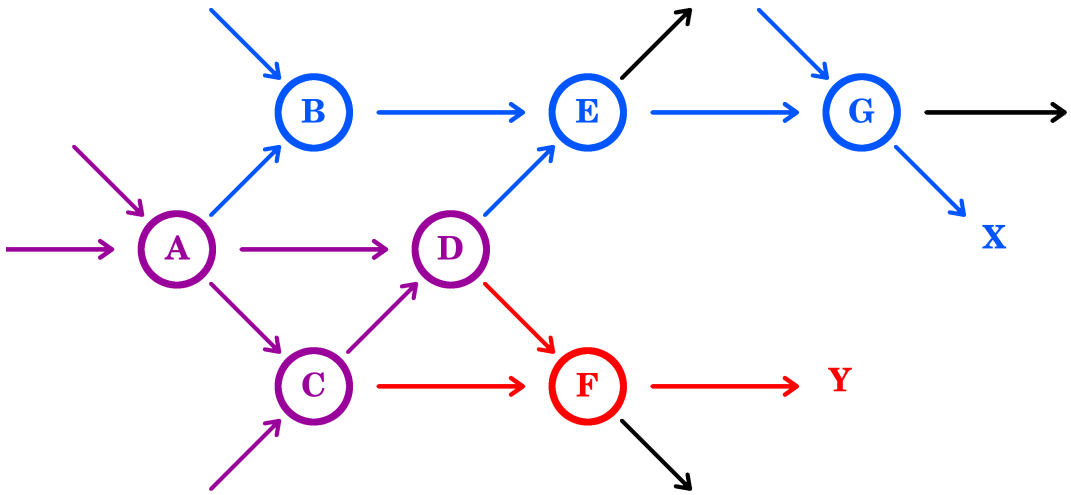

Figure V.1: Simplified example of an intra-nuclear cascade represented as a time ordered graph. Circles and arrows represent binary collisions and the propagation of the particles, respectively. The blue (red) and purple part of the graph is the history of the X (Y) particle.

any of the binary collision represented by a later vertex. As a consequence, only strangeness production in the first collision can be promoted. This would lead to differences between the importances for the events that produced strangeness in the first collision and the events that produced strangeness in secondary collisions. Thus, it would be a new source of variance, *i.e.*, exactly what should be avoided. The second solution is to bias each vertex (each elementary binary collision) along the entire cascade in such a way that the same importance is obtained for every strange particle. The second solution was chosen for INCL and the importance associated to each final particle is provided in the final ROOT file.

In our solution, the promotion of strangeness production can change from one binary collision to the next. However, if different channels are producing strangeness in a given binary collision, they should be promoted in the same way in order to get the same importance as the other strange particles whatever the channel chosen. Once again, this should be done in order to minimise the variance.

With the INCL variance reduction scheme, we introduce a new input parameter to INCL. This input is a scalar, which is used to define the wanted importance of strange particles. This allows to have the same importance for strange particles in the different events, which are independent. This input scalar will be called the *bias factor* in the following. The VRS implemented in INCL tries to force the final importances of strange particles to be the reciprocal value of the bias factor. Consequently, the bias factor is a multiplication factor of the probability to create a strange particle. However, the effective increase is lower in some cases. This is discussed in sect. V.5 with the way to optimise the bias factor.

Before I explain how the VRS forces the final importances of strange particles to be a specific value, we describe how the importances of particles are calculated. Doing so, we start with the general formula:

$$P(N \cap M) = P(N|M) \times P(M), \tag{V.5}$$

with $P(N \cap M)$ the probability of realisation of N and M, $P(N|M)$ the probability of realisation of N knowing that M is realised, and $P(M)$ the probability of realisation of M.

In Figure V.1 the vertex B can happen only if the vertex A has been realised, therefore:

$$P(A|B) = 1. \tag{V.6}$$

Combining eq. V.5 and eq. V.6 we get:

$$P(A \cap B) = P(A|B) \times P(B) = P(B). \tag{V.7}$$

For the same reason:

$$P(A|F) = P(C|F) = P(D|F) = 1, \tag{V.8}$$
$$\Rightarrow P(A \cap C \cap D \cap F) = P(F). \tag{V.9}$$

Therefore, in the version using the VRS the probability of producing the final particle Y, which is produced in vertex F, must be corrected by the importance W_Y, which is given by:

$$\begin{aligned}
W_Y = W_F &= \frac{P(F|\text{no-bias})}{P(F|\text{bias})}, \\
&= \frac{P(A \cap C \cap D \cap F|\text{no-bias})}{P(A \cap C \cap D \cap F|\text{bias})}, \\
&= \frac{P(A|\text{no-bias})}{P(A|\text{bias})} \times \frac{P(C|A,\text{no-bias})}{P(C|A,\text{bias})} \\
&\times \frac{P(D|A,C,\text{no-bias})}{P(D|A,C,\text{bias})} \times \frac{P(F|A,C,D,\text{no-bias})}{P(F|A,C,D,\text{bias})}, \\
&= \frac{\sigma(A)/\sigma_{tot}(A)}{\sigma'(A)/\sigma_{tot}(A)} \times \frac{\sigma(C)/\sigma_{tot}(C)}{\sigma'(C)/\sigma_{tot}(C)} \\
&\times \frac{\sigma(D)/\sigma_{tot}(D)}{\sigma'(D)/\sigma_{tot}(D)} \times \frac{\sigma(F)/\sigma_{tot}(F)}{\sigma'(F)/\sigma_{tot}(F)}, \\
&= \frac{\sigma(A)}{\sigma'(A)} \times \frac{\sigma(C)}{\sigma'(C)} \times \frac{\sigma(D)}{\sigma'(D)} \times \frac{\sigma(F)}{\sigma'(F)}, \\
&= CSR(A) \times CSR(C) \times CSR(D) \times CSR(F),
\end{aligned} \tag{V.10}$$

with $CSR(I)$ the cross section ratio of vertex I, $\sigma(I)$ and $\sigma'(I)$ the standard and biased cross section of the reaction that took place in vertex I, and $\sigma_{tot}(I)$ the total interaction cross for vertex I. $W_Y = W_F$ because the propagation is not biased.

The cross section ratios are easily determined during an event since both terms in the ratio σ/σ' are known for all possible reactions when a binary collision happens. Some examples are discussed in appendix E.

In the VRS of INCL, the cross section ratio of the vertices are stored. Therefore, whenever a binary collision happens, the cross section ratio of the previous vertices are known. This allows to calculate what should be the cross section ratio of the vertex representing the next binary collision (*e.g.*, the vertex F for the case in eq. V.10) to match the importance of outgoing particles (the particle Y in our example) to the desired importance. This calculated cross section ratio defines how the strangeness production should be promoted (see examples in appendix E).

In the special case of a binary collision between a strange particle and another particle, a strange particle will be present in the final state regardless of the channel chosen in INCL. Therefore, the strangeness cannot be promoted and the cross section ratio will be equal to 1. Such a binary collision can result in a strange particle that does not have the aimed importance of the strange particles. No solution was found to solve this problem. However, the dispersion of particle importances due to this phenomenon in most cases is marginal thanks to the precautions discussed below and this problem therefore does not introduce a new significant source of variance.

The main source of importance dispersion for strange particles in INCL, which is itself source of variance, is due to the two constraints discussed before. First, the non-strange cross sections cannot be

null but no lower bound is forced. Therefore, when a reaction cross section is drastically reduced but the corresponding reaction is chosen anyway, the cross section ratio of the binary collision is extremely large. Second, the total cross section must remain unchanged. This fixes a lower bound for the cross section ratio of a vertex that produces strangeness ($=\sigma^{strange}/\sigma^{tot}$). Therefore, if the cross section ratio required for a vertex is below this limit, the effective strangeness promotion will not correspond to the one required.

The first constraint can lead to extremely large cross section ratios, which cannot be counterbalanced by the following ratios because of the second constraint. If a strange particle is produced on such a path, it would result in a strange particle with a large importance compared to others and, therefore, it will strongly contribute to the observables. Such high contributions produced by single particles will make the convergence slower, lead to variance *jumps* and, therefore, to large uncertainties for the observables (see subsection V.5). If pronounced *jumps* are seen, all the observables estimated using the corresponding INCL results should not be trusted. In such a case, the associated uncertainty estimated according to eq. V.3 or eq. V.4 might be highly underestimated because of the bad sampling. This situation indicates that the bias factor was chosen way too large and paths important for strangeness production were suppressed too much.

To avoid these problems, a compromise should be found between the increase of statistics, obtained using high bias factors, and the maintain of equal importances for strange particles, which is most easily achieved using small bias factors.

Therefore, a safeguard was implemented in the variance reduction scheme. This safeguard aims at optimising the convergence efficiency for observables of interest by modifying the used bias factor. The safeguard does it by preventing the decrease of channel cross sections below half of the initial cross sections. Therefore, a vertex cross section ratio cannot be higher than 2. This strongly limits the product of vertex cross section ratios for a given history and it will be easier to counterbalance it. At the end of an event, this procedure strongly reduces the variance *jumps* even if the bias factor was chosen too high. A less restrictive safeguard has been tested but the actual one presents a better compromise. However, this safeguard is not perfect. If a particle has a history with numerous vertices with cross section ratios between 1 and 2, it can have a large importance anyway and will result in variance *jumps* and a slow convergence.

V.3 Event importance reversal

As previously mentioned, eq. V.2 is used to estimate the observables. Two types of summation can be used: a sum over the events using the importance of the events where x_i is an integer (not used in our case) or a sum over the particles using the importance of the particles where $x_i = 0$ or 1. However, the dynamic adjustment of the bias factor depending on the history of events and their importances introduces some sort of dependency between particles of a same event. If working at the level of particle importances as we do, eq. V.2 is probably not correct when correlations must be considered (*e.g.*, when studying cross section of hyperon emission in coincidence with a kaon).

There is an alternative possible type of summation for eq. V.2. The summation can be done over the particles ($x_i = 0$ or 1) but using the event importances instead of the individual particle importances.

The event importance is equal to the product of every vertex cross section ratio of the entire event. It is, a priori, different from the importance of an observation X (let us say a particle) because it includes the contribution of extra vertices, which are not on the path of the particle X, and are therefore not relevant. However, the expected value of the cross section ratio of a vertex A is:

$$\begin{aligned} E(CSR(A)) &= \sum_{\text{reac}} \frac{\sigma(\text{reac})}{\sigma'(\text{reac})} \times P(\text{reac}|\text{init. state}, \text{bias}), \\ &= \sum_{\text{reac}} \frac{\sigma(\text{reac})}{\sigma_{tot}} = 1, \end{aligned} \tag{V.11}$$

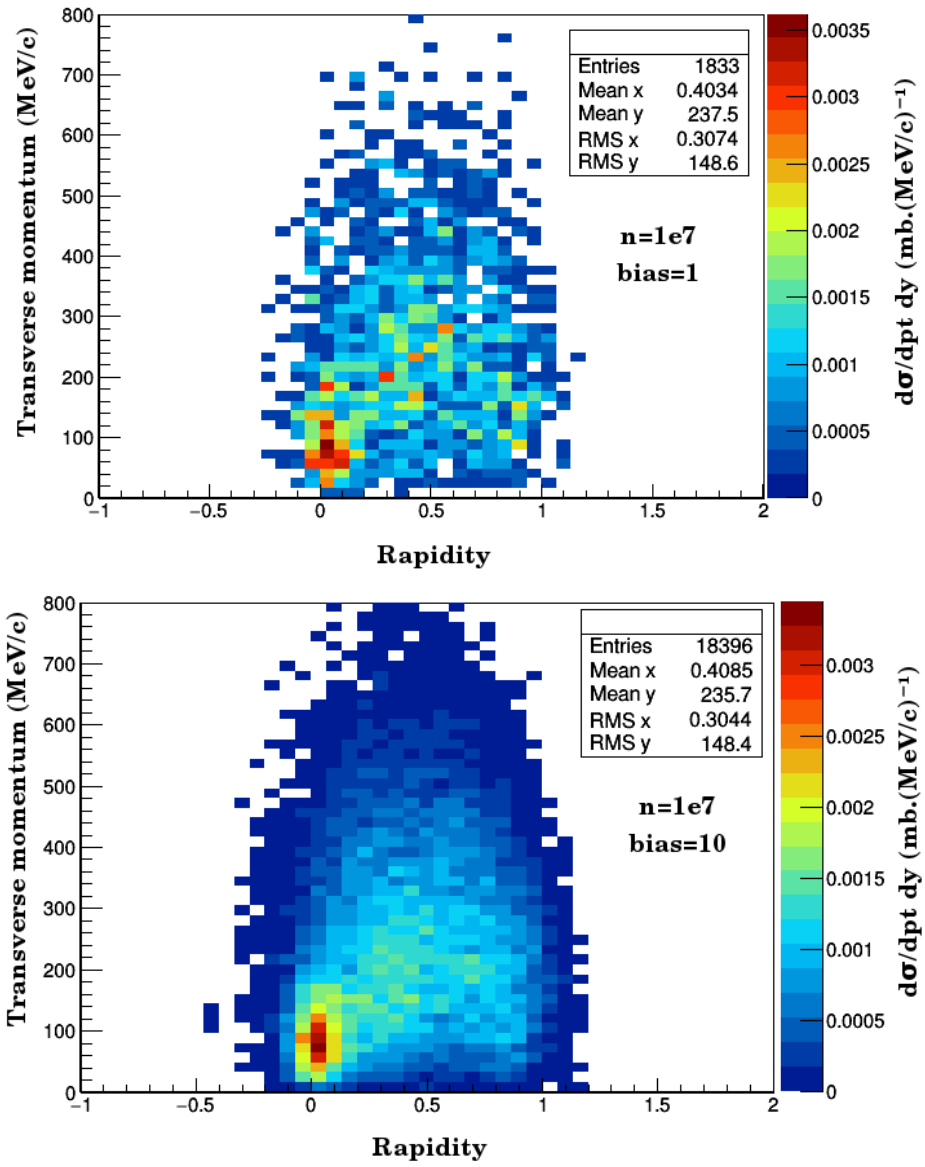

Figure V.2: Λ transverse momentum versus rapidity distribution in $p(1.7\ GeV) + Ca$ collision. Both plots are obtained using the same number of events (10^7). Top: no bias. Bottom: bias factor = 10.

with the same notation as in eq. V.10. Noteworthy, this equation is true only if no reaction of the non biased version is forbidden in the biased version, which is the case in INCL. The same argument can be used for any sub-structure in a cascade, which has no constraints on its final state. In particular, the extra vertices, which are not on the path of the particle X, have no constraint on their final state since they play no role in the production of particle X. Therefore, the contribution of extra vertices is statistically null and the expected value of the event importance knowing the particle X has been produced is equal to the importance of this particle X.

Then, it is trivial to prove that the expected value of the estimator is the same using w_i ($= E(w_{\text{event}})$) or w_{event} by taking into account $x_i = 0$ or 1 in eq. V.2 when using the summation over the particles.

The event importance is provided in the final ROOT file. The convergence being slower or equal, it is recommended to use the particle importance for the reversal of independent observables. However, it was decided to conserve only a scalar importance for each particle and an event importance in order to limit the quantity of information recorded in the output file. Doing so, the correlations are lost. Therefore, if the observable is a coincidence production, the event importances must be used regardless of the type of

summation. Additionally, if INCL is connected to another program (*e.g.*, a transport code) that is not able to keep track of the importance of the individual particles, this program can use the event importance to weight its own results.

V.4 Validation

As a first test of whether the VRS works reliably and as expected, the results obtained using the variance reduction method are compared with results obtained using the non-biased version. Not only the observables obtained with the VRS must be the same as the observables obtained without it (no residual bias), but the uncertainties must also be reduced for the same calculation time (variance reduction). Various representative comparisons are discussed in the following.

A comparison of simulations with and without the VRS indicates that the calculation time is independent of the bias factor used. Therefore, the number of events can be used as a measure of the computational time and/or to compare the efficiency of calculations using different bias factors.

Figure V.2 shows a comparison of calculations with and without bias. The two calculations have identical inputs except for the bias factor (1 and 10). It can be clearly seen that the calculation using the bias factor = 10 (right panel) produced a much more precise distribution using the same binning thanks to the statistic increased by a factor of around 10. Additionally, there is no significant difference for the amplitude, the mean values, and the standard deviations shown for both bias factors in the frames. Consequently, the objectives of the VRS are perfectly fulfilled.

A test of convergence was carried out for the reaction $p(1.7\ GeV) + ^{12}C$ using different bias factors (no bias, 10, and 100) using 4500 simulations with various numbers of events per calculation. The observable chosen to test the convergence efficiency is the K^+ mean momentum. What is considered as the true value for the K^+ mean momentum was estimated in an additional calculation using no bias and 10^9

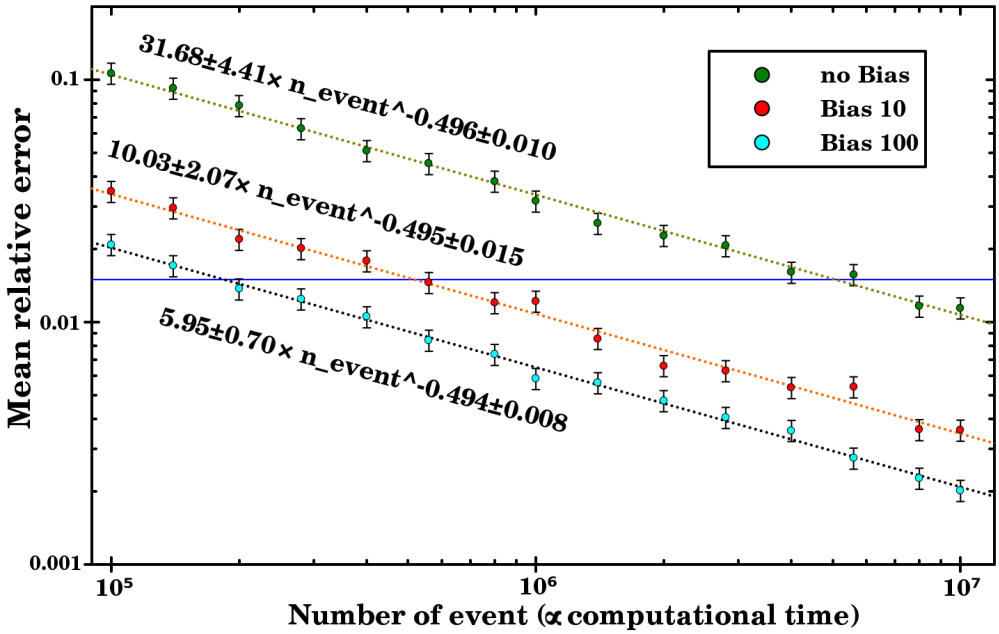

Figure V.3: Mean relative error on the K^+ mean momentum estimator as a function of the number of events. The number of events corresponds to a simulation time. The true value taken for the kaons mean momentum is estimated with a 10^9 unbiased event calculation. The reaction is $p(1.7\ GeV) + ^{12}C$ with $bias\ factor = 10$ (red), 100 (cyan) and not using a variance reduction method (green). Dotted lines are fits of the shape $a\ n^b$. The horizontal blue line is here to guide eyes (see text).

events, which resulted in an uncertainty of 0.1% for the true value. We then compared the estimator of the K^+ mean momentum for the 4500 simulations to the true value. The absolute value of the difference between an estimator and the true value is the error. Figure V.3 shows the mean relative error for the different bias factors as a function of the number of events, which corresponds to a computational time, which is independent on the bias factor. Fits of the form $a\ n^b$ are plotted and the parameters and their uncertainties are shown.

Since the true value has been estimated with an uncertainty of 0.1%, a mean relative error lower than 0.001 cannot be interpreted in Figure V.3.

A horizontal line was added in Figure V.3. It represents a relative error of 1.5%. According to this, the precision of 1.5% is obtained with about 5×10^6 events without the VRS and with only $5 \times 10^5 (1.8 \times 10^5)$ events with a bias factor 10(100). Therefore, the 1.5% precision is reached with about 10 times less events using a bias factor 10, while using a bias factor of 100 the gain in time is not 100, but only 30. This reduction of the computational time needed to reach the same precision is called the effective bias factor. The effective bias 30 for the bias factor 100 indicates that the optimal bias is probably around 30 and the safeguard (see sect. V.2) forced the effective bias factor to be closer to this value.

In Figure V.3, a decreasing mean relative error that is inversely proportional to the square root of the number of events is observed for every bias factor used. This includes the bias factor that is clearly above the optimal bias factor. Additionally, the dispersion of the results for the 4500 calculations follows a normal distribution around the true K^+ mean momentum (estimated using the calculation with 10^9 events) with respect to their statistical uncertainties. This confirms that every calculation converges to the same limit regardless of the bias factor used. Therefore, the VRS (bias + reversal) does not introduce any bias in the final observables. They all converge to the true value.

V.5 Examples

Let us remind the important nomenclature introduced in this chapter:

bias factor The increase of the statistics of strange particles required at the beginning of the calculation.

effective bias factor The real increase of the statistics of strange particles observed.

optimal bias factor The bias factor minimising the uncertainties linked to strange particles for a given number of events.

The use of the VRS in INCL++6 requires two steps in addition to the standard use of INCL. First, the user must provide the bias factor and second, the user must weight the final observables with the corresponding importances stored in the output file.

The a priori bias factor optimisation is not trivial because the optimal bias factor strongly depends on the initial parameters, like the target size and the projectile kinetic energy, but it depends also on the final observables. However, the bias factor does not need to be perfectly optimised; a sensible choice for the bias factor already helps significantly to speed up the convergence of estimator of observables involving strangeness production. By starting with a sensible choice, the safeguard presented above is able to finalise the optimisation. A work on the bias optimisation was carried out. However, the observables multiplicity and the possibilities of initial parameters being too large, a simple way to determine the optimal bias factor cannot be provided by the authors. The simplest way to evaluate the optimal bias factor is an interpolation taking into account the energy and the mass number of the target, given that it is safer to be below the optimal bias factor. Examples of sensible choices can be found in chapter VI for each figure plotted.

In Figure V.4, we show the results of a study dedicated to understand the limits of the variance reduction methods implemented in INCL. The limits discussed are problematic only for some *extreme*

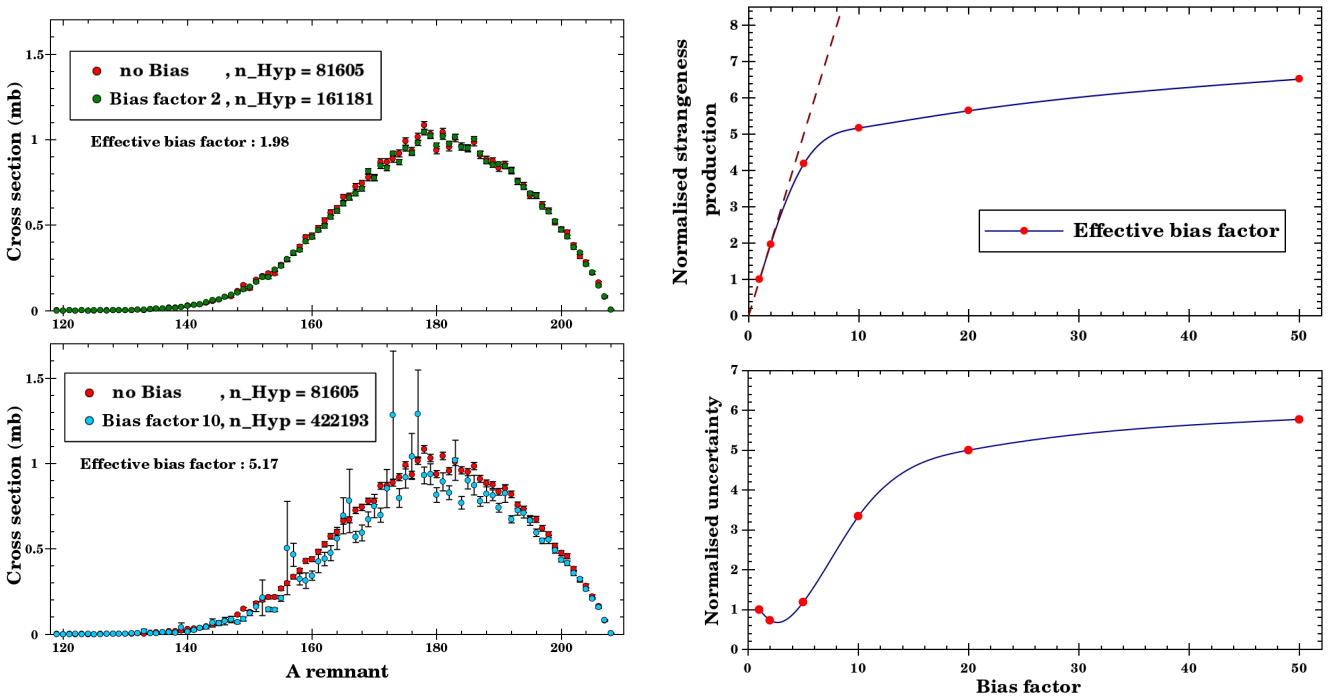

Figure V.4: Left: Hyperremnant mass distribution in $p(10\ GeV) +^{208} Pb$ collisions with 10^7 shots. Calculations with bias factors = 2 (top) and 10 (bottom) are compared to the calculation without variance reduction scheme used. Right: Evolution of uncertainties and statistics as a function of the bias factor (see text). The uncertainties and statistics are normalised to 1 for bias factor=1 (no variance reduction scheme used).

(high projectile energy and high target mass) reactions where the choice of the bias factor was not sensible. However, this case illustrates perfectly the problem of the importance dispersion, which produces large uncertainties in terms of variance *jumps* even when the statistics is increased.

Here, we studied the mass distribution of hyperremnants in $p\ (10\ GeV) +\ ^{208}Pb$ collisions. The bias factors used were 1 (no variance reduction method used), 2, 5, 10, 20, and 50. The number of events was the same (10^7) for all calculations and the computational time was equivalent. The upper and lower panels in the left column shows the results obtained using the variance reduction scheme, with a bias factor 2 and 10 respectively, together with the result from the standard calculation. The increase of the statistics (n_Hyp) and the normalised mean uncertainty as a function of the bias factor are displayed in the right column. The left panels clearly show the minimal variance (*i.e.*, the smallest uncertainties) is not achieved with the highest statistics in this case.

An interpolation (shown as a blue line) of the normalised uncertainties predicts an optimal bias factor of around 2.5. This is illustrated by the significantly better description of the hyperremnants spectrum obtained using a bias factor 2 compared to the calculation using a bias factor 10. The large uncertainties obtained using a bias factor 10 are purely linked to the dispersion of hyperremnant importances. It is interesting to note that the interpolation of the effective bias factor (blue line) in the top right panel deviates from the nominal bias factor (dashed brown line) around the optimal bias factor (2.5). The effective bias factor is reduced by the safeguard as discussed before and the reduction starts to be significant slightly above the optimal bias factor. This demonstrates that the safeguard worked well in this case, though it is not perfect.

Generally, variance *jumps* result in a global underestimation compared to the standard calculation and in some strongly overestimated bins. This can be dangerous if an underestimated bin is studied because the error bars for this bin are not significantly large but they can be far from the true value (see bottom left panel in Figure V.4). This is why it is crucial to minimise the importance dispersion. Remember,

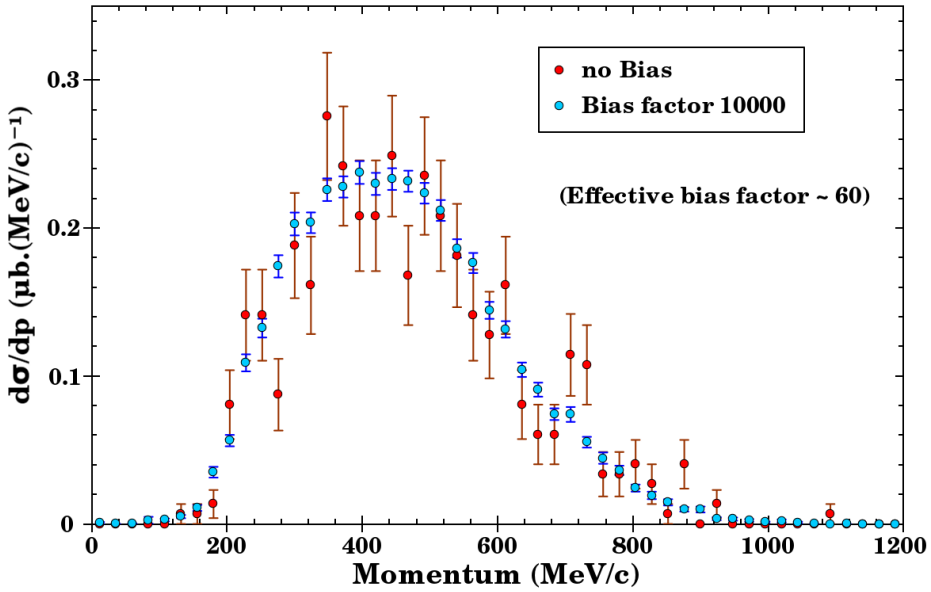

Figure V.5: K^+ momentum in $p(1.6\ GeV) +^{12} C$ with 10^7 events. INCL using a bias factor 10^4 (blue) is compared to INCL using not the variance reduction scheme (red).

however, that every calculation converges to the same limit. Once again, the variance *jumps* just make the convergence slower. The problem is that the variance, and by extension the error bars, might be underestimated because of the bad sampling.

Figure V.5 shows a reaction in which the number of nucleons in the target is too low to produce variance *jumps* thanks to the safeguard regardless of the bias factor. The number of target nucleons being low, this leads to short intranuclear cascades with a low number of vertices. Additionally, the cross section ratio of vertices is limited by the safeguard. This results in strong constraints for the importances of final particles.

In such cases (low mass number) associated to a low energy, the safeguard matches automatically the effective bias factor to the optimal bias factor when the bias factor has been chosen too high. This is well illustrated in Figure V.5. Although the nominal bias factor (10^4) is clearly above the optimal bias factor, which is 60, the spectrum obtained using the VRS exhibits no variance *jump*.

Chapter VI

INCL++6 results

In this chapter, results of INCL calculations are compared to experimental data and to other model predictions. It corresponds to the second part of my work published in ref. [43]. This work was important for the validation of both studies described in chapter IV and chapter V.

The different strengths and weaknesses observed in INCL are discussed. The hypernucleus production is not presented here because it depends strongly on the de-excitation stage of the spallation reaction, which was not a direct part of my work. A following paper will be dedicated to the strange degree of freedom in the de-excitation model and the hypernucleus production. Here, we focus on the intra-nuclear cascade and single particle production.

The particles studied for the validation of INCL++6 are the charged kaons (K^+ and K^-), the Λ, and the neutral kaons. The K^+ was clearly the most studied particle in the past. Experimental data exist near the threshold, and even in the sub-threshold region, up to high energies ($\sim$ 14 GeV). Additionally, various targets were studied and the emitted K^+ were observed at different angles. Moreover, the K^+ is the only particle together with the K^0 in our energy range that carries a positive hypercharge. Therefore, every strangeness production results in kaon production. Because the production modes of the two kaons are similar, studying the K^+ also gives an estimate of the reliability of the total strangeness production in INCL. The K^- was less intensively studied because of the lower production rate (about two orders of magnitude compared to the K^+). However, double differential experimental data can be found in the literature. Since the Λ and the neutral kaons have no electric charge, their detection is more complex and less experimental data are available. However, their analysis can help to understand the different processes in competition for the strangeness production.

The bias factors (see chapter V) used to obtain the INCL results are given in the captions of respective figures.

VI.1 KaoS

The KaoS [104] (Kaon Spectrometer) experiment was performed at the heavy-ion synchrotron SIS at GSI in Darmstadt. The KaoS collaboration measured the K^+ and K^- production in $p + C$ and $p + Au$ collisions at 1.6, 2.5, and 3.5 GeV proton beam kinetic energies. The kaon momentum was measured from $p_{lab} = 0.3$ to 1.1 GeV/c.

Most of the data measured for the K^+ production are well described by INCL. Fig. VI.1 shows the K^+ production invariant cross section in two configurations measured by the KaoS collaboration in comparison to INCL and to the Bertini cascade model [56]. For the left panel showing K^+ production near threshold on a light nucleus (carbon) and for the right panel showing K^+ production at higher energy on a heavy nucleus (gold), the results of INCL match very well the experimental data. The comparison with the KaoS data indicates a reliable total strangeness production cross section for a relatively large range of nuclei,

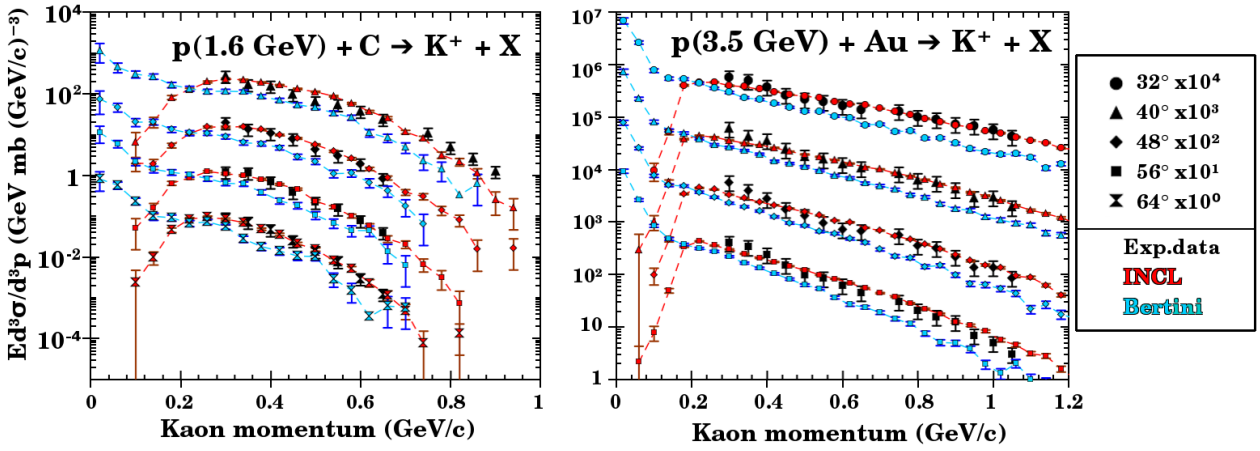

Figure VI.1: K^+ invariant cross section for various angles in (left) $p(1.6\ GeV) + C$ and (right) $p(3.5\ GeV) + Au$ collisions. Experimental data [104] (black symbols) are compared to INCL (red) and to the Bertini cascade model [56] (blue). Bias factor used: 10

energies, and angles. It can be seen that the Bertini cascade model gives a shape similar to INCL in the momentum range of the experimental data but underestimates these data by roughly 40%. This difference can be explained by the Δ-induced strangeness production, which is not included in the Bertini model. Figure VI.1 depicts for the low momenta region huge differences between the predictions from INCL and Bertini models. This is due to the different values used for the K^+ potential. In our approach, the K^+ repulsive potential in INCL reduces drastically the invariant cross section at low momenta. Experimental data at low momenta would help to test the K^+ potential.

Figure VI.2 shows the invariant cross section for K^- production for the reaction proton on Au at 3.5 GeV. It can be seen that the data are well described by INCL for momenta above 0.5 GeV/c. However,

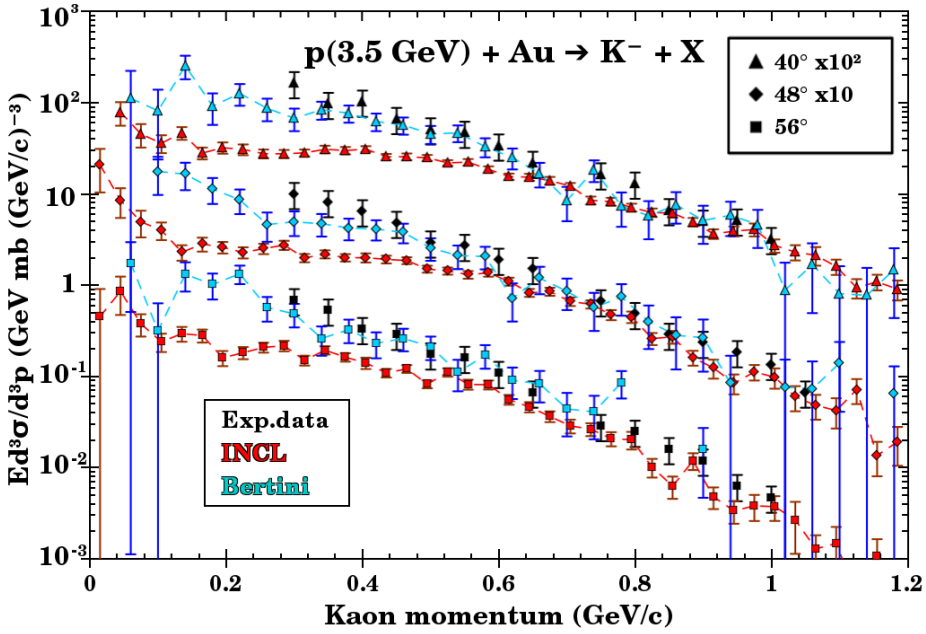

Figure VI.2: K^- invariant cross section at 40°, 48°, and 56° in $p(3.5\ GeV)+Au$ collisions. Experimental data [104] (black) are compared to INCL (red) and to the Bertini cascade model [56] (blue). Bias factor used: 10.

below this energy, the cross section is clearly underestimated and INCL does not reproduce the shape of the experimental data. In ref. [104], the authors conclude that the K^- production is mostly due to the $NY \rightarrow K^-NN$ reaction and to a lesser extent to the $\pi Y \rightarrow K^-N$ reaction. Both reactions are not considered in INCL because of the lack of experimental data. This is probably the explanation. The low energy production being dominated by secondary reactions and the high energy production by primary reactions, our result seems consistent with a predominance of antikaon production through strangeness exchange ($NY \rightarrow K^-NN$ and $\pi Y \rightarrow K^-N$) for low momenta and through direct production ($NN \rightarrow NNK\overline{K}$) for high momenta. The Bertini cascade model, which includes the $NY \rightarrow K^-NN$ (but not the $\pi Y \rightarrow K^-N$) reaction, shows a significantly better description over the entire momentum range covered by the experimental data. This would argue for adding the extra strangeness exchange reactions even if they have a low confidence level.

VI.2 ITEP

The study carried out at the Institute of Theoretical and Experimental Physics (ITEP) accelerator in Russia [105] measured the K^+ production in proton-nucleus collisions. The nuclei studied were Be, Al, Cu, and Ta. This choice covers a mass range from $A = 9$ to 181 ($Z = 4$ to 73). The projectile energy range from 1.65 up to 2.91 GeV. The experiment measured the production of K^+ with a momentum $p = 1.280 \pm 0.014$ GeV/c and with an emission angle $\theta = 10.5°$. This very specific phase space constraint was used to drastically reduce the contribution of the K^+ production in $\pi N \rightarrow YK$ secondary reactions (see ref. [105] for details). This simplified their analysis by considering only the $NN \rightarrow NYK$ primary reactions.

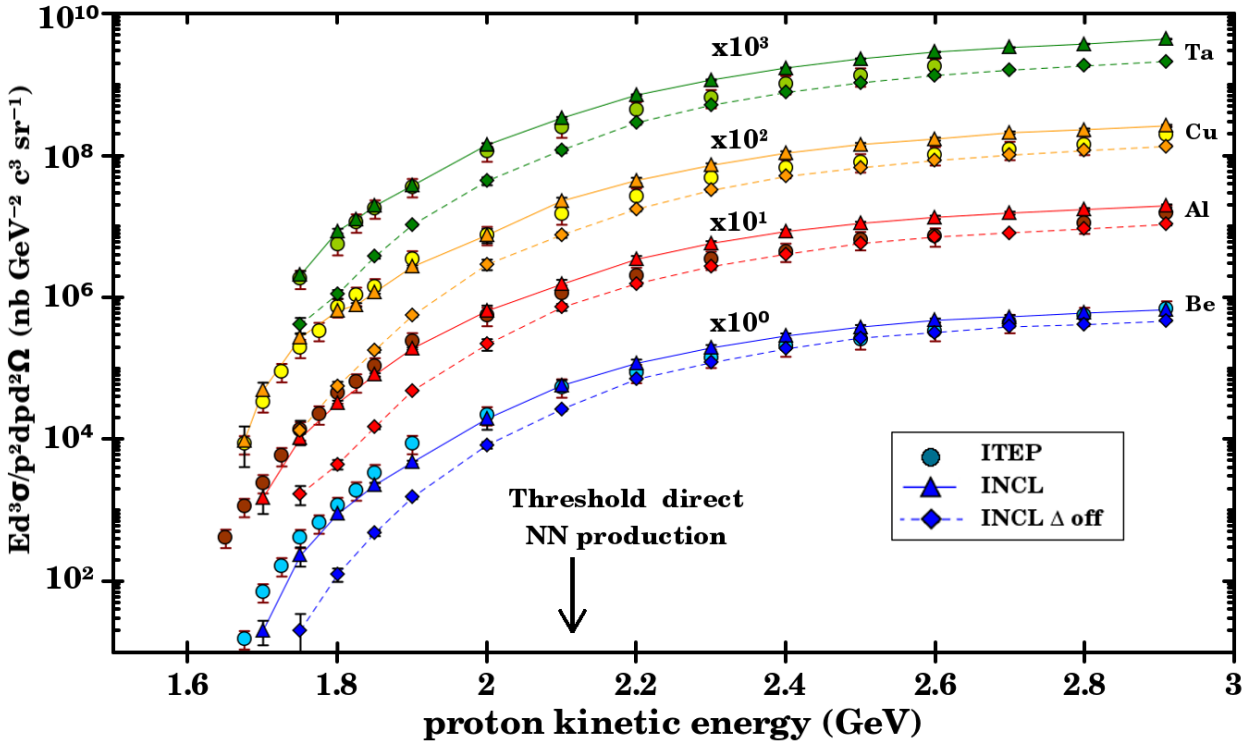

Figure VI.3: K^+ invariant cross section in $p + A \rightarrow K^+ + X$ reactions for kaons emitted with a momentum of 1.280 ± 0.014 GeV/c at $\theta = 10.5°$. The experimental data from [105] (circles) are compared to INCL with (triangles) and without Δ-induced strangeness production (squares). Bias factor used: 50 for INCL without Δ-induced strangeness production for $T_p < 2$ GeV, 20 otherwise.

In our analysis, we tested the implemented Δ-induced strangeness production, which is not based on experimental data. In contrast, the corresponding cross sections are based on theoretical calculations from Tsushima et al. [63] (see ref. [44] for more details). In Figure VI.3 we compare INCL calculations with and without Δ-induced strangeness production to experimental data [105]. This allows to study the impact of $\Delta N \rightarrow NYK$ secondary reactions compared to $NN \rightarrow NYK$ primary reactions; the $\pi N \rightarrow YK$ secondary reactions being naturally suppressed by the phase space constraint. The Bertini model, which has no variance reduction method, is not plotted in Figure VI.3 because of the unreasonable computing time needed to get comparable uncertainties. The threshold for the direct production of K^+ with a momentum $p = 1.280 \pm 0.014$ GeV/c is $T = 2.115$ GeV in nucleon-nucleon collisions. The sub-threshold production is allowed thanks to collective effects like the Fermi momentum, and also to secondary reactions (*e.g.*, ΔN) as explained below.

Figure VI.3 shows that the standard INCL calculations (with Δ-induced strangeness production) reproduce relatively well the shape and the absolute values of the experimental data, especially for energies below 2.1 GeV, which correspond to the sub-threshold production. However, the standard INCL model overestimates the $2.1 - 2.9$ GeV energy region by around 50%. In comparison, INCL without Δ-induced strangeness production underestimates the experimental data over the entire energy range. Above $T = 2\ GeV$, the underestimation is around 20%. This underestimation becomes above one order of magnitude for the lowest momenta. This demonstrates the crucial role of Δ's in the strangeness production. Going deeper in the analysis, the overestimation in the $2.1 - 2.9$ GeV energy range indicates that the Δ-induced kaon production in this region is likely overestimated. This seems consistent with observations made in ref. [63] where the authors observed an overestimation of the cross sections for such reactions with center-of-mass energies 200 MeV above the threshold.

The assumption that cross sections are very well described near the threshold but are overestimated at higher energy could be due to the negligence of hyperonic resonances in the model used in ref. [63]. This choice was made because of the low confidence level associated to such resonances. However, they could play a significant role, especially at high energies.

A precise evaluation of Δ-induced strangeness production cross sections with INCL is difficult to realise because of the complexity of the spallation process. However, the impossibility to measure the Δ-induced strangeness production cross sections and the limitations of the theoretical calculations make simulation models like INCL valuable candidates to estimate and/or test such cross sections.

VI.3 ANKE

The ANKE experiment [106] investigated the production of K^+ in the forward direction in proton-nucleus collisions with proton kinetic energies between 1 and 2.3 GeV. The targets were $A = {}^{2}H, {}^{12}C, Cu$, Ag, and ${}^{197}Au$. The experiment took place at the COoler SYnchrotron COSY-Jülich in Germany. The angular acceptance was $\pm 12°$ horizontally and $\pm 7°$ vertically.

In Figure VI.4, calculations from LAQGSM [54], Bertini [56], and INCL are compared to ANKE experimental data. It can be seen that the three models fit relatively well the experimental data at low momenta (below 300 MeV/c) with INCL being slightly closer to the experimental data than the other two models. At higher momenta, INCL and LAQGSM still reproduce the data while Bertini underestimates them. At higher energies where no experimental data exist, every model gives a different shape. Whereas LAQGSM decreases rapidly, INCL continues to increase, and Bertini predicts a bump. The maxima are of around 600 MeV/c, 800 MeV/c, and 900 MeV/c for LAQGSM, INCL, and Bertini, respectively. An extrapolation from Figure VI.3 suggests that INCL overestimates the production cross section for K^+ with $p_{K^+} = 1.280$ GeV/c in forward direction by roughly 30%. This would be compatible with the Bertini's value at $p_{K^+} = 1.280$ GeV/c. Again, the INCL Δ-induced kaon production is probably overestimated.

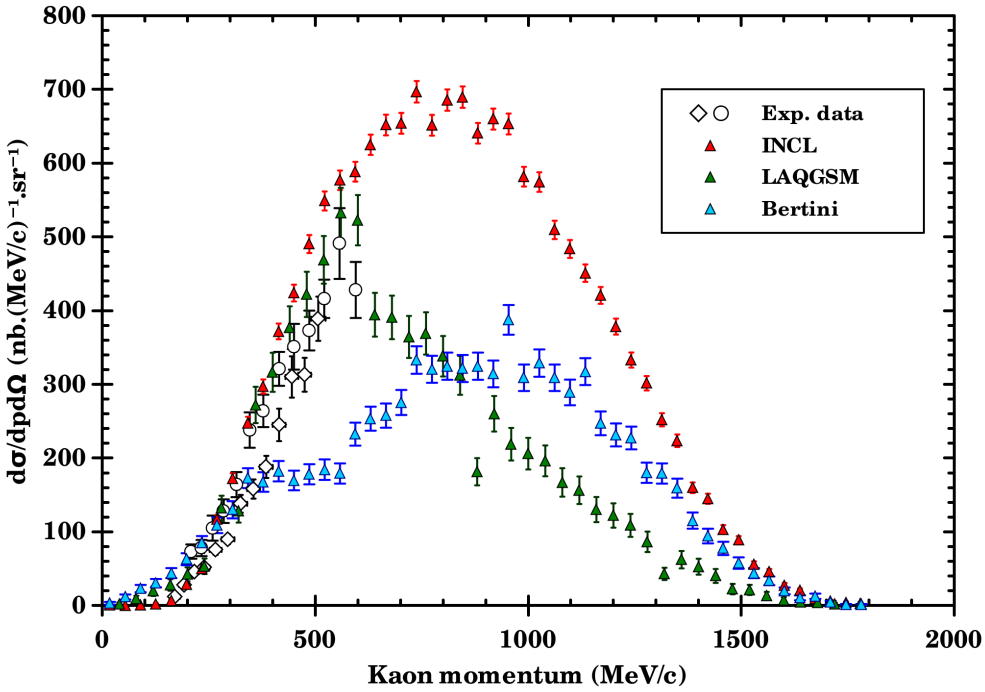

Figure VI.4: K^+ momentum spectrum in $p(2.3\ GeV) + ^{12}C$ collisions within the angular acceptance of the ANKE experiment. Two sets of experimental data [106] (circles and squares) are compared to INCL (red), LAQGSM [54] (green), and the Bertini cascade model [56] (blue). Bias factor used: 10.

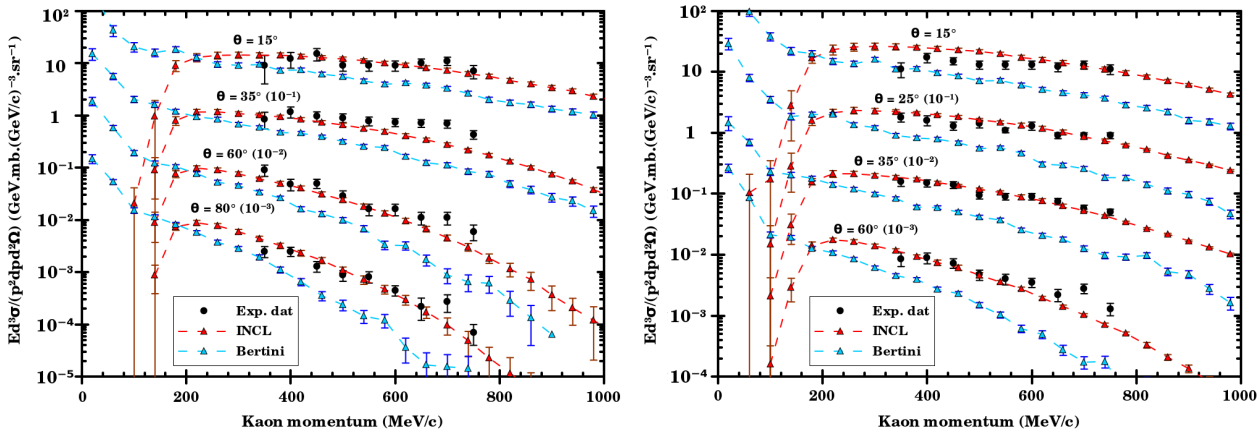

Figure VI.5: K^+ invariant cross section at 2.1 GeV/Nucleon for the reactions $p + ^{208}Pb$ (upper panel) and $^2H + ^{208}Pb$ (lower panel). The experimental data [107] (black dots) measured at the LBL are compared to the Bertini cascade model [56] (blue) and INCL (red). Bias factor used: 10.

VI.4 LBL

The experiment carried out at the Lawrence Berkeley Laboratory (LBL) [107] studied the inclusive K^+ production using projectiles with $T = 2.1\ GeV/nucleon$. Several projectile types and targets were tested but a direct comparison between measured and modelled data is only possible for the reactions $p + ^{208}Pb$ and $^2H + ^{208}Pb$.

In order to estimate the inclusive K^+ production cross section, the collaboration measured K^+ spectra at four different angles: $\theta = 15°$, $35°$, $60°$, and $80°$ for the $p + ^{208}Pb$ reaction and at $\theta = 15°$, $25°$, $35°$,

and 60° for the $^2H + ^{208}Pb$ reaction. Spectra were measured for kaon momenta from 350 to 750 MeV/c.

The two panels in Figure VI.5 shows that there is good agreement between INCL predictions and experimental data both for proton and deuteron induced reactions. It must be mentioned that this experiment is very similar to the one carried out by the KaoS collaboration. Though, the angles studied, the energies, the projectiles, and the targets used are slightly different but the conclusions are the same. Again, the good agreement not only in the absolute values but also in the energy dependence of the data demonstrates the reliability of the implemented strange physics in the new INCL version. This is also a first validation that INCL can handle light clusters as projectile.

VI.5 HADES

The HADES (High Acceptance DiElectron Spectrometer) collaboration studied Λ and K^0_s productions in $p+p$ and $p+Nb$ collisions at 3.5 GeV [108, 109]. The Experiment took place at GSI in Germany. The Λ particles were measured in the $[0.1, 1.3]$ rapidity (y) range in the laboratory frame and the K^0_s particles were measured in the $[-0.85, 0.55]$ rapidity range in the nucleon-nucleon center of mass ($y_{lab} = -1.118$).

The hypernucleus production is strongly correlated to the Λ production since most of the observed hypernuclei involve one or more Λ's. Therefore, the Λ production must be tested before studying the hypernucleus production, which implies more complex processes.

In Figure VI.6 we compare the Λ production yield as function of rapidity calculated using INCL to predictions from UrQMD [110] and GiBUU [51] and to experimental data [108]. The original plot is taken from [108]. The Bertini cascade model does not handle Σ^0's decay, which plays a role in the Λ production. Therefore, results from the Bertini code are not plotted here.

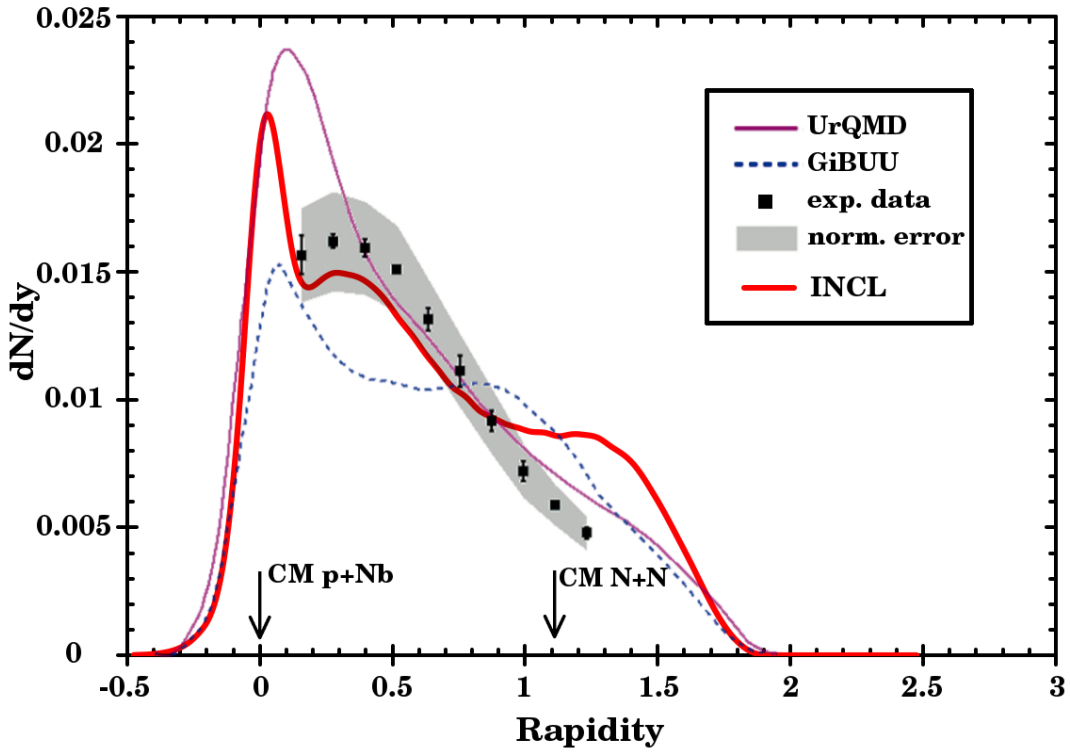

Figure VI.6: Λ production yield in $p(3.5\ GeV) + Nb$ collisions as a function of rapidity. The HADES experimental data (black square) are compared to GiBUU (blue dashed line), UrQMD (purple line), and INCL (red line) model predictions. The original plot can be found in [108]. Bias factor used: 10.

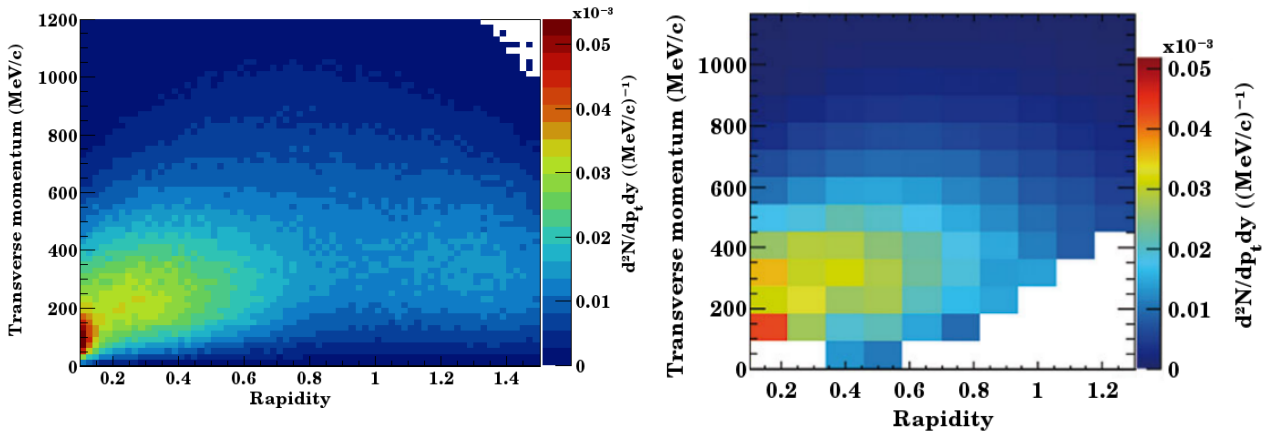

Figure VI.7: Λ rapidity versus transverse momentum yield in $p(3.5\ GeV) + Nb$ collisions. Left panel: INCL predictions. Right panel: Experimental data from [108] after correction of efficiency.

Figure VI.6 depicts a rather good agreement between INCL and the experimental data if taking into account systematic errors. An exception are the data at rapidities higher than 0.9. The bump observed in the INCL predictions around $y = 1.3$ can also be seen in the GiBUU model, but for this model at lower rapidity. The UrQMD model does not exhibit such a behaviour and is close to the experimental data, but it misses the first two data points at the lowest rapidities.

Aiming at understanding the INCL bump, we show in Figure VI.7 the transverse momentum versus the rapidity of Λ particles. It can be seen that the left (INCL) and right (HADES data) panels match well. For the problematic rapidities (above $y = 0.9$) one can find an overabundance of Λ particles in the prediction of INCL compared to HADES in the rapidity range $[1, 1.4]$ and the transverse momentum range $[200, 500]$ MeV/c. This corresponds to emission angles between 5 and 19 degrees if the experiment acceptance is between 18 to 85 degrees.

With the acceptance of the HADES experiment being limited, data for the unmeasured region visible in the right panel of Figure VI.7 have been estimated by extrapolating the transverse momentum spectra using Maxwell-Boltzmann distributions. The thus determined data are in disagreement with the INCL prediction. Consequently, the bump around $y = 1.3$ predicted by INCL is in a phase space not measured experimentally. Therefore, there is no strict contradiction between experimental data and INCL model predictions

In the region around $y = 0$, every model predicts a peak. This peak is high and broad using UrQMD, narrow and smaller using GiBUU, and high and narrow using INCL. A comparison between INCL with and without Σ^0 in-flight decay showed that the peak in INCL predictions is entirely due to the in-medium Λ production. Additionally, studying the origin of the Λ's indicated that this peak is the result of the hyperremnant de-excitation for INCL.

The second particle measured by the HADES collaboration is the K^0_s. In Figure VI.8 the experimental data [109] are compared to GiBUU calculations with and without a chiral potential, to the Bertini cascade model, and to INCL. It can be seen that the best description of the experimental data are obtained using GiBUU. However, the version of GiBUU used here is a modified version in which the K^0 production has been artificially reduced to fit the $p+p$ HADES experimental data (see ref. [109] for details). Additionally, this GiBUU version is not the same as the one used in ref. [108], although the reaction studied is the same. This makes their results difficult to interpret. INCL gives a good shape but overestimates the experimental data by roughly 65%. Similarly to the case for the K^+ production, the Δ-induced reactions could be an explanation for the overestimation but some part of this overestimation might also be due to the normalisation. The total reaction cross section σ_{tot}^{p+Nb} used by HADES is $848 \pm 127\ mb$, while INCL calculates a value of 1048 mb. A measurement of the total reaction cross section for the same system

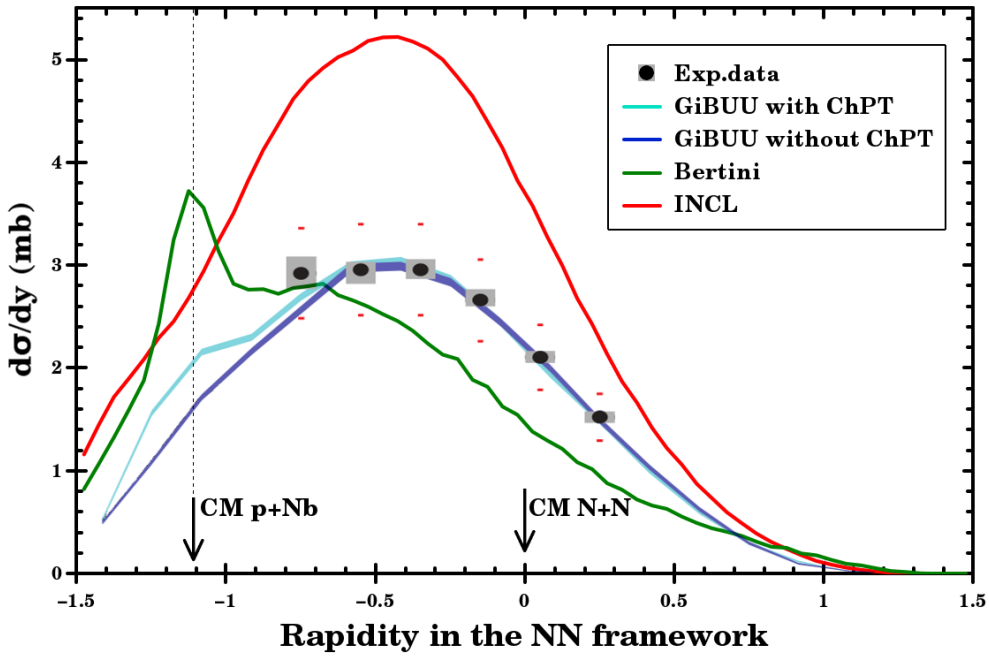

Figure VI.8: K^0_s production cross section in $p(3.5\ GeV) + Nb$ collisions in function of the rapidity in the nucleon-nucleon center of mass. HADES experimental data [109] (black circles) are compared to GiBUU with (cyan) and without (blue) a chiral potential, the Bertini cascade model (green) and INCL (red). The original plot comes from ref. [109]. Bias factor used: 10.

at a lower energy (1.2 GeV instead of 3.5 GeV) gave $1063 \pm 40\ mb$ [111], which is consistent with the INCL value. The Bertini cascade model does not reproduce the energy dependence of the experimental data, but the predicted absolute yield of K^0_s corresponds to the experimental data. The bump around the laboratory rapidity ($y_{lab} = -1.118$) can also be seen in GiBUU predictions with the chiral potential. This is likely due to the attractive potential used by these models for the K^0, whereas INCL uses a repulsive potential.

VI.6 FOPI

The FOPI collaboration [112] measured the in-medium neutral kaon inclusive cross sections in π^--induced reactions on various targets: C, Al, Cu, Sn, and Pb. The pion beam had a kinetic energy $T \simeq 1.02$ GeV ($p_\pi = 1150\ MeV/c$). The experiment took place at the heavy-ion synchrotron SIS at GSI. The geometrical acceptance of the detector was restricted to polar angles in the range $25° < \theta < 150°$. An a posteriori correction was applied by the FOPI collaboration to obtain the total inclusive cross sections.

Figure VI.9 depicts the production of neutral kaons measured by the FOPI collaboration. In the original paper [112], the authors compared their experimental data to two models: the quark-meson coupling model (QMC) [113] and the hadron-string-dynamics model (HSD) [114, 115]. By fitting the data, the FOPI collaboration found that the inclusive cross sections can be described by a A-dependent cross section of the form $\sigma(A) = \sigma_{eff} \times A^b$, with $b = 0.67 \pm 0.03$. This would indicate that K^0 production is dominated by peripheral collision. Therefore, they developed the function:

$$\sigma(A) = \sigma(\pi^-(1150\ MeV/c) + N \rightarrow K^0 + X) \times A^{2/3}, \tag{VI.1}$$

with N a target nucleon. The nucleon cross section was obtained by summing all $\sigma(\pi^- + N \rightarrow K^0 + Y)$ processes weighted with the relative proton and neutron numbers of the target nucleus. The thus developed function is represented as a hatched band in Figure VI.9. The bandwidth corresponds to an uncertainty

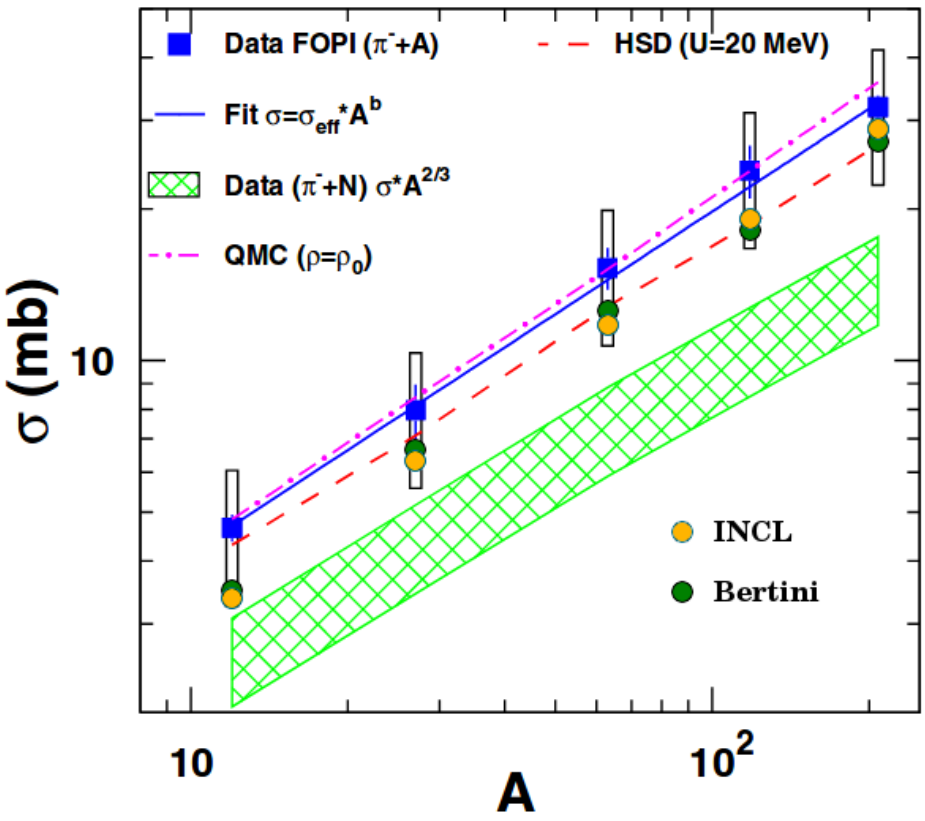

Figure VI.9: Neutral kaon production cross section in the collision $\pi^-(1020\ MeV) + A$ (p_π = 1150 MeV/c). The FOPI experimental data [112] (blue squares) are compared to QMC [113] (pink dash-dotted line), HSD [114, 115] (red dashed line), Bertini [56] (green circles), and INCL (orange circles) models. The meaning of the hatched area is explained in the text. The original figure comes from ref. [112]. Bias factor used: 10.

of 20%. It appears that the experimental data do not plot in the region defined by this band, which indicates that the simple dependence expressed in eq. VI.1 cannot explain the observed cross sections. Therefore, there must be an additional process.

The INCL calculations slightly underestimate the experimental data but they are within the experimental systematic uncertainties (rectangular bars). The inclusive cross sections predicted by INCL are proportionnal to $A^{3/4}$, which promote a different interpretation of the K^0 production processes with larger contributions of secondary reactions and a deeper strangeness production. The Bertini cascade model [56] shows a result similar to INCL but with a slightly lower slope. Both INCL and Bertini cross sections are consistent with eq. VI.1 using a dependence of $A^{3/4}$ instead of the proposed $A^{2/3}$.

VI.7 E-802

The INCL model has been extended to work up to incident energies of about $\sim$ 15 GeV. However, most of the experiments studying strangeness production focus on energies below 3.5 GeV. A notable exception is the experiment realised by the E-802 collaboration [116] at the Brookhaven National Laboratory (US) using a proton beam momentum of 14.6 GeV/c ($T_p \simeq 13.7\ GeV$). This experiment measured various particle production cross sections in proton-nucleus reactions and, notably, it also measured the K^+ production cross sections. Therefore, it provides a good opportunity to test INCL strangeness physics at the high energies. The nuclei studied by the E-802 collaboration were Be, Al, Cu, and Au.

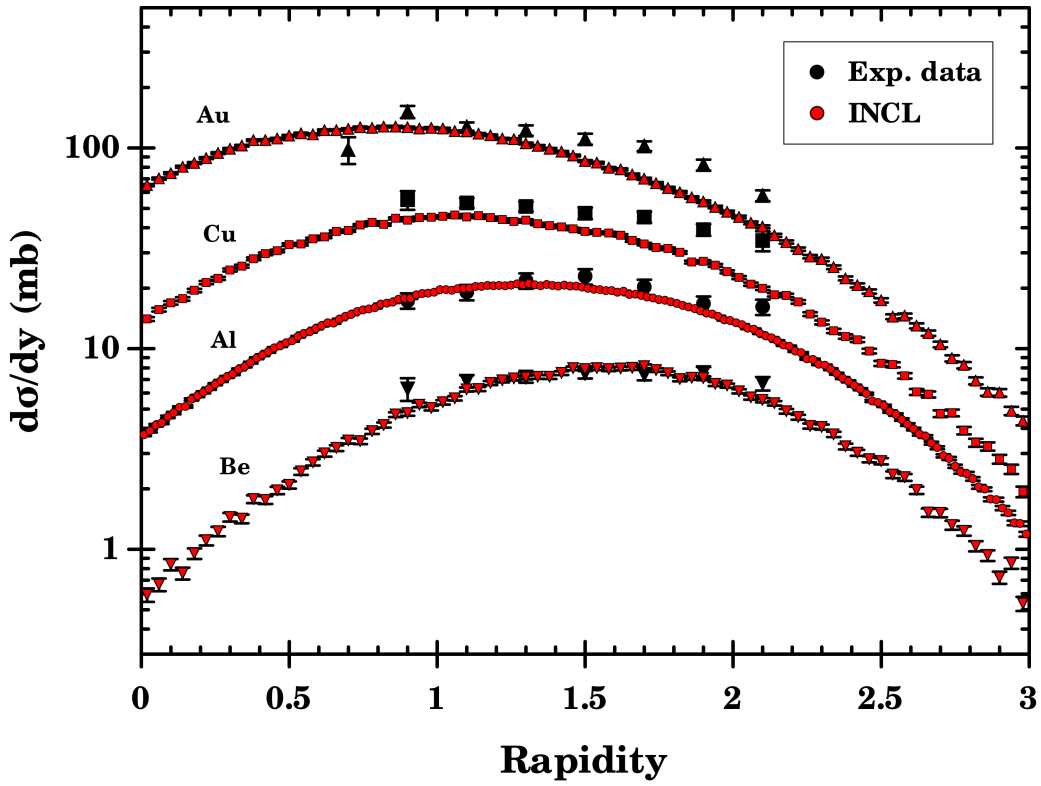

Figure VI.10: K^+ production cross sections in $p(14.6\ \mathrm{GeV/c}) + A$ collisions as a function of rapidity. The experimental data [116] (black) are compared to INCL predictions (red). No variance reduction method was used.

Fig. VI.10 shows a comparison of INCL predictions with E-802 experimental data. The Bertini model predictions are not plotted because the upper energy limit for this model is about 10 GeV. Considering that the experimental data are close to the upper energy limit of INCL, the shape as well as the absolute values are in excellent agreement. However, a slight underestimation at high rapidities can be observed for Cu and Au. The observed deviations are difficult to analyse because they are only for two target elements and the discrepancies differ: a bump for Au and a linear deviation for Cu.

VI.8 LINP

The experiment carried out at the Leningrad Institute of Nuclear Physics (LINP) [117] studied the sub-threshold K^+ production on various nuclei, from beryllium to uranium. A measurement of the total cross sections as a function of energy was performed in the $800 - 1000$ MeV energy range for Be, C, Cu, Sn, and Pb.

In Figure VI.11 INCL predictions are compared to the experimental data. The first observation is a clear overestimation of the experimental data. This overestimation is about a factor 6 for Be and about a factor 4 for the other nuclei. The prediction of the slope is good, especially for C, Sn, and Pb. While the agreement between model predictions and experimental data is only fair, the major success of these calculations is the variance reduction (see chapter V). The effective bias factors of these calculations are around 1000 depending on the configuration with a maximum at about 2000. This allowed to obtain cross sections below the nano-barn scale using a relatively short calculation time (half a day for the entire set by using parallelisation). Such a result cannot be obtained in a reasonable time without a variance reduction method.

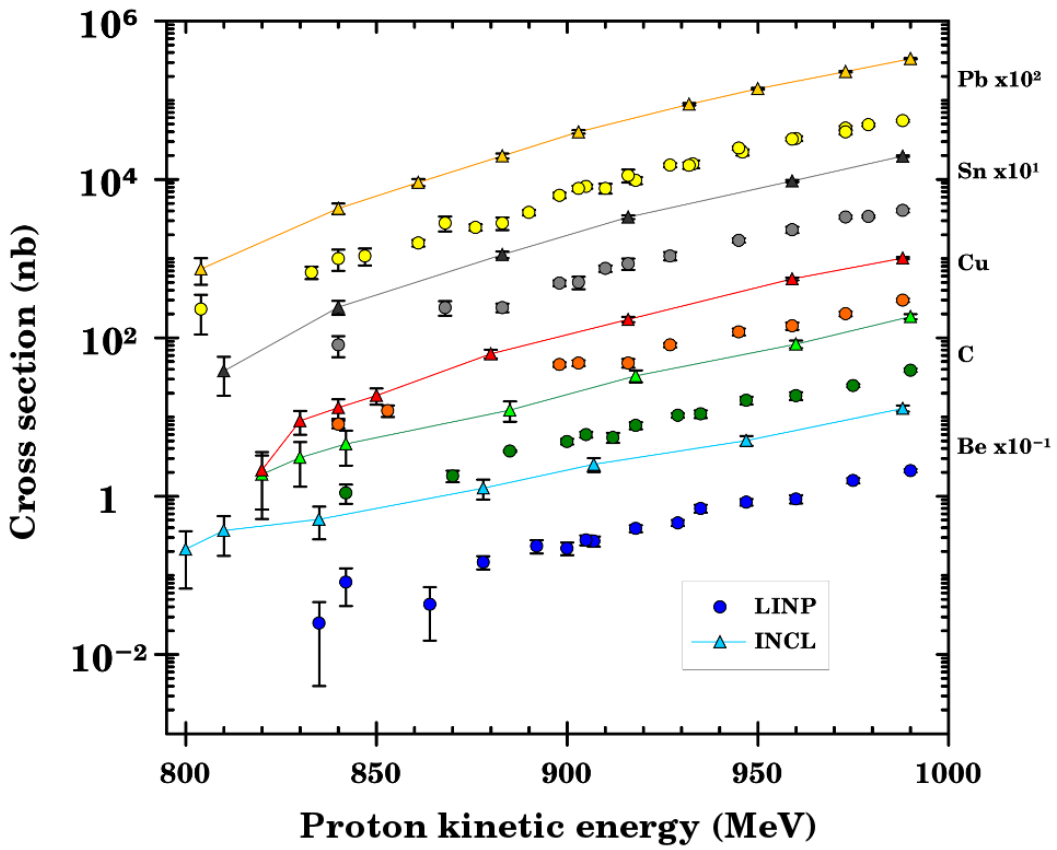

Figure VI.11: Subthreshold K^+ production cross sections in $p+A$ collisions as a function of the initial proton kinetic energy. The experimental data [117] (circles) are compared to INCL predictions (triangles).

Different explanations are possible for the observed overestimation. To understand the problem, it is important to remember that the beam energies in this experiment are far below the K^+ production threshold for $p+p$ collisions (1.582 GeV). Therefore, the strangeness production requires strong collective effects, which are complex and not very well understood. Such effects include effects related to the momentum spectra of particles inside the nucleus and effects related to successive collisions. Additionally, Δ particles seem to play a crucial role in this experiment. An explanation for the overestimation could therefore be the treatment of Δ particles in INCL. Another explanation could be the semi-classical description of the nucleus by INCL, which does not consider every quantum mechanical effect that could play a significant role in sub-threshold processes. A following study has been carried out in order to better understand the discrepancies. The effect and limitations of the semi-classical approach cannot be tested but modifications related to the physics of Δ particles or to collective effects showed a sensible reduction of the strangeness production. None of the modifications, however, could fully explain the observed discrepancies. Therefore, the overestimation is likely due to a combination of the three explanations proposed above. However, it is difficult to proof or reject this hypothesis considering the complexity of the processes involved.

Chapter VII

CosmicTransmutation

In the previous chapters, I discussed in detail nuclear spallation reactions. In the following chapters, I focus on the production of cosmogenic nuclides.

In this chapter I discuss the CosmicTransmutation model created during the second phase of the PhD. Here I will discuss in some detail the applied astrophysical approaches and the used algorithms implemented in the CosmicTransmutation code.

The purpose of this chapter is to help understanding and using the CosmicTransmutation code. Doing so, this chapter is divided into six sections. First, the objectives of this model are introduced. Second, the global operation of the program is demonstrated. Following there are two sections detailing the special features for simulation of meteoroids and planets. Next, the algorithms developed in this PhD to treat special aspects of the simulation are discussed. Finally, some biases and problems that must be considered for the analysis of the CosmicTransmutation results are explained.

VII.1 Objectives

The major objective of this thesis and of this code is to calculate the production of cosmogenic nuclides in various targets. However, the entire process of cosmogenic nuclide production is too complex to be simulated by one code created from scratch and developed by one single person. Some aspects of physics must be delegated to other codes. Such an association of models is usually made in transport codes; therefore, the CosmicTransmutation model is based on one of them. Since cosmogenic nuclides are predominantly produced in spallation reactions or in reactions resulting from spallation, the used transport code must be able to handle energies ranging from tens of MeV to tens of GeV for primary particles like protons and alpha particles; and energies down to eV for secondary particles like neutrons. A famous transport model that is able to handle the energy range is the Geant4 toolkit [10]. Therefore, it has been decided that the CosmicTransmutation model is be based on the Geant4 toolkit.

The Geant4 toolkit is a transport model originally designed for high energy interactions. However, it also enables to make simulations for neutron induced reactions and neutron transport down to energies of a few meV. These features allow the CosmicTransmutation model to calculate cosmogenic nuclides production over the entire relevant energy range. Effects induced by radioactive decay, *e.g.*, the fact that the final nuclide very often is the nuclide at the end of the radioactive decay chain and not the nuclide directly at the end of the nuclear reaction, is not fully treated in Geant4 and therefore also not in CosmicTransmutation. When a particle is stopped in Geant4, this particle is not tracked any more. The decay of nuclei is considered only while nuclei are moving. Therefore, the objective of the CosmicTransmutation code is limited to, first, calculating the outcome of the nuclear reaction (before the radioactive decay) and, second, to calculate the location of the production. The production of cosmogenic nuclides after the radioactive chains is left as a post-treatment of the results of the CosmicTransmutation

model.

VII.2 Global operation

Basically, a Geant4 based model has only two steps, the initialisation and the creation of the outputs. The simulation itself is then done by the Monte Carlo code. In the Geant4 based model, the simulation of the physics is computed by the various implemented, but hidden, models in the toolkit, which plays the role of a coordinator.

For a better understanding, some terms from the nomenclature of Geant4 that are also used in this chapter are defined here:

- Event: The simulation of a collision of a single initial particle with the target (*e.g.*, a meteoroid).
- Run: A set of events simulated in a same configuration.
- Track: The path of a particle from its creation to its absorption or decay.
- Physics list: The set of physics models used to process the different aspects of the physics in Geant4.
- Logical volume: A volume used to construct the detector geometry in Geant4, including its properties and characteristics.
- Sensitive detector: A logical volume that produces an output, which can be used by the primary program (*i.e.*, CosmicTransmutation).

VII.2.1 Initialisation

The initialisation of the CosmicTransmutation model can be divided into three main parts: the target, the irradiation spectrum, and the initialisation of the physics list.

The first step for running the CosmicTransmutation model is to define the target. The relevant parameters are size, shape, and composition. The shapes currently available for users are limited to spherical and ellipsoidal objects. The pre-atmospheric shapes of meteorites are difficult to know but with the spherical and ellipsoidal shapes provided, the majority of the meteoroids should be covered reasonably well. The composition of the meteoroid is a crucial parameter for the production of cosmogenic nuclides. The compositions, including the density of the material, of C-chondrites, L-chondrites, and iron meteorites, which are the most common meteorite types, are directly available in the code. However, other compositions can be handled using a user-defined input file.

The second step of the CosmicTransmutation model is the definition of the irradiation spectrum. In terms of energy, two possibilities are pre-programmed for the user. The standard cosmic ray spectrum that can be used to simulate a realistic cosmic ray irradiation flux (see sect. VII.3). In addition, a mono-energetic flux, which can be used to study the impact of one specific energy. Next, the user can choose the type of the irradiating particles. In the cosmic ray spectrum, the major part of the flux is made of protons, which contributes about 90% of the total flux. In addition, the alpha particles represent almost all the other 10%. The heavy ions represent less than one percent and can therefore be neglected in this first approximation. However, while alpha particles are less numerous than protons, they consist of four nucleons, which results in a significantly higher cosmogenic nuclide production per collision. In the CosmicTransmutation model, the choice between an irradiation spectrum completely made of protons, alpha particles, or using the natural elemental composition is given. This allows us to simulate the natural irradiation as well as to study the different components of the cosmic ray spectrum separately. In addition, also the possibility of neutron irradiation is implemented, though mostly for theoretical analyses.

For example, this set-up allows us to test the usual hypothesis that the alpha particles can be replaced by 2 protons and 2 neutrons carrying each one fourth of the total kinetic energy.

For the definition of the physics list, Geant4 proposes various model combinations to treat the different aspects of the physics [10, 59]. The user is free to choose any of the physics lists proposed in Geant4. However, the default physics list used by CosmicTransmutation is "FTFP_INCLXX_HP". In this physics list, the Fritiof model [58] is used for high energies (*i.e.*, above 15 GeV for hadrons and 2.9 GeV/Nucleon for ions) and INCL takes care of the intermediate energies. The question what is an intermediate energy depends on the particle type. In Geant4.10.05, the latest public version available at the date of publication of this thesis, the energies treated by INCL for nucleons, *i.e.*, protons and neutrons, are between 1 MeV and 20 GeV. For ions, and notably for alpha particles, INCL is used between 0 and 3 GeV/Nucleon. Since neutron physics is crucial for cosmogenic nuclide production the physics list "FTFP_INCLXX_HP" is preferred to "FTFP_INCLXX". In the former, the lower limit for neutron handled by INCL is 20 MeV and lower energies are treated by the use of tabulations providing a very high precision down to 10^{-12} MeV. On the other hand, in the second physics list, a precompound model is used for energies below 2 MeV. In the chosen physics list, there are sufficient overlaps between the energy ranges to allow for smooth transitions between the individual models.

VII.2.2 Running and outputs

After the initialisation, there is the running of the program. As already mentioned, the processing of a run is fully treated by the Geant4 environment. During this stage, the improvements of the INCL code discussed in the previous chapters influence the final results. This, however, is not visible to the user. During the computational run, the CosmicTransmutation model collects all necessary information generated by the Geant4 environment and creates the outputs files. In our case, we want to calculate the differential fluxes of light particles, *i.e.*, protons, neutrons, alphas, together with the production of cosmogenic nuclides as a function of the location within the target.

The CosmicTransmutation model produces two different outputs. First, a ROOT file is generated in which all the relevant information is stored in three TTree's, which allows a large number of combinations between the different TLeaf's. A second output stores in data files only the information on proton, neutron, and alpha particle fluxes as a function of the depth within the meteoroid. It is left to the user to decide which output (potentially both) will be created.

Two methods can be used to study cosmogenic nuclide production using the CosmicTransmutation model. The simplest method is to take the results of the model in the ROOT file in which all the information about the production of cosmogenic nuclides is stored. This method is very direct, however, the statistics for the production of rare nuclei can be problematic. Thus, this method requires a significant computational time for the study of specific cosmogenic nuclides. The second method is by using the CosmicTransmutation model as a code to calculate the depth dependent fluxes of particles like protons, neutrons, and alpha particles. The fluxes can be obtained both from the ROOT file or from the data files. The thus calculated particle fluxes must then be combined with the cross sections of the relevant nuclear reactions of the elements in the target to calculate the production of cosmogenic nuclides. The cross sections, *i.e.*, the excitation functions, can be obtained using spallation models like INCL. In the latter case, the spallation model (INCL) is used twice: once in Geant4, where it is used, first, to calculate the differential particle spectra, and, second, to calculate relevant cross sections. The reliability of the spallation model used in this second approach is even more crucial. It explains why so much effort was, and is still, put into the development in the validation of the INCL model as demonstrated in the previous chapters.

VII.3 Meteoroids, asteroids, and moons

From the irradiation point of view, there is no major difference between meteoroids, asteroids, and moons. The main difference between the different objects is in their composition. However, the principals of the irradiation processes are the same.

Once the composition, the density, the shape, and the size of the target are given by the user as input parameters, the final step is to define the irradiation spectrum.

Two irradiation spectra are implemented in the CosmicTransmutation model in addition to a mono-energetic particle beam. They correspond to differential galactic cosmic ray particle spectra for protons and alpha-particles.

The formula used in CosmicTransmutation for the differential galactic cosmic ray proton flux is a modified version of the formula used in ref. [118].

$$J_p(T, M) = c_p \times \frac{T\ (T + 2m_pc^2)\ (T + x + M)^{-2.65}}{(T + M)\ (T + 2m_pc^2 + M)} \tag{VII.1}$$

with T the kinetic energy, M the solar modulation parameter, and m_p the proton rest mass. The factor x is defined as:

$$x = 780 \times e^{-2.5\ 10^{-4} \times T} \qquad \text{[MeV]} \tag{VII.2}$$

For a flux in the unit [particle m^{-2} s^{-1} sr^{-1} MeV^{-1}], the parameter T, M, x, and m_pc^2 must be expressed in MeV and the normalisation factor is $c_p = 10^9$.

The solar modulation parameter M is used to take into account the variations in the cosmic rays flux due to solar activity. This parameter varies between 300 MeV (low solar activity) and 1100 MeV (high activity) [119–122]. The best average for the last millions years for the solar modulation parameter is $M = 550$ MeV at 1 au [123, 124].

The differential alpha particle flux used in the CosmicTransmutation model is given by a formula developed within this thesis:

$$J_\alpha(T, K) = c_\alpha \times \frac{T^K \times (T + 2m_\alpha c^2)}{(T + 700)(T + 2m_\alpha c^2 + 700)(T + 312500\ T^{-2.5} + 700)^{1.65+K}} \tag{VII.3}$$

with T the kinetic energy per nucleon expressed in MeV/nucleon and $c_\alpha = 5.5\ 10^7$ for a flux in [particle m^{-2} s^{-1} sr^{-1} $(MeV/nucleon)^{-1}$]. The K parameter takes into account the solar activity and is based on the solar modulation parameter M as:

$$K = (1.786\ 10^{-3} \times M) - 0.1323 \tag{VII.4}$$

Equations VII.1 and VII.3 are used in the energy range between 10 MeV/nucleon and 100 GeV/nucleon.

It is important to mention that the integration of these two formulae must be done for a solid angle of 2π and not 4π, as it is often done wrongly, to get the integrated flux at the surface of the target in the unit [particle m^{-2} s^{-1} $(MeV/nucleon)^{-1}$]. This is due to the fact that the target surface is irradiated only from the outside. The particles coming from the inside are secondary particles, which are not part of the primary cosmic ray spectrum.

VII.4 The planetary model

The irradiation of planets by cosmic rays is very different to the irradiation of meteoroids or moon. The main difference does not come from the gaseous nature of the overlying atmosphere as we could assume. If the production of secondary particles and the absorption of primary particles is discussed

in the unit g/cm^2 (*i.e.*, as a function of the volumetric mass density integrated over the deepness), the curves for planets and meteoroids actually look very similar. The main difference between planets and meteoroids actually is in the presence of a magnetosphere around the planets.

The magnetic fields around planets modify the trajectory of the particles. Some of these trajectories, particularly for the low energy particles, are curved in such a way that they never cross the planet's atmosphere. Therefore, a part of the *standard* cosmic ray spectrum is rejected and the remaining part is modified. This must be considered for the simulations. Details on the planet irradiation process are given in subsection VII.5.3.

In the CosmicTransmutation model, the processing of a run including a magnetosphere has been divided into two parts. The first part is devoted to the computation of the trajectories in the magnetosphere where no collision happens and the second part corresponds to the irradiation of the atmosphere.

The magnetic fields of planets are usually not simple dipoles. The dipole, however, is very often the dominant term of the magnetic field. Nevertheless, major perturbations like the solar magnetic field and/or the solar wind strongly influence the shape of the local magnetic field. Moreover, the dipole generated by the planet is not necessary aligned to the rotational axis of the planet and/or it can be shifted with respect to the center of the planet. In some cases, the magnetic field generated by the planet is not a dipole at all. At the current stage, the magnetic fields that can be handled in the CosmicTransmutation model are relatively simple. Two components are considered: the dipole generated by the planet, which can be shifted and/or rotated, and a constant magnetic flux representing exterior perturbations.

Another difference between simulations for planets and meteoroids/asteroids is caused by the Geant4 toolkit. Unfortunately, Geant4 does not allow to create logical volumes with a variation in density and/or composition as a function of the location in this volume. Therefore, the atmosphere with its variation in composition, density, and temperature must be decomposed into several layers in which these characteristics are assumed to be constant. The number of layers, which will directly affect the precision, has to be defined by the user. The temperature is not relevant for the CosmicTransmutation model. Therefore, the temperature used is the default value of Geant4 (293.15 K) for all layers. On the other hand, the composition and the density of the atmosphere are obviously highly relevant for the outcome of the simulation. It is not realistic to know the exact composition and density of the atmosphere for each of the defined layer. Two models are used: one for the composition and one for the density. The composition model requires knowledge of the composition at the bottom and the top of the atmosphere. From this, the composition of intermediate layers are calculated using a simple linear interpolation. Whereas, for the density, the developed model only requires the density of the atmosphere at the ground level. Then, an exponential decrease as a function of altitude is applied and the top layer density is defined as 10^{-4} times the density of the bottom layer.

While the magnetic field is really crucial in the magnetosphere, it becomes of secondary importance in the atmosphere. Therefore, for sake of simplicity, the magnetic field within the atmosphere is considered constant along the irradiation phase of the simulation. This is justified by the relative short path of particles within the atmosphere with respect to their path in the magnetosphere. Moreover, the variations of the magnetic field along tracks in the Earth's atmosphere are less than 5%.

VII.5 Algorithms

In the course of the current thesis, some algorithms were developed for the CosmicTransmutation model. Here I summarise the relevant developments.

VII.5.1 Irradiation

Once the cosmic ray spectrum has been defined, the CosmicTransmutation model must generate a homogeneous flux to irradiate the meteoroid, the asteroid, and/or the moon.

For spherical objects, the special symmetry reduces the characteristics of the location and direction of the incoming cosmic ray particles to only one relevant parameter: the impact zenith angle. Indeed, on a spherical target, no impact location can be distinguished from one another. Therefore, the impact location is not relevant. In addition, a rotation of the target around an axis connecting the impact location with the center of the sphere leaves the target unchanged. Therefore, the impact azimuth angle is not relevant either.

For a uniform irradiation of a spherical object, the impact zenith angle θ must be generated between 0 and $\pi/2$ with a probability density proportional to $\sin(\theta)$. This comes from the Jacobian in spherical coordinates. It is often convenient to use the impact parameter instead of the zenith angle. The impact parameter corresponds to the normalised radial distance ρ in the cylindrical coordinate system with the z axis aligned with the direction of the incoming cosmic ray particle. In such case, the impact parameters ρ must be generated between 0 and 1 with a probability density proportional to $\sqrt{\rho}$.

In the CosmicTransmutation model, the cosmic rays irradiating the spherical objects are generated along the z axis. Therefore, the particle type, the kinetic energy, and the impact parameter fully characterise the incoming cosmic rays. All three parameters are stored in the output ROOT file.

If the target is of any shape, the location and the direction of the incoming cosmic rays cannot be reduced to less than 4 parameters (2 for the location and 2 for the direction). A system of 2 parameters defining the impact location on the surface of the target can generally not be found. Moreover, some locations can be partially shielded by parts of the target. Therefore, the simplest way to irradiate such an object with a non regular shape is to generate the irradiation on a virtual sphere surrounding the target. Therefore, a random initial location for the incoming cosmic ray must be chosen on the virtual sphere as well as random impact zenith and azimuth angles as a function of the corresponding probability density. However, this method might generate events in which the cosmic ray particle does not hit the target and it is therefore not very effective.

In the case of ellipsoidal objects, the symmetries do not allow to reduce the location and the direction of the incoming cosmic rays to less than 4 parameters, as it was possible for spherical objects. However, a specific algorithm is implemented in the CosmicTransmutation model to generate a homogeneous irradiation of ellipsoid in which no cosmic ray particle misses the target. This optimises the computational time and helps to estimate the relative uncertainties of future results, which decrease with the square root of the number of hitting cosmic rays. This algorithm is given in Appendix F.

VII.5.2 Irradiation time

One of the main components needed for the normalisation of the results obtained using the CosmicTransmutation model is the irradiation time. However, the irradiation time is not a relevant parameter to estimate a priori the precision of the results. For a given irradiation time, large objects (*e.g.*, moons) are more exposed to cosmic rays than smaller objects (*e.g.*, micro-meteoroid). Thus the statistics is related to the size of the object and the irradiation time. Therefore, the relevant input parameter that affects the precision of the results is the number of computed events.

An algorithm is implemented in the CosmicTransmutation model to compute the equivalent irradiation time of a run. This algorithm is divided into three parts. First, the differential flux of cosmic ray particles parametrised by the solar modulation parameter M, which is provided by the user, is integrated over the solid angle and the energy. Second, the surface of the target is calculated, and finally, the integrated flux

I_F, the target surface S, and the number of events N_{event} are combined to get the irradiation time t via:

$$t = \frac{N_{event}}{I_F \times S} \tag{VII.5}$$

The irradiation time given in s and the target surface given in m^2 are both stored in the output ROOT file as well as in the output data files.

VII.5.3 Magnetic field cut-off

As mentioned above, the particle trajectories in the magnetosphere of a planet are curved. This results in constraints on the characteristics of the particles entering the atmosphere. Consequently, the particles entering the atmosphere can only have limited combinations of location and momentum

Here, it is useful to introduce the concept of rigidity. The rigidity of a particle is defined as the ratio of its momentum norm divided by its electrical charge and is commonly express in GV/c (or in GV using the convention $c = 1$). This concept is useful as two particles with the same rigidity and the same initial position and direction follow the same trajectory in a magnetic field independently of their nature. Therefore, the set of allowed values for rigidity, direction, and location in a magnetic field are the same for all the particles.

Considering the size of the magnetosphere compared to the size of the planet and the proportion of the cosmic ray spectrum rejected, it is not realistic to generate the irradiation on a virtual sphere surrounding the magnetosphere. This would be extremely CPU time consuming. Moreover, the interest of the user is very often focused on cosmogenic nuclide production at a specific latitude-longitude location (the altitude can vary with the applications). Therefore, the usual solution is to divide the simulation into two parts. First, a map of the allowed rigidity-direction pairs at the top of the atmosphere is determined for a given latitude-longitude location. Next, the irradiation of the planet from the top of the atmosphere is calculated. However, the process is too complex for an analytical solution [125]; therefore, an algorithm has been designed to draw the map of allowed rigidity-direction pairs.

For a given impact location and direction, the map of allowed and forbidden rigidities always follows the same structure [125]. In this scheme, all rigidities below a certain rigidity called R_l (the lower cut-off) are forbidden while all the rigidities above the rigidity R_u (the upper cut-off) are allowed. Between R_l and R_u, a rigidity range called the penumbra consist of a succession of bandwidths, which could be of various sizes.

Since the user is usually interested in cosmogenic nuclide production at a specific location, the common solution to generate the map of allowed rigidity-direction pairs is to compute the trajectories in the magnetic field using reverse kinematics as shown in Figure VII.2. Thus, the starting point of the trajectory is at the top of the atmosphere and corresponds to the latitude and the longitude of interest for the user. Next, the trajectories of the particles in the magnetic field, which has been defined by the user

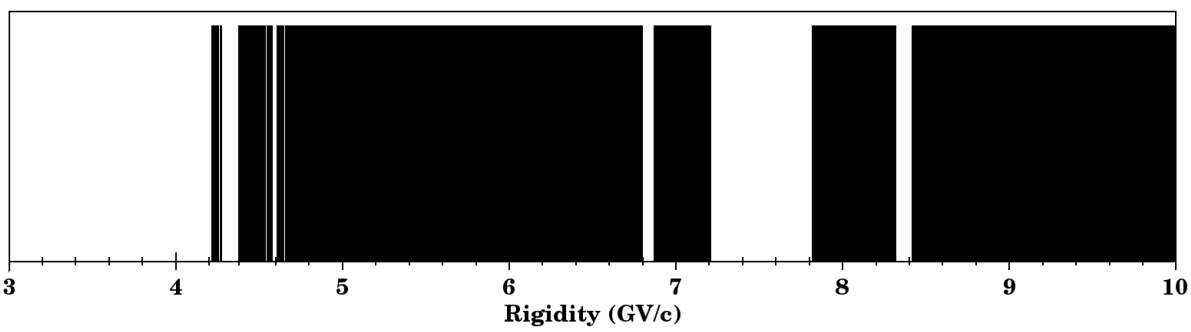

Figure VII.1: Example of a penumbra region in a typical complex configuration.

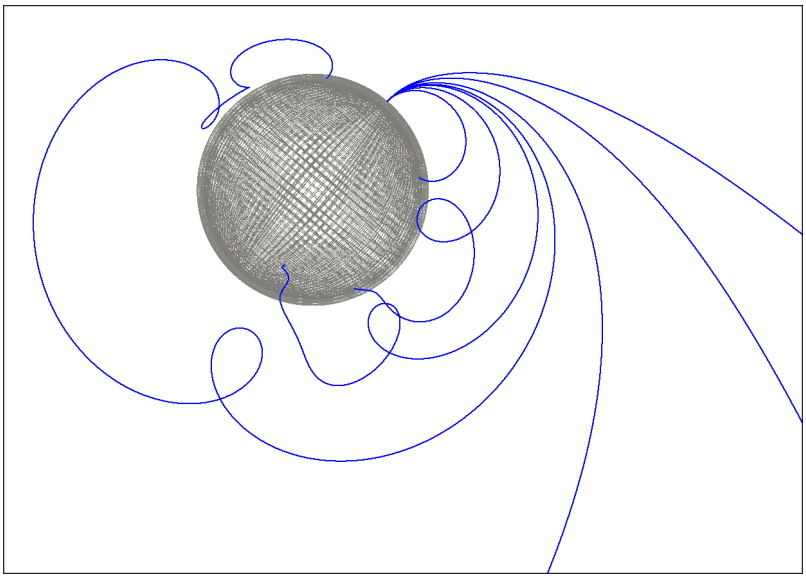

Figure VII.2: Examples of trajectories in a complex magnetic field. The curves have been computed using the CosmicTransmutation model. The trajectories connecting two points of the atmosphere are "closed" trajectories and are therefore forbidden for cosmic rays.

are computed with the help of the Geant4 environment [10, 59]. Particles that start from the surface, following the computed trajectories and are able to escape the planet magnetosphere correspond to allowed trajectories and, in contrast, particles falling back on the atmosphere correspond to forbidden trajectories. The map of allowed rigidity-direction pairs is then constructed by scanning over all possible zenith and azimuth angles as well as by considering all relevant rigidities ($R \in [0\text{ GV}, 20\text{ GV}]$ for the Earth).

Usually, the penumbra has a complex structure. In other algorithms [125, 126], the median of the allowed rigidities between R_l and R_u is determined. This rigidity (often called R_c) depends on the location and the direction of the incoming cosmic rays and is used as a hard cut-off. Rigidities above and below R_c would be considered allowed and forbidden respectively. This significantly simplifies the generation of the irradiation spectrum during the irradiation phase. However, due to the improvement of computing power realised in recent decades, we can improve on this situation. Therefore, this crude approximation is not used in the algorithm implemented in the CosmicTransmutation model. Instead, the entire structure of the penumbra is kept, which is supposed to improve the results of the model.

The rejection of specific trajectories changes the fluxes of the irradiating particles. These modifications do not affect all particle fluxes the same. This changes the ratio of cosmic ray particles, *i.e.*, it affects the chemical composition of the relevant galactic cosmic rays. Some partial tests carried out with the algorithm developed for the CosmicTransmutation model shows the proportion of α particles can range from 10% to 15% of the total flux at the top of the atmosphere depending on the latitude and the magnetic field.

VII.5.4 The funnel effect

As discussed before, magnetic fields of planets forbid some particle trajectories. However, this is not the only effect produced by magnetic fields. They can also focus or disperse the allowed trajectories. This modifies the probability of a specific trajectory. The magnetic field can act like a funnel or it can dissipate the particles depending on the special configuration.

During the determination of allowed trajectories, an optional step can be added to the algorithm presented in subsection VII.5.3. This step measures the dispersion of particles for a given rigidity, zenith, and azimuth angles together with the latitude and longitude of the hitting location. This is done by

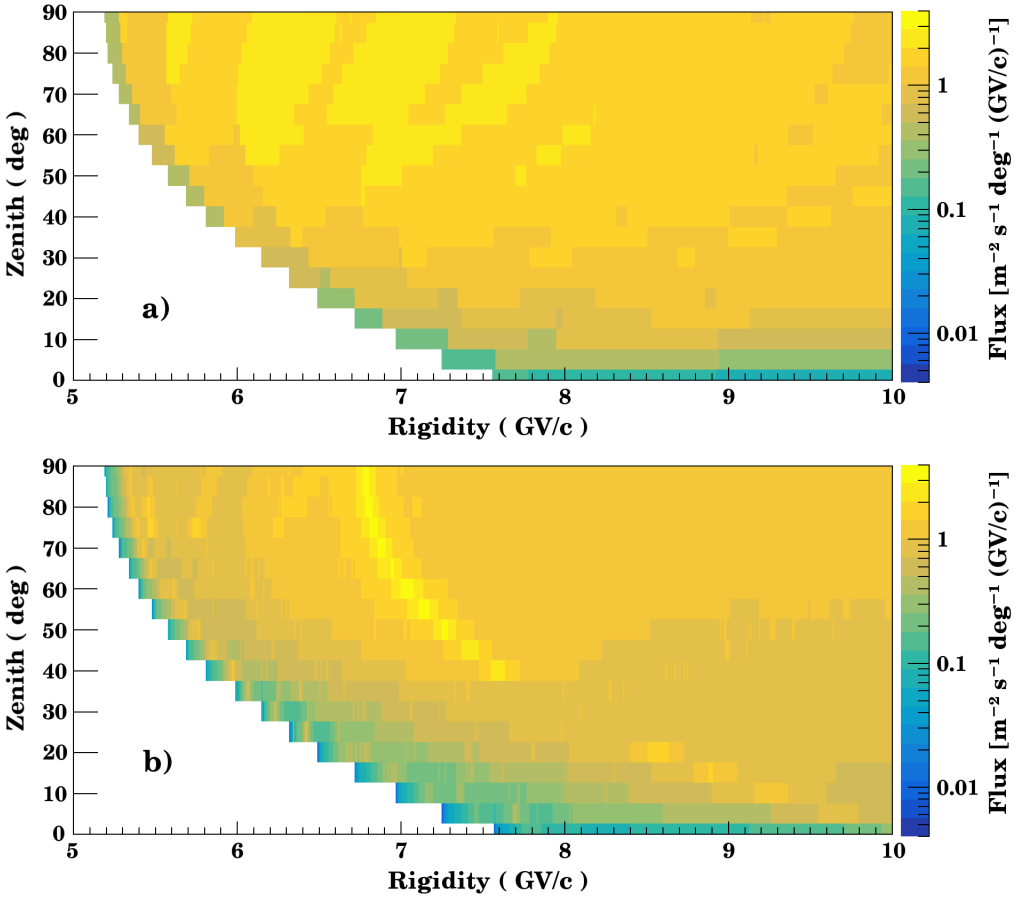

Figure VII.3: Irradiation fluxes estimated at the top of the atmosphere as functions of the rigidity and the zenith angle with (b) and without (a) taking into account the funnel effect. See text for the details.

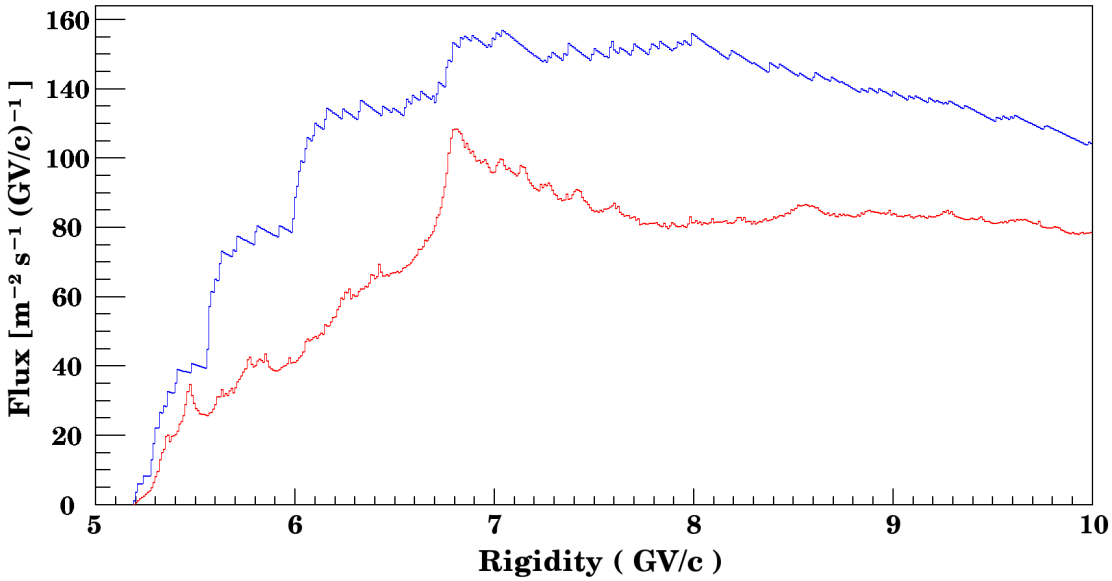

Figure VII.4: Irradiation flux as a function of the rigidity. Red: taking into account the funnel effect. Blue: without taking into account the funnel effect.

reversing the final momentum of particles, which successfully escaped the planet's magnetosphere during the initial cut-off calculation. Consequently, the calculations in this part of the algorithm are done in direct kinematics. Each allowed trajectory is tested several times with minor variations on the initial position and direction. These variations correspond to a predefined phase space. Finally, the phase space covered by the hitting locations on the top of atmosphere of these trajectories is compared to the initial phase space scanned. If the final phase space is smaller than the scanned phase space, the trajectories are focused. This increases the probability to observe the trajectories. Otherwise, the trajectories are dispersed and the probability is reduced. The ratio of the two phase spaces is stored and is used to modify this probability during the second part of the simulation: the irradiation phase.

Figure VII.3 represents the irradiation fluxes at the top of an atmosphere as functions of rigidity and zenith angle. The geometry corresponds to a planet with a radius of 5000 km and an atmosphere, which is 50 km thick. The associated magnetic field is a simple dipole aligned with the rotational axis of the planet, and with an intensity of 20 μT at the top of the atmosphere. The tested location is at latitude and longitude = $(0, 0)$.

Many differences and similarities can be observed between the two plots in Figure VII.3. As for the similarities, the limits of the two plots (the cut-offs) are the same. However, the detailed structures differ between both set-ups. No clear structure appears in Figure VII.3.a except for some variations induced by the phase space along the y axis and by the initial galactic cosmic ray flux along the x axis. These variations are apparent in both panels. In Figure VII.3.b, a clear structure appears. For highly dispersed trajectories, a thin band in the diagram zenith versus rigidity starts at around $R = 6.8$ GV and $\theta = 90°$ and finishes around $R = 7.6$ GV and $\theta = 40°$. This band indicates that corresponding trajectories are indeed focussed. Numerically, the band seems to extend down to $R = 10$ GV and $\theta = 0°$. However, the apparent focusing is low and it therefore hard to conclude if there is any relevant focussing effect

In Figure VII.4 the flux is plotted as a function of the rigidity for two different set ups; the blue line is for the set-up without the funnel effect and the red line is for the calculated flux by considering the funnel effect.

One important point is immediately obvious: the flux estimated without considering the funnel effect is very erratic. This is easily explained by the occurrence of what we call saddle rigidities. In this original approach, the tracks can only have two statuses: allowed or forbidden. When a new trajectory is allowed with a slight increase in rigidity, this trajectory is completely accepted, which creates jumps in the irradiation spectrum. It can also be seen that the flux decreases very regularly between the jumps. The decrease in Figure VII.4 is proportional to $R^{-2.65}$ originating from the proton flux formula given in eq. VII.1. If the binning of the zenith angle is reduced in the algorithm, the jumps are less intense but more numerous. However, the overall shape of the curve is not changed

With the new approach, the probability density for a cosmic ray to follow allowed trajectories is taken into account. This reduces the jumps seen in Figure VII.4 with the previous approach. Moreover, the irradiation flux determined is more stable. This is due to the fact that, whenever a new trajectory is opened, the probability density associated to the trajectory is very low. Then, the amplitude of this trajectory increases most of the time with increasing rigidity. The competition between the increasing amplitude and the decrease in the initial flux, which is proportional to $R^{-2.65}$, lifts the curve.

It is important to mention two points to recognise on Figures VII.3 and VII.4. First, the tested location is for a latitude and longitude = $(0, 0)$. At this location, the planet's magnetic field is perpendicular to the normal, which maximises the shielding effect of the magnetic field. This explains why the flux calculated by considering the funnel effect is lower than the flux calculated using the original approach, *i.e.*, without considering the funnel effect. This, however, is not the general trend. At different locations, the flux can also be increased. Some other examples are given in Appendix G in order to show different possible configurations. Second, the occurrence of small bumps seen in Figure VII.4 with the new approach are majorly due to the binning used for the zenith angle. A figure showing the impact of the binning in the two approaches can be seen in Appendix G.

VII.6 Elements of analysis

The simulation of physical processes needs hypotheses and approximations to start with but they can also introduce biases in the results. These biases must be considered during the analysis of the simulation results. This section summarises the weaknesses and potential biases but also the strengths of the newly developed CosmicTransmutation model, which all must be considered for the analysis of the modelled results. In addition, some useful tools are implemented in the CosmicTransmutation model. Here I give a short summary.

VII.6.1 Double counting

Some issues arise with the use of Geant4; namely with the system of sensitive detectors (see ref. [59]). In the Geant4 environment, the tracks are computed within logical volumes, which can be sensitive detectors. When a track passes through one volume associated to a sensitive detector into another volume, this track can be detected twice. Once upon leaving the first volume and then again when entering the second volume. In such cases, the particle associated to the track is detected twice in a very small interval.

For meteoroids, the logical volume can be defined as the entire object. Therefore, the just discussed effect is limited to the surface of the meteoroid. As this surface is typically lost because of ablation while the meteor falls in the atmosphere, this effect can be neglected. However, another problem arise with this solution. If the mean free path of a particle is long, the particle can travel a layer of interest without being detected and therefore, the fluxes of particle can be underestimated. The flux of high energy neutrons is particularly concerned by this problem. For the flux of particles, the solution is then to define thin sensitive detectors (*i.e.*, thinner than the particles mean free path) at the depths of interest, whereas the rest of the target is not a sensitive detector. For planets, however, it is more complicated because the atmosphere cannot be defined as only one logical volume. As mentioned above, Geant4 does not allow the creation of logical volumes with a variation of density and/or composition as a function of the location within this volume. This is why the atmosphere in the CosmicTransmutation model is made of several layers with the composition and the density corresponding to the elevation. In this case, effects due to double counting must corrected.

VII.6.2 Radioactive nuclei

As already mentioned, the CosmicTransmutation model calculates the direct production of cosmogenic nuclides in meteoroids, planetary surfaces, and planetary atmospheres. However, the indirect production, *i.e.*, the final outcome after the full radioactive decay, is not treated. For most of the cosmogenic nuclides, the indirect production is extremely important. The corresponding corrections can easily be applied a posteriori.

VII.6.3 Funnel effect

The funnel effect has been introduced in order to consider the focussing or the dispersion of trajectories in the magnetic fields. However, the algorithm developed in the CosmicTransmutation model is by far not perfect. One example is the aforementioned binning bias, which can be seen in Figure VII.3 and which has been manually minimised by tuning the binning, while keeping a reasonable computational time.

The approach of the funnel effect, which is described in this chapter, is entirely new in the field of cosmogenic nuclide studies. It is worth emphasising that the principle of the approach has been validated but the algorithm is not. It is important to consider the deflection of cosmic rays in the planet's magnetic fields. The evaluation of the funnel effect in the CosmicTransmutation model showed various effects on the irradiation spectra and, by extension, on the production rate of cosmogenic nuclides. However, the

method used to calculate this deflection has not been controlled rigorously in the course of this thesis. Therefore, any conclusions based on the funnel effect should be considered carefully.

The algorithm in the CosmicTransmutation model computes the probability density for a cosmic ray to follow trajectories in the magnetic field. This probability density arises from a comparison between a phase space at the top of the atmosphere with the corresponding phase space outside the magnetosphere. However, the computational time needed for a proper evaluation of this entire funnel effect was unreasonably long. In the current version, I decided to compare a predefined phase space outside the magnetosphere to the corresponding phase space at the top of the atmosphere. Starting with a predefined phase space makes the computational time reasonable. However, the method is more sensible to the dispersion of the trajectories than to the focusing. The algorithm I developed for the CosmicTransmutation model has been tested with a predefined phase space at the top of the atmosphere instead of outside the magnetosphere. This alternative algorithm was efficient for the measurement of the focusing of trajectories but it was less efficient in measuring the dispersion. Comparisons between the two methods showed significant differences near the cut-off threshold but a convergence of the two models with increasing energy. Therefore, the irradiation spectra obtained using the actual algorithm (with a predefined phase space at the top of the magnetosphere) are likely slightly underestimated.

VII.6.4 Stable bias

One of the main strength by using only the model to calculate production of cosmogenic nuclides comes from the "stable bias" of models like INCL. It is obvious that simulations are not perfect. An infinite statistics does not mean a model converges to the true observables. This difference between the true value of an observable and the value estimated by the model with a good statistic is called the bias of the model. A recent study of the INCL biases [127] showed that they are very "stable": if an observable is overestimated in a given configuration, the same observable will also similarly be overestimated in another configuration, if it is close to the first one. Moreover, close observables (*e.g.*, the production rates of ^{40}K and ^{41}K) will also present similar biases. Therefore, when we are interested in cosmogenic nuclide ratios, such biases usually vanish. Consequently, it is preferable to use full theoretical approaches in such situations instead of mixing theoretical and experimental approaches, even if the last ones are sometimes more reliable.

VII.6.5 Exposure time and exposed surface

One of the most important steps during the analysis of theoretical as well as experimental data is the normalisation. In the output of the CosmicTransmutation model, the observables are the production rates of cosmogenic nuclides, which are expressed in $kg^{-1}s^{-1}$ in SI units, and the particle fluxes, which can be expressed in $m^{-2}s^{-1}$ or in related units (*e.g.*, $m^{-2}s^{-1}sr^{-1}$ or $m^{-2}s^{-1}(MeV/Nucleon)^{-1}$). In order to simplify the analysis of the results, the irradiation spectrum is automatically integrated by the CosmicTransmutation model taking into account the number of events and the exposed surface. Thus, the exposure time is determined and provided in the output files. This exposure time can be used for the normalisation of the observables. The exposed surface of the target is also provided in the output files. The is particularly useful in the case of a general ellipsoid, since no analytical formula exists for the calculation of the surface. In such a case, the surface of the target determined by the CosmicTransmutation model must be used for the normalisation.

VII.6.6 Unidirectional irradiation

For a spherical meteoroid the irradiation algorithm considers symmetries to make the simulation and the analysis simpler. The relevant parameters to define a collision are the impact parameter and the characteristics of the cosmic rays. Therefore, the direction and the impact location of the cosmic ray can

be modified if the impact parameter is conserved. In the CosmicTransmutation model, the choice has been made to have an unidirectional irradiation flux along the positive z axis direction. This constraint can be used to easily determine various observables, for example if a particle has been reflected.

Chapter VIII

Cosmogenic nuclides production

Similarly to the discussion in chapter VI, where we presented the results at the INCL model, this chapter summarises the results of the CosmicTransmutation model.

Comparisons between a model and experimental data require a perfect control of the initial state of the studied systems and of the processes relevant for these experiments. In the case of cosmic ray irradiation, the irradiation spectrum, the exposure time, as well as the initial characteristics of the target must all be reproduced in a good experimental set-up. However, the main difficulty in astrophysics is that most of the studied observables and relevant parameters cannot be reproduced and/or fully controlled in the laboratories. For example, we are not able to produce a beam with the characteristics of the cosmic rays. The few attempts to reproduce the effects of cosmic ray irradiation in the laboratory often used mono-energetic proton beams, which required inter- and extrapolations and the experiments are not fully representative of the real conditions in space. The experimental data coming from real meteorites are also challenging; several assumptions are necessary to interpret the measured data. For example, the outer layer of a meteoroid usually gets ablated while the object is travelling through the atmosphere. Furthermore, some meteoroids break-up during atmospheric entry. Therefore, the shape and the size of the initial meteoroid is not known and must somehow be reconstructed either from measurement alone or from a combination of measured data and model predictions. All these problems and interferences make comparisons of the results obtained using the CosmicTransmutation model with experimental data extremely complex and debatable. Therefore, the best solution for the validation of the model is a comparison with other models, whenever possible. In addition, a priori knowledge can be also used for a rough estimate of the quality of the results.

In this chapter, comparisons with previous theoretical calculations will be discussed and the results of the CosmicTransmutation model will be presented. This analysis requires to always remember biases discussed in sect. VII.6.

VIII.1 Meteoroids

The core of this thesis is the study of cosmogenic nuclide production in, first, meteoroids and, second, planetary surfaces and planetary atmospheres. In this section, the results of the CosmicTransmutation model are compared to previous calculations [124] obtained using the LAHET code [23]. For the comparisons I consider differential particle fluxes for protons and neutrons and their dependence on the chemical composition of the meteoroid and the size of the irradiated object.

Figure VIII.1 shows the simulated neutron fluxes at the surface of two C-chondrites of radius 10 cm and 50 cm calculated using either the CosmicTransmutation model or the LAHET code. While the shapes obtained with the two models are very similar, the fluxes calculated using the CosmicTransmutation code are for both cases 2 times lower than the fluxes calculated using LAHET. The most likely explanation

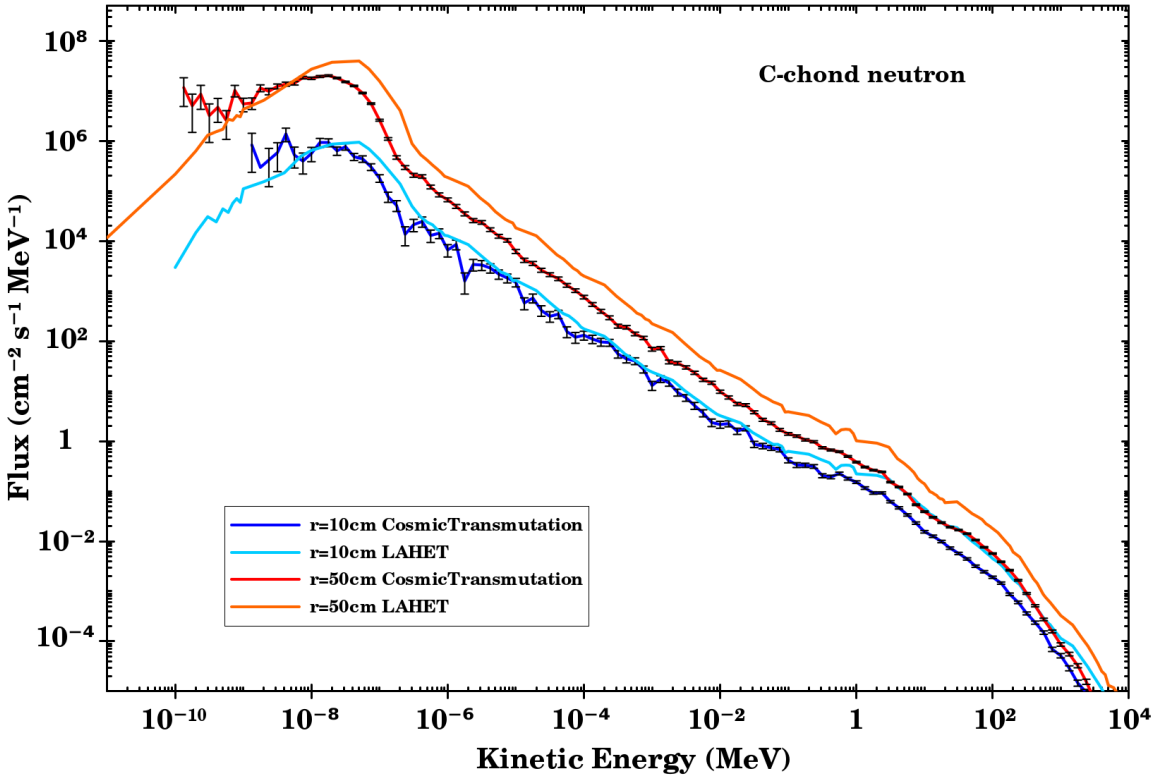

Figure VIII.1: Neutron fluxes at the surface (depth = 0 to 1 cm) of C-chondrites with pre-atmospheric radii of 10 and 50 cm.

for this discrepancy is in the normalisation of the primary GCR spectrum. The normalisation of the results requires to integrate the cosmic ray spectrum, which is usually expressed in [particle m^{-2} s^{-1} sr^{-1} $(MeV/nucleon)^{-1}$]. As we already discussed before, the integration over the solid angle must be done over 2π, as opposed to 4π as it is very often wrongly done. This is because the irradiation comes only from half of the phase space, the other side is hidden by the irradiated object itself. If this is not taken into account, all the results, *i.e.*, particle spectra and production rates, are increased by a factor of 2.

Ignoring the factor 2 of difference likely caused by the normalisation of the primary GCR spectrum, the neutron fluxes calculated for the surface of a 10 cm C-chondrite by using either the CosmicTransmutation or the LAHET model correspond very well for neutrons with kinetic energies ranging from 10^{-7} to 1 MeV. For lower energies, the flux obtained using the CosmicTransmutation code is consistently higher with respect to the flux calculated using LAHET. However, this difference is not significant for the total neutron production cross sections considering the integral of the total neutron flux in this energy range. Considering the bumps predicted by each of the models at low energy, the finding is the same as for the 10 cm C-chondrite, *i.e.*, the neutron flux predicted using CosmicTransmutation is higher than the flux predicted using LAHET but once again is not significant. If we consider the factor of 2 difference likely caused by the normalisation, the LAHET flux is still 1.5 times higher than the CosmicTransmutation flux in the energy range 10^{-7} to 1 MeV. This energy range corresponds to neutron capture reactions, which are very important for some cosmogenic nuclides production studies.

Figure VIII.2 is the same as Figure VIII.1 but here for protons and not for neutrons. In addition, the proton flux used to irradiate the meteoroid is plotted. The proton flux predicted by the CosmicTransmutation model can be divided into four energy ranges corresponding to as many physical phenomena. First, the protons with energies above 4 GeV correspond to the original primary cosmic ray flux. For the meteoroid with a radius of 10 cm, this flux is 60% higher than the primary GCR spectrum. This is due to the high energetic particle from the other side of the meteoroid and passing through it with only "light" elastic collisions. For the 50 cm C-chondrite, on the other hand, the flux at the surface of the meteoroid is

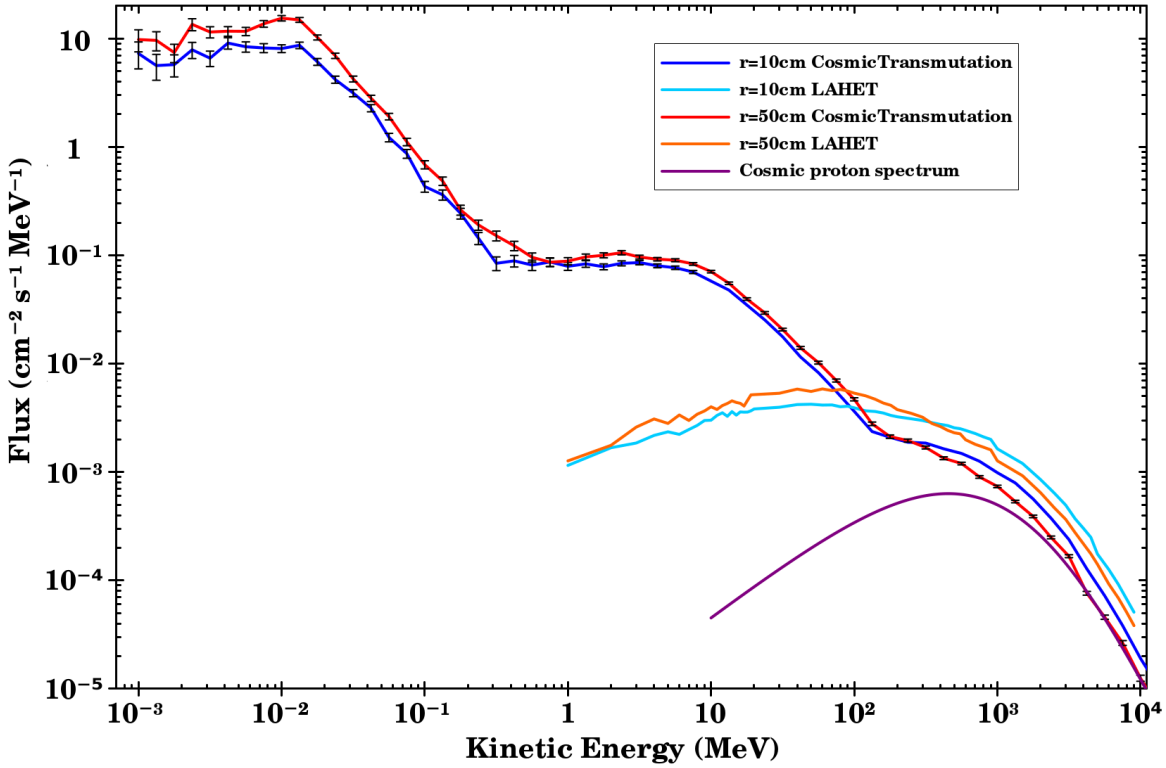

Figure VIII.2: Proton flux at the surface (depth = 0-1 cm) of C-chondrites with pre-atmospheric radii of 10 and 50 cm.

almost identical to the primary flux, which is expected because essentially no particle can come from the other side, *i.e.*, passing the object without interaction. Second, in the energy range 100 MeV to 4 GeV, additional protons appear, which are mainly produced in the intra-nuclear phase of spallation reactions, either induced by primary galactic cosmic ray particles or by secondary particles. Third, the energy range 1 to 100 MeV is dominated by protons that are produced in the second phase of the spallation reaction; the de-excitation phase (see chapter III). Here, the proton flux is higher for the larger meteoroid than for the smaller meteoroids because secondary reactions are more numerous in larger meteoroids than in smaller ones. Finally, the last part of the flux with energies below 1 MeV corresponds to secondary protons that have been slowed down through elastic collisions and/or bremsstrahlung. It is worth emphasising that protons with energies below a few MeV are not relevant for the study of cosmogenic nuclides because they can neither induce spallation reactions nor can they be captured by a nucleus.

The first comparison between the proton fluxes calculated using either CosmicTransmutation or LAHET indicates the same factor 2 difference as already discussed for the neutrons (see above). By dividing the LAHET flux by a factor of 2, the total flux of protons, *i.e.*, the integral of the spectra, match perfectly between the two models. In addition the spectra calculated using LAHET agrees with the primary galactic cosmic ray flux for energies above 4 GeV only if the LAHET predictions are divided by a factor of 2. This reinforces the hypothesis that there is a normalisation problem with the LAHET results. However, the major differences between both models are for protons with energies below 100 MeV. Protons below 1 MeV were not tracked in this version of the LAHET model; but the main difference is in the energy range 1 to 100 MeV where the flux calculated by LAHET is orders of magnitude lower than flux calculated using the CosmicTransmutation model. This is likely due to the de-excitation in LAHET, which seems to produce either no or only very few protons.

The results of the LAHET model have previously been used extensively for the study of cosmogenic nuclides. All tests showed a rather good agreement between the experimental data and the model prediction taking into account the uncertainties, which are often significant The similarities between the

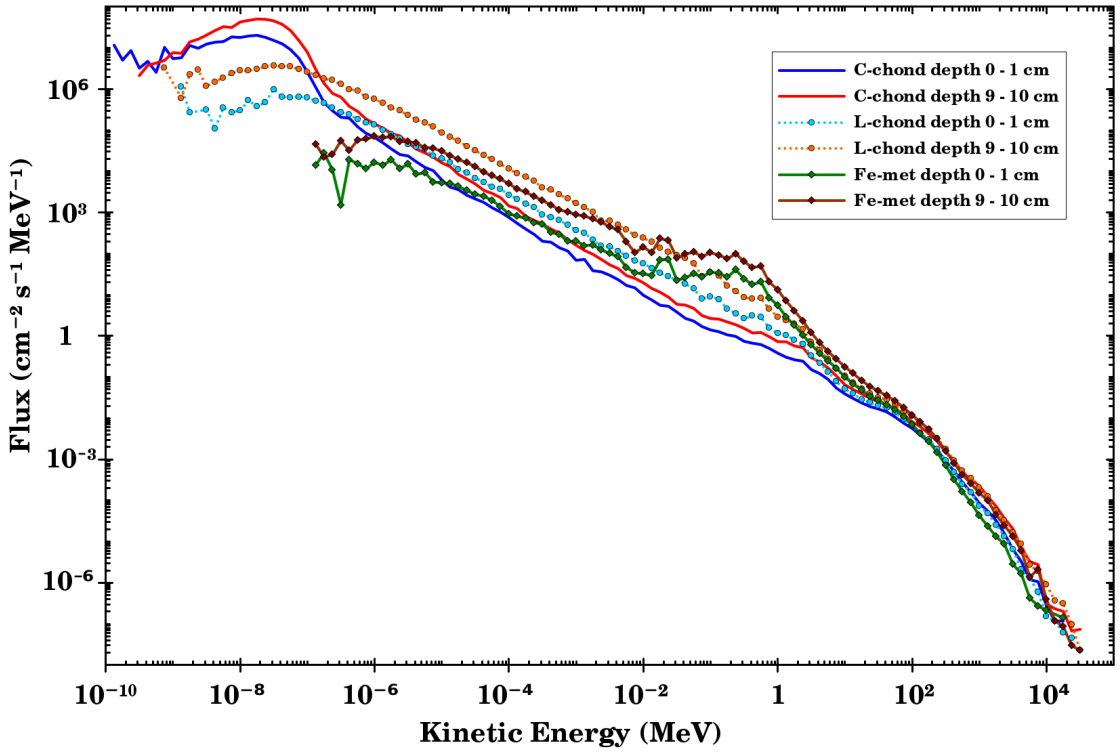

Figure VIII.3: Comparison of the neutron fluxes for different types of meteoroid and at different depth.

CosmicTransmutation and the LAHET model and the fact that the observed discrepancies can easily be explained and are not expected to produce major differences for the production of cosmogenic nuclides indirectly validate the CosmicTransmutation model. For a more profound validation of the model, the predictions of cosmogenic nuclide should be tested against experimental data. However, this is outside the scope of my thesis.

After having at least indirectly validated the model, it is interesting to study the differences of the fluxes calculated for the three major types of meteoroids and for different depths within the meteoroids. Figure VIII.3 depicts the neutron fluxes for C-chondrites, L-chondrites, and iron meteoroids, all with a radius of 50 cm. The fluxes are given for the surface (depth 0 to 1 cm) and for a depth between 9 and 10 cm below the surface.

For energies above 10 MeV, the neutron fluxes at the surface are very similar for the different meteoroid types. The differences of the fluxes between the surface layer and the deeper layer thereby depend on the chemical composition of the irradiated object. In general, the denser the material, the faster is the development of the spallation cascade, which results in an increased flux close to the surface. In the case of iron meteoroid, which is made of 95% iron and 5% nickel in the simulation, the thermal neutrons are easily captured because of the high capture cross sections (2.5 and 4.5 barns respectively [128]). This explains why no neutron is observed below 0.1 eV. The differences between the neutron fluxes in the energy range 1 eV-10 MeV are explained by the combination of the aforementioned statements at the exception of the bump between 100 keV and 1 MeV for the iron meteoroid. This bump is due to the presence of heavy elements like iron and nickel. The coulomb barrier of such elements induces a higher emission of neutrons during the deexcitation phase of the spallation than for light elements because protons cannot easily be emitted. In comparison, the C and L-chondrites contain only 6% and 11% of heavy elements ($Z > 18$) respectively, which explains why the bump is not observed for them.

VIII.2 Planets

The objective of this section is not necessarily to validate the model and to analyse the production of cosmogenic nuclides in atmospheres having different configurations but to analyse the impact of these configurations on the production of cosmogenic nuclides. In a later step, this analysis will be useful to study the propagation of uncertainties in the model and therefore to estimate systematic errors.

Systematic errors are often neglected in simulation models because the more complex a model is the more difficult it is to estimate the systematic errors. However, due to the crucial need of high precision in state-of-the-art sciences, and notably in astrophysics, there is an ever demanding interest in systematic errors of the used models. Studies trying to estimate systematic errors have become more and more common. In the context of this thesis, one can cite the works carried out on INCL [127] and on Geant4 [129]. In such approaches, several variations of the relevant parameters as a function of their respective uncertainties are tested. Then, the variations in the final outputs are compared to the variations of the chosen input. Thus, the sensitivity of the final result on each independent parameter as well as correlations can be studied.

For studies of cosmogenic nuclide production in planetary atmospheres, the most relevant information, but unfortunately with significant uncertainties, is the irradiation spectrum at the top of the atmosphere. Currently, the cosmic ray spectrum is likely the biggest source of systematic uncertainties for such type of model calculations. The cosmic ray spectrum outside the magnetosphere used in the CosmicTransmutation model is fully defined by using the solar modulation parameter M (see eq. VII.1 and eq. VII.3). From this, in the CosmicTransmutation model the irradiation spectrum at the top of the atmosphere is obtained considering the effects induced by the magnetic field applying the cut-off algorithm (with or without the funnel effect). In this section, the impact of the funnel effect, the M parameter, and the magnetic field on nuclide production is studied.

In order to compare the results of the CosmicTransmutation model to results coming from other models, the Earth's geometry has been used. The standard input corresponds to a planet with a radius of 6378 km and an atmosphere 70 km thick (the top of the atmosphere is defined as the altitude where the density is one thousandth to that of the ground level). The standard magnetosphere is defined as a dipole centred in the core of the Earth and that is aligned to the rotational axis of the planet. The magnetic field intensity is 30.2 μT at the top of the atmosphere and at latitude zero. The standard M parameter used is 550 MeV, which is the best average over the last millions years at 1 AU.

It is important to mention that the error bars given in this section are purely statistical errors. They do not take into account the sampling of the irradiation flux, which is limited due to time constraints. The uncertainties due to sampling are estimated to be less than 10%.

VIII.2.1 The funnel effect

The first parameter to be tested is whether considering the funnel effect in the cut-off algorithm or not has any significant influence on the production of cosmogenic nuclides. Figure VIII.4 shows the ^{14}C production rate in the atmosphere as a function of latitude calculated by considering the funnel effect (red line) and calculated without considering the funnel effect (blue line).

The results of the model calculations indicate that the funnel effect indeed has a significant influence on the ^{14}C production rates (see Figure VIII.4). For the latitudes lower than 30°, the production is decreased by approximatively 30%, whereas the rate is increased by a factor 3 when the latitude is higher than 50°. These observations are consistent with the fact that the magnetic field is orthogonal to the normal for the lowest latitudes, which leads to strong deflections, but is parallel to the normal for the highest latitudes, which results in a focusing of particles.

The integration of the ^{14}C productions over all latitudes shows a total increase of around 90% when considering the funnel effect compared to the case without funnel effect. Very similar effects have been

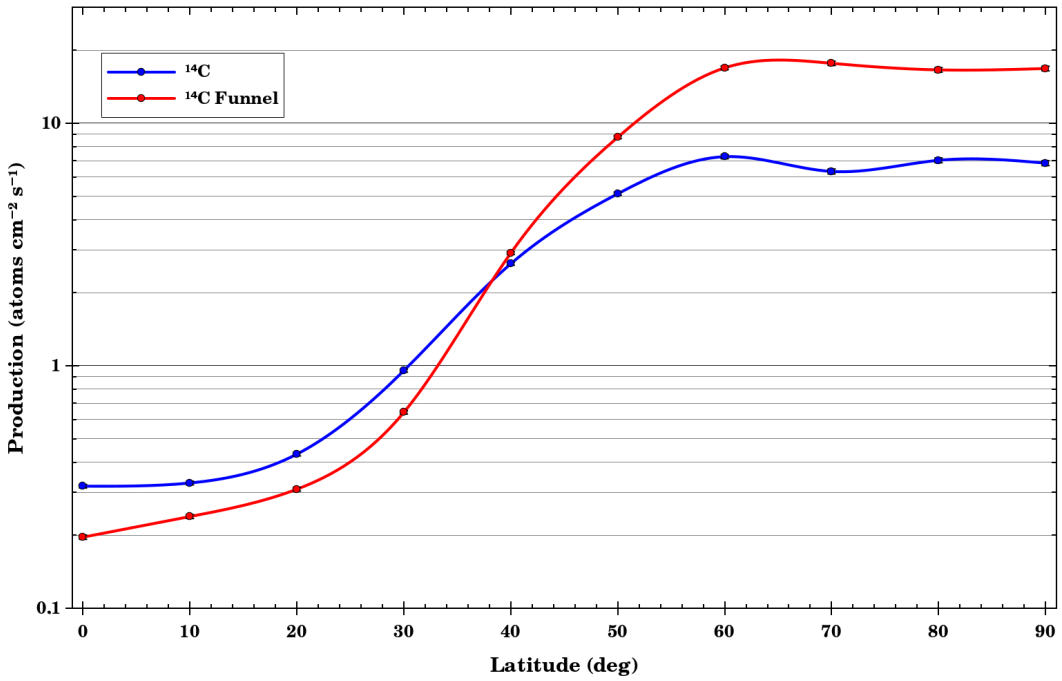

Figure VIII.4: ^{14}C production rate in the atmosphere as a function of latitude. Red: calculated by considering the funnel effect. Blue: without considering the funnel effect.

calculated for other cosmogenic nuclides. This clearly demonstrates that the funnel effect is crucial for the study of cosmogenic nuclide production in the atmosphere.

VIII.2.2 The solar modulation parameter

One of the major parameter influencing cosmogenic nuclide production is caused by the variation of the solar activity. Basically, during phases of high solar activity the strength of the solar magnetic field increases. The solar magnetosphere acts like a magnetosphere of a planet (see sect. VII.4) with a rejection of low energetic particles. The so-called solar modulation parameter M varies between 300 MeV (low solar activity, high particle flux) and 1100 MeV (high activity, low particle flux) [119–122]. The best average for the solar modulation parameter over the last few million years is $M = 550$ MeV at 1 au [123, 124].

Figure VIII.5 shows the ^{14}C production rate in the atmosphere calculated using the CosmicTransmutation model as a function of latitude for different solar modulation parameters; $M = 400$, 550 (standard), and 1000 MeV. In comparison, Figure VIII.6 shows the production rate calculated by Masarik and Beer [130] using a modified version of the LAHET code. A major difference between the two models is that in the model by Masarik and Beer only protons are considered as primary galactic cosmic ray particles, whereas primary galactic cosmic ray alpha particles are also considered in the CosmicTransmutation model.

A comparison between the model by Masarik and Beer and the CosmicTransmutation model without funnel effect indicates that the two models predict very similar production rates. For latitudes higher than 45°, the shapes are similar (the slight oscillation seen in the results of the CosmicTransmutation model are likely due to sampling of the irradiation flux, there is no physical meaning), but the production rate given by the CosmicTransmutation model is 30% higher than the data given by Masarik and Beer. This difference can be explained by the fact that we also consider alpha particles, which represent 10% of the total flux but have a larger impact per incoming particle. For latitudes below 30°, the model by Masarik and Beer predicts an almost constant ^{14}C production rate of about 1 $atom\ cm^{-2}\ s^{-1}$, whereas the CosmicTransmutation model predicts a continuous decrease down to 0.3 $atom\ cm^{-2}\ s^{-1}$. Currently, I

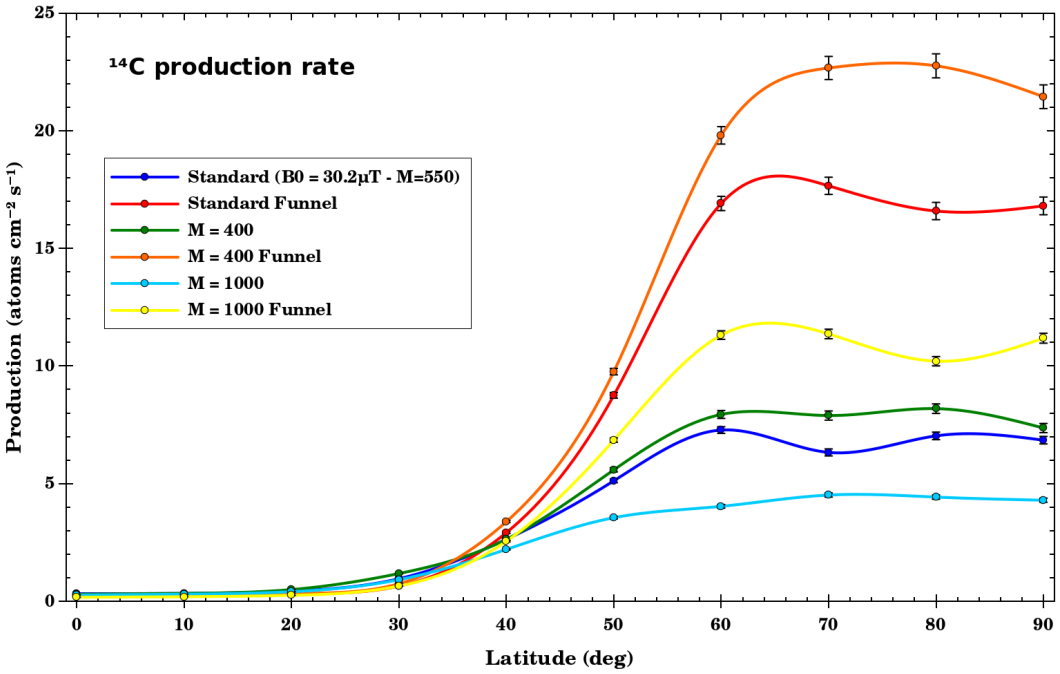

Figure VIII.5: ^{14}C production rate in atmosphere as a function of latitude for different solar modulation parameters and with or without the consideration the funnel effect.

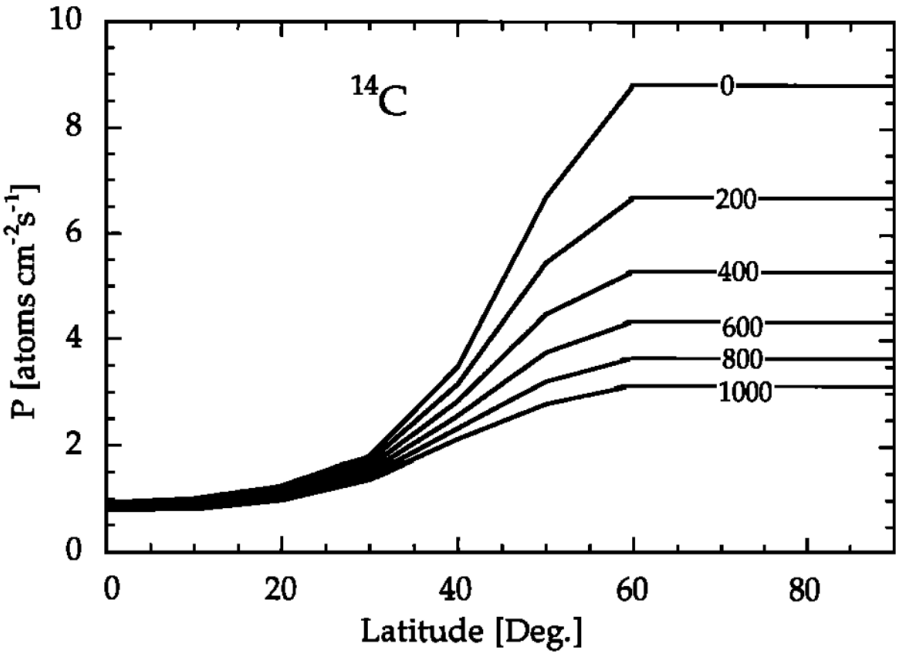

Figure VIII.6: ^{14}C production rate in atmosphere as a function of latitude for different solar modulation parameters as calculated by Masarik and Beer [130].

have no explanation for this discrepancy. The differences between the irradiation flux calculated and used by the CosmicTransmutation model between 0° latitude and 30° latitude indicate a significantly higher primary flux at the top of the atmosphere at 30°, which naturally ends in higher production rates (as seen in Figure VIII.5 but not in Figure VIII.6, see also Appendix G). The ^{14}C production rate is increased by 40% with the CosmicTransmutation model without the funnel effect with respect to the model by Masarik and Beer at high latitude. This is easily explained with the consideration of α particles in the primary

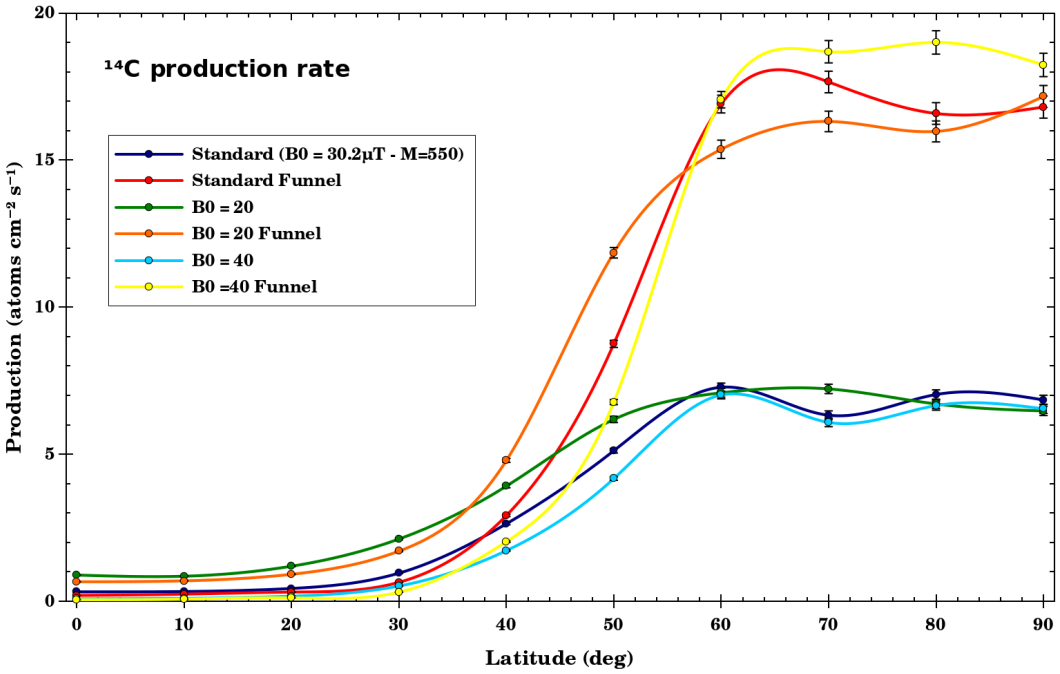

Figure VIII.7: ^{14}C production rate in the atmosphere as a function of latitude, for different magnetic field values and with or without considering the funnel effect.

galactic cosmic ray flux.

A comparison between the simulations considering the funnel effect with those not considering funnelling indicate some very interesting results. The increase in the production rates at the highest latitudes is more pronounced for a low solar modulation parameter (400 MeV) than for higher solar modulation parameters. For this special example, the production rate calculated using M = 400 and considering funnelling is a factor of 2.8 higher than for the case without funnelling. At higher solar modulation parameters, the difference is a factor of 2.4. On the other hand, the variations in the calculated production rates obtained with and without considering the funnel effect is almost independent on the solar modulation parameter.

VIII.2.3 The magnetic field

Considering the relatively simple possible magnetic field configurations implemented in the Cosmic-Transmutation model, only the impact of two parameters is studied here. First, the intensity of the magnetic field (B_0) and the shift of the magnetic field relative to the geometric center of the planet.

Figure VIII.7 shows the ^{14}C production rate as a function of latitudes for different intensities of the solar magnetic field. The tests were performed with magnetic field values of 20, 30.2 (standard value), and 40 μT at the top of the atmosphere at 0°.

The results for the ^{14}C production rates without funnel effect shown in Figure VIII.7 indicate that the changes in the magnetic field intensity has no relevant effect for latitudes larger than about 60°. In contrast, for latitudes lower than 50°, there is a significant dependence of the modelled ^{14}C production rates on the strength of the magnetic field. To be more quantitative, for a B_0 value of 20 μT the production rates is on average 30% lower than the production rate calculated by assuming $B_0 = 30.2$ μT. On the other hand, by assuming $B_0 = 40$ μT we calculate ^{14}C production rates about 20% lower than the ones calculated using $B_0 = 30.2$ μT.

Interestingly, the funnel effect significantly changes the results, *i.e.*, the dependence of the production

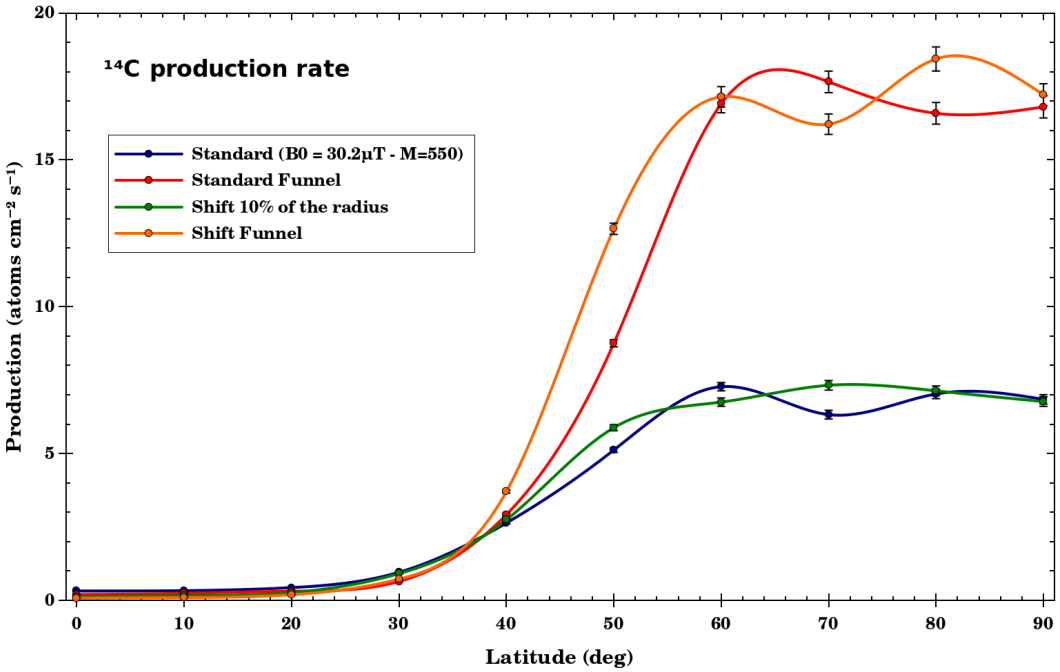

Figure VIII.8: ^{14}C production rate in the atmosphere as a function of latitude, for different magnetic field locations and with or without considering the funnel effect.

rates on the magnetic field values. While the ^{14}C production rate for latitudes lower than 50° is lowered with increasing magnetic field like without the funnel effect, at high latitudes the ^{14}C production rate is higher for high magnetic field values.

This suggests that the higher intensity of the magnetic field increases the focusing of cosmic rays in the polar regions. The differences in the ^{14}C production rates due to the variations in the magnetic field values are significant, *i.e.*, 15% higher for $B_0 = 20\ \mu T$ than for $B_0 = 30.2\ \mu T$ or 5% lower for $B_0 = 40\ \mu T$, but they are smaller than the effects introduced by the funnel effect. This is due to the increased focusing at high latitudes, which is in competition with the higher rejection of incoming cosmic rays for low latitudes.

The last studied parameter is the shift of the magnetic field with respect to the center of the planet. In Figure VIII.8 I compare the results obtained using the standard set-up to results from a calculation done by assuming a magnetic field offset by 10% of the planet radius in direction of longitude-latitude 0° - 0°. No significant differences are observable at low ($< 30°$) and high ($> 60°$) latitudes. However, at intermediate latitudes the ^{14}C production rate is slightly increased relative to the standard model.

VIII.2.4 Isotope ratio

I also tested the influence of the funnel effect on other observables than the ^{14}C production rate. Here I exemplarily focus on some isotope rates, which are very often crucial for dating systems. For example, in our group two main dating techniques based on isotope ratios are commonly in use: the ratio $^{40}K/K$ for iron meteorites and the $^{10}Be/^{14}C$ ratio for stony meteorites. Here the argument is as follows, the funnel effect does not only modify the overall irradiation flux but it also gives preference to specific rigidities and thus, it can also increase or decrease specific production rates depending on the relevant rigidity.

Figures VIII.9 and VIII.10 show $^{10}Be/^{14}C$ and $^{7}Be/^{3}H$ production rate ratios as a function of latitude, respectively. For the isotope ratio $^{10}Be/^{14}C$ no significant modification of the ratio as a function of latitude can be seen. For the ratio $^{7}Be/^{3}H$ there is a dependence on latitude, which is due to the fact that the production processes of the two isotopes are different. For example, ^{3}H can easily be produced as a cluster during spallation reactions. Interestingly, for both isotope ratios there is no dependence on whether or

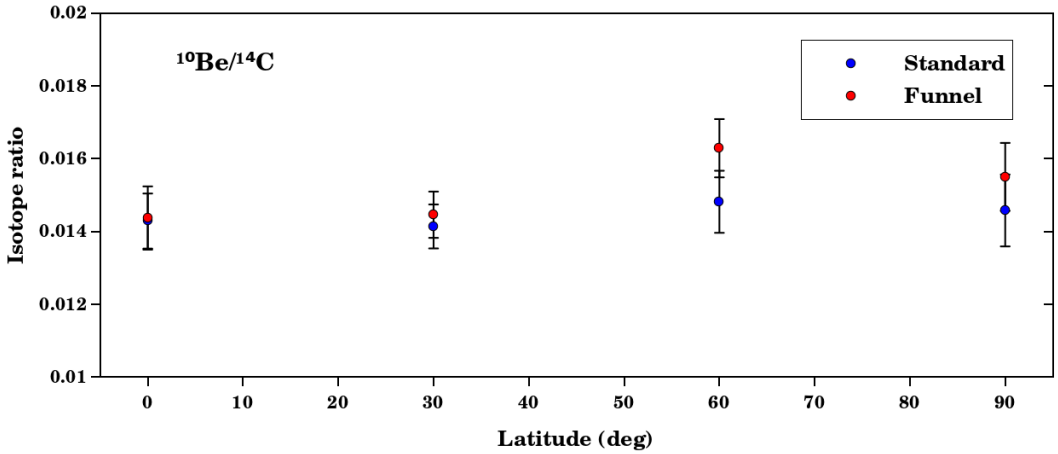

Figure VIII.9: $^{10}Be/^{14}C$ production ratio in the atmosphere as a function of latitude calculated with (blue dots) and without (red dots) considering the funnel effect.

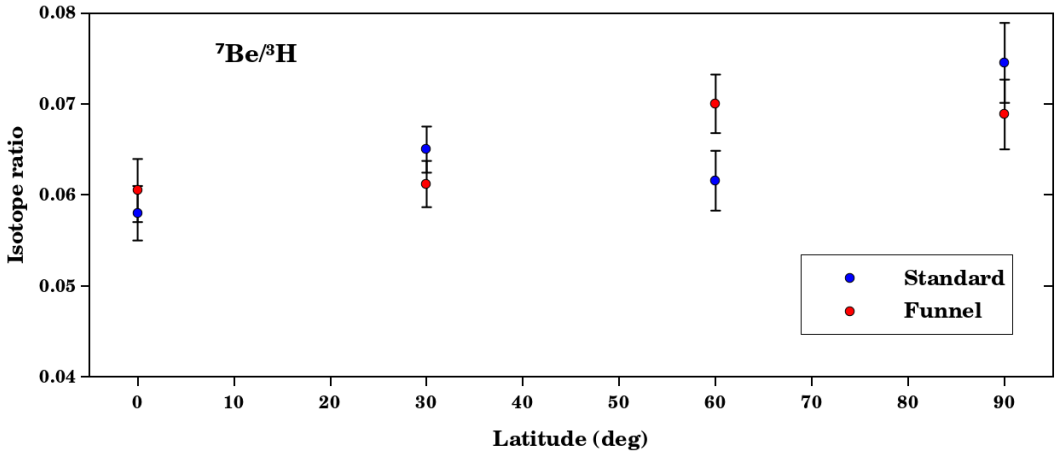

Figure VIII.10: $^{7}Be/^{3}H$ production ratio in the atmosphere as a function of latitude calculated with (blue dots) and without (red dots) considering the funnel effect.

not the funnel effect is considered. Due to computational time, not all isotopes typically used in dating techniques could be studied. In particular, isotopes with $A > 20$ produced in spallation reactions on argon, which represent less than 1% of the entire atmosphere, are left for future studies.

Chapter IX

Conclusion

Cosmogenic nuclides are a wonderful tool to study the dynamics of small bodies in the solar system and of the temporal history of galactic cosmic rays themself. More than 80 years after their discovery, cosmogenic nuclides are still of major interest for many scientific applications. This research field is in constant progress and new applications appear regularly. However, using the production of cosmogenic nuclides as a tool requires a profound understanding of astrophysics, nuclear physics, and high energy physics. This interdisciplinarity is a real challenge for all scientists working in this field.

The first part of my PhD has been the successful implementation of strange particles into the INCL model, which is used to simulate nuclear spallation reactions. Doing so, I provided a comprehensive and consistent description of all relevant elementary reactions involving strangeness production, scattering, and absorption for cases when a light particle hits a nucleus. Here I focused on energies below 15 GeV in order to fit the energy range relevant for cosmogenic nuclide production. This work was motivated by the need to improve the high energy parts (beyond 2-3 GeV) of the models usually used for calculating cosmogenic nuclide production. In addition, this study provided also the opportunity for the INCL collaboration to contribute to hypernucleus studies. My work included the parametrisation of reaction cross sections, charge repartition, and phase space generation. These parametrisations has been based on experimental measurements, whenever available, in order to be as model independent as possible. Unfortunately, less than 20% of the information needed for the reaction cross sections can be obtained directly in this way. Therefore hypotheses and models were used to complete the parametrisation. The isospin symmetry allowed to parametrise a large number of cross sections by linking known and unknown cross sections. This procedure has been applied in two different ways, either by taking into account only the initial and final states (with the so-called Bystricky procedure) or by considering the isospin symmetry at each vertex of the Feynman diagrams used in a hadron exchange model. Even after this extended procedure, still roughly one third of the cross sections needed additional information for a full characterisation. In a few cases where experimental data are rare, it was necessary to use similarities, *e.g.*, in the cross section ratios when one pion is added. Finally, two reaction types are entirely based on modelling, *i.e.*, without using any experimental data at all: reactions with numerous particles in the final state (with increasing energy) and Δ-induced reactions.

For quality control, I compared the developed parametrisation for the cross sections to experimental data as well as to parametrisations used in other models. My results reproduce reasonably well the measurements, but assessing the quality of my cross section parametrisations for reactions and in energy ranges where no experimental data exist is still a problem. Comparing the parametrisations done by me to parametrisation used in other models indicates large differences for reactions and/or energy range where no experimental data exist. A prominent example are the Δ-induced reactions for which no measurements exist and my parametrisation relies on a theoretical model stating that those channels significantly contribute to kaon and hyperon production [63].

This set of newly parametrised cross sections, handling strangeness, has been implemented in the INCL

code, which resulted in a new major version: INCL++6. This version was validated. For this purpose, calculations of kaon and hyperon production have been performed and the results have been compared to experimental data. The study of hypernuclei production has been performed by one of my collaborator, Jose-Luis Rodríguez-Sánchez, and resulted in a paper to be published.

For the validation of INCL++6, different projectiles (proton, deuteron, and pion) were tested at various kinetic energies: from 1.6 to 13.7 GeV for protons, 1.02 GeV for pions, and 2.1 GeV/nucleon for deuterons. Various targets ranging from ^{9}Be to ^{208}Pb were considered and a wide range of angles was covered. For most of the studied cases there is a good agreement between experimental data and INCL++6 predictions. Notably, the dependence of the experimental data on either energy or target mass number is often well reproduced, which demonstrates that the physics of strangeness has been sucessfully implemented. However, slight discrepancies still exist. In some cases experimental data are overestimated. Different explanations were proposed in oder to understand these discrepancies but the lack of experimental data prevents definitive conclusions. The dominant problem is likely in the Δ-induced reactions. Implementing Δ-induced reactions significantly improved the description of strangeness production. However, the cross sections used are probably overestimated at high energies, which is consistent with the conclusions in ref. [63].

During validating the INCL results, and more generally with the simulation of strangeness production, the problem of statistics and computational time arose. This problem has been solved with the implementation of a variance reduction scheme in INCL. The developed method increases the strangeness production artificially by respecting some mathematical constraints, which results in an increased statistical relevance for observables linked to the physics of strangeness, and therefore, to a significant reduction of the required calculation time. This variance reduction scheme does not only solve the problem of computation time associated to strangeness production but can also be adapted to simulations of any rare process (*e.g.*, the production of backward η meson production). The gain in computational time depends on the process studied but, to simplify, the rarer the process the more efficient is the developed scheme. This enables the possibility to simulate extremely rare cases like neutrino-nucleus interactions, which have interaction cross sections of the order of 10^{-16} mb for the energies considered.

In addition, INCL++6 has been implemented into the transport code Geant4 [10, 59]. Thus, it can be used in the simulation of macroscopic systems. This also permits other collaborations to have a full access to the latest version of the model. They can use it for the design of new experiments dedicated to the study of strange particles and/or hypernuclei in the near future, such as for the HypHI [60], Panda [61], and CBM [62] experiments at the FAIR facility.

The second part of my PhD started with the development of the CosmicTransmutation model. This model has been created from scratch. Its objective is to calculate the differential fluxes of light particles, *i.e.*, protons, neutrons, alphas, together with the production of cosmogenic nuclides in objects exposed to cosmic rays. The programming was challenging for three reasons. First, the model has been created in such a way it can easily be used by other members of the group. Therefore, major efforts have been made to create a user friendly program, which does not require a specific knowledge of the physics involved. The second challenge was the interdisciplinarity of the research area. The development of the model required a profound knowledge in nuclear physics, high energy physics, and astrophysics. Many of the aspects presented in this thesis were new for me when I started this PhD. The last challenge was the creativity needed to solve the problems faced. In comparison, the work done for the implementation of strange particles in INCL was much more guided. For example, the steps were well defined and the methods used to determine the missing cross sections were simple adaptations or extensions of already existing methods. The most original work carried out in the development of INCL is the implementation of the variance reduction scheme. In contrast, for the development of the CosmicTransmutation model, no such guideline existed. Most of the models developed in the same field are not open source and/or focus on very specific targets. Luckily I had access to the PlanetoCosmic model [126], which guided me for the creation of an algorithm for planet irradiation (namely, the cut-off algorithm). However, I had to develop many other algorithms in order to produce the observables required, anticipate future needs, simulate specific physical

process, or simply optimise the computational time. The large range of possible applications leaves some space for future improvements of the CosmicTransmutation model.

The validation of the CosmicTransmutation model was also more complex than the validation of INCL++6. Direct comparisons with experimental data were impossible or irrelevant. Therefore, the CosmicTransmutation model has been compared to other models. The comparisons showed similarities but also differencies, which have been studied. The results of the CosmicTransmutation model applied to meteoroids are compatible with previous results obtained using the LAHET model [23]. However, there is a systematic difference of a factor of 2, which can be explained by differences in the normalisation. Some of the differences observed between the model are due to the additional features added to the CosmicTransmutation model. In the case of cosmogenic nuclide production in atmospheres, the impact of the input parameters on the outcome of the simulation has been investigated in order to study the sensitivity of the results on the initial conditions. This in turn allows to estimate systematic errors of the CosmicTransmutation model. Most of the studied parameters have a significant impact on the production of cosmogenic nuclides in planetary atmospheres. A comparison of the new results with predictions from the model by Masarik and Beer shows a good agreement between both approaches. The problem of the funnel effect and its major impact has been analysed in some detail. In addition, the significant dependence of the results on the magnetic field characteristics shows that a reliable description of the magnetic field is crucial to analyse cosmogenic nuclide production. The variability of the magnetosphere of the Earth is mainly caused by the variations of the solar activity, the solar magnetosphere, and the orientation of the Earth's magnetic field relative to the solar magnetic field. All such variations can result in significant modifications of the incoming cosmic ray particle spectrum and therefore of the production of cosmogenic nuclides. The consideration of the funnel effect raises a problem linked to cosmic ray flux measurements. To be more precise, galactic cosmic ray flux measurements inside the Earth's magnetosphere can be biased or even wrong if the funnel effect is not taken into account. For example, the BESS-Polar collaboration [4, 5] measured the cosmic-ray spectrum over Antarctica where the cut-off algorithm predicts a high focussing of cosmic ray particles.

Based on the results of the CosmicTransmutation model it is hard to conclude if and how all the different input parameters affect cosmogenic nuclide production in the atmosphere because the model used for the magnetosphere is relatively simple. However, the model clearly indicates that there is a need to rethink the production of cosmogenic nuclides in atmospheres with a better consideration of magnetic field effects.

To conclude, the development of the nuclear reaction codes has been carried out with the goal to estimate cosmogenic nuclide production in meteoroids and planetary atmospheres. This goal has been successfully finished. However, both the development of the INCL model and the CosmicTransmutation model indicates that the field of application for both models is much wider than cosmogenic nuclide production alone. The INCL model was already used in a wide range of applications and the modifications I applied improved the quality of the model. In addition, my work also opened new possibilities to study the physics of strangeness and other rare processes like hypernuclei and the far subthreshold kaon production. The CosmicTransmutation model has been designed from scratch to study cosmogenic nuclides production in meteoroids and atmospheres. The comparisons with other theoretical calculations showed that the model is able to produce consistent results, which can be used for the analysis of experimental data. However, the developed model can also be used to study the propagation of cosmic rays in magnetospheres. Finally, the work carried out in this thesis represents a new step forward for studies of nuclear spallation, cosmic rays, and cosmogenic nuclides.

Bibliography

[1] A. V. Grosse. *"An Unknown Radioactivity"*. J. Am. Chem. Soc. 56, 9 (1934)

[2] V.F. Hess. Physikalische Zeitschrschift 13, 1084 (1912).

[3] Glenn T. Seaborg, *"The interaction of fast neutrons with lead"*. 1937

[4] BESS-Polar Collaboration. *"Measurements of Cosmic-Ray Proton and Helium Spectra from the BESS-Polar Long-Duration Balloon Flights over Antarctica"* Astrophys. J. 822, 65 (2016)

[5] BESS-Polar Collaboration. *"Measurement of the Cosmic-Ray Antiproton Spectrum at Solar Minimumwith a Long-Duration Balloon Flight over Antarctica"* Phys. Rev. Lett. 108, 051102 (2012)

[6] AMS collaboration. *"Electron and Positron Fluxes in Primary Cosmic Rays Measured with the Alpha Magnetic Spectrometer on the International Space Station"* Phys. Rev. Lett. 113, 121102 (2014)

[7] R. Serber. *"Nuclear Reactions at High Energies"*. Phys. Rev. 72, 1114 (1947)

[8] W. Libby. *"Atmospheric Helium Three and Radiocarbon from Cosmic Radiation* Phys. Rev. 69, 671 (1946)

[9] J-.C. David and I. Leya. *"Spallation, cosmicRays, meteorites, and planetology"*. to be published (2019)

[10] Geant4 Collaboration. *"Geant4 - a simulation toolkit"*. NIM A 506, 250 (2003)

[11] J.Cugnon, T.Mizutani, and J.Vandermeulen. *"Equilibration in relativistic nuclear collisions. A Monte Carlo calculation"*. Nucl. Phys. A 352, 505 (1981)

[12] J.Cugnon, D.Kinet, and J.Vandermeulen. *"Pion production in central high energy nuclear collisions"*. Nucl. Phys. A 379, 553 (1982)

[13] J. Cugnon and J. Vandermeulen. *"Transfer of energy following on nuclei"*. Nucl. Phys. A 445, 717 (1985)

[14] J. Cugnon. *"Proton-nucleus interaction at high energy"*. Nucl. Phys. A 462, 751 (1987)

[15] J. Cugnon and M.-C.Lemaire. *"Medium effects in pion production"*. Nucl. Phys. A 489, 781 (1988)

[16] J. Cugnon, P. Deneye, and J. Vandermeulen. *"Strangeness production in antiproton annihilation on nuclei"*. Phys. Rev. C 41, 1701 (1990)

[17] J. Cugnon, D. L'Hôte, and J. Vandermeulen. *"Simple parametrization of cross-sections for nuclear transport studies up to the GeV range"*. NIM B 111, 215 (1996)

[18] J. Cugnon, C. Volant, and S. Vuillier. *"Improved intranuclear cascade model for nucleon-nucleus interactions"*. Nucl. Phys. A 620, 475 (1997)

[19] J. Cugnon, C. Volant, and S. Vuillier. *"Nucleon and deuteron-induced spallation reactions"*. Nucl. Phys. A 625, 729 (1997)

[20] J. Cugnon et al. *"New constraints on the Δ production cross section"*. Phys. Rev. C 56, 2431 (1997)

[21] J. Cugnon and P. Henriotte. *"The Liège Intranuclear Cascade Model"*. Proceedings of the Fifth Workshop on Simulating Accelerator Radiation Environments (SARE-5) (2000)

[22] A. Boudard, J. Cugnon, S. Leray, and C. Volant. *"Intranuclear cascade model for a comprehensive description of spallation reaction data"*. Phys. Rev. C 66, 044615 (2002)

[23] R. Prael and H. Lichtenstein. *"User Guide to LCS: The LAHET Code System"* LA-UR-89-3014, (1989)

[24] Y. Yariv and Z. Fraenkel. *"Intranuclear cascade calculation of high-energy heavy-ion interactions."* Phys. Rev. C 20(6), 2227 (1979)

[25] S. Leray et al. J. Korean Phys. Soc. 59 791-796 (2011) IAEA Benchmark of Spallation Models

[26] A. Kelić, M. V. Ricciardi, and K.-H. Schmidt. *"Proceedings of Joint ICTP-IAEA Advanced Workshop on Model Codes for Spallation Reactions, ICTP Trieste, Italy, 4-8 February 2008"*, edited by D. Filges, S. Leray, Y. Yariv, A. Mengoni, A. Stanculescu, and G. Mank (IAEA, Vienna, 2008), pp. 181-221.

[27] J. Cugnon and P. Henrotte. *"The low-energy limit of validity of the intranuclear cascade model"*. Eur. Phys. J. A 16, 393 (2003)

[28] S. Pedoux, J. Cugnon, et al. *"Extension of INCL4 between 2 and 15 GeV"*. Advances in Space Research 44, 926 (2009)

[29] C. Villagrasa-Canton et al. *"Spallation residues in the reaction* $^{56}Fe + p$ *at* $0.3A$*,* $0.5A$*,* $0.75A$*,* $1.0A$*, and* $1.5A$ *GeV"* Phys. Rev. C 75, 044603 (2007)

[30] P. Napolitani et al. *"High-resolution velocity measurements on fully identified light nuclides produced in* ^{56}Fe*+hydrogen and* ^{56}Fe*+titanium systems"* Phys. Rev. C 70, 054607 (2004)

[31] L. Audouin et al. *"Evaporation residues produced in spallation of* ^{208}Pb *by protons at 500 A MeV"* Nucl. Phys. A 768, 1 (2006)

[32] T. Enqvist et al. *"Isotopic yields and kinetic energies of primary residues in 1 A GeV* ^{208}Pb *reactions"* Nucl. Phys. A 686, 481 (2001)

[33] J. Taïeb et al. *"Evaporation residues produced in the spallation reaction* $^{238}U + p$ *at 1 A GeV"* Nucl. Phys. A 724, 413 (2003)

[34] M. Bernas et al. *"Fission-residues produced in the spallation reaction* $^{238}U + p$ *at 1 A GeV"* Nucl. Phys. A 725, 213 (2003)

[35] M.V. Ricciardi et al. *"Light nuclides produced in the proton-induced spallation of* ^{238}U *at 1 GeV"* Phys. Rev. C 73, 014607 (2006)

[36] M. Bernas et al. *"Very heavy fission fragments produced in the spallation reaction* $^{238}U + p$ *at 1 A GeV"* Nucl. Phys. A 765, 197 (2006)

[37] P. Kaitaniemi, A. Boudard, S. Leray, J. Cugnon, D. Mancusi. *"INCL Intra-nuclear Cascade and ABLA De-excitation Models in Geant4"*. Progress in Nucl. Sci. Tech. 2, 788 (2011)

[38] A. Boudard, J. Cugnon, J.-C. David, S. Leray, and D. Mancusi. *"New potentialities of the Liège intranuclear cascade model for reactions induced by nucleons and light charged particles"*. Phys. Rev. C 87, 014606 (2013)

[39] D. Mancusi et al. *"Extension of the Liège intranuclear-cascade model to reactions induced by light nuclei"*. Phys. Rev. C 90, 054602 (2014)

[40] D. Mancusi et al. *"Improving the description of proton-induced one-nucleon removal in intranuclear-cascade models"* Phys. Rev. C 91 034602 (2015)

[41] J.-L. Rodríguez-Sánchez et al. *"Improvement of one-nucleon removal and total reaction cross sections in the Liège intranuclear-cascade model using Hartree-Fock-Bogoliubov calculations"* Phys. Rev. C 96 054602 (2017)

[42] J.-C. David et al. *"*η *and* ω *mesons as new degrees of freedom in the intranuclear cascade model INCL"* Eur. Phys. J. Plus 133, 253 (2018)

[43] J. Hirtz, J-.C. David, et al. *"Strangeness production in the new version of the Liège Intra-Nuclear Cascade model"* arXiv:1909.02246 [nucl-th]

[44] J. Hirtz, J.-C. David, et al. *"Parametrization of cross sections for elementary hadronic collisions involving strange particles"*. Eur. Phys. J. Plus 133, 436 (2018)

[45] J.-C. David et al. Memorie della Società Astronomica Italiana 82, 909 (2011) and references therein

[46] H. Weber et al. *"Excitation function of energy density and partonic degrees of freedom in relativistic heavy ion collisions"* Phys. Let. B 442, 443 (1998)

[47] H. D. Vries, C. W. D. Jager, and C. D. Vries. *"Nuclear charger-density-distribution parameters from elastic electron scattering"* At. Data Nucl. Data Tables 36, 495 (1987)

[48] M. Tanabashi et al. *"Particle Data Group"*. Phys. Rev. D 98, 030001 (2018)

[49] G. Gamow. *"Quantum Theory of the Atomic Nucleus"* Z. Phys. 51, 204 (1928)

[50] J.-L. Rodríguez-Sánchez et al. to be published

[51] O. Buss et al. *"Transport-theoretical description of nuclear reactions"* Physics Reports 512 1–124 (2012)

[52] G. Agakishiev et al. (HADES Collaboration). *"Medium effects in proton-induced K^0 production at 3.5 GeV"* Phys. Rev. C 90, 054906 (2014)

[53] Y. Nara et al. *"Relativistic nuclear collisions at 10A GeV energies from p+Be to Au+Au with the hadronic cascade model"* Phys. Rev. C61 (1999) 024901, arXiv:nucl-th/9904059 [nucl-th] (1999)

[54] N.V. Mokhov, K.K. Gudima, and S.I. Striganov. *"Hadron Production Model Developments and Benchmarking in the 0.7 - 12 GeV Energy Region"*. arXiv:1409.1086 [nucl-ex]

[55] Pierre Deneye. PhD thesis, University of Liège, 1991

[56] D.H. Wright, M.H. Kelsey. *"The Geant4 Bertini Cascade"* Nuclear Instruments and Methods in Physics Research A804 175-188 (2015)

[57] B. Andersson et al. *"Parton fragmentation and string dynamics"* Phys. Rep. 97, 31-145 (1983)

[58] V. Uzhinsky. *"Development of the Fritiof Model in Geant4"* (SNA + MC2010) Hitotsubashi Memorial Hall, Tokyo, Japan, October 17-21, 2010

[59] Geant4 Collaboration. *"Physics Reference Manual - Release 10.5"*. Geant4 Physics Reference Manual Release 10.5

[60] T. Saito et al. *"The HypHI project at GSI and FAIR."* Proceedings of the IX International Conference on Hypernuclear and Strange Particle Physics. Springer, Berlin, Heidelberg (2007)

[61] J. Messchendorp. *"The PANDA Experiment at FAIR - Subatomic Physics with Antiprotons"* arXiv:1610.02804 [nucl-ex]

[62] V. Friese. *"The CBM Experiment at FAIR"* Proceedings of Science 47 (2008))

[63] K. Tsushima, A. Sibirtsev, A. W. Thomas, and G. Q. Li. *"Resonance model study of kaon production in baryon-baryon reactions for heavy-ion collisions"* Phys. Rev. C59, 369, Erratum: Phys. Rev. C61, 029903 (2000).

[64] A. Baldini et al. Landolt-Börnstein Numerical Data and Functional Relationships in Science and Technology. (Springer-Verlag, Berlin, 1988), Vol. 12 a and b.

[65] J. L. Rodríguez-Sánchez, J.-C. David, J. Hirtz, et al. *"Constraining the Λ-nucleus potential within the Liège intranuclear cascade model"* Phys. Rev. C 98, 021602(R) (2018)

[66] V. Metag, M. Nanova and E.Ya. Paryev. *"Meson-nucleus potentials and the search for meson-nucleus bound states"*. Prog. Part. Nucl. Phys. 97, 199-260 (2017).

[67] Th. A. Rijken and H.-J. Schulze. *"Hyperon-hyperon interactions with the Nijmegen ESC08 model"*. Eur. Phys. J. A 52, 21 (2016).

[68] HIRES Collaboration. *"Cross sections of the $pp \to K^+\Sigma^+n$ reaction close to threshold"* Physics Letters B692 10-14 (2010)

[69] A. Sibirtsev and al. *"The $pp \to K^+\Sigma^+n$ cross-section from missing-mass spectra"* Eur. Phys. J. A32, 229 (2007)

[70] C. Gini, (1912). *"Variabilità e mutabilità"* C. Cuppini, Bologna, 156 pages.

[71] J. Bystricky, P. La France, F. Lehar, F. Perrot, T. Siemiarczuk, and P. Winternitz. *"Energy dependence of nucleon-nucleon inelastic total cross-sections"*. Journal de Physique, 1987, 48(11), pp.1901-1924. <10.1051/jphys:0198700480110190100>

[72] S. Pedoux and J. Cugnon. *"Extension of the Liège intranuclear cascade model at incident energies between 2 and 12 GeV. Aspects of pion production"* Nucl. Phys. A866 16-36 (2011)

[73] G.Q. Li and C.M. Ko. *"Kaon production cross sections from baryon-baryon interactions"* Nucl. Phys. A594 439-459 (1995)

[74] A. Sibirtsev, W. Cassing, and C.M. Ko. *"Antikaon production in nucleon- nucleon reactions near threshold"* Z Phys A - Particles and Fields (1997) 358: 101

[75] A.S. Iljinov, et al. *"Extension of the intranuclear cascade model for photonuclear reactions at energies up to 10 GeV"* Nucl. Phys. A616 575 (1997)

[76] G.I. Kopylov. *"A model for the process of multiple production"* translation Soviet Physics JETP 8, 996 (1959)

[77] F. James. *"Monte Carlo phase space"* CERN 68-15 (1968)

[78] C. Daum et al. *"Elastic scattering of negative kaons on polarized protons between 1.4 and 2.4 GeV/c"* Nucl. Phys. B6 273-324 (1968)

[79] S. Andersson-Almehed et al. *"Polarization in elastic K^-p scattering at six momenta between 982 MeV/c and 1732 MeV/c"* Nucl. Phys. B21 515-527 (1970)

[80] J. Griselin et al. *"K^-p cross sections between 1.1 and 1.4 GeV/c"* Nucl. Phys. B93 189-216 (1975)

[81] C.J. Adams et al. *"Measurement of K^-p elastic differential cross sections between 610 and 943 MeV/c"* Nucl. Phys. B96 54-66 (1975)

[82] K. Abe et al. *"Differential cross sections for K^-p elastic scattering from 1.4 to 1.9 GeV/c"* Phys. Rev. D 12, 6 (1975)

[83] B. Conforto et al. *"An improved partial wave analysis of $KN \to KN$ from 800 to 1200 MeV/c"* Nucl. Phys. B34 41-70 (1971)

[84] Terry S. Mast et al. *"Elastic, charge-exchange, and total K^-p cross sections in the momentum range 220 to 470 MeV/c"* Phys. Rev. D14, 13 (1976)

[85] R. Armenteros et al. *"K^-p cross sections from 440 to 800 MeV/c"* Nucl. Phys. B21 15-76 (1970)

[86] B. Conforto et al. *"K^-p reactions from 0.960 to 1.355 GeV/c involving two-body final states"* Nucl. Phys. B105 189-221 (1976)

[87] M. Jones, R. Levi Setti and D. Merrill. *"K^-p charge exchange and hyperon production cross sections from 860 to 1000 MeV/c"* Nucl. Phys. B90 349-383 (1975)

[88] M. Alston-Garnjost et al. *"Differential cross section of the reaction $K^-p \to \overline{K}^0 n$ from 515 to 956 MeV/c"* Phys. Rev. D17, 2226 (1978)

[89] G.W. London et al. *"Study of the reactions $K^-p \to \Lambda^0$ + neutrals in the C.M. energy range from 1580 to 1750 MeV"* Nucl. Phys. B85 289-310 (1975)

[90] A. Berthon, L.K. Rangan, J. Vrana. *"The reaction $K^-p \to \Lambda\pi^0$ in the c.m. energy range 1915 to 2168 MeV"* Nucl. Phys. B20 476-492 (1970)

[91] A. Berthon, J. Vrana. *"The reactions $K^-p \to \Sigma^\pm\pi^\mp$ in the c.m. energy range 1915 to 2168 MeV"* Nucl. Phys. B24 417-440 (197)

[92] T.M. Knasel et al. *"Experimental study of the reaction $\pi^-p \to \Lambda K^0$ at beam momenta between 930 and 1130 MeV/c"* Phys.Rev.D11, 1 (1975)

[93] R.D. Baker et al. *"The reaction $\pi^-p \to K^0\Lambda^0$ up to 1334 MeV/c"* Nucl. Phys. B141, 29 (1978)

[94] D.H. Saxon et al. *"The reaction $\pi^-p \to K^0\Lambda^0$ up to 2375 MeV/c: New results and analysis"* Nucl. Phys. B162, 522 (1980)

[95] R.D. Baker et al. *"Study of the reaction $\pi^-p \to K^0\Sigma^0$ from threshold up to 1334 MeV/c"* Nucl. Phys. B145 402-408 (1978)

[96] J.C. Hart et al. *"The reaction $\pi^-p \to K^0\Sigma^0$ up to 2375 MeV/c"* Nucl. Phys. B166, 73 (1980)

[97] M. Winik, S. Toaff, D. Revel, J. Goldberg, L. Berny. *"Study of the reaction $\pi^+p \to K^+\Sigma^+$ between 1.721-1.954 GeV c.m. energy"* Nucl. Phys. B128, 66 (1977)

[98] D. Candlin et al. *"Differential cross section and polarisation for $\pi^+p \to K^+\Sigma^+$ at 26 momenta between 1.282 and 2.473 GeV/c"* Nucl. Phys. B226, 1 (1983)

[99] E. Nadaraya. *"On Estimating Regression"* Theory Probab. Appl., 9(1), 141-142 (1963)

[100] C. Reinsch. *"Smoothing by spline functions"* Numerische Mathematik 10, 177 (1967)

[101] T. Sjöstrand, S. Mrenna, and P. Z. Skands. *"PYTHIA 6.4 physics and manual"* JHEP 05, 026 (2006)

[102] B.Andersson, G.Gustafson, G.Ingelman and T.Sjöstrand. *"Parton fragmentation and string dynamics"* Phys. Rep. 97, 31 (1983)

[103] A. Owen. Monte Carlo theory, methods and examples (2013)

[104] W. Scheinast et al. *"In-Medium Effects on Phase Space Distributions of Antikaons Measured in Proton-Nucleus Collisions"*. PRL 96, 072301 (2006)

[105] A.V. Akindinov et al. *"Experimental study of the subthreshold production of K+-mesons in proton-nucleus collisions"*. JETP Letters, Vol. 72, 100 (2000)

[106] Büscher, M., Koptev, V., Nekipelov, M. et al. *"Inclusive K^+-meson production in proton-nucleus interactions"*. Eur. Phys. J. A 22, 301 (2004)

[107] S. Schnetzer, R. M. Lombard et al. *"Inclusive production of K^+ mesons in 2.1-GeV/nucleon nuclear collisions"*. Phys. Rev. C 40, 640 (1990). Erratum Phys. Rev. C 41, 1320 (1990)

[108] HADES Collaboration. *"Lambda hyperon production and polarization in collisions of p(3.5 GeV)+Nb"*. Eur. Phys. J. A 50, 81 (2014)

[109] HADES Collaboration. *"Medium effects in proton-induced K^0 production at 3.5 GeV"*. Phys. Rev. C 90, 054906 (2014)

[110] S. A. Bass et al. *"Microscopic Models for Ultrarelativistic Heavy Ion Collisions"*. arXiv:nucl-th/9803035v2

[111] C.-M. Herbach et al. *"Systematic investigation of 1.2-GeV proton-induced spallation reactions on targets between Al and U"* NIM A 562, 729 (2006)

[112] M. L. Benabderrahmane et al. *"Measurement of the In-Medium K^0 Inclusive Cross Section in π^--Induced Reactions at 1.15 GeV/c"*. Phys. Rev. Lett. 102, 182501 (2009)

[113] K. Tsushima, A. Sibirtsev, and A. W. Thomas. *"Strangeness production from πN collisions in nuclear matter"*. Phys. Rev.C 62, 064904 (2000)

[114] W. Cassing et al. *"Hadronic and electromagnetic probes of hot and dense nuclear matter"*. Phys. Rep. 308, 65 (1999),

[115] W. Cassing et al. *"Kaon versus antikaon production at SIS energies"*. Nucl. Phys.A 614, 415 (1997)

[116] T. Abbott et al. (E-802 Collaboration). *"Measurement of particle production in proton-induced reactions at 14.6 GeV/c"*. Phys. Rev. D 45, 3906 (1992).

[117] V.P. Koptev et al. Zh. Eksp. Teor. Fiz. 94,1-14 (1988).

[118] G. Castagnoli, D. Lal. *"Solar Modulation Effects in Terrestrial Production of Carbon-14"*. Radiocarbon 22, 133 (1980)

[119] J.F. Ormes and W.R. Webber. *"Proton and helium nuclei cosmic-ray spectra and modulations between 100 and 2000 Mev/nucleon"* J. Geophys Res. 73, 4231 (1968)

[120] K.C. Hsieh, G.M. Mason, J.A. Simpson. *"Cosmic-ray ^2H from satellite measurements, 1965-1969"* Astrophys. J. 166, 221 (1971)

[121] R. Kroeger. *"Measurements of hydrogen and helium isotopes in Galactic cosmic rays from 1978 through 1984"* Astrophys. J. 303, 816 (1986)

[122] W.R. Webber et al. *"A measurement of the cosmic-ray ^2H and ^3He spectra and $^2H/^4He$ and $^3He/^4He$ ratios in 1989"* Astrophys. J. 380, 230 (1991)

[123] K. Ammon, J. Masarik, and I. Leya. *"New model calculations for the production rates of cosmogenic nuclides in iron meteorites "*. Met. & Planet. Sci. 44, 485 (2009)

[124] I. Leya and J. Masarik. *"Cosmogenic nuclides in stony meteorites revisited"*. Met. & Planet. Sci. 44, 1061 (2009)

[125] D.F. Smart, M.A. Shea, and E.O. Flückiger. *"Magnetospheric Models and Trajectory Computations"*. Space Sci. Rev. 93 (1-2), 305 (2000)

[126] L. Desorgher et al. *"Atmocosmics: a Geant 4 Code for Computing the Interaction of Cosmic Rayswith the Earth's Atmosphere."* International Journal of Modern Physics A 20, 6802 (2005)
Website

[127] G, Schnabel. *"Estimating model bias over the complete nuclide chart with sparse Gaussian processes at the example of INCL/ABLA and double-differential neutron spectra"* EPJ Nuclear Sci. Technol. 4, 33 (2018)

[128] V. Sears. *"Neutron scattering lengths and cross sections"*. Neutron News 3, 26 (1992)

[129] K, Genser et al. *"A Software Toolkit to Study Systematic Uncertainties of the Physics Models of the Geant4 Simulation Package"* Journal of Physics: Conference Series 898, 42052 (2017)

[130] J. Masarik and J. Beer. *"Simulation of particle fluxes and cosmogenic nuclide production in the Earth's atmosphere"*. J. Geophys. Res. 104, 12099 (1999)

Appendix A

Cross sections parametrisations

A.1 Elastic

A.1.1 $NY \to NY$

$$\begin{cases} \sigma = 200\ [mb] & if \quad 0 \quad < P_{lab} \quad < 145 MeV/c \\ \sigma = 869 \exp(-P_{lab}[MeV/c]/100)\ [mb] & if\ 145 MeV/c \quad < P_{lab} \quad < 425 MeV/c \\ \sigma = 12.8 \exp(-6.2e^{-5} P_{lab}[MeV/c])\ [mb] & if\ 425 MeV/c \quad < P_{lab} \quad < 20 GeV/c \\ \sigma = 0 & if\ 20 GeV/c \quad < P_{lab} \end{cases} \tag{A.1}$$

A.1.2 $NK \to NK$

$$\begin{cases} \sigma = 12\ [mb] & if \quad 0 \quad < P_{lab} \quad < 935 MeV/c \\ \sigma = 17.4 - 3 \exp(6.3e^{-4} P_{lab}[MeV/c])\ [mb] & if\ 935 MeV/c \quad < P_{lab} \quad < 2080 MeV/c \\ \sigma = 832 P_{lab}[MeV/c]^{-0.64}\ [mb] & if\ 2080 MeV/c \quad < P_{lab} \quad < 5.5 GeV/c \\ \sigma = 3.36\ [mb] & if\ 5.5 GeV/c \quad < P_{lab} \quad < 20 GeV/c \\ \sigma = 0 & if\ 20 GeV/c \quad < P_{lab} \end{cases} \tag{A.2}$$

A.1.3 $N\overline{K} \to N\overline{K}$

$$\begin{cases} \sigma = 200\ [mb] & if \quad 0 \quad < P_{lab} \quad < 135 MeV/c \\ \sigma = 56368 P_{lab}[MeV/c]^{-1.15} + 30 \exp \dfrac{-(P_{lab}[MeV/c] - 395^2)}{500}\ [mb] & if\ 135 MeV/c \quad < P_{lab} \quad < 625 MeV/c \\ \sigma = 90.19 P_{lab}[MeV/c]^{-0.15} + 7 \exp \dfrac{-(P_{lab}[MeV/c] - 790)^2}{3000} \\ \quad + 20 \exp(-(P_{lab}[MeV/c] - 1030)^2/19000)\ [mb] & if\ 625 MeV/c \quad < P_{lab} \quad < 20 GeV/c \\ \quad + 4.4 \exp(-(P_{lab}[MeV/c] - 1640)^2/42000) \\ \sigma = 0 & if\ 20 GeV/c \quad < P_{lab} \end{cases} \tag{A.3}$$

A.2 Inelastic

A.2.1 $NN \to N\Lambda K$

$$\begin{cases} \sigma(pp \to p\Lambda K^+) = 1.11875 \dfrac{(P_{lab}[GeV/c] - P_{th})^{1.0951}}{(P_{lab}[GeV/c] + P_{th})^{2.0958}}\ [mb] & if\ P_{threshold} < P_{lab} < 30 GeV/c \\ \sigma(pp \to p\Lambda K^+) = 0 & else \end{cases} \tag{A.4}$$

A.2.2 $NN \to N\Sigma K$

$$\begin{cases} \sigma(pp \to n\Sigma^+ K^+) = 0\ [mb] & if\ 0 < P_{lab} < 2.57 GeV/c \\ \sigma(pp \to n\Sigma^+ K^+) = 6.38(P_{lab}[GeV/c] - 2.57)^{2.1} / P_{lab}[GeV/c]^{4.162}\ [mb] & else \end{cases} \tag{A.5}$$

A.2.3 $NN \to NNK\overline{K}$

$$\begin{cases} \sigma(pp \to ppK^+K^-) = 0\ [mb] & if\ 0 < \sqrt{s} < 2.872 GeV \\ \sigma(pp \to ppK^+K^-) = 4/70 \left(1 - \dfrac{2.872}{\sqrt{s}[GeV/c]}\right)^3 \left(\dfrac{2.872}{\sqrt{s}[GeV/c]}\right)^{0.8}\ [mb] & else \end{cases} \tag{A.6}$$

A.2.4 $\pi N \to \Lambda K$

$$\begin{cases} \sigma(p\pi^- \to \Lambda K^0) = 0\ [mb] & if\ 0 < P_{Lab} < 0.911 GeV/c \\ \sigma(p\pi^- \to \Lambda K^0) = 0.3936 P_{Lab}[GeV/c]^{-1.357} & \\ \qquad - 6.052 \exp(-(P_{Lab}[GeV/c] - 0.7154)^2 / 0.02026) & \\ \qquad + 0.489 \exp(-(P_{Lab}[GeV/c] - 0.8886)^2 / 0.08378) & else \\ \qquad - 0.16 \exp(-(P_{Lab}[GeV/c] - 0.9684)^2 / 0.001432)\ [mb] & \end{cases} \tag{A.7}$$

A.2.5 $\pi N \to \Sigma K$

$$\begin{cases} \sigma(p\pi^- \to \Sigma^- K^+) = 0\ [mb] & if\ 0 < P_{Lab} < 1.035 GeV/c \\ \sigma(p\pi^- \to \Sigma^- K^+) = 4.352(P_{Lab}[GeV/c] - 1.035)^{1.006} / P_{Lab}[GeV/c]^{5.375}\ [mb] & else \end{cases} \tag{A.8}$$

$$\begin{cases} \sigma(p\pi^+ \to \Sigma^+ K^+) = 0\ [mb] & if\ 0 < P_{Lab} < 1.020 GeV/c \\ \sigma(p\pi^+ \to \Sigma^+ K^+) = 11.44(P_{Lab}[GeV/c] - 1.02)^{1.631} / P_{Lab}[GeV/c]^{5.052}\ [mb] & else \end{cases} \tag{A.9}$$

$$\begin{cases} \sigma(p\pi^- \to \Sigma^0 K^0) = 0 \ [mb] & if\ 0 < P_{Lab} < 1.034 GeV/c \\ \sigma(p\pi^- \to \Sigma^0 K^0) = 0.3474(P_{Lab}[GeV/c] - 1.034)^{0.07678}/P_{Lab}[GeV/c]^{1.627} \ [mb] & else \end{cases} \tag{A.10}$$

$$\begin{cases} \sigma(p\pi^0 \to \Sigma^+ K^0) = 0 \ [mb] & if\ 0 < P_{Lab} < 1.030 GeV/c \\ \sigma(p\pi^- \to \Sigma^+ K^0) = 3.624(P_{Lab}[GeV/c] - 1.03)^{1.4}/P_{Lab}[GeV/c]^{5.14} \ [mb] & else \end{cases} \tag{A.11}$$

A.2.6 $\pi N \to \Lambda K \pi$

$$\begin{cases} \sigma(p\pi^+ \to \Lambda K^+ \pi^+) = 0 \ [mb] & if\ 0 < \ P_{Lab} < 1.142 GeV \\ \sigma(p\pi^+ \to \Lambda K^+ \pi^+) = 146.2 \dfrac{(P_{Lab}[GeV/c] - 1.142)^{1.996}}{(P_{Lab}[GeV/c] + 1.142)^{5.921}} \ [mb] & else \end{cases} \tag{A.12}$$

A.2.7 $\pi N \to \Sigma K \pi$

$$\begin{cases} \sigma(p\pi^0 \to \Sigma^0 K^+ \pi^0) = 0 \ [mb] & if\ 0 < \ P_{Lab} < 1.29 GeV \\ \sigma(p\pi^0 \to \Sigma^0 K^+ \pi^0) = 47.5 \dfrac{(P_{Lab}[GeV/c] - 1.290)^{3.41}}{(P_{Lab}[GeV/c])^{7.276}} \ [mb] & else \end{cases} \tag{A.13}$$

A.2.8 $\pi N \to \Lambda K \pi \pi$

$$\begin{cases} \sigma(p\pi^+ \to \Lambda K^+ \pi^+ \pi^0) = 0 \ [mb] & if\ 0 < \ P_{Lab} < 1.405 GeV \\ \sigma(p\pi^+ \to \Lambda K^+ \pi^+ \pi^0) = 18.77 \dfrac{(P_{Lab}[GeV/c] - 1.405)^{4.597}}{(P_{Lab}[GeV/c])^{6.877}} \ [mb] & else \end{cases} \tag{A.14}$$

A.2.9 $\pi N \to \Sigma K \pi \pi$

$$\begin{cases} \sigma(p\pi^+ \to \Sigma^+ K^+ \pi^+ \pi^-) = 0 \ [mb] & if\ 0 < \ P_{Lab} < 1.563 GeV \\ \sigma(p\pi^+ \to \Sigma^+ K^+ \pi^+ \pi^-) = 137.6 \dfrac{(P_{Lab}[GeV/c] - 1.563)^{5.856}}{(P_{Lab}[GeV/c])^{9.295}} \ [mb] & else \end{cases} \tag{A.15}$$

A.2.10 $\pi N \to N K \overline{K}$

$$\begin{cases} \sigma(p\pi^0 \to n K^+ \overline{K}^0) = 3.367 \dfrac{(P_{Lab}[GeV/c] - 1.49)^{2.047}}{(P_{Lab}[GeV/c])^{3.75}} \ [mb] & if\ 1.49 GeV \ < P_{lab} \ < 30 GeV/c \\ \sigma(p\pi^0 \to n K^+ \overline{K}^0) = 0 & else \end{cases} \tag{A.16}$$

A.2.11 $N\Lambda \to N\Sigma$

$$\begin{cases} \sigma(p\Lambda \to \Sigma^0 p) = 0 & if\ P_{lab} < 0.6578 GeV \\ \sigma(p\Lambda \to \Sigma^0 p) = 8.74 \dfrac{(P_{Lab}[GeV/c] - 0.6578)^{0.438}}{(P_{Lab}[GeV/c])^{2.717}}\ [mb] & if\ 0.6578 GeV < P_{lab} \end{cases} \tag{A.17}$$

A.2.12 $N\Sigma \to N\Lambda$

$$\begin{cases} \sigma(p\Sigma^0 \to p\Lambda) = 100\ [mb] & if\ \ 0 < P_{lab} < 100 MeV/c \\ \sigma(p\Sigma^0 \to p\Lambda) = 8.23 P_{lab}[GeV/c]^{-1.087}\ [mb] & if\ 100 MeV/c < P_{lab} \end{cases} \tag{A.18}$$

A.2.13 $N\Sigma \to N\Sigma$

$$\begin{cases} \sigma(p\Sigma^0 \to n\Sigma^+) = 100\ [mb] & if\ \ 0 < P_{lab} < 100 MeV/c \\ \sigma(p\Sigma^0 \to n\Sigma^+) = 13.79 P_{lab}[GeV/c]^{-1.181}\ [mb] & else \end{cases} \tag{A.19}$$

A.2.14 $N\overline{K} \to \Lambda\pi$

$$\begin{cases} \sigma(pK^- \to \Lambda\pi^0) = 40.24\ [mb] & if\ 0 < P_{lab} < 86.636 MeV/c \\ \sigma(pK^- \to \Lambda\pi^0) = 0.97 P_{lab}[GeV/c]^{-1.523}\ [mb] & if\ 200 MeV < P_{lab} < 500 MeV/c \\ \sigma(pK^- \to \Lambda\pi^0) = 1.23 P_{lab}[GeV/c]^{-1.467} & \\ \qquad + 0.872 \exp\left(-\dfrac{P_{lab}[GeV/c] - 0.749)^2}{0.0045}\right) & if\ 500 MeV < P_{lab} < 2 GeV/c \\ \qquad + 2.337 \exp\left(-\dfrac{P_{lab}[GeV/c] - 0.95)^2}{0.017}\right) & \\ \qquad + 0.476 \exp\left(-\dfrac{P_{lab}[GeV/c] - 1.434)^2}{0.136}\right)\ [mb] & \\ \sigma(pK^- \to \Lambda\pi^0) = 3 P_{lab}[GeV/c]^{-2.57}\ [mb] & if\ 2 GeV < P_{lab} < 20 GeV/c \\ \sigma(pK^- \to \Lambda\pi^0) = 0 & else \end{cases} \tag{A.20}$$

A.2.15 $N\overline{K} \to \Sigma\pi$

$$\begin{cases} \sigma(pK^- \to \Sigma^+\pi^-) = 69\ [mb] & if\ 0 < \ P_{lab} < 100MeV/c \\ \sigma(pK^- \to \Sigma^+\pi^-) = 1.4P_{lab}[GeV/c]^{-1.7} & \\ \qquad + 1.88\exp\left(-\dfrac{P_{lab}[GeV/c]-0.747)^2}{0.005}\right) & else \\ \qquad + 8\exp\left(-\dfrac{P_{lab}[GeV/c]-0.4)^2}{0.002}\right) & \\ \qquad + 0.8\exp\left(-\dfrac{P_{lab}[GeV/c]-1.07)^2}{0.01}\right)\ [mb] & \end{cases} \tag{A.21}$$

A.2.16 $N\overline{K} \to N\overline{K}$

special case (there are a minor discontinuity in the fit function)

$$\begin{cases} \sigma(pK^- \to n\overline{K}^0) = 0 & if\ 0 < P_{lab} < 89.21MeV/c \\ \sigma(pK^- \to n\overline{K}^0) = 0.4977\dfrac{(P_{lab}[GeV/c]-0.08921)^{0.5581}}{P_{lab}[GeV/c]^{2.704}}\ [mb] & if\ 89.21MeV/c < P_{lab} < 0.2GeV \\ \sigma(pK^- \to n\overline{K}^0) = 2P_{lab}[GeV/c]^{-1.2} & \\ \qquad + 6.493\exp\left(-0.5\left(\dfrac{P_{lab}[GeV/c]-0.3962}{0.02}\right)^2\right)\ [mb] & if\ 0.2GeV/c < P_{lab} < 0.73GeV \\ \sigma(pK^- \to n\overline{K}^0) = 2.3P_{lab}[GeV/c]^{-0.9} & \\ \qquad + 1.1\exp\left(-0.5\left(\dfrac{P_{lab}[GeV/c]-0.82}{0.04}\right)^2\right)\ [mb] & if\ 0.73GeV/c < P_{lab} < 1.38GeV \\ \qquad + 5\exp\left(-0.5\left(\dfrac{P_{lab}[GeV/c]-1.04}{0.1}\right)^2\right) & \\ \sigma(pK^- \to n\overline{K}^0) = 2.5P_{lab}[GeV/c]^{-1.68} & \\ \qquad + 0.7\exp\left(-0.5\left(\dfrac{P_{lab}[GeV/c]-1.6}{0.2}\right)^2\right)\ [mb] & if\ 1.38GeV/c < P_{lab} < 30GeV \\ \qquad + 0.2\exp\left(-0.5\left(\dfrac{P_{lab}[GeV/c]-2.3}{0.2}\right)^2\right) & \\ \sigma(pK^- \to n\overline{K}^0) = 0 & if\ P_{lab} > 30GeV/c \end{cases} \tag{A.22}$$

$$\begin{cases} \sigma(n\overline{K}^0 \to pK^-) = 30\ [mb] & if\ 0 < P_{lab} < 100MeV/c \\ \sigma(n\overline{K}^0 \to pK^-) = 2P_{lab}[GeV/c]^{-1.2} & \\ \qquad + 6.493 \exp\left(-0.5\left(\dfrac{P_{lab}[GeV/c] - 0.386}{0.02}\right)^2\right)\ [mb] & if\ 0.1GeV/c < P_{lab} < 0.73GeV \\ \sigma(n\overline{K}^0 \to pK^-) = 2.3P_{lab}[GeV/c]^{-0.9} & \\ \qquad + 1.1 \exp\left(-0.5\left(\dfrac{P_{lab}[GeV/c] - 0.812}{0.04}\right)^2\right)\ [mb] & if\ 0.73GeV/c < P_{lab} < 1.38GeV \\ \qquad + 5 \exp\left(-0.5\left(\dfrac{P_{lab}[GeV/c] - 1.032}{0.1}\right)^2\right) & \\ \sigma(n\overline{K}^0 \to pK^-) = 2.5P_{lab}[GeV/c]^{-1.68} & \\ \qquad + 0.7 \exp\left(-0.5\left(\dfrac{P_{lab}[GeV/c] - 1.592}{0.2}\right)^2\right)\ [mb] & if\ 1.38GeV/c < P_{lab} < 30GeV \\ \qquad + 0.2 \exp\left(-0.5\left(\dfrac{P_{lab}[GeV/c] - 2.291}{0.2}\right)^2\right) & \\ \sigma(n\overline{K}^0 \to pK^-) = 0 & if\ P_{lab} > 30GeV/c \end{cases} \tag{A.23}$$

A.2.17 $N\overline{K} \to N\overline{K}\pi$

$$\begin{cases} \sigma(p\overline{K}^0 \to pK^-\pi^+) = 0 & if\ 0 < P_{lab} < 510MeV/c \\ \sigma(p\overline{K}^0 \to pK^-\pi^+) = 109.8\dfrac{(P_{lab}[GeV/c] - 0.51)^{6.248}}{P_{lab}[GeV/c]^{8.769}} & else \end{cases} \tag{A.24}$$

A.2.18 $N\overline{K} \to \Sigma\pi\pi$

$$\begin{cases} \sigma(pK^- \to \Sigma^+\pi^0\pi^-) = 0\ [mb] & if\ 0 < P_{lab} < 226MeV/c \\ \sigma(pK^- \to \Sigma^+\pi^0\pi^-) = 85.46\dfrac{(P_{lab}[GeV/c] - 0.226)^{8.118}}{(P_{lab}[GeV/c] + 0.226)^{11.69}} & \\ \qquad + 0.1451 \exp\left(-\dfrac{P_{lab}[GeV/c] - 0.4031)^2}{0.00115}\right)\ [mb] & else \end{cases} \tag{A.25}$$

A.2.19 $N\overline{K} \to \Lambda\pi\pi$

$$\begin{cases} \sigma(pK^- \to \Lambda\pi^+\pi^-) = 6364\dfrac{P_{lab}[GeV/c]^{6.07}}{(P_{lab}[GeV/c]+1.)^{10.58}} \\ \qquad\qquad + 2.158\exp\left(-\dfrac{1}{2}\left(\dfrac{P_{lab}[GeV/c]-0.395}{.01984}\right)^2\right)\ [mb] & if\ 0 < P_{lab} < 970MeV/c \\ \sigma(pK^- \to \Lambda\pi^+\pi^-) = 46.3\dfrac{P_{lab}[GeV/c]^{0.62}}{(P_{lab}[GeV/c]+1.)^{3.565}}\ [mb] & if\ 970MeV/c < P_{lab} < 20GeV \\ \sigma(pK^- \to \Lambda\pi^+\pi^-) = 0 & else \end{cases} \tag{A.26}$$

A.2.20 $N\overline{K} \to N\overline{K}\pi\pi$

$$\begin{cases} \sigma(pK^- \to pK^-\pi^+\pi^-) = 0 & if\ 0 < P_{lab} < 850MeV/c \\ \sigma(pK^- \to pK^-\pi^+\pi^-) = 26.8\dfrac{(P_{lab}[GeV/c]-0.85)^{4.9}}{P_{lab}[GeV/c]^{6.34}} & else \end{cases} \tag{A.27}$$

A.2.21 $NK \to NK$

This is a special case because of the threshold effect:

$$\begin{cases} \sigma(nK^+ \to pK^0) = 0 & if\ 0 < P_{lab} < 63MeV/c \\ \sigma(nK^+ \to pK^0) = 12.84\dfrac{(P_{lab}[GeV/c]-0.063)^{18.19}}{(P_{lab}[GeV/c])^{20.41}}\ [mb] & if\ 63MeV/c < P_{lab} \end{cases} \tag{A.28}$$

$$\left\{\sigma(pK^0 \to nK^+) = 12.84\frac{(P_{lab}[GeV/c]+0.063)^{18.19}}{(P_{lab}[GeV/c]+0.126)^{20.41}}\ [mb]\right. \tag{A.29}$$

A.2.22 $NK \to NK\pi$

$$\begin{cases} \sigma(pK^0 \to pK^+\pi^-) = 0 & if\ P_{lab} < 530MeV/c \\ \sigma(pK^0 \to pK^+\pi^-) = 116.8\dfrac{(P_{lab}[GeV/c]-0.53)^{6.874}}{P_{lab}[GeV/c]^{10.11}}\ [mb] & if\ 530MeV/c < P_{lab} \end{cases} \tag{A.30}$$

A.2.23 $NK \rightarrow NK\pi\pi$

$$\begin{cases} \sigma(pK^0 \rightarrow pK^+\pi^0\pi^-) = 0 & if \quad P_{lab} < 812MeV/c \\ \sigma(pK^0 \rightarrow pK^+\pi^0\pi^-) = 26.41\dfrac{(P_{lab}[GeV/c] - 0.812)^{7.138}}{P_{lab}[GeV/c]^{5.337}}\ [mb] & if\ 812MeV/c < P_{lab} < 1.744GeV/c \\ \sigma(pK^0 \rightarrow pK^+\pi^0\pi^-) = 1572\dfrac{(P_{lab}[GeV/c] - 0.812)^{9.069}}{P_{lab}[GeV/c]^{12.44}}\ [mb] & if\ 1.744GeV/c < P_{lab} < 3.728GeV/c \\ \sigma(pK^0 \rightarrow pK^+\pi^0\pi^-) = 60.23\dfrac{(P_{lab}[GeV/c] - 0.812)^{5.084}}{P_{lab}[GeV/c]^{6.72}}\ [mb] & if\ 3.728GeV/c < P_{lab} \end{cases} \tag{A.31}$$

Appendix B

Relations extracted from the HEM and Bystricky procedures.

This appendix summarises the relations obtained from the hadron exchange model (normal style) and the relation obtain from the Bystricky procedure (in bold) (see subsection IV.4.2 and subsection IV.4.3).

In what follows, N represents a nucleon, Δ a Delta particle, B a nucleon or a Delta particle, Y a hyperon, π a pion, K a kaon (excluding $\overline{K}^0$ and K^-), and $\overline{K}$ an antikaon.

The reliability of the shown equations are discussed in chapter IV. In summary, bold equations (coming from the Bystricky procedure) are highly reliable. Normal style equations (coming from the hadron exchange model) often use debatable hypotheses, which can produce surprising results but there are always consistent with equations in bold.

Reaction type: $NK(\overline{K},\Lambda) \to NK(\overline{K},\Lambda)$

The reactions $NK \to NK$, $N\overline{K} \to N\overline{K}$, and $N\Lambda \to N\Lambda$ do not have symmetries, except the trivial ones. They also have threshold effects, therefore the hadron exchange model is not applicable for these reactions.

Reaction type: $NN \to NYK$

$$\sigma(pp \to p\Lambda K^+) = \sigma(nn \to n\Lambda K^0)$$
$$\sigma(pn \to p\Lambda K^0) = \sigma(pn \to n\Lambda K^+)$$

$$4\sigma(pp \to p\Sigma^+ K^0) = 4\sigma(nn \to n\Sigma^- K^+) = 8\sigma(pp \to p\Sigma^0 K^+) = 8\sigma(nn \to n\Sigma^0 K^0)$$
$$= \sigma(pp \to n\Sigma^+ K^+) = \sigma(nn \to p\Sigma^- K^0) = \frac{8}{5}\sigma(pn \to p\Sigma^0 K^0) = \frac{8}{5}\sigma(pn \to n\Sigma^0 K^+)$$
$$= 4\sigma(pn \to p\Sigma^- K^+) = 4\sigma(pn \to n\Sigma^+ K^0)$$

$$\boldsymbol{\sigma(pn \to p\Sigma^- K^+) + \sigma(pp \to n\Sigma^+ K^+) + \sigma(pp \to p\Sigma^+ K^0)}$$
$$\boldsymbol{= 2\sigma(pn \to p\Sigma^0 K^0) + 2\sigma(pp \to p\Sigma^0 K^+)}$$

Reaction type: $NN \to NYK\pi$

Calculation are based on $NN \to \Delta YK \to NYK\pi$.

$$\frac{4}{9}\sigma(pp \to p\Lambda K^0\pi^+) = \frac{4}{9}\sigma(nn \to n\Lambda K^+\pi^-) = 2\sigma(pp \to p\Lambda K^+\pi^0) = 2\sigma(nn \to n\Lambda K^0\pi^0)$$
$$= 4\sigma(pp \to n\Lambda K^+\pi^+) = 4\sigma(nn \to p\Lambda K^0\pi^-) = 2\sigma(pn \to p\Lambda K^+\pi^-) = 2\sigma(pn \to n\Lambda K^0\pi^+)$$
$$= \sigma(pn \to p\Lambda K^0\pi^0) = \sigma(pn \to n\Lambda K^+\pi^0)$$

$$\boldsymbol{\sigma(pn \to p\Lambda K^+\pi^-) + \sigma(pp \to n\Lambda K^+\pi^+) + \sigma(pp \to p\Lambda K^0\pi^+)}$$
$$\boldsymbol{= 2\sigma(pn \to p\Lambda K^0\pi^0) + 2\sigma(pp \to p\Lambda K^+\pi^0)}$$

$$\boldsymbol{\sigma(pn \to p\Sigma^- K^+\pi^0) + \sigma(pp \to n\Sigma^+ K^+\pi^0) + \sigma(pp \to p\Sigma^+ K^0\pi^0)}$$
$$\boldsymbol{= \sigma(pn \to p\Sigma^0 K^+\pi^-) + \sigma(pp \to n\Sigma^0 K^+\pi^+) + \sigma(pp \to p\Sigma^0 K^0\pi^+)}$$

$$\boldsymbol{\sigma(pn \to p\Sigma^- K^0\pi^+) + \sigma(pn \to p\Sigma^+ K^0\pi^-) + \sigma(pp \to n\Sigma^+ K^0\pi^+)}$$
$$\boldsymbol{+\sigma(pp \to p\Sigma^- K^+\pi^+) + \sigma(pp \to p\Sigma^+ K^+\pi^-)}$$
$$\boldsymbol{= \sigma(pn \to p\Sigma^0 K^+\pi^-) + 2\sigma(pn \to p\Sigma^0 K^0\pi^0) + \sigma(pp \to n\Sigma^0 K^+\pi^+)}$$
$$\boldsymbol{+2\sigma(pp \to p\Sigma^0 K^+\pi^0) + \sigma(pp \to p\Sigma^0 K^0\pi^+)}$$

$$\sigma(pp \to p\Sigma^+ K^0\pi^0) = \sigma(nn \to n\Sigma^- K^+\pi^0) = 2\sigma(pp \to n\Sigma^+ K^0\pi^+) = 2\sigma(nn \to p\Sigma^- K^+\pi^-)$$
$$= \sigma(pp \to n\Sigma^+ K^+\pi^0) = \sigma(nn \to p\Sigma^- K^0\pi^0) = 2\sigma(pp \to p\Sigma^+ K^+\pi^-) = 2\sigma(nn \to n\Sigma^- K^0\pi^+)$$
$$= \sigma(pp \to p\Sigma^0 K^+\pi^0) = \sigma(nn \to n\Sigma^0 K^0\pi^0) = 2\sigma(pp \to n\Sigma^0 K^+\pi^+) = 2\sigma(nn \to p\Sigma^0 K^0\pi^-)$$
$$= \frac{4}{9}\sigma(pp \to p\Sigma^0 K^0\pi^+) = \frac{4}{9}\sigma(nn \to n\Sigma^0 K^+\pi^-) = \frac{4}{9}\sigma(pp \to p\Sigma^- K^+\pi^+) = \frac{4}{9}\sigma(nn \to n\Sigma^+ K^0\pi^-)$$
$$= \frac{4}{9}\sigma(pn \to p\Sigma^- K^0\pi^+) = \frac{4}{9}\sigma(pn \to n\Sigma^+ K^+\pi^-) = 2\sigma(pn \to p\Sigma^0 K^0\pi^0) = 2\sigma(pn \to n\Sigma^0 K^+\pi^0)$$
$$= 4\sigma(pn \to p\Sigma^0 K^+\pi^-) = 4\sigma(pn \to n\Sigma^0 K^0\pi^+) = \sigma(pn \to p\Sigma^- K^+\pi^0) = \sigma(pn \to n\Sigma^+ K^0\pi^0)$$
$$= 2\sigma(pn \to p\Sigma^+ K^0\pi^-) = 2\sigma(pn \to n\Sigma^- K^+\pi^+)$$

Reaction type: $NN \to NNK\overline{K}$

$$4\sigma(pp \to ppK^+K^-) = 4\sigma(nn \to nnK^0\overline{K}^0) = 4\sigma(pp \to ppK^0\overline{K}^0) = 4\sigma(nn \to nnK^+K^-)$$
$$= \sigma(pp \to pnK^+\overline{K}^0) = \sigma(nn \to pnK^0K^-) = \sigma(pn \to ppK^0K^-) = \sigma(pn \to nnK^+\overline{K}^0)$$
$$= 4/9\ \sigma(pn \to pnK^+K^-) = 4/9\ \sigma(pn \to pnK^0\overline{K}^0)$$

No solution found with the Bystricky procedure

Reaction type: $NK \to NK\pi$

$$0.83\sigma(pK^+ \to pK^+\pi^0) = 0.83\sigma(nK^0 \to nK^0\pi^0) = \frac{1}{3}\sigma(pK^+ \to pK^0\pi^+) = \frac{1}{3}\sigma(nK^0 \to nK^+\pi^-)$$
$$= 1.25\sigma(pK^+ \to nK^+\pi^+) = 1.25\sigma(nK^0 \to pK^0\pi^-) = \sigma(pK^0 \to pK^+\pi^-) = \sigma(nK^+ \to nK^0\pi^+)$$
$$= 1.18\sigma(pK^0 \to pK^0\pi^0) = 1.18\sigma(nK^+ \to nK^+\pi^0) = 0.68\sigma(pK^0 \to nK^+\pi^0) = 0.68\sigma(nK^+ \to pK^0\pi^0)$$
$$= 0.45\sigma(pK^0 \to nK^0\pi^+) = 0.45\sigma(nK^+ \to pK^+\pi^-)$$

$$\boldsymbol{\sigma(pK^0 \to nK^0\pi^+) + \sigma(pK^0 \to pK^+\pi^-) + \sigma(pK^+ \to nK^+\pi^+) + \sigma(pK^+ \to pK^0\pi^+)}$$
$$\boldsymbol{= 2\sigma(pK^0 \to nK^+\pi^0) + 2\sigma(pK^0 \to pK^0\pi^0) + 2\sigma(pK^+ \to pK^+\pi^0)}$$

Reaction type: $NK \to NK\pi\pi$

$$\sigma(pK^+ \to pK^+\pi^+\pi^-) = \sigma(nK^0 \to nK^0\pi^+\pi^-) = 8\sigma(pK^+ \to pK^+\pi^0\pi^0) = 8\sigma(nK^0 \to nK^0\pi^0\pi^0)$$
$$= \sigma(pK^+ \to pK^0\pi^+\pi^0) = \sigma(nK^0 \to nK^+\pi^0\pi^-) = 2\sigma(pK^+ \to nK^+\pi^+\pi^0) = 2\sigma(nK^0 \to pK^0\pi^0\pi^-)$$
$$= 4\sigma(pK^+ \to nK^0\pi^+\pi^+) = 4\sigma(nK^0 \to pK^+\pi^-\pi^-) = \sigma(pK^0 \to pK^+\pi^0\pi^-) = \sigma(nK^+ \to nK^0\pi^+\pi^0)$$
$$= \sigma(pK^0 \to pK^0\pi^+\pi^-) = \sigma(nK^+ \to nK^+\pi^+\pi^-) = 8\sigma(pK^0 \to pK^0\pi^0\pi^0) = 8\sigma(nK^+ \to nK^+\pi^0\pi^0)$$
$$= 4\sigma(pK^0 \to nK^+\pi^+\pi^-) = 4\sigma(nK^+ \to pK^0\pi^+\pi^-) = 4\sigma(pK^0 \to nK^+\pi^0\pi^0) = 4\sigma(nK^+ \to pK^0\pi^0\pi^0)$$
$$= 2\sigma(pK^0 \to nK^0\pi^+\pi^0) = 2\sigma(nK^+ \to pK^+\pi^0\pi^-)$$

$$\boldsymbol{\sigma(pK^0 \to nK^0\pi^+\pi^0) + 4\sigma(pK^0 \to nK^+\pi^0\pi^0) + 4\sigma(pK^0 \to pK^0\pi^0\pi^0) + \sigma(pK^0 \to pK^+\pi^0\pi^-)}$$
$$\boldsymbol{+\sigma(pK^+ \to nK^+\pi^+\pi^0) + \sigma(pK^+ \to pK^0\pi^+\pi^0) + 4\sigma(pK^+ \to pK^+\pi^0\pi^0) = 2\sigma(pK^0 \to nK^+\pi^+\pi^-)}$$
$$\boldsymbol{+2\sigma(pK^0 \to pK^0\pi^+\pi^-) + 2\sigma(pK^+ \to nK^0\pi^+\pi^+) + 2\sigma(pK^+ \to pK^+\pi^+\pi^-)}$$

Reaction type: $N\overline{K} \to N\overline{K}\pi$

$$12\sigma(p\overline{K}^0 \to p\overline{K}^0\pi^0) = 12\sigma(nK^- \to nK^-\pi^0) = 6\sigma(p\overline{K}^0 \to pK^-\pi^+) = 6\sigma(nK^- \to n\overline{K}^0\pi^-)$$
$$= 12\sigma(p\overline{K}^0 \to n\overline{K}^0\pi^+) = 12\sigma(nK^- \to pK^-\pi^-) = 9\sigma(pK^- \to p\overline{K}^0\pi^-) = 9\sigma(n\overline{K}^0 \to nK^-\pi^+)$$
$$= 12\sigma(pK^- \to pK^-\pi^0) = 12\sigma(n\overline{K}^0 \to n\overline{K}^0\pi^0) = 3\sigma(pK^- \to n\overline{K}^0\pi^0) = 3\sigma(n\overline{K}^0 \to pK^-\pi^0)$$
$$= 8\sigma(pK^- \to nK^-\pi^+) = 8\sigma(n\overline{K}^0 \to p\overline{K}^0\pi^-)$$

$$\boldsymbol{\sigma(pK^- \to nK^-\pi^+) + \sigma(pK^- \to p\overline{K}^0\pi^-) + \sigma(p\overline{K}^0 \to n\overline{K}^0\pi^+) + \sigma(p\overline{K}^0 \to pK^-\pi^+)}$$
$$\boldsymbol{= 2\sigma(pK^- \to n\overline{K}^0\pi^0) + 2\sigma(pK^- \to pK^-\pi^0) + 2\sigma(p\overline{K}^0 \to p\overline{K}^0\pi^0)}$$

Reaction type: $N\overline{K} \to N\overline{K}\pi\pi$

$$\sigma(p\overline{K}^0 \to p\overline{K}^0\pi^+\pi^-) = \sigma(nK^- \to nK^-\pi^+\pi^-) = 4\sigma(p\overline{K}^0 \to p\overline{K}^0\pi^0\pi^0) = 4\sigma(nK^- \to nK^-\pi^0\pi^0)$$
$$= \sigma(p\overline{K}^0 \to pK^-\pi^+\pi^0) = \sigma(nK^- \to n\overline{K}^0\pi^0\pi^-) = \sigma(p\overline{K}^0 \to n\overline{K}^0\pi^+\pi^0) = \sigma(nK^- \to pK^-\pi^0\pi^-)$$
$$= \sigma(p\overline{K}^0 \to nK^-\pi^+\pi^+) = \sigma(nK^- \to p\overline{K}^0\pi^-\pi^-) = \sigma(pK^- \to p\overline{K}^0\pi^0\pi^-) = \sigma(n\overline{K}^0 \to nK^-\pi^+\pi^0)$$
$$= \sigma(pK^- \to pK^-\pi^+\pi^-) = \sigma(n\overline{K}^0 \to n\overline{K}^0\pi^+\pi^-) = 4\sigma(pK^- \to pK^-\pi^0\pi^0) = 4\sigma(n\overline{K}^0 \to n\overline{K}^0\pi^0\pi^0)$$
$$= \sigma(pK^- \to n\overline{K}^0\pi^+\pi^-) = \sigma(n\overline{K}^0 \to pK^-\pi^+\pi^-) = 2\sigma(pK^- \to n\overline{K}^0\pi^0\pi^0) = 2\sigma(n\overline{K}^0 \to pK^-\pi^0\pi^0)$$
$$= \sigma(pK^- \to nK^-\pi^+\pi^0) = \sigma(n\overline{K}^0 \to p\overline{K}^0\pi^0\pi^-)$$

$$\boldsymbol{\sigma(pK^- \to nK^-\pi^+\pi^0) + 4\sigma(pK^- \to n\overline{K}^0\pi^0\pi^0) + 4\sigma(pK^- \to pK^-\pi^0\pi^0)}$$
$$\boldsymbol{+\sigma(pK^- \to p\overline{K}^0\pi^0\pi^-) + \sigma(p\overline{K}^0 \to n\overline{K}^0\pi^+\pi^0)}$$
$$\boldsymbol{+\sigma(p\overline{K}^0 \to pK^-\pi^+\pi^0) + 4\sigma(p\overline{K}^0 \to p\overline{K}^0\pi^0\pi^0)}$$
$$\boldsymbol{= 2\sigma(pK^- \to n\overline{K}^0\pi^+\pi^-) + 2\sigma(pK^- \to pK^-\pi^+\pi^-)}$$
$$\boldsymbol{+2\sigma(p\overline{K}^0 \to nK^-\pi^+\pi^+) + 2\sigma(p\overline{K}^0 \to p\overline{K}^0\pi^+\pi^-)}$$

Reaction type: $N\overline{K} \to Y\pi$

$$\sigma(p\overline{K}^0 \to \Lambda\pi^+) = \sigma(nK^- \to \Lambda\pi^-) = 2\sigma(pK^- \to \Lambda\pi^0) = 2\sigma(n\overline{K}^0 \to \Lambda\pi^0)$$

$$\boldsymbol{\sigma(p\overline{K}^0 \to \Lambda\pi^+) = 2\sigma(pK^- \to \Lambda\pi^0)}$$

$$\sigma(p\overline{K}^0 \to \Sigma^+\pi^0) = \sigma(nK^- \to \Sigma^-\pi^0) = \sigma(p\overline{K}^0 \to \Sigma^0\pi^+) = \sigma(nK^- \to \Sigma^0\pi^-)$$
$$= \frac{3}{4}\sigma(pK^- \to \Sigma^+\pi^-) = \frac{3}{4}\sigma(n\overline{K}^0 \to \Sigma^-\pi^+) = \frac{3}{2}\sigma(pK^- \to \Sigma^0\pi^0) = \frac{3}{2}\sigma(n\overline{K}^0 \to \Sigma^0\pi^0)$$
$$= \sigma(pK^- \to \Sigma^-\pi^+) = \sigma(n\overline{K}^0 \to \Sigma^+\pi^-)$$

$$\boldsymbol{\sigma(p\overline{K}^0 \to \Sigma^+\pi^0) = \sigma(p\overline{K}^0 \to \Sigma^0\pi^+)}$$

$$\boldsymbol{\sigma(pK^- \to \Sigma^-\pi^+) + \sigma(pK^- \to \Sigma^+\pi^-) = 2\sigma(pK^- \to \Sigma^0\pi^0) + \sigma(p\overline{K}^0 \to \Sigma^+\pi^0)}$$

Reaction type: $N\overline{K} \to Y\pi\pi$

$$\sigma(p\overline{K}^0 \to \Lambda\pi^+\pi^0) = \sigma(nK^- \to \Lambda\pi^0\pi^-) = \sigma(pK^- \to \Lambda\pi^+\pi^-) = \sigma(n\overline{K}^0 \to \Lambda\pi^+\pi^-)$$
$$= 4\sigma(pK^- \to \Lambda\pi^0\pi^0) = 4\sigma(n\overline{K}^0 \to \Lambda\pi^0\pi^0)$$

$$\boldsymbol{4\sigma(pK^- \to \Lambda\pi^0\pi^0) + \sigma(p\overline{K}^0 \to \Lambda\pi^+\pi^0) = 2\sigma(pK^- \to \Lambda\pi^+\pi^-)}$$

$$\frac{3}{2}\sigma(p\overline{K}^0 \to \Sigma^+\pi^+\pi^-) = \frac{3}{2}\sigma(nK^- \to \Sigma^-\pi^+\pi^-) = 4\sigma(p\overline{K}^0 \to \Sigma^+\pi^0\pi^0) = 4\sigma(nK^- \to \Sigma^-\pi^0\pi^0)$$
$$= \frac{6}{5}\sigma(p\overline{K}^0 \to \Sigma^0\pi^+\pi^0) = \frac{6}{5}\sigma(nK^- \to \Sigma^0\pi^0\pi^-) = \frac{3}{2}\sigma(p\overline{K}^0 \to \Sigma^-\pi^+\pi^+) = \frac{3}{2}\sigma(nK^- \to \Sigma^+\pi^-\pi^-)$$
$$= \sigma(pK^- \to \Sigma^+\pi^0\pi^-) = \sigma(n\overline{K}^0 \to \Sigma^-\pi^+\pi^0) = \frac{3}{2}\sigma(pK^- \to \Sigma^0\pi^+\pi^-) = \frac{3}{2}\sigma(n\overline{K}^0 \to \Sigma^0\pi^+\pi^-)$$
$$= 8\sigma(pK^- \to \Sigma^0\pi^0\pi^0) = 8\sigma(n\overline{K}^0 \to \Sigma^0\pi^0\pi^0) = \frac{3}{2}\sigma(pK^- \to \Sigma^-\pi^+\pi^0) = \frac{3}{2}\sigma(n\overline{K}^0 \to \Sigma^+\pi^0\pi^-)$$

$$\boldsymbol{\sigma(pK^- \to \Sigma^-\pi^+\pi^0) + \sigma(pK^- \to \Sigma^+\pi^0\pi^-) + 2\sigma(p\overline{K}^0 \to \Sigma^+\pi^0\pi^0)}$$
$$\boldsymbol{= 2\sigma(pK^- \to \Sigma^0\pi^+\pi^-) + \sigma(p\overline{K}^0 \to \Sigma^0\pi^+\pi^0)}$$

$$\boldsymbol{\sigma(p\overline{K}^0 \to \Sigma^-\pi^+\pi^+) + \sigma(p\overline{K}^0 \to \Sigma^+\pi^+\pi^-)}$$
$$\boldsymbol{= 2\sigma(pK^- \to \Sigma^0\pi^0\pi^0) + \sigma(p\overline{K}^0 \to \Sigma^0\pi^+\pi^0) + \sigma(p\overline{K}^0 \to \Sigma^+\pi^0\pi^0)}$$

Reaction type: $NY \to N'Y'$

$$2\sigma(p\Lambda \to p\Sigma^0) = 2\sigma(n\Lambda \to n\Sigma^0) = \sigma(p\Lambda \to n\Sigma^+) = \sigma(n\Lambda \to p\Sigma^-)$$
$$\boldsymbol{\sigma(p\Lambda \to n\Sigma^+) = 2\sigma(p\Lambda \to p\Sigma^0)}$$

$$2\sigma(p\Sigma^0 \to p\Lambda) = 2\sigma(n\Sigma^0 \to n\Lambda) = \sigma(p\Sigma^- \to n\Lambda) = \sigma(n\Sigma^+ \to p\Lambda)$$
$$\boldsymbol{\sigma(p\Sigma^- \to n\Lambda) = 2\sigma(p\Sigma^0 \to p\Lambda)}$$

$$\sigma(p\Sigma^- \to p\Sigma^-) = \sigma(n\Sigma^+ \to n\Sigma^+) = \sigma(p\Sigma^+ \to p\Sigma^+) = \sigma(n\Sigma^- \to n\Sigma^-)$$
$$\sigma(p\Sigma^0 \to n\Sigma^+) = \sigma(n\Sigma^0 \to p\Sigma^-) = \sigma(p\Sigma^0 \to p\Sigma^0) = \sigma(n\Sigma^0 \to n\Sigma^0)$$

Reaction type: $\Delta N \to NNK\overline{K}$

$$\sigma(\Delta^{++}p \to ppK^+\overline{K}^0) = \sigma(\Delta^-n \to nnK^0K^-) = 2\sigma(\Delta^{++}n \to ppK^+K^-) = 2\sigma(\Delta^-p \to nnK^0\overline{K}^0)$$
$$= 2\sigma(\Delta^{++}n \to pnK^+\overline{K}^0) = 2\sigma(\Delta^-p \to npK^0K^-) = 2\sigma(\Delta^{++}n \to ppK^0\overline{K}^0) = 2\sigma(\Delta^-p \to nnK^+K^-)$$
$$= 2\sigma(\Delta^+p \to ppK^+K^-) = 2\sigma(\Delta^0n \to nnK^0\overline{K}^0) = 6\sigma(\Delta^+p \to ppK^0\overline{K}^0) = 6\sigma(\Delta^0n \to nnK^+K^-)$$
$$= 2\sigma(\Delta^+p \to pnK^+\overline{K}^0) = 2\sigma(\Delta^0n \to npK^0K^-) = 3\sigma(\Delta^+n \to ppK^0K^-) = 3\sigma(\Delta^0p \to nnK^+\overline{K}^0)$$
$$= 6\sigma(\Delta^+n \to pnK^+K^-) = 6\sigma(\Delta^0p \to npK^0\overline{K}^0) = 3\sigma(\Delta^+n \to pnK^0\overline{K}^0) = 3\sigma(\Delta^0p \to npK^+K^-)$$
$$= 2\sigma(\Delta^+n \to nnK^+\overline{K}^0) = 2\sigma(\Delta^0p \to ppK^0K^-)$$

$$\boldsymbol{3\sigma(\Delta^{+}n \to nnK^{+}\overline{K}^{0}) = 2\sigma(\Delta^{++}n \to pnK^{+}\overline{K}^{0})}$$

$$\begin{aligned}\boldsymbol{3\sigma(\Delta^{+}n \to pnK^{0}\overline{K}^{0}) + \sigma(\Delta^{++}n \to pnK^{+}\overline{K}^{0})}\\ \boldsymbol{= 3\sigma(\Delta^{+}p \to ppK^{+}K^{-}) + \sigma(\Delta^{++}n \to ppK^{0}\overline{K}^{0})}\end{aligned}$$

$$\begin{aligned}\boldsymbol{3\sigma(\Delta^{+}n \to pnK^{+}K^{-}) + \sigma(\Delta^{++}n \to pnK^{+}\overline{K}^{0})}\\ \boldsymbol{= 3\sigma(\Delta^{+}p \to ppK^{0}\overline{K}^{0}) + \sigma(\Delta^{++}n \to ppK^{+}K^{-})}\end{aligned}$$

$$\begin{aligned}\boldsymbol{3\sigma(\Delta^{+}n \to ppK^{0}K^{-}) + 3\sigma(\Delta^{+}p \to ppK^{0}\overline{K}^{0}) + 3\sigma(\Delta^{+}p \to ppK^{+}K^{-})}\\ \boldsymbol{= 2\sigma(\Delta^{++}n \to pnK^{+}\overline{K}^{0}) + \sigma(\Delta^{++}n \to ppK^{0}\overline{K}^{0})}\\ \boldsymbol{+\sigma(\Delta^{++}n \to ppK^{+}K^{-}) + \sigma(\Delta^{++}p \to ppK^{+}\overline{K}^{0})}\end{aligned}$$

$$\begin{aligned}\boldsymbol{3\sigma(\Delta^{+}p \to pnK^{+}\overline{K}^{0}) + 3\sigma(\Delta^{+}p \to ppK^{0}\overline{K}^{0}) + 3\sigma(\Delta^{+}p \to ppK^{+}K^{-})}\\ \boldsymbol{= \sigma(\Delta^{++}n \to pnK^{+}\overline{K}^{0}) + \sigma(\Delta^{++}n \to ppK^{0}\overline{K}^{0})}\\ \boldsymbol{+\sigma(\Delta^{++}n \to ppK^{+}K^{-}) + 2\sigma(\Delta^{++}p \to ppK^{+}\overline{K}^{0})}\end{aligned}$$

Reaction type: $\Delta N \to BYK$

$$\begin{aligned}\sigma(\Delta^{++}n \to p\Lambda K^{+}) = \sigma(\Delta^{-}p \to n\Lambda K^{0}) = 3\sigma(\Delta^{+}p \to p\Lambda K^{+}) = 3\sigma(\Delta^{0}n \to n\Lambda K^{0})\\ = 3\sigma(\Delta^{+}n \to p\Lambda K^{0}) = 3\sigma(\Delta^{0}p \to n\Lambda K^{+}) = 3\sigma(\Delta^{+}n \to n\Lambda K^{+}) = 3\sigma(\Delta^{0}p \to p\Lambda K^{0})\end{aligned}$$

$$\boldsymbol{\sigma(\Delta^{++}n \to p\Lambda K^{+}) = 3\sigma(\Delta^{+}p \to p\Lambda K^{+}) = 3\sigma(\Delta^{+}p \to p\Lambda K^{0}) = 3\sigma(\Delta^{+}n \to p\Lambda K^{+})}$$

$$\begin{aligned}\sigma(\Delta^{++}p \to p\Sigma^{+}K^{+}) = \sigma(\Delta^{-}n \to n\Sigma^{-}K^{0}) = 2\sigma(\Delta^{++}n \to p\Sigma^{+}K^{0}) = 2\sigma(\Delta^{-}p \to n\Sigma^{-}K^{+})\\ = 2\sigma(\Delta^{++}n \to p\Sigma^{0}K^{+}) = 2\sigma(\Delta^{-}p \to n\Sigma^{0}K^{0}) = 2\sigma(\Delta^{++}n \to n\Sigma^{+}K^{+}) = 2\sigma(\Delta^{-}p \to p\Sigma^{-}K^{0})\\ = 3\sigma(\Delta^{+}p \to p\Sigma^{+}K^{0}) = 3\sigma(\Delta^{0}n \to n\Sigma^{-}K^{+}) = 3\sigma(\Delta^{+}p \to p\Sigma^{0}K^{+}) = 3\sigma(\Delta^{0}n \to n\Sigma^{0}K^{0})\\ = 2\sigma(\Delta^{+}p \to n\Sigma^{+}K^{+}) = 2\sigma(\Delta^{0}n \to p\Sigma^{-}K^{0}) = 2\sigma(\Delta^{+}n \to p\Sigma^{0}K^{0}) = 2\sigma(\Delta^{0}p \to n\Sigma^{0}K^{+})\\ = 3\sigma(\Delta^{+}n \to p\Sigma^{-}K^{+}) = 3\sigma(\Delta^{0}p \to n\Sigma^{+}K^{0}) = 3\sigma(\Delta^{+}n \to n\Sigma^{+}K^{0}) = 3\sigma(\Delta^{0}p \to p\Sigma^{-}K^{+})\\ = 3\sigma(\Delta^{+}n \to n\Sigma^{0}K^{+}) = 3\sigma(\Delta^{0}p \to p\Sigma^{0}K^{0})\end{aligned}$$

$$\boldsymbol{3\sigma(\Delta^{+}n \to n\Sigma^{0}K^{+}) + \sigma(\Delta^{++}n \to p\Sigma^{0}K^{+}) = 3\sigma(\Delta^{+}p \to p\Sigma^{+}K^{0}) + \sigma(\Delta^{++}n \to n\Sigma^{+}K^{+})}$$

$$\boldsymbol{3\sigma(\Delta^{+}n \to n\Sigma^{+}K^{0}) + \sigma(\Delta^{++}p \to p\Sigma^{+}K^{+}) = 3\sigma(\Delta^{+}p \to p\Sigma^{0}K^{+}) + \sigma(\Delta^{++}n \to p\Sigma^{0}K^{+})}$$

$$\boldsymbol{3\sigma(\Delta^{+}n \to p\Sigma^{-}K^{+}) = 2\sigma(\Delta^{++}n \to p\Sigma^{0}K^{+})}$$

$$\begin{gathered}\boldsymbol{3\sigma(\Delta^{+}n \to p\Sigma^{0}K^{0}) + 3\sigma(\Delta^{+}p \to p\Sigma^{0}K^{+}) + 3\sigma(\Delta^{+}p \to p\Sigma^{+}K^{0})} \\ \boldsymbol{= \sigma(\Delta^{++}n \to n\Sigma^{+}K^{+}) + 2\sigma(\Delta^{++}n \to p\Sigma^{+}K^{0}) + 2\sigma(\Delta^{++}p \to p\Sigma^{+}K^{+})}\end{gathered}$$

$$\begin{gathered}\boldsymbol{3\sigma(\Delta^{+}p \to n\Sigma^{+}K^{+}) + 3\sigma(\Delta^{+}p \to p\Sigma^{0}K^{+}) + 3\sigma(\Delta^{+}p \to p\Sigma^{+}K^{0})} \\ \boldsymbol{= \sigma(\Delta^{++}n \to n\Sigma^{+}K^{+}) + \sigma(\Delta^{++}n \to p\Sigma^{0}K^{+})} \\ \boldsymbol{+\sigma(\Delta^{++}n \to p\Sigma^{+}K^{0}) + 2\sigma(\Delta^{++}p \to p\Sigma^{+}K^{+})}\end{gathered}$$

$$\begin{gathered}3\sigma(\Delta^{++}p \to \Lambda K^{+}\Delta^{++}) = 3\sigma(\Delta^{-}n \to \Lambda K^{0}\Delta^{-}) = 4\sigma(\Delta^{++}n \to \Lambda K^{+}\Delta^{+}) = 4\sigma(\Delta^{-}p \to \Lambda K^{0}\Delta^{0}) \\ = 3\sigma(\Delta^{++}n \to \Lambda K^{0}\Delta^{++}) = 3\sigma(\Delta^{-}p \to \Lambda K^{+}\Delta^{-}) = 4\sigma(\Delta^{+}p \to \Lambda K^{+}\Delta^{+}) = 4\sigma(\Delta^{0}n \to \Lambda K^{0}\Delta^{0}) \\ = 6\sigma(\Delta^{+}p \to \Lambda K^{0}\Delta^{++}) = 6\sigma(\Delta^{0}n \to \Lambda K^{+}\Delta^{-}) = 3\sigma(\Delta^{+}n \to \Lambda K^{+}\Delta^{0}) = 3\sigma(\Delta^{0}p \to \Lambda K^{0}\Delta^{+}) \\ = 6\sigma(\Delta^{+}n \to \Lambda K^{0}\Delta^{+}) = 6\sigma(\Delta^{0}p \to \Lambda K^{+}\Delta^{0})\end{gathered}$$

$$\boldsymbol{3\sigma(\Delta^{+}n \to \Lambda K^{0}\Delta^{+}) + 2\sigma(\Delta^{++}n \to \Lambda K^{+}\Delta^{+}) = 2\sigma(\Delta^{++}n \to \Lambda K^{0}\Delta^{++}) + \sigma(\Delta^{++}p \to \Lambda K^{+}\Delta^{++})}$$

$$\boldsymbol{3\sigma(\Delta^{+}n \to \Lambda K^{+}\Delta^{0}) = 4\sigma(\Delta^{++}n \to \Lambda K^{+}\Delta^{+})}$$

$$\boldsymbol{3\sigma(\Delta^{+}p \to \Lambda K^{+}\Delta^{+}) + 2\sigma(\Delta^{++}n \to \Lambda K^{+}\Delta^{+}) = \sigma(\Delta^{++}n \to \Lambda K^{0}\Delta^{++}) + 2\sigma(\Delta^{++}p \to \Lambda K^{+}\Delta^{++})}$$

$$\begin{gathered}6\sigma(\Delta^{++}p \to \Sigma^{0}K^{+}\Delta^{++}) = 6\sigma(\Delta^{-}n \to \Sigma^{0}K^{0}\Delta^{-}) = 6\sigma(\Delta^{++}n \to \Sigma^{0}K^{+}\Delta^{+}) = 6\sigma(\Delta^{-}p \to \Sigma^{0}K^{0}\Delta^{0}) \\ = 12\sigma(\Delta^{++}p \to \Sigma^{+}K^{0}\Delta^{++}) = 12\sigma(\Delta^{-}n \to \Sigma^{-}K^{+}\Delta^{-}) = 12\sigma(\Delta^{++}n \to \Sigma^{0}K^{0}\Delta^{++}) = 12\sigma(\Delta^{-}p \to \Sigma^{0}K^{+}\Delta^{-}) \\ = 2\sigma(\Delta^{++}n \to \Sigma^{+}K^{+}\Delta^{0}) = 2\sigma(\Delta^{-}p \to \Sigma^{-}K^{0}\Delta^{+}) = 2\sigma(\Delta^{++}n \to \Sigma^{+}K^{0}\Delta^{+}) = 2\sigma(\Delta^{-}p \to \Sigma^{-}K^{+}\Delta^{0}) \\ = 3\sigma(\Delta^{++}n \to \Sigma^{-}K^{+}\Delta^{++}) = 3\sigma(\Delta^{-}p \to \Sigma^{+}K^{0}\Delta^{-}) = 3\sigma(\Delta^{+}p \to \Sigma^{0}K^{0}\Delta^{++}) = 3\sigma(\Delta^{0}n \to \Sigma^{0}K^{+}\Delta^{-}) \\ = 6\sigma(\Delta^{+}p \to \Sigma^{+}K^{+}\Delta^{0}) = 6\sigma(\Delta^{0}n \to \Sigma^{-}K^{0}\Delta^{+}) = 6\sigma(\Delta^{+}p \to \Sigma^{-}K^{+}\Delta^{++}) = 6\sigma(\Delta^{0}n \to \Sigma^{+}K^{0}\Delta^{-}) \\ = 12\sigma(\Delta^{+}p \to \Sigma^{0}K^{+}\Delta^{+}) = 12\sigma(\Delta^{0}n \to \Sigma^{0}K^{0}\Delta^{0}) = 12\sigma(\Delta^{+}n \to \Sigma^{0}K^{0}\Delta^{+}) = 12\sigma(\Delta^{0}p \to \Sigma^{0}K^{+}\Delta^{0}) \\ = 6\sigma(\Delta^{+}p \to \Sigma^{+}K^{0}\Delta^{+}) = 6\sigma(\Delta^{0}n \to \Sigma^{-}K^{+}\Delta^{0}) = 6\sigma(\Delta^{+}n \to \Sigma^{+}K^{+}\Delta^{-}) = 6\sigma(\Delta^{0}p \to \Sigma^{-}K^{0}\Delta^{++}) \\ = 3\sigma(\Delta^{+}n \to \Sigma^{0}K^{+}\Delta^{0}) = 3\sigma(\Delta^{0}p \to \Sigma^{0}K^{0}\Delta^{+}) = 6\sigma(\Delta^{+}n \to \Sigma^{-}K^{+}\Delta^{+}) = 6\sigma(\Delta^{0}p \to \Sigma^{+}K^{0}\Delta^{0}) \\ = 6\sigma(\Delta^{+}n \to \Sigma^{+}K^{0}\Delta^{0}) = 6\sigma(\Delta^{0}p \to \Sigma^{-}K^{+}\Delta^{+}) = 6\sigma(\Delta^{+}n \to \Sigma^{-}K^{0}\Delta^{++}) = 6\sigma(\Delta^{0}p \to \Sigma^{+}K^{+}\Delta^{-})\end{gathered}$$

$$\begin{gathered}\boldsymbol{2\sigma(\Delta^{+}n \to \Sigma^{-}K^{0}\Delta^{++}) + 2\sigma(\Delta^{++}p \to \Sigma^{+}K^{+}\Delta^{+})} \\ \boldsymbol{= 3\sigma(\Delta^{+}p \to \Sigma^{+}K^{+}\Delta^{0}) + \sigma(\Delta^{++}n \to \Sigma^{+}K^{+}\Delta^{0})}\end{gathered}$$

$$\begin{gathered}\boldsymbol{12\sigma(\Delta^{+}n \to \Sigma^{0}K^{0}\Delta^{+}) + 15\sigma(\Delta^{+}p \to \Sigma^{+}K^{+}\Delta^{0}) + 2\sigma(\Delta^{++}n \to \Sigma^{+}K^{0}\Delta^{+})} \\ \boldsymbol{+2\sigma(\Delta^{++}n \to \Sigma^{-}K^{+}\Delta^{++}) + 9\sigma(\Delta^{++}n \to \Sigma^{+}K^{+}\Delta^{0}) + 2\sigma(\Delta^{++}p \to \Sigma^{+}K^{0}\Delta^{++})} \\ \boldsymbol{+4\sigma(\Delta^{++}p \to \Sigma^{0}K^{+}\Delta^{++}) = 18\sigma(\Delta^{+}p \to \Sigma^{0}K^{+}\Delta^{+})} \\ \boldsymbol{+6\sigma(\Delta^{++}n \to \Sigma^{0}K^{0}\Delta^{++}) + 8\sigma(\Delta^{++}n \to \Sigma^{0}K^{+}\Delta^{+}) + 18\sigma(\Delta^{++}p \to \Sigma^{+}K^{+}\Delta^{+})}\end{gathered}$$

$$\begin{gathered}\mathbf{6\sigma(\Delta^{+}n\to\Sigma^{+}K^{0}\Delta^{0})+9\sigma(\Delta^{+}p\to\Sigma^{+}K^{+}\Delta^{0})+2\sigma(\Delta^{++}n\to\Sigma^{-}K^{+}\Delta^{++})}\\ \mathbf{+9\sigma(\Delta^{++}n\to\Sigma^{+}K^{+}\Delta^{0})+2\sigma(\Delta^{++}p\to\Sigma^{+}K^{0}\Delta^{++})}\\ \mathbf{=6\sigma(\Delta^{+}p\to\Sigma^{0}K^{+}\Delta^{+})+2\sigma(\Delta^{++}n\to\Sigma^{0}K^{0}\Delta^{++})+6\sigma(\Delta^{++}n\to\Sigma^{+}K^{0}\Delta^{+})}\\ \mathbf{+8\sigma(\Delta^{++}n\to\Sigma^{0}K^{+}\Delta^{+})+10\sigma(\Delta^{++}p\to\Sigma^{+}K^{+}\Delta^{+})}\end{gathered}$$

$$\begin{gathered}\mathbf{12\sigma(\Delta^{+}n\to\Sigma^{-}K^{+}\Delta^{+})+18\sigma(\Delta^{+}p\to\Sigma^{0}K^{+}\Delta^{+})+6\sigma(\Delta^{++}n\to\Sigma^{+}K^{0}\Delta^{+})}\\ \mathbf{+16\sigma(\Delta^{++}n\to\Sigma^{0}K^{+}\Delta^{+})+18\sigma(\Delta^{++}p\to\Sigma^{+}K^{+}\Delta^{+})}\\ \mathbf{=9\sigma(\Delta^{+}p\to\Sigma^{+}K^{+}\Delta^{0})+2\sigma(\Delta^{++}n\to\Sigma^{0}K^{0}\Delta^{++})+10\sigma(\Delta^{++}n\to\Sigma^{-}K^{+}\Delta^{++})}\\ \mathbf{+15\sigma(\Delta^{++}n\to\Sigma^{+}K^{+}\Delta^{0})+6\sigma(\Delta^{++}p\to\Sigma^{+}K^{0}\Delta^{++})+8\sigma(\Delta^{++}p\to\Sigma^{0}K^{+}\Delta^{++})}\end{gathered}$$

$$\begin{gathered}\mathbf{6\sigma(\Delta^{+}n\to\Sigma^{0}K^{+}\Delta^{0})+6\sigma(\Delta^{+}p\to\Sigma^{0}K^{+}\Delta^{+})+2\sigma(\Delta^{++}n\to\Sigma^{0}K^{0}\Delta^{++})}\\ \mathbf{+2\sigma(\Delta^{++}p\to\Sigma^{+}K^{+}\Delta^{+})=3\sigma(\Delta^{+}p\to\Sigma^{+}K^{+}\Delta^{0})+2\sigma(\Delta^{++}n\to\Sigma^{+}K^{0}\Delta^{+})}\\ \mathbf{+2\sigma(\Delta^{++}n\to\Sigma^{-}K^{+}\Delta^{++})+\sigma(\Delta^{++}n\to\Sigma^{+}K^{+}\Delta^{0})+2\sigma(\Delta^{++}p\to\Sigma^{+}K^{0}\Delta^{++})}\end{gathered}$$

$$\begin{gathered}\mathbf{4\sigma(\Delta^{+}p\to\Sigma^{0}K^{0}\Delta^{++})+6\sigma(\Delta^{+}p\to\Sigma^{0}K^{+}\Delta^{+})+2\sigma(\Delta^{++}n\to\Sigma^{0}K^{0}\Delta^{++})}\\ \mathbf{+4\sigma(\Delta^{++}n\to\Sigma^{0}K^{+}\Delta^{+})+2\sigma(\Delta^{++}p\to\Sigma^{+}K^{+}\Delta^{+})}\\ \mathbf{=3\sigma(\Delta^{+}p\to\Sigma^{+}K^{+}\Delta^{0})+2\sigma(\Delta^{++}n\to\Sigma^{+}K^{0}\Delta^{+})+2\sigma(\Delta^{++}n\to\Sigma^{-}K^{+}\Delta^{++})}\\ \mathbf{+5\sigma(\Delta^{++}n\to\Sigma^{+}K^{+}\Delta^{0})+2\sigma(\Delta^{++}p\to\Sigma^{+}K^{0}\Delta^{++})}\end{gathered}$$

$$\begin{gathered}\mathbf{6\sigma(\Delta^{+}p\to\Sigma^{+}K^{0}\Delta^{+})+6\sigma(\Delta^{+}p\to\Sigma^{0}K^{+}\Delta^{+})+4\sigma(\Delta^{++}n\to\Sigma^{+}K^{0}\Delta^{+})}\\ \mathbf{+4\sigma(\Delta^{++}n\to\Sigma^{0}K^{+}\Delta^{+})+8\sigma(\Delta^{++}p\to\Sigma^{+}K^{+}\Delta^{+})}\\ \mathbf{=3\sigma(\Delta^{+}p\to\Sigma^{+}K^{+}\Delta^{0})+2\sigma(\Delta^{++}n\to\Sigma^{0}K^{0}\Delta^{++})+2\sigma(\Delta^{++}n\to\Sigma^{-}K^{+}\Delta^{++})}\\ \mathbf{+5\sigma(\Delta^{++}n\to\Sigma^{+}K^{+}\Delta^{0})+4\sigma(\Delta^{++}p\to\Sigma^{+}K^{0}\Delta^{++})+4\sigma(\Delta^{++}p\to\Sigma^{0}K^{+}\Delta^{++})}\end{gathered}$$

$$\begin{gathered}\mathbf{4\sigma(\Delta^{+}p\to\Sigma^{-}K^{+}\Delta^{++})+9\sigma(\Delta^{+}p\to\Sigma^{+}K^{+}\Delta^{0})+2\sigma(\Delta^{++}n\to\Sigma^{-}K^{+}\Delta^{++})}\\ \mathbf{+7\sigma(\Delta^{++}n\to\Sigma^{+}K^{+}\Delta^{0})+2\sigma(\Delta^{++}p\to\Sigma^{+}K^{0}\Delta^{++})}\\ \mathbf{=6\sigma(\Delta^{+}p\to\Sigma^{0}K^{+}\Delta^{+})+2\sigma(\Delta^{++}n\to\Sigma^{0}K^{0}\Delta^{++})+2\sigma(\Delta^{++}n\to\Sigma^{+}K^{0}\Delta^{+})}\\ \mathbf{+8\sigma(\Delta^{++}n\to\Sigma^{0}K^{+}\Delta^{+})+10\sigma(\Delta^{++}p\to\Sigma^{+}K^{+}\Delta^{+})}\end{gathered}$$

Reaction type: $\pi N\to YK$

$$2\sigma(\pi^{0}p\to\Lambda K^{+})=2\sigma(\pi^{0}n\to\Lambda K^{0})=\sigma(\pi^{-}p\to\Lambda K^{0})=\sigma(\pi^{+}n\to\Lambda K^{+})$$

$$\boldsymbol{\sigma(\pi^{-}p\to\Lambda K^{0})=2\sigma(\pi^{0}p\to\Lambda K^{+})}$$

The case of the reaction $\pi N\to\Sigma K$ is given is some detail in subsection IV.4.3.

Reaction type: $\pi N \to YK\pi$

$$\sigma(\pi^+ p \to \Lambda K^+ \pi^+) = \sigma(\pi^- n \to \Lambda K^0 \pi^-) = \sigma(\pi^0 p \to \Lambda K^0 \pi^+) = \sigma(\pi^- p \to \Lambda K^0 \pi^0)$$
$$= \sigma(\pi^+ n \to \Lambda K^+ \pi^0) = \sigma(\pi^0 n \to \Lambda K^+ \pi^-) = 2\sigma(\pi^0 p \to \Lambda K^+ \pi^0) = 2\sigma(\pi^0 n \to \Lambda K^0 \pi^0)$$
$$= \sigma(\pi^- p \to \Lambda K^+ \pi^-) = \sigma(\pi^+ n \to \Lambda K^0 \pi^+)$$

$$\boldsymbol{\sigma(\pi^0 p \to \Lambda K^0 \pi^+) = \sigma(\pi^- p \to \Lambda K^0 \pi^0)}$$

$$\boldsymbol{\sigma(\pi^- p \to \Lambda \pi^- K^+) + \sigma(\pi^+ p \to \Lambda \pi^+ K^+) = 2\sigma(\pi^0 p \to \Lambda \pi^0 K^+) + \sigma(\pi^0 p \to \Lambda \pi^+ K^0)}$$

$$\frac{4}{5}\sigma(\pi^+ p \to \Sigma^+ K^0 \pi^+) = \frac{4}{5}\sigma(\pi^- n \to \Sigma^- K^+ \pi^-) = \frac{4}{3}\sigma(\pi^+ p \to \Sigma^+ K^+ \pi^0) = \frac{4}{3}\sigma(\pi^- n \to \Sigma^- K^0 \pi^0)$$
$$= 4\sigma(\pi^+ p \to \Sigma^0 K^+ \pi^+) = 4\sigma(\pi^- n \to \Sigma^0 K^0 \pi^-) = 2\sigma(\pi^0 p \to \Sigma^+ K^0 \pi^0) = 2\sigma(\pi^0 n \to \Sigma^- K^+ \pi^0)$$
$$= 2\sigma(\pi^0 p \to \Sigma^+ K^+ \pi^-) = 2\sigma(\pi^0 n \to \Sigma^- K^0 \pi^+) = \frac{4}{3}\sigma(\pi^0 p \to \Sigma^0 K^0 \pi^+) = \frac{4}{3}\sigma(\pi^0 n \to \Sigma^0 K^+ \pi^-)$$
$$= \frac{8}{3}\sigma(\pi^0 p \to \Sigma^0 K^+ \pi^0) = \frac{8}{3}\sigma(\pi^0 n \to \Sigma^0 K^0 \pi^0) = 2\sigma(\pi^0 p \to \Sigma^- K^+ \pi^+) = 2\sigma(\pi^0 n \to \Sigma^+ K^0 \pi^-)$$
$$= \frac{8}{3}\sigma(\pi^- p \to \Sigma^+ K^0 \pi^-) = \frac{8}{3}\sigma(\pi^+ n \to \Sigma^- K^+ \pi^+) = \frac{8}{5}\sigma(\pi^- p \to \Sigma^0 K^0 \pi^0) = \frac{8}{5}\sigma(\pi^+ n \to \Sigma^0 K^+ \pi^0)$$
$$= \frac{8}{5}\sigma(\pi^- p \to \Sigma^0 K^+ \pi^-) = \frac{8}{5}\sigma(\pi^+ n \to \Sigma^0 K^0 \pi^+) = \sigma(\pi^- p \to \Sigma^- K^0 \pi^+) = \sigma(\pi^+ n \to \Sigma^+ K^+ \pi^-)$$
$$= \frac{8}{3}\sigma(\pi^- p \to \Sigma^- K^+ \pi^0) = \frac{8}{3}\sigma(\pi^+ n \to \Sigma^+ K^0 \pi^0)$$

$$\boldsymbol{\sigma(\pi^- p \to \Sigma^- \pi^0 K^+) + \sigma(\pi^- p \to \Sigma^0 \pi^0 K^0) + \sigma(\pi^+ p \to \Sigma^+ \pi^0 K^+)}$$
$$\boldsymbol{= \sigma(\pi^0 p \to \Sigma^- \pi^+ K^+) + \sigma(\pi^0 p \to \Sigma^0 \pi^+ K^0) + \sigma(\pi^0 p \to \Sigma^+ \pi^- K^+)}$$

$$\boldsymbol{\sigma(\pi^- p \to \Sigma^- \pi^+ K^0) + \sigma(\pi^- p \to \Sigma^+ \pi^- K^0) + \sigma(\pi^+ p \to \Sigma^+ \pi^+ K^0)}$$
$$\boldsymbol{= \sigma(\pi^- p \to \Sigma^0 \pi^0 K^0) + 2\sigma(\pi^0 p \to \Sigma^0 \pi^0 K^+) + \sigma(\pi^0 p \to \Sigma^0 \pi^+ K^0) + \sigma(\pi^0 p \to \Sigma^+ \pi^0 K^0)}$$

$$\boldsymbol{\sigma(\pi^- p \to \Sigma^0 \pi^- K^+) + \sigma(\pi^- p \to \Sigma^0 \pi^0 K^0) + \sigma(\pi^+ p \to \Sigma^0 \pi^+ K^+)}$$
$$\boldsymbol{= \sigma(\pi^0 p \to \Sigma^- \pi^+ K^+) + \sigma(\pi^0 p \to \Sigma^+ \pi^- K^+) + \sigma(\pi^0 p \to \Sigma^+ \pi^0 K^0)}$$

Reaction type: $\pi N \to NK\overline{K}$

$$2\sigma(\pi^+p \to pK^+\overline{K}^0) = 2\sigma(\pi^-n \to nK^0K^-) = 4\sigma(\pi^0p \to pK^+K^-) = 4\sigma(\pi^0n \to nK^0\overline{K}^0)$$
$$= 4\sigma(\pi^0p \to pK^0\overline{K}^0) = 4\sigma(\pi^0n \to nK^+K^-) = \sigma(\pi^0p \to nK^+\overline{K}^0) = \sigma(\pi^0n \to pK^0K^-)$$
$$= 2\sigma(\pi^-p \to pK^0K^-) = 2\sigma(\pi^+n \to nK^+\overline{K}^0) = \sigma(\pi^-p \to nK^+K^-) = \sigma(\pi^+n \to pK^0\overline{K}^0)$$
$$= \sigma(\pi^-p \to nK^0\overline{K}^0) = \sigma(\pi^+n \to pK^+K^-)$$

$$\boldsymbol{\sigma(\pi^-p \to nK^0\overline{K}^0) + \sigma(\pi^-p \to nK^+K^-) + \sigma(\pi^-p \to pK^0K^-) + \sigma(\pi^+p \to pK^+\overline{K}^0)}$$
$$\boldsymbol{= 2\sigma(\pi^0p \to nK^+\overline{K}^0) + 2\sigma(\pi^0p \to pK^0\overline{K}^0) + 2\sigma(\pi^0p \to pK^+K^-)}$$

Reaction type: $\pi N \to YK\pi\pi$

$$\sigma(\pi^+p \to \Lambda K^0\pi^+\pi^+) = \sigma(\pi^-n \to \Lambda K^+\pi^-\pi^-) \quad = \sigma(\pi^+p \to \Lambda K^+\pi^+\pi^0) = \sigma(\pi^-n \to \Lambda K^0\pi^0\pi^-)$$
$$= 2\sigma(\pi^0p \to \Lambda K^0\pi^+\pi^0) = 2\sigma(\pi^0n \to \Lambda K^+\pi^0\pi^-) \quad = \sigma(\pi^0p \to \Lambda K^+\pi^+\pi^-) = \sigma(\pi^0n \to \Lambda K^0\pi^+\pi^-)$$
$$= 4\sigma(\pi^0p \to \Lambda K^+\pi^0\pi^0) = 4\sigma(\pi^0n \to \Lambda K^0\pi^0\pi^0) \quad = \sigma(\pi^-p \to \Lambda K^0\pi^+\pi^-) = \sigma(\pi^+n \to \Lambda K^+\pi^+\pi^-)$$
$$= 2\sigma(\pi^-p \to \Lambda K^0\pi^0\pi^0) = 2\sigma(\pi^+n \to \Lambda K^+\pi^0\pi^0) \quad = \sigma(\pi^-p \to \Lambda K^+\pi^0\pi^-) = \sigma(\pi^+n \to \Lambda K^0\pi^+\pi^0)$$

$$\boldsymbol{\sigma(\pi^-p \to \Lambda K^+\pi^0\pi^-) + 2\sigma(\pi^-p \to \Lambda K^0\pi^+\pi^-)}$$
$$\boldsymbol{+\sigma(\pi^+p \to \Lambda K^+\pi^+\pi^0) + 2\sigma(\pi^+p \to \Lambda K^0\pi^+\pi^+)}$$
$$\boldsymbol{= 4\sigma(\pi^0p \to \Lambda K^+\pi^0\pi^0) + 2\sigma(\pi^0p \to \Lambda K^+\pi^+\pi^-) + 3\sigma(\pi^0p \to \Lambda K^0\pi^+\pi^0)}$$

$$\boldsymbol{\sigma(\pi^-p \to \Lambda K^0\pi^0\pi^0) + 2\sigma(\pi^0p \to \Lambda K^+\pi^0\pi^0) + \sigma(\pi^0p \to \Lambda K^0\pi^+\pi^0)}$$
$$\boldsymbol{= \sigma(\pi^-p \to \Lambda K^0\pi^+\pi^-) + \sigma(\pi^+p \to \Lambda K^0\pi^+\pi^+)}$$

$$\sigma(\pi^+p \to \Sigma^+K^+\pi^+\pi^-) = \sigma(\pi^-n \to \Sigma^-K^0\pi^+\pi^-) = 4\sigma(\pi^+p \to \Sigma^+K^+\pi^0\pi^0)$$
$$= 4\sigma(\pi^-n \to \Sigma^-K^0\pi^0\pi^0) = 2\sigma(\pi^+p \to \Sigma^0K^+\pi^+\pi^0) = 2\sigma(\pi^-n \to \Sigma^0K^0\pi^0\pi^-)$$
$$= 4\sigma(\pi^+p \to \Sigma^-K^+\pi^+\pi^+) = 4\sigma(\pi^-n \to \Sigma^+K^0\pi^-\pi^-) = \sigma(\pi^+p \to \Sigma^+K^0\pi^+\pi^0)$$
$$= \sigma(\pi^-n \to \Sigma^-K^+\pi^0\pi^-) = 4\sigma(\pi^+p \to \Sigma^0K^0\pi^+\pi^+) = 4\sigma(\pi^-n \to \Sigma^0K^+\pi^-\pi^-)$$
$$= 2\sigma(\pi^0p \to \Sigma^+K^+\pi^0\pi^-) = 2\sigma(\pi^0n \to \Sigma^-K^0\pi^+\pi^0) = 2\sigma(\pi^0p \to \Sigma^0K^+\pi^+\pi^-)$$
$$= 2\sigma(\pi^0n \to \Sigma^0K^0\pi^+\pi^-) = 4\sigma(\pi^0p \to \Sigma^0K^+\pi^0\pi^0) = 4\sigma(\pi^0n \to \Sigma^0K^0\pi^0\pi^0)$$
$$= 4\sigma(\pi^0p \to \Sigma^-K^+\pi^+\pi^0) = 4\sigma(\pi^0n \to \Sigma^+K^0\pi^0\pi^-) = \sigma(\pi^0p \to \Sigma^+K^0\pi^+\pi^-)$$
$$= \sigma(\pi^0n \to \Sigma^-K^+\pi^+\pi^-) = 4\sigma(\pi^0p \to \Sigma^+K^0\pi^0\pi^0) = 4\sigma(\pi^0n \to \Sigma^-K^+\pi^0\pi^0)$$
$$= 4\sigma(\pi^0p \to \Sigma^0K^0\pi^+\pi^0) = 4\sigma(\pi^0n \to \Sigma^0K^+\pi^0\pi^-) = 2\sigma(\pi^0p \to \Sigma^-K^0\pi^+\pi^+)$$
$$= 2\sigma(\pi^0n \to \Sigma^+K^+\pi^-\pi^-) = 4\sigma(\pi^-p \to \Sigma^+K^+\pi^-\pi^-) = 4\sigma(\pi^+n \to \Sigma^-K^0\pi^+\pi^+)$$
$$= 2\sigma(\pi^-p \to \Sigma^0K^+\pi^0\pi^-) = 2\sigma(\pi^+n \to \Sigma^0K^0\pi^+\pi^0) = 4\sigma(\pi^-p \to \Sigma^-K^+\pi^+\pi^-)$$
$$= 4\sigma(\pi^+n \to \Sigma^+K^0\pi^+\pi^-) = 4\sigma(\pi^-p \to \Sigma^-K^+\pi^0\pi^0) = 4\sigma(\pi^+n \to \Sigma^+K^0\pi^0\pi^0)$$
$$= 2\sigma(\pi^-p \to \Sigma^+K^0\pi^0\pi^-) = 2\sigma(\pi^+n \to \Sigma^-K^+\pi^+\pi^0) = \sigma(\pi^-p \to \Sigma^0K^0\pi^+\pi^-)$$
$$= \sigma(\pi^+n \to \Sigma^0K^+\pi^+\pi^-) = 2\sigma(\pi^-p \to \Sigma^0K^0\pi^0\pi^0) = 2\sigma(\pi^+n \to \Sigma^0K^+\pi^0\pi^0)$$
$$= 2\sigma(\pi^-p \to \Sigma^-K^0\pi^+\pi^0) = 2\sigma(\pi^+n \to \Sigma^+K^+\pi^0\pi^-)$$

$$\sigma(\pi^- p \to \Sigma^- K^0 \pi^+ \pi^0) + \sigma(\pi^- p \to \Sigma^+ K^0 \pi^0 \pi^-) + \sigma(\pi^- p \to \Sigma^- K^+ \pi^0 \pi^0)$$
$$+\sigma(\pi^- p \to \Sigma^- K^+ \pi^+ \pi^-) + \sigma(\pi^- p \to \Sigma^+ K^+ \pi^- \pi^-) + \sigma(\pi^+ p \to \Sigma^+ K^0 \pi^+ \pi^0)$$
$$+\sigma(\pi^+ p \to \Sigma^- K^+ \pi^+ \pi^+) + \sigma(\pi^+ p \to \Sigma^+ K^+ \pi^0 \pi^0) + \sigma(\pi^+ p \to \Sigma^+ K^+ \pi^+ \pi^-)$$
$$= \sigma(\pi^0 p \to \Sigma^- K^0 \pi^+ \pi^+) + 2\sigma(\pi^0 p \to \Sigma^0 K^0 \pi^+ \pi^0) + \sigma(\pi^0 p \to \Sigma^+ K^0 \pi^0 \pi^0)$$
$$+\sigma(\pi^0 p \to \Sigma^+ K^0 \pi^+ \pi^-) + \sigma(\pi^0 p \to \Sigma^- K^+ \pi^+ \pi^0) + 2\sigma(\pi^0 p \to \Sigma^0 K^+ \pi^0 \pi^0)$$
$$+2\sigma(\pi^0 p \to \Sigma^0 K^+ \pi^+ \pi^-) + \sigma(\pi^0 p \to \Sigma^+ K^+ \pi^0 \pi^-)$$

$$\sigma(\pi^- p \to \Sigma^- K^+ \pi^+ \pi^-) + \sigma(\pi^- p \to \Sigma^+ K^+ \pi^- \pi^-) + \sigma(\pi^0 p \to \Sigma^- K^0 \pi^+ \pi^+)$$
$$+\sigma(\pi^0 p \to \Sigma^+ K^0 \pi^+ \pi^-) + \sigma(\pi^+ p \to \Sigma^- K^+ \pi^+ \pi^+) + \sigma(\pi^+ p \to \Sigma^+ K^+ \pi^+ \pi^-)$$
$$= 2\sigma(\pi^- p \to \Sigma^0 K^0 \pi^0 \pi^0) + \sigma(\pi^- p \to \Sigma^- K^+ \pi^0 \pi^0) + \sigma(\pi^- p \to \Sigma^0 K^+ \pi^0 \pi^-)$$
$$+\sigma(\pi^0 p \to \Sigma^0 K^0 \pi^+ \pi^0) + \sigma(\pi^0 p \to \Sigma^+ K^0 \pi^0 \pi^0) + 2\sigma(\pi^0 p \to \Sigma^0 K^+ \pi^0 \pi^0)$$
$$+\sigma(\pi^+ p \to \Sigma^0 K^+ \pi^+ \pi^0) + \sigma(\pi^+ p \to \Sigma^+ K^+ \pi^0 \pi^0)$$

$$\sigma(\pi^- p \to \Sigma^- K^+ \pi^0 \pi^0) + \sigma(\pi^0 p \to \Sigma^- K^0 \pi^+ \pi^+) + \sigma(\pi^0 p \to \Sigma^0 K^0 \pi^+ \pi^0)$$
$$+3\sigma(\pi^0 p \to \Sigma^+ K^0 \pi^0 \pi^0) + \sigma(\pi^0 p \to \Sigma^+ K^0 \pi^+ \pi^-) + 2\sigma(\pi^0 p \to \Sigma^- K^+ \pi^+ \pi^0)$$
$$+2\sigma(\pi^0 p \to \Sigma^0 K^+ \pi^0 \pi^0) + 2\sigma(\pi^0 p \to \Sigma^+ K^+ \pi^0 \pi^-) + \sigma(\pi^+ p \to \Sigma^+ K^+ \pi^0 \pi^0)$$
$$= 2\sigma(\pi^- p \to \Sigma^0 K^0 \pi^+ \pi^-) + \sigma(\pi^- p \to \Sigma^- K^+ \pi^+ \pi^-) + \sigma(\pi^- p \to \Sigma^0 K^+ \pi^0 \pi^-)$$
$$+\sigma(\pi^- p \to \Sigma^+ K^+ \pi^- \pi^-) + 2\sigma(\pi^+ p \to \Sigma^0 K^0 \pi^+ \pi^+) + \sigma(\pi^+ p \to \Sigma^- K^+ \pi^+ \pi^+)$$
$$+\sigma(\pi^+ p \to \Sigma^0 K^+ \pi^+ \pi^0) + \sigma(\pi^+ p \to \Sigma^+ K^+ \pi^+ \pi^-)$$

Appendix C

The $\pi^+ p \to K^+\Sigma^+$ Legendre coefficients with p_π from 1282 up to 2473 MeV/c

Table C.1 summarises the 9 first Legendre coefficients extracted from the differential cross sections published in [98]. The reaction studied is $\pi^+ p \to K^+\Sigma^+$ with the pion momentum ranging from 1282 to 2473 MeV/c. The coefficients were determined using a ROOT minimisation with a smoothness constraint.

Table C.1: Legendre coefficients extracted from differential cross sections published in [98].

P_{lab} (MeV/c)	A_0	A_1	A_2	A_3	A_4	A_5	A_6	A_7	A_8	χ^2/NDF
1282	0.120	-0.030	-0.011	0.121	-0.001	-0.012	-0.026	0.008	-0.008	1.476
1328	0.144	-0.029	-0.014	0.135	0.018	0.007	-0.020	-0.004	-0.003	1.665
1377	0.175	-0.033	0.006	0.168	0.032	0.010	-0.003	0.016	-0.004	1.240
1419	0.203	-0.023	0.004	0.201	0.058	0.031	-0.025	-0.005	-0.028	1.330
1490	0.247	-0.042	0.111	0.174	0.142	-0.015	0.059	-0.027	-0.004	1.289
1518	0.264	-0.043	0.142	0.189	0.175	-0.003	0.089	-0.055	-0.023	0.861
1582	0.247	-0.018	0.138	0.176	0.161	0.008	0.084	-0.031	-0.008	1.177
1614	0.266	-0.007	0.174	0.181	0.195	0.039	0.118	-0.003	-0.039	1.094
1687	0.259	0.015	0.170	0.165	0.211	0.075	0.162	-0.036	-0.009	1.155
1712	0.261	0.021	0.199	0.158	0.252	0.088	0.192	-0.003	-0.018	1.781
1775	0.267	0.037	0.226	0.133	0.260	0.107	0.170	-0.003	-0.007	1.201
1808	0.256	0.066	0.231	0.108	0.269	0.104	0.180	-0.020	0.030	1.033
1879	0.230	0.076	0.220	0.102	0.249	0.072	0.153	-0.063	0.002	1.914
1906	0.262	0.065	0.202	0.110	0.233	0.082	0.185	-0.025	-0.031	1.194
1971	0.265	0.085	0.218	0.100	0.263	0.131	0.165	-0.048	-0.015	1.108
1997	0.238	0.085	0.207	0.056	0.224	0.122	0 .154	-0.009	-0.027	0.981
2067	0.259	0.103	0.186	0.081	0.203	0.181	0.148	-0.008	-0.063	1.011
2099	0.246	0.158	0.183	0.112	0.200	0.200	0.114	0.001	-0.085	0.779
2152	0.242	0.121	0.224	0.064	0.209	0.188	0.174	0.041	-0.086	1.339
2197	0.248	0.101	0.230	0.051	0.218	0.223	0.211	-0.013	-0.058	1.491
2241	0.252	0.121	0.246	0.061	0.186	0.199	0.161	0.044	-0.070	1.129
2291	0.254	0.154	0.235	0.125	0.170	0.269	0.208	0.092	-0.071	1.324
2344	0.264	0.144	0.279	0.110	0.242	0.254	0.215	0.087	-0.040	0.911
2379	0.245	0.172	0.246	0.114	0.206	0.278	0.237	0.133	-0.040	1.239
2437	0.262	0.167	0.315	0.106	0.286	0.249	0.281	0.150	0.016	1.308
2473	0.281	0.158	0.347	0.095	0.344	0.230	0.345	0.083	0.088	1.306

Appendix D

Variance minimisation

One of the main theorems used in chapter V is that minimal uncertainties for a given number of events are achieved when all the importances of strange particles are equal. Two approaches have been proposed to calculate the uncertainties: the natural approach via calculating the variance and a simplified approach with a direct calculation of relative uncertainties.

In this annexe, the proof of this theorem is given.

D.1 Variance

We start with the definition of the variance and the expected value proposed in chapter V, *i.e.*,

$$E(X) = \frac{\sum_{i=1}^{M} w_i x_i}{M}, \tag{D.1}$$

$$V(X) = \frac{\sum_{i=1}^{M} (w_i x_i - E(X))^2}{N}, \tag{D.2}$$

with w_i the importance of the i^{th} observation x_i of the observable X and N the number of events.

The summation is over all particles, *i.e.*, $x_i = 0$ or 1. Therefore, a set of data will be of the shape:

$$W = \begin{pmatrix} w_1 \\ \vdots \\ w_m \\ w_{m+1} \\ \vdots \\ w_M \end{pmatrix} \qquad \text{and} \qquad X = \begin{pmatrix} 1 \\ \vdots \\ 1 \\ 0 \\ \vdots \\ 0 \end{pmatrix} \tag{D.3}$$

with W the set of weights associated to the set of observation X. Here, $x_i = 1$ for $i \leq m$ and $x_i = 0$ otherwise.

An important constraint is that the expected value $E(X)$ must remain unchanged.

$$\begin{aligned} 0 \stackrel{!}{=} \partial E(X) &= \frac{1}{N} \quad \partial \left(\sum_{i=1}^{M} w_i x_i \right) \\ &= \frac{1}{N} \quad \partial \left(\sum_{i=1}^{m} w_i \right) \end{aligned} \tag{D.4}$$

Here, $\stackrel{!}{=}$ stands for "must be equal". eq. D.4 removes one degree of freedom for W. Here, we choose w_m:

$$\partial w_m \stackrel{!}{=} -\sum_{i=1}^{m-1} \partial w_i \tag{D.5}$$

From this:

$$\frac{\partial w_m}{\partial w_j} \stackrel{!}{=} -1 \qquad \forall j \in [1, m-1] \tag{D.6}$$

The variance is at a local extremum if, and only if, any partial derivate of the variance is zero. It can be written as:

$$0 \stackrel{!}{=} \partial V(X) \quad \Leftrightarrow \quad \frac{\partial V(X)}{\partial w_j} = 0 \qquad \forall j \in [1, m-1] \cup [m+1, M] \tag{D.7}$$

It is trivial to show that:

$$\frac{\partial V(X)}{\partial w_j} = 0 \qquad \forall j \in [m+1, M] \tag{D.8}$$

Thus, the variance is at a local extremum when:

$$0 = \frac{\partial V(X)}{\partial w_j} = \frac{1}{M} \frac{\partial}{\partial w_j} \sum_{i=1}^{M} (w_i x_i - E(X))^2 \qquad \forall j \in [1, m-1] \tag{D.9}$$

Then, we have:

$$\begin{aligned} 0 \stackrel{!}{=} \frac{\partial V(X)}{\partial w_j} &= \frac{1}{M} \frac{\partial}{\partial w_j} \left[(w_j x_j - E(X))^2 + (w_m x_m - E(X))^2 \right] \quad \forall j \in [1, m-1] \\ &= \frac{1}{M} \left(2x_j (w_j x_j - E(X)) - 2x_m (w_m x_m - E(X)) \right) \end{aligned} \tag{D.10}$$

$$x_j (w_j x_j - E(X)) \stackrel{!}{=} x_m (w_m x_m - E(X)) \qquad \forall j \in [1, m-1] \tag{D.11}$$

From eq. D.3, we know that: $x_j = 1 = x_m$. This leads to the conclusion that the variance is at a local extremum when:

$$w_j = w_m \qquad \forall j \in [1, m-1] \tag{D.12}$$

The second derivate should be calculated to know if the extremum is a minimum or a maximum:

$$\begin{aligned} \frac{\partial^2 V(X)}{\partial {w_j}^2} &= \frac{\partial}{\partial w_j} \left(\frac{1}{M} \left(2x_j (w_j x_j - E(X)) - 2x_m (w_m x_m - E(X)) \right) \right) \\ &= \frac{2}{M} \left(x_j^2 + x_m^2 \right) = \frac{4}{M} > 0 \qquad \forall j \in [1, m-1] \end{aligned} \tag{D.13}$$

Therefore, $w_j = w_m \; \forall j \in [1, m-1]$ is a local minimum and, since it is the only one, we can conclude that the minimal variance for a given number of events is achieved when all w_j for $j \leq m$, which are the strange particle importances, are equal.

D.2 Relative uncertainties

The formula given in chapter V for the relative uncertainties is:

$$relat.\ uncer. = RU(X) = \frac{\sqrt{\sum (w_i x_i)^2}}{\sum w_i x_i}, \tag{D.1}$$

We restart from eq. D.7 changing $V(X)$ by $RU(X)$:

$$0 \stackrel{!}{=} \partial RU(X) \quad \Leftrightarrow \quad \frac{\partial RU(X)}{\partial w_j} \stackrel{!}{=} 0 \qquad \forall j \in [1, m-1] \cup [m+1, M] \tag{D.2}$$

Once again, it is trivial to show that:

$$\frac{\partial RU(X)}{\partial w_j} = 0 \qquad \forall j \in [m+1, M] \tag{D.3}$$

Thus, a relative uncertainty is at a local extremum when:

$$\begin{aligned} 0 = \frac{\partial RU(X)}{\partial w_j} &= \frac{\partial}{\partial w_j} \frac{\sqrt{\sum (w_i x_i)^2}}{\sum w_i x_i} \\ &= \frac{N}{E(X)} \frac{\partial}{\partial w_j} \sqrt{\sum (w_i x_i)^2} \\ &= \frac{N}{2\ E(X)} \frac{\frac{\partial}{\partial w_j} \sum (w_i x_i)^2}{\sqrt{\sum (w_i x_i)^2}} \\ &= \frac{N}{E(X)} \frac{x_j^2 w_j - x_m^2 w_m}{\sqrt{\sum (w_i x_i)^2}} \qquad \forall j \in [1, m-1] \end{aligned} \tag{D.4}$$

Considering $x_k = 1$ for $k \leq m$, we deduce that the relative uncertainty is at a local extremum when:

$$w_j = w_m \qquad \forall j \in [1, m-1] \tag{D.5}$$

With the second derivative we get:

$$\begin{aligned} \frac{\partial^2 RU(X)}{\partial {w_j}^2} &= \frac{N}{E(X)} \frac{\partial}{\partial w_j} \frac{x_j^2 w_j - x_m^2 w_m}{\sqrt{\sum (w_i x_i)^2}} \\ &= \frac{N}{E(X)} \frac{\sqrt{\sum (w_i x_i)^2} \frac{\partial}{\partial w_j} (x_j^2 w_j - x_m^2 w_m) - (x_j^2 w_j - x_m^2 w_m) \frac{\partial}{\partial w_j} \sqrt{\sum (w_i x_i)^2}}{\sum (w_i x_i)^2} \\ &= \frac{N}{E(X)} \frac{2}{\sqrt{\sum (w_i x_i)^2}} > 0 \qquad \forall j \in [1, m-1] \end{aligned} \tag{D.6}$$

Thus, $w_j = w_m\ \forall j \in [1, m-1]$ is once again a local minimum and the only one. Therefore, the minimal relative uncertainty for a given number of events is achieved when all w_j for $j \leq m$, which are the strange particle importances, are equal.

Appendix E

Vertex cross section ratio

Here, some examples for calculations of cross section ratios are shown. This helps understanding the biasing steps of the variance reduction scheme.

E.1 Example 1

In the first example (Figure E.1) I consider two successive binary collisions. The two non-strange particles at the origin of the vertex A are considered without any history. Let us assume that the total cross section for vertex A is 20 mb, with the reaction cross section for the production of strangeness is 0.1 mb and therefore the non-strangeness production cross section is 19.9 mb. Our goal is an increase of the total strangeness production by a factor of 10 (= bias factor).

It is important to remember, to say that the probability of creation of a particle has been increased by 10 is equivalent to say that its importance is $W = 1/10$ (see eq. V.1).

Because initial particles in A have no history, the probability of strangeness production at this time of the cascade is directly proportional to the strangeness production cross section. This means, to increase the probability of strangeness production by a factor of 10, the corresponding cross section should be multiplied by 10. Therefore, the modified strangeness production cross section is 1 mb and, because the total cross section should be conserved, the modified non-strangeness production cross section is 19 mb.

At this stage of the variance reduction scheme the cascade is biased. Now, the vertex cross section ratio of vertex A should be determined. The vertex cross section ratio is the ratio of the event importance before versus the same value after this vertex. This ratio is directly equal to the inverse of the cross

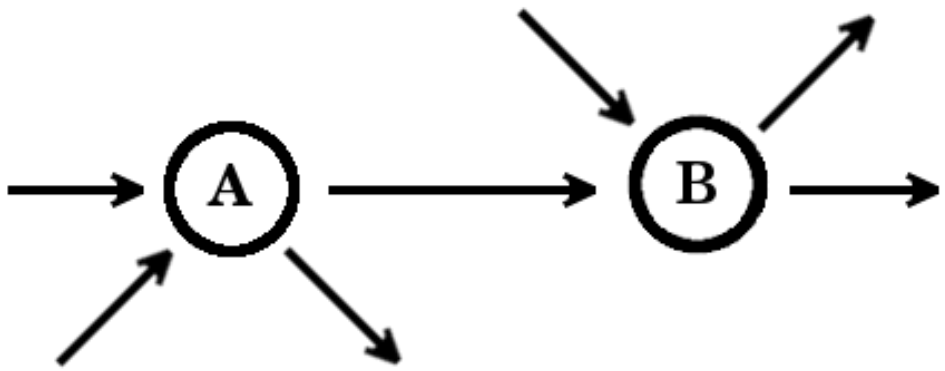

Figure E.1: Example of a basic intranuclear cascade represented as a time ordered graph. Circles and arrows represent binary collisions and the particles propagating, respectively.

section multiplying factor of the chosen channel. This means that the vertex cross section ratio will be equal, in this case, to 0.1 $mb/1\ mb = 0.1$ if strangeness is produced and equal to 19.9 $mb/19\ mb \simeq 1.047$ otherwise. Let us assume that no strange particle is produced. At this stage, the probability of realisation for this cascade is decreased by a factor 1.047 and the importances of outgoing particles are increased by 1.047. In INCL, the cross section ratio is registered for future uses.

Let us assume that one of the particles produced in vertex A collide with another non-strange particle without history in vertex B. We want to increase the probability of creating strange particles by a factor of 10. Therefore, the importance of a strange particle produced in vertex B should be $W = 0.1$. The importance is the product of every cross section ratio on the path:

$$0.1 = W = CSR(A) \times CSR(B). \tag{E.1}$$

Therefore, if a strange particle is produced, the cross section ratio of vertex B should be $CSR(B)_S = 1/(10 \times CSR(A))$. This determines the modified strangeness production cross section of this vertex ($\sigma'_S = \sigma_S / CSR(B)_S$), the modified non-strangeness production cross section ($\sigma'_{NS} = \sigma_{tot} - \sigma'_S$), and the cross section ratio of vertex B in case of non-strangeness production ($CSR(B)_{NS} = \sigma_{NS}/\sigma'_{NS}$).

In the general case, the importance of a vertex following a set K of previous vertices and with strange particles in its final state must be:

$$CSR(X) = \frac{1}{\text{bias ratio} \times \prod_{I \in K} CSR(I)}. \tag{E.2}$$

E.2 Example 2

The second example in Figure E.2 illustrates the case of branch recombination. Here, a particle coming from vertex B, itself induced by a particle from vertex A, collides with a particle directly produced by vertex A.

Eq. E.2 gives the $CSR(C)$ in case of strangeness production.

$$CSR(C) = \frac{1}{\text{bias ratio} \times CSR(A) \times CSR(B)}. \tag{E.1}$$

We also know $CSR(B)$, which produced strangeness:

$$CSR(B) = \frac{1}{\text{bias ratio} \times CSR(A)}. \tag{E.2}$$

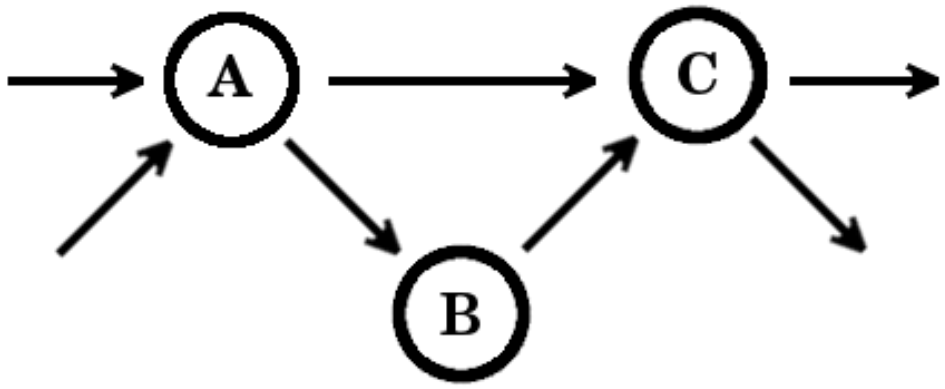

Figure E.2: Same as Figure E.1 with three vertices and a branch recombination.

Therefore $CSR(C) = 1$. In this case, the cross sections are not modified because the probability to reach the initial state of vertex C has already been increased by a factor equal to the bias ratio.

E.3 Example 3

The last example in Figure E.3 is a more complex case of branch recombination. Let us assume no strange particles were produced in vertices A and B but strangeness production occurred in vertex C. $CSR(A)$ and $CSR(B)$ are determined as given in sect. E.1 in the case of non-strangeness production. $CSR(C)$ follows eq. E.2 because it produced strangeness:

$$CSR(C) = \frac{1}{\text{bias ratio} \times CSR(A)}. \tag{E.1}$$

If strangeness is produced in vertex D, $CSR(D)$ also follows the eq. E.2:

$$\begin{aligned} CSR(D) &= \frac{1}{\text{bias ratio} \times CSR(A) \times CSR(B) \times CSR(C)} \\ &= \frac{1}{CSR(B)}. \end{aligned} \tag{E.2}$$

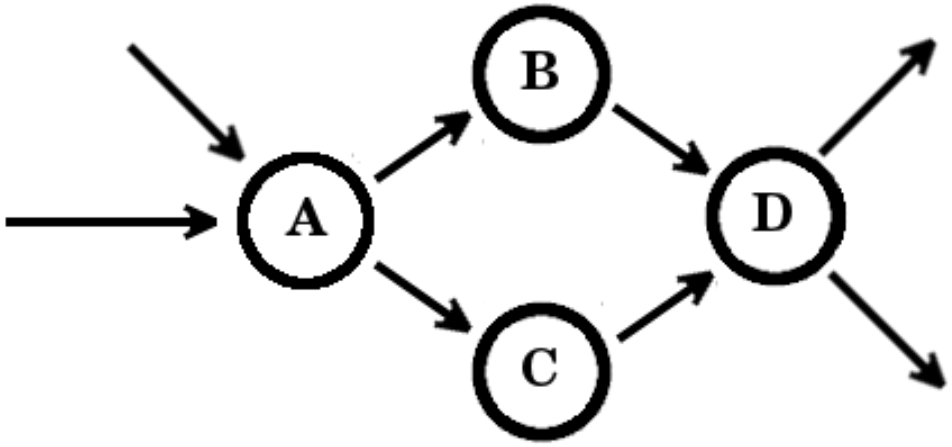

Figure E.3: Same as Figure E.2 with four vertices.

Appendix F

Ellipsoidal meteoroid irradiation

One of the objectives of the CosmicTransmutation model developed during this PhD was the simulation of the irradiation of ellipsoidal meteoroids. Therefore, an algorithm has been created to generate a uniform irradiation for such type of meteoroids. This appendix details the mathematics associated to this algorithm.

The algorithm is divided into three parts. The first part determines the geometrical cross section of the ellipsoidal meteorite when seen from the point of view of a cosmic ray particle with a specific direction of propagation $\overrightarrow{n} = (u, v, w)$. This gives the probability density to hit the meteoroid with this specific direction. Next, the impact location for a uniform irradiation is determined. Finally, the initial position and direction are chosen. In addition, symmetries are considered in order to improve the visualisation in reducing the possibilities of irradiation direction but keeping outputs strictly equivalent to a uniform irradiation.

In order to simplify the problem, the semi-axes of the ellipsoid defines the coordinate system $Oxyz$. Therefore, the equation of a general ellipsoid oriented in the coordinate system $Oxyz$ is:

$$\mathcal{E} : \left(\frac{x}{a}\right)^2 + \left(\frac{y}{b}\right)^2 + \left(\frac{z}{c}\right)^2 = 1, \tag{F.1}$$

with a, b, and c the norms of the semi-axes.

The probability density for a cosmic ray to hit a meteoroid is proportional to the apparent geometrical cross section. Therefore, we want to know the area of the projection of a general ellipsoid on a plane orthogonal to $\overrightarrow{n} = (u, v, w)$.

The orthogonal plane to the direction including the origin is:

$$P(\overrightarrow{n}) : ux + vy + wz = 0. \tag{F.2}$$

The direction will be normalised to be convenient. Therefore, the vector $\overrightarrow{n}$ can be reduced to two parameters (θ, ϕ) as:

$$\begin{cases} u = \sin(\theta)\cos(\phi) \\ v = \sin(\theta)\sin(\phi) \\ w = \cos(\theta) \end{cases} \tag{F.3}$$

The generators of the full cylinder C circumscribed to the ellipsoid $\mathcal{E}$, with the direction (θ, ϕ) orthogonal to P are:

$$L := \begin{cases} x = x_0 + \lambda\ u \\ y = y_0 + \lambda\ v \\ z = z_0 + \lambda\ w \end{cases} \tag{F.4}$$

with M_0 (x_0, y_0, z_0) a dot belonging to the ellipsoid which can be defined in term of (Θ, Φ) by:

$$M_0(\Theta, \Phi) := \begin{cases} x_0 = a\sin(\Theta)\cos(\Phi) \\ y_0 = b\sin(\Theta)\sin(\Phi) \\ z_0 = c\cos(\Theta) \end{cases} \tag{F.5}$$

The equation of the plane tangent to the ellipsoid in M_0 should be determined. The simplest way to determine this equation is to find a vector orthogonal to the ellipsoid in M_0. This vector can be easily constructed by the vectorial product of two vectors tangent to $\mathcal{E}$ in M_0, which are $\frac{d\overrightarrow{M_0}}{d\Theta}$ and $\frac{d\overrightarrow{M_0}}{d\Phi}$.

$$\overrightarrow{e_r} = \frac{d\overrightarrow{M_0}}{d\Theta} \wedge \frac{d\overrightarrow{M_0}}{d\Phi} = \begin{pmatrix} a\cos(\Theta)\cos(\Phi) \\ b\cos(\Theta)\sin(\Phi) \\ -c\sin(\Theta) \end{pmatrix} \wedge \begin{pmatrix} -a\sin(\Theta)\sin(\Phi) \\ b\sin(\Theta)\cos(\Phi) \\ 0 \end{pmatrix} = \begin{pmatrix} bc\sin(\Theta)^2\cos(\Phi) \\ ac\sin(\Theta)^2\sin(\Phi) \\ ab\sin(\Theta)\cos(\Theta) \end{pmatrix} \tag{F.6}$$

Only the direction of the vector is needed to determine the plane. Therefore, the vector $\overrightarrow{e_r}$ can be scaled to simplify the notation as:

$$\widehat{e_r} = \begin{pmatrix} \sin(\Theta)\cos(\Phi)/a \\ \sin(\Theta)\sin(\Phi)/b \\ \cos(\Theta)/c \end{pmatrix} = \begin{pmatrix} x_0/a^2 \\ y_0/b^2 \\ z_0/c^2 \end{pmatrix} \tag{F.7}$$

Using $\widehat{e_r}$, the equation of the tangent plane is given by:

$$T : \frac{xx_0}{a^2} + \frac{yy_0}{b^2} + \frac{zz_0}{c^2} = d \tag{F.8}$$

with d as a parameter that must be determined.

We know that $M_0 \in T$ and $M_0 \in \mathcal{E}$; therefore:

$$T : \frac{xx_0}{a^2} + \frac{yy_0}{b^2} + \frac{zz_0}{c^2} = 1 \tag{F.9}$$

Now, the equation for S, the empty cylinder circumscribe to $\mathcal{E}$, will be calculated. The generators of S are the generators L of the full cylinder C, which belong to T. Combining eq. F.4 and eq. F.9, we get:

$$\frac{(x_0 + \lambda u)x_0}{a^2} + \frac{(y_0 + \lambda v)y_0}{b^2} + \frac{(z_0 + \lambda w)z_0}{c^2} = 1, \tag{F.10}$$

which can be factorised as:

$$\frac{x_0^2}{a^2} + \frac{y_0^2}{b^2} + \frac{z_0^2}{c^2} + \lambda\left(\frac{ux_0}{a^2} + \frac{vy_0}{b^2} + \frac{wz_0}{c^2}\right) = 1. \tag{F.11}$$

This equation should always be true independent of the generator parameter λ for $M_0 \in S$. Knowing $M_0 \in \mathcal{E}$, we have:

$$\frac{ux_0}{a^2} + \frac{vy_0}{b^2} + \frac{wz_0}{c^2} = 0. \tag{F.12}$$

The generators of C, the full cylinder, can be redefined as:

$$L := \begin{cases} 0 = x_0 - x + \lambda\ u \\ 0 = y_0 - y + \lambda\ v \\ 0 = z_0 - z + \lambda\ w \end{cases} \tag{F.13}$$

This new definition therefore leads to the equation:

$$\frac{u(x_0 - x + \lambda u)}{a^2} + \frac{v(y_0 - y + \lambda v)}{b^2} + \frac{w(z_0 - z + \lambda w)}{c^2} = 0 \tag{F.14}$$

Using eq. F.12, the generator parameter λ will be given by:

$$\lambda = \left(\frac{xu}{a^2} + \frac{yv}{b^2} + \frac{zw}{c^2}\right)/\gamma^2, \tag{F.15}$$

with:

$$\gamma^2 = \frac{u^2}{a^2} + \frac{v^2}{b^2} + \frac{w^2}{c^2}. \tag{F.16}$$

Knowing that $M_0 \in \mathcal{E}$, $M_0 \in S$, eq. F.1, and eq. F.4, we have:

$$\begin{aligned} 1 &= \frac{x_0^2}{a^2} + \frac{y_0^2}{b^2} + \frac{z_0^2}{c^2} \\ &= \frac{(x - \lambda u)^2}{a^2} + \frac{(y - \lambda v)^2}{b^2} + \frac{(z - \lambda w)^2}{c^2} \\ &= \frac{x^2}{a^2} + \frac{y^2}{b^2} + \frac{z^2}{c^2} - 2\lambda\left(\frac{xu}{a^2} + \frac{yv}{b^2} + \frac{zw}{c^2}\right) + \lambda^2\left(\frac{u^2}{a^2} + \frac{v^2}{b^2} + \frac{w^2}{c^2}\right) \end{aligned} \tag{F.17}$$

Replacing λ using eq. F.15, we get the equation of the cylinder circumscribed to the ellipsoid that is orthogonal to P:

$$S : 1 = \frac{x^2}{a^2} + \frac{y^2}{b^2} + \frac{z^2}{c^2} - \left(\frac{xu}{a^2} + \frac{yv}{b^2} + \frac{zw}{c^2}\right)^2/\gamma^2 \tag{F.18}$$

The geometrical cross section of the ellipsoid corresponds to the area of the base of the cylinder. The equation of the base is determined by the intersection of the cylinder S and the orthogonal plane P. This is done in two steps. First, the equation of the intersection of the cylinder S with plane Oxy is determined. Next, this intersection is projected on P to obtain the real intersection of S and P after a change of reference frame.

The intersection of the cylinder S with the plane Oxy is given by:

$$E := \begin{cases} z = 0 \\ 1 = \dfrac{x^2}{a^2} + \dfrac{y^2}{b^2} - \left(\dfrac{xu}{a^2} + \dfrac{yv}{b^2}\right)^2/\gamma^2 \end{cases} \tag{F.19}$$

The factorisation of x and y gives the following equation:

$$1 = x^2\left(\frac{1}{a^2} - \frac{u^2}{\gamma^2 a^4}\right) + y^2\left(\frac{1}{b^2} - \frac{v^2}{\gamma^2 b^4}\right) - 2xy\frac{uv}{a^2 b^2 \gamma^2} \tag{F.20}$$

The general formula for a quadric equation can be written as:

$$X^T A X + BX + C = 0 \tag{F.21}$$

with X the position vector, A the symmetric matrix of the quadratic form, B a vector linked to the translation, and C a scalar.

Here, A, B, and C are:

$$A = \begin{pmatrix} \dfrac{1}{a^2} - \dfrac{u^2}{\gamma^2 a^4} & -\dfrac{uv}{a^2 b^2 \gamma^2} \\ -\dfrac{uv}{a^2 b^2 \gamma^2} & \dfrac{1}{b^2} - \dfrac{v^2}{\gamma^2 b^4} \end{pmatrix} \quad ; \quad B = (0, 0) \quad ; \quad C = -1. \tag{F.22}$$

Remark: the definition $A_{01} = A_{10}$ forces the eigenvectors to be orthogonal. In addition to $B = (0, 0)$ and $C = -1$, this makes the eigenvalues of A corresponding to the squared of the inverse norm of the semi-axes and the eigenvectors to the semi-axis directions. This can be proven with a diagonalisation of the matrix A:

$$\begin{aligned} X^T AX &= 1 \\ X^T RDR^{-1}X &= 1 \end{aligned} \tag{F.23}$$

with D the diagonal matrix and R the matrix responsible for changes of reference frame.

Thereafter, the equation becomes:

$$\lambda_1 x'^2 + \lambda_2 y'^2 = 1, \tag{F.24}$$

with λ_1 and λ_2 the eigenvalues of D and, by association, (x', y') a point in the new system of coordinate defined by the transfer matrix R. This equation correspond to an oriented ellipse. Therefore, the lengths a_i of semi-axes can be associated to the eigenvalues as:

$$a_i = \frac{1}{\sqrt{\lambda_i}}. \tag{F.25}$$

Since the eigenvectors of A are orthogonal as for D, the transfer matrix is a simple matrix of rotation. In addition, the semi-axes of an oriented ellipse are following the direction $(1, 0)$ and $(0, 1)$. These vectors are also the eigenvectors of the matrix D since it is diagonal. Reversing the change of reference frame with the reverse rotation matrix, the direction of the semi-axes of the original ellipse correspond to the eigenvectors of A.

There follows, the area of the ellipse resulting of the intersection of S and Oxy is:

$$Area(E) = \pi \times \frac{1}{\sqrt{\lambda_1}} \times \frac{1}{\sqrt{\lambda_2}} = \frac{\pi}{\sqrt{Det(A)}} = \frac{\pi abc\gamma}{|w|} \tag{F.26}$$

A $|w| = 0$ corresponds to a cylinder with a direction in the plane Oxy. In this case, the projection plane can be on the planes Oxz or Oyz and will not change the final result.

This area must now be projected on the plane P. The angle θ' between the two planes gives the geometric cross section of the meteoroid using the formula:

$$\sigma = Area(E) \times |\cos(\theta')| = \pi abc\gamma, \tag{F.27}$$

with σ the area of the ellipse resulting from the intersection of the cylinder S and the plane P. This corresponds to the geometrical cross section of the ellipsoid when seen from the point of view of a cosmic ray particle with a specific direction of propagation $\overrightarrow{n} = (u, v, w)$.

The previous equation is used in the algorithm developed in the CosmicTransmutation model. First, a couple $(\cos(\theta_i), \phi_i)$ is generated uniformly in $([0, 1], [0, 2\pi[)$. Then, a random number r is generated in $[0, 1]$ and, if $\sigma \geq r\sigma_{max}$, the couple $(\cos(\theta_i), \phi_i)$ is kept for the generation of one cosmic ray.

The second part of the algorithm determines the impact location of the irradiation. Here, the intersection of P and S should be considered directly without intermediate projection. The equation of the intersection is:

$$\mathbb{E} := P \cap S : \begin{cases} z = -\dfrac{ux + vy}{w} \\ 1 = x^2 \left(\dfrac{1}{a^2} + \dfrac{u^2}{c^2 w^2} - \dfrac{u^2(c^2 - a^2)^2}{\gamma^2 a^4 c^4} \right) + y^2 \left(\dfrac{1}{b^2} + \dfrac{v^2}{c^2 w^2} - \dfrac{v^2(c^2 - b^2)^2}{\gamma^2 b^4 c^4} \right) \\ \qquad + 2xy \left(\dfrac{uv}{c^2 w^2} - \dfrac{uv(c^2 - a^2)(c^2 - b^2)}{a^2 b^2 c^4 \gamma^2} \right) \end{cases} \tag{F.28}$$

If $w = 0$, we get eq. F.19. Otherwise, a change of reference frame is implemented as: $(\in P) \Leftrightarrow (Z = 0)$ and $X \in Oxy$. This will lead to a two dimensional ellipse equation which will be used to determine the semi-axes. The change of reference frame is written as:

$$\begin{cases} X = -\sin(\phi)x + \cos(\phi)y \\ Y = -\cos(\theta)\cos(\phi)x - \cos(\theta)\sin(\phi)y + \sin(\theta)z \\ Z = \sin(\theta)\cos(\phi)x + \sin(\theta)\sin(\phi)y + \cos(\theta)z \end{cases} \tag{F.29}$$

and its reversion is:

$$\begin{cases} x = -\sin(\phi)X - \cos(\theta)\cos(\phi)Y + \sin(\theta)\cos(\phi)Z \\ y = \cos(\phi)X - \cos(\theta)\sin(\phi)Y + \sin(\theta)\sin(\phi)Z \\ z = \sin(\theta)Y + \cos(\theta)Z \end{cases} \tag{F.30}$$

The equation of the ellipse becomes:

$$\mathbb{E} : \begin{cases} Z = 0 \\ 1 = (\sin(\phi)X + \cos(\theta)\cos(\phi)Y)^2 \left(\dfrac{1}{a^2} + \dfrac{u^2}{c^2w^2} - \dfrac{u^2(c^2-a^2)^2}{\gamma^2 a^4 c^4}\right) \\ \quad + (\cos(\phi)X - \cos(\theta)\sin(\phi)Y)^2 \left(\dfrac{1}{b^2} + \dfrac{v^2}{c^2w^2} - \dfrac{v^2(c^2-b^2)^2}{\gamma^2 b^4 c^4}\right) \\ \quad - 2(\sin(\phi)X + \cos(\theta)\cos(\phi)Y)(\cos(\phi)X - \cos(\theta)\sin(\phi)Y) \left(\dfrac{uv}{c^2w^2} - \dfrac{uv(c^2-a^2)(c^2-b^2)}{a^2b^2c^4\gamma^2}\right) \end{cases} \tag{F.31}$$

After factorisation we have:

$$\mathbb{E} : \begin{cases} Z = 0 \\ 1 = X^2 \left(\dfrac{\sin^2(\phi)}{a^2} + \dfrac{\cos^2(\phi)}{b^2} - \left(\dfrac{\sin(\theta)\cos(\phi)\sin(\phi)(b^2-a^2)}{\gamma a^2 b^2}\right)^2\right) \\ \quad + \ Y^2 \left(\cos^2(\theta)\left(\dfrac{\cos^2(\phi)}{a^2} + \dfrac{\sin^2(\phi)}{b^2}\right) + \dfrac{\sin^2(\theta)}{c^2} \right. \\ \qquad \left. - \dfrac{\cos^2(\theta)\sin^2(\theta)}{\gamma^2 c^4}\left(\dfrac{\cos^2(\phi)b^2(c^2-a^2) + \sin^2(\phi)a^2(c^2-b^2)}{a^2b^2}\right)^2\right) \\ \quad + 2XY \left(\dfrac{\sin(\phi)\cos(\theta)\cos(\phi)}{\gamma^2 a^4 b^4}\right)\Big((b^2-a^2)a^2b^2(\gamma^2 + \sin^2(\theta)/c^2) \\ \qquad + \sin^2(\theta)\left[a^2b^2(\cos^2(\phi) - \sin^2(\phi)) + \sin^2(\phi)a^4 - \cos^2(\phi)b^4\right]\Big) \end{cases} \tag{F.32}$$

To simplify the notation, eq. F.32 is rewritten as:

$$\mathbb{E} : \begin{cases} Z = 0 \\ 1 = X^2 A_{X^2} + \ Y^2 A_{Y^2} + 2XY A_{XY} \end{cases} \tag{F.33}$$

Therefore, the two dimensional symmetric matrix of the quadratic form is given by:

$$A = \begin{pmatrix} A_{X^2} & A_{XY} \\ A_{XY} & A_{Y^2} \end{pmatrix} \tag{F.34}$$

The next steps have analytical solutions, which are well known, and therefore, will not be discussed here. First, the eigenvectors $\overrightarrow{v_1}$ and $\overrightarrow{v_2}$ and eigenvalues λ'_1 and λ'_2 can be calculated. They give the semi-axes in the plane P. Then, the change of the reference frame is reversed using eq. F.30.

Next, the impact location on the ellipse $\mathbb{E}$ is determined. This impact location is characterised by two parameters: Ψ, the angle with $\overrightarrow{v_1}$, and r, the impact parameter. The probability density for a couple of parameters is given by:

$$\frac{d^2p(\Psi,r)}{d\Psi dr} \propto \sqrt{\frac{\cos^2(\Psi)}{\lambda_1'} + \frac{\sin^2(\Psi)}{\lambda_2'}} \times r = R(\Psi) \times r \tag{F.35}$$

with $R(\Psi)$ as the radius of the ellipse along the axis defined by Ψ and with:

$$\begin{cases} \Psi \in [0, 2\pi[\\ r \in [0, 1[\end{cases} \tag{F.36}$$

Actually, both variables are independent and can be generated using the differential probabilities :

$$\frac{dp(\Psi)}{d\Psi} \propto \sqrt{\frac{\cos^2(\Psi)}{\lambda_1'} + \frac{\sin^2(\Psi)}{\lambda_2'}} = R(\Psi) \tag{F.37}$$

$$\frac{dp(r)}{dr} = 2r \tag{F.38}$$

With these two formulae, the two parameters are generated easily in the CosmicTransmutation model.

The last step consists of a simple move back following the direction (u, v, w) to be sure the cosmic ray particles are generated out of the meteoroid.

An additional constrained has been applied to the algorithm for visualisation reasons. Looking at the symmetries of an oriented ellipsoid, the planes Oxy, Oxz, and Oyz are planes of symmetry. Then, the couple (θ, ϕ) are generated in $([0, \pi/2[, [0, \pi/2[)$. This does not change the results of the irradiation but the cosmic rays are generated only in directions with x, y, and z positive.

Appendix G

Example of planet irradiation fluxes

In this appendix, some examples of the rigidity map are displayed.

G.1 Binning

In Figure G.1, I illustrate the impact of the binning of the zenith angle used in the algorithm determining the cut-off rigidity maps on the flux.

In the case not considering the funnel effect, the differences between the two curves are small. In contrast, the case considering the funnel effect presents significant differences. Some of the bumps observed with a binning of 10° are strongly reduced.

Considering the computational time, the final binning retained for the zenith angle is 5°. The computation of the funnel effect is the longest part of the algorithm. In the case not considering the funnel effect, the computational time is relatively short. Smaller bins would not significantly improve the description of the cut-off rigidity map and a reduction will not result in a significant gain of time. On the other hand, the precision obtained in the case considering the funnel effect seems correct keeping a reasonable computation time with a binning of 5°. An augmentation of the binning could remove the small unphysical variations but the time lost is judged unreasonable considering the poor gain of precision for the final

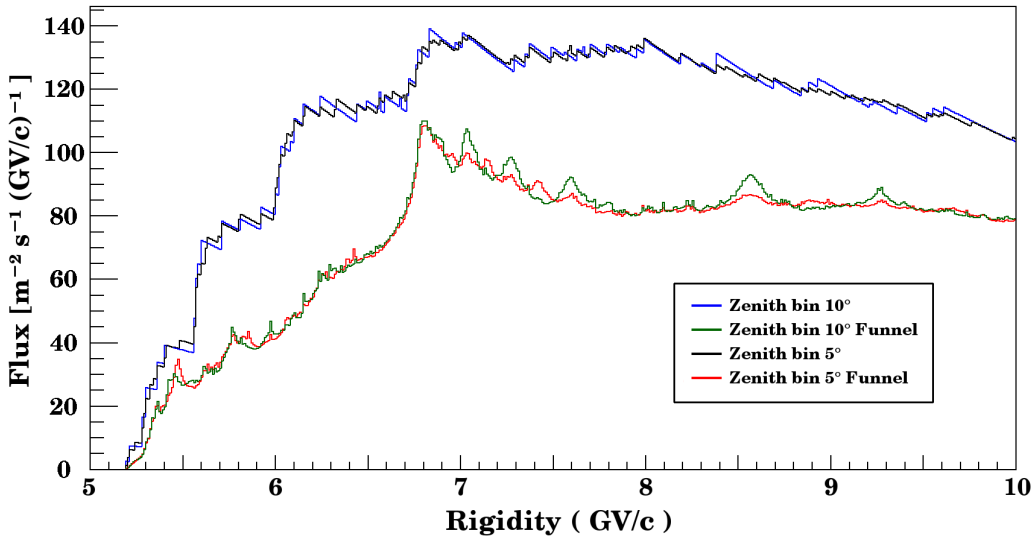

Figure G.1: Comparison of the flux as a function of the rigidity for two different zenith angle binning in the cases considering or not the funnel effect in the same configuration that Figure VII.4.

results. Moreover, the known biases of the algorithm related to the binning makes the improvements meaningless.

G.2 Variation with the latitude

Magnetic fields around planets are various. Moreover, the perception of these magnetic fields highly depends on the location at the surface of the planet. Therefore, when a map of the allowed trajectories is drawn for a specific location (see subsection VII.5.3), this map is not likely to be representative for the other locations elsewhere on the same planet.

Here are plotted some example of cut-off maps for different latitudes.

The geometry used for the following figures is inspired by the Earth's characteristics. It is a spherical planet with a radius of 6378 km and an atmosphere 70 km thick. The magnetic field is a simple dipole with an intensity of 30.2 μT at the top of the atmosphere.

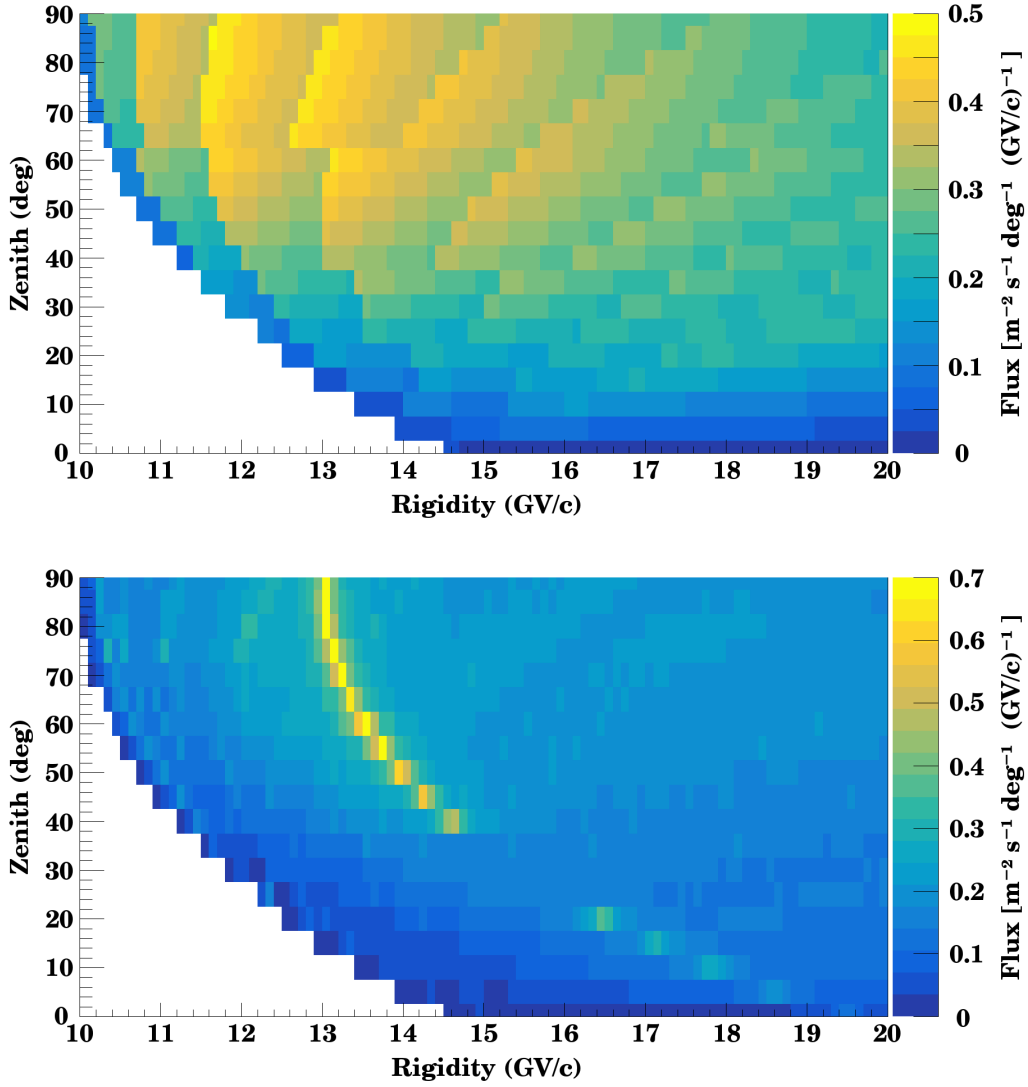

Figure G.2: Comparison of the cut-off maps for latitude 0°. Upper panel: map without considering the funnel effect. Lower panel: map considering the funnel effect.

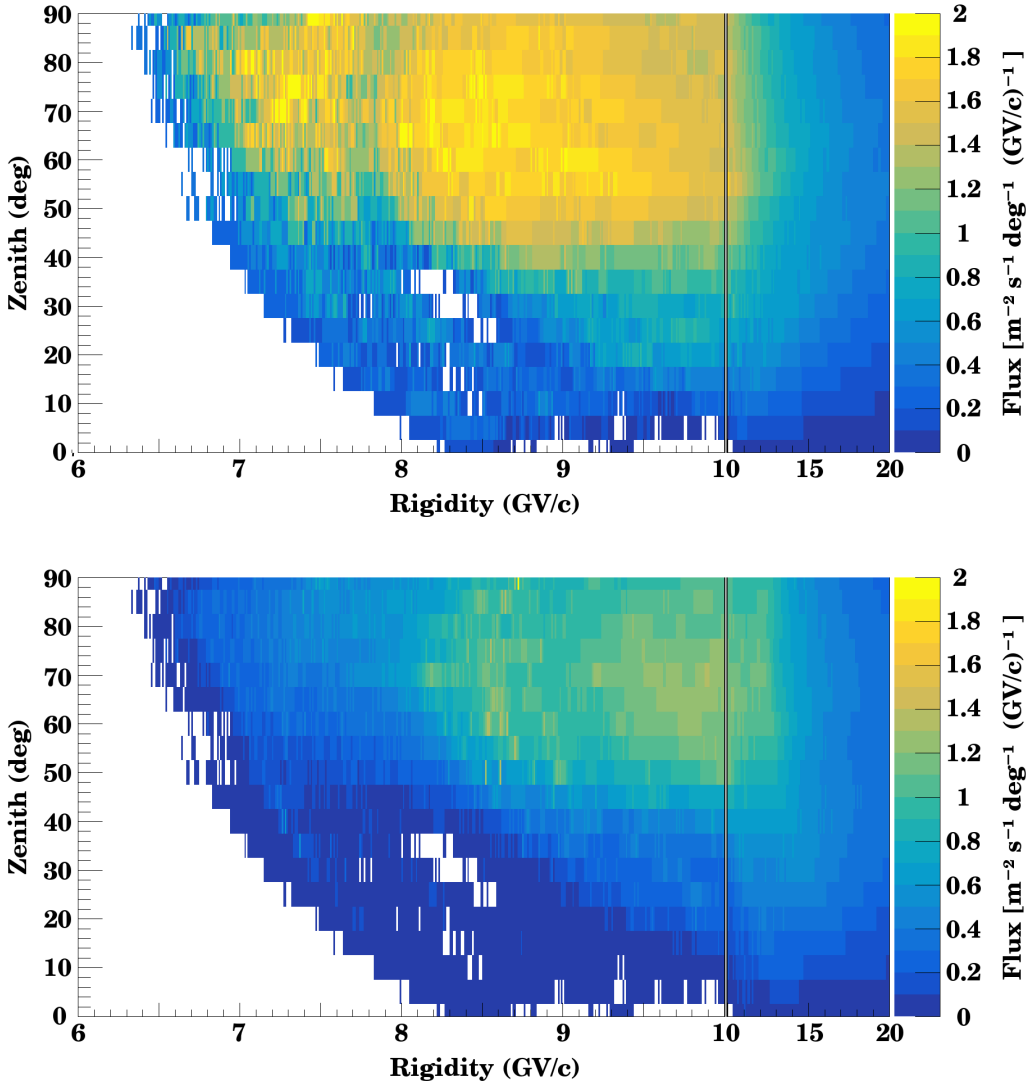

Figure G.3: Same as Figure G.2 for latitude 30°

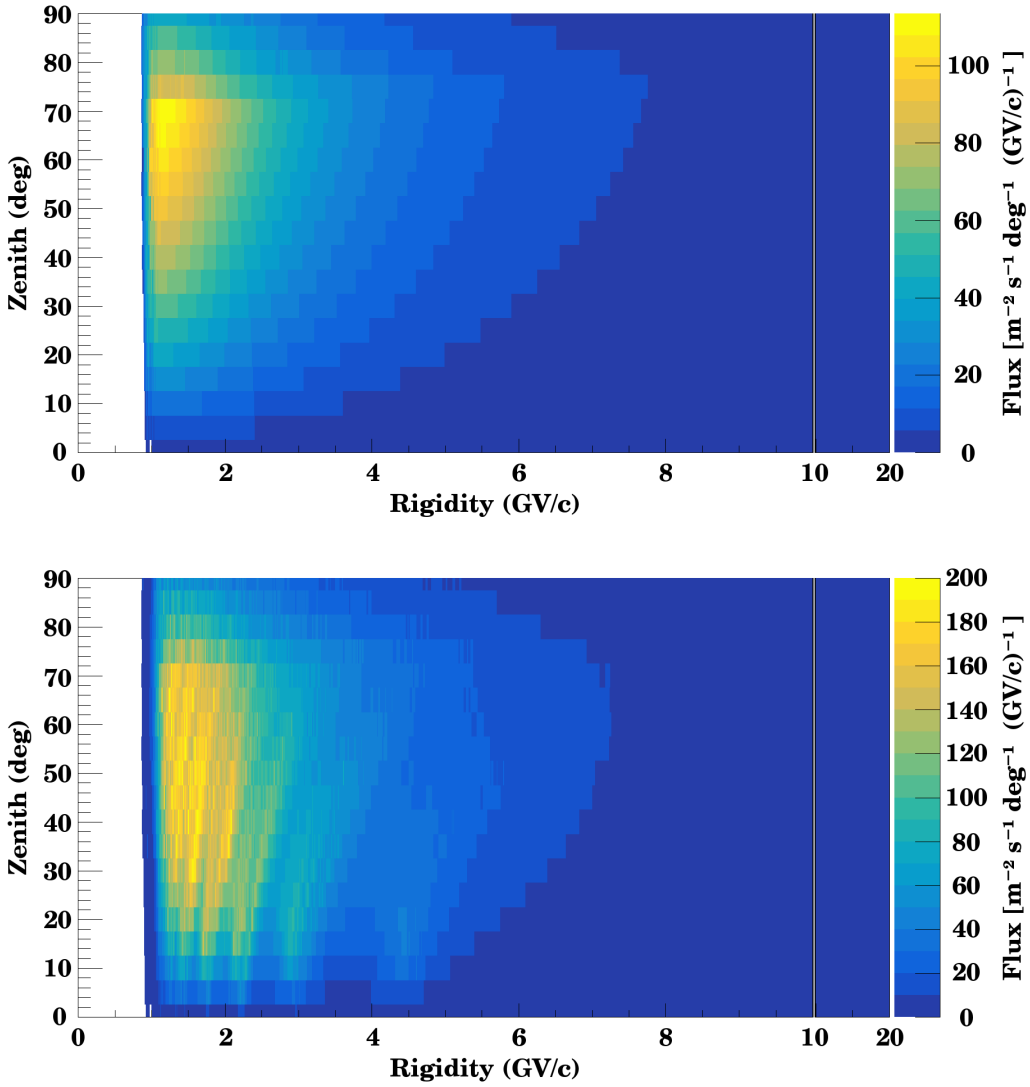

Figure G.4: Same as Figure G.2 for latitude 60°

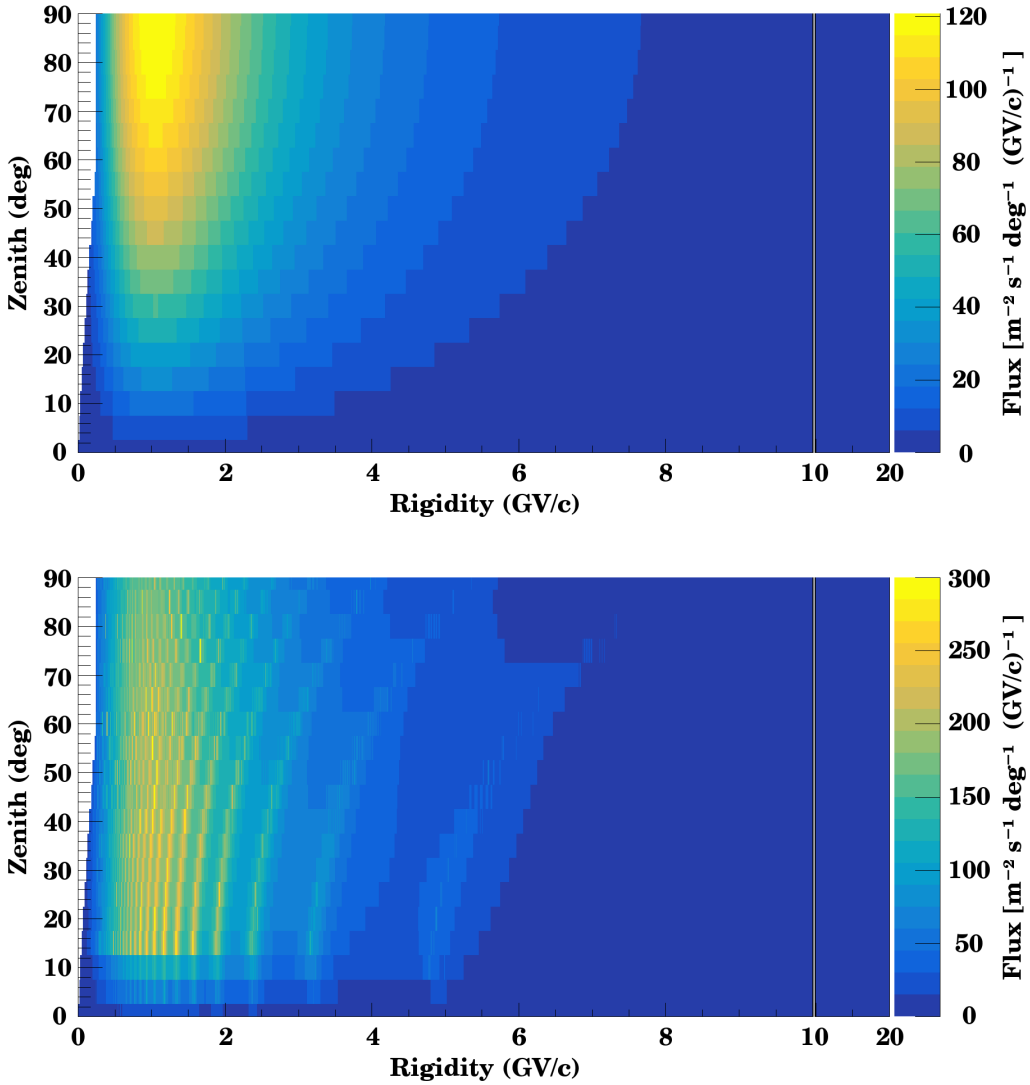

Figure G.5: Same as Figure G.2 for latitude 90°